

Journal of
Mechanics of
Materials and Structures

Volume 4, N° 1

January 2009

 mathematical sciences publishers

JOURNAL OF MECHANICS OF MATERIALS AND STRUCTURES

<http://www.jomms.org>

EDITOR-IN-CHIEF Charles R. Steele
ASSOCIATE EDITOR Marie-Louise Steele
Division of Mechanics and Computation
Stanford University
Stanford, CA 94305
USA

BOARD OF EDITORS

D. BIGONI University of Trento, Italy
H. D. BUI École Polytechnique, France
J. P. CARTER University of Sydney, Australia
R. M. CHRISTENSEN Stanford University, U.S.A.
G. M. L. GLADWELL University of Waterloo, Canada
D. H. HODGES Georgia Institute of Technology, U.S.A.
J. HUTCHINSON Harvard University, U.S.A.
C. HWU National Cheng Kung University, R.O. China
IWONA JASIUK University of Illinois at Urbana-Champaign
B. L. KARIHALOO University of Wales, U.K.
Y. Y. KIM Seoul National University, Republic of Korea
Z. MROZ Academy of Science, Poland
D. PAMPLONA Universidade Católica do Rio de Janeiro, Brazil
M. B. RUBIN Technion, Haifa, Israel
Y. SHINDO Tohoku University, Japan
A. N. SHUPIKOV Ukrainian Academy of Sciences, Ukraine
T. TARNAI University Budapest, Hungary
F. Y. M. WAN University of California, Irvine, U.S.A.
P. WRIGGERS Universität Hannover, Germany
W. YANG Tsinghua University, P.R. China
F. ZIEGLER Technische Universität Wien, Austria

PRODUCTION


PAULO NEY DE SOUZA Production Manager
SHEILA NEWBERY Senior Production Editor
SILVIO LEVY Scientific Editor

See inside back cover or <http://www.jomms.org> for submission guidelines.

Regular subscription rate: \$600 a year (print and electronic); \$460 a year (electronic only).

Subscriptions, requests for back issues, and changes of address should be sent to contact@mathscipub.org or to Mathematical Sciences Publishers, 798 Evans Hall, Department of Mathematics, University of California, Berkeley, CA 94720-3840.

©Copyright 2009. Journal of Mechanics of Materials and Structures. All rights reserved.

 mathematical sciences publishers

ANALYSIS OF MULTIPLE AXISYMMETRIC ANNULAR CRACKS

EBRAHIM ASADI, SHAHRIAR FARIBORZ AND MOJTABA AYATOLLAHI

The solution of axisymmetric Volterra climb and glide dislocations in an infinite domain is obtained by means of the Hankel transforms. The distributed dislocation technique is used to construct integral equations for a system of coaxial annular cracks where the domain is under axisymmetric tensile load. These equations are solved numerically to obtain the dislocation density on the surfaces of the cracks. The dislocation densities are employed to determine stress intensity factors for annular and penny-shaped cracks.

1. Introduction

Large elastic bodies containing multiple interacting cracks situated far from the boundary may be considered as infinite regions weakened by cracks. An infinite domain containing a penny-shaped crack under axisymmetric tension is the simplest three-dimensional problem in fracture mechanics. The solution of this problem dates back to an article by [Sneddon \[1946\]](#), wherein the exact solution to the problem was derived. The solution of a penny-shaped crack under general loading in the form of Fourier series is rendered in the book by [Kassir and Sih \[1975\]](#). [Guidera and Lardner \[1975\]](#) used the Somigliana formula to analyze a penny-shaped crack. The component of displacement discontinuity was presented as the solution of a system of three integral equations. A penny-shaped crack in a transversely isotropic infinite body subjected to arbitrary normal and shear tractions was solved by [Fabrikant \[1987\]](#). [Collins \[1962\]](#) treated the problem of an infinite elastic solid containing two parallel penny-shaped cracks where the axis of symmetry of the problem passed through the centers of the cracks. In his study, the representation of displacement field devised by [Green and Zerna \[1954\]](#) was used to reduce the problem to the solution of a system of four Fredholm integral equations. The formulation, however, becomes extremely involved where the number of cracks increases. [Isida et al. \[1985\]](#) analyzed two elliptical parallel cracks by means of the body force method. Interaction among multiple penny-shaped cracks was studied by several investigators, see for example [\[Kachanov and Laures 1989\]](#) and for the most recently published article [\[Zhan and Wang 2006\]](#). In the former article, the method developed by the first author for the analysis of several cracks was employed to study the interaction of arbitrarily located penny-shaped cracks in a three-dimensional body. In the latter study, the boundary collocation technique and average method for surface traction of cracks were used to solve the governing equations. The stress intensity factor for an annular crack situated in an infinite space under general loading was determined by [Nied and Erdogan \[1983\]](#) and by [Selvadurai and Singh \[1985\]](#) and [Clements and Ang \[1988\]](#) under axisymmetric normal loading. Eigenstrain solutions for axisymmetric crack problems in terms of Lipschitz–Hankel integrals was derived by [Korsunsky \[1995\]](#). The stress fields are hypersingular at the eigenstrain ring yielding hypersingular integral equations for the ensuing crack problem.

Keywords: infinite domain, axisymmetric, annular crack, Volterra dislocation, dislocation density, Hankel transform.

In the present paper, utilizing the Popkovich–Neuber potentials, the solution of axisymmetric climb and glide edge dislocations is carried out by means of the Hankel transformation in an infinite isotropic domain. The stress components exhibit the well-known Cauchy-type singularity at dislocation location. The distributed dislocation method Hills et al. [1996] is employed to formulate integral equations for the dislocation density functions on a system of annular and/or penny-shaped coaxial cracks under the axisymmetric remote tensile load. These equations are of Cauchy singular type which are solved numerically. The modes I and II stress intensity factors at the crack edges are obtained and the interaction of two coaxial cracks is investigated. The interaction of annular cracks embedded in a half-space or strip under axisymmetric conditions may be analyzed by the procedure devised in this article.

2. Solution of the Volterra ring dislocation

In the linear theory of elasticity for isotropic materials neglecting the body force, the displacement vector \underline{u} may be represented in terms of a harmonic vector \underline{B} and a harmonic scalar B_0 that is, the well-known Popkovich–Neuber solution [Lur'e 1964] as

$$\underline{u} = \underline{B} - \frac{1}{4(1-\nu)} \text{grad}(\underline{R} \cdot \underline{B} + B_0), \quad (1)$$

where ν is the Poisson's ratio of the material and \underline{R} is the position vector. For axisymmetric problems it is convenient to utilize cylindrical coordinates and choose $\underline{B} = B_3 \underline{k}$, where \underline{k} is the unit vector in axial direction. Therefore, the components of displacement vector by virtue of $\underline{R} = r \underline{e}_r + z \underline{e}_z$ yield

$$u_r = -\frac{1}{4(1-\nu)} \left(\frac{\partial B_0}{\partial r} + z \frac{\partial B_3}{\partial r} \right), \quad u_\theta = 0, \quad u_z = \frac{3-4\nu}{4(1-\nu)} B_3 - \frac{1}{4(1-\nu)} \left(\frac{\partial B_0}{\partial z} + z \frac{\partial B_3}{\partial z} \right). \quad (2)$$

The constitutive relationships in axisymmetric problems of linear elasticity are

$$\begin{aligned} \sigma_{rr} &= \frac{2\mu}{1-2\nu} \left[(1-\nu) \frac{\partial u_r}{\partial r} + \nu \left(\frac{u_r}{r} + \frac{\partial u_z}{\partial z} \right) \right], & \sigma_{\theta\theta} &= \frac{2\mu}{1-2\nu} \left[(1-\nu) \frac{u_r}{r} + \nu \left(\frac{\partial u_r}{\partial r} + \frac{\partial u_z}{\partial z} \right) \right], \\ \sigma_{zz} &= \frac{2\mu}{1-2\nu} \left[(1-\nu) \frac{\partial u_z}{\partial z} + \nu \left(\frac{u_r}{r} + \frac{\partial u_r}{\partial r} \right) \right], & \sigma_{rz} &= \mu \left(\frac{\partial u_r}{\partial z} + \frac{\partial u_z}{\partial r} \right), & \sigma_{r\theta} &= \sigma_{\theta z} = 0, \end{aligned} \quad (3)$$

where μ is the elastic shear modulus of the material. Substituting (2) into (3), we arrive at the stress components in terms of the potentials B_0 and B_3 :

$$\begin{Bmatrix} \sigma_{rr} \\ \sigma_{\theta\theta} \\ \sigma_{zz} \\ \sigma_{rz} \end{Bmatrix} = \frac{\mu}{2(1-\nu)} \begin{Bmatrix} 2\nu \frac{\partial B_3}{\partial z} - \frac{\partial^2}{\partial r^2} (B_0 + z B_3) \\ 2\nu \frac{\partial B_3}{\partial z} - \frac{1}{r} \frac{\partial}{\partial r} (B_0 + z B_3) \\ 2(1-\nu) \frac{\partial B_3}{\partial z} - \left(\frac{\partial^2 B_0}{\partial z^2} + z \frac{\partial^2 B_3}{\partial z^2} \right) \\ (1-2\nu) \frac{\partial B_3}{\partial r} - \frac{\partial}{\partial r} \left(\frac{\partial B_0}{\partial z} + z \frac{\partial B_3}{\partial z} \right) \end{Bmatrix}. \quad (4)$$

The conditions representing a Volterra-type climb ring dislocation located at $r = a$, $z = 0$ in a three dimensional infinite domain with the line of dislocation in radial direction are

$$u_z(r, 0^+) - u_z(r, 0^-) = \delta_z H(a - r). \quad (5)$$

The conditions for a glide dislocation read as

$$u_r(r, 0^+) - u_r(r, 0^-) = \delta_r H(a - r), \quad (6)$$

where in (5) and (6), δ_z and δ_r designate the dislocation Burgers vectors and $H(\dots)$ is the Heaviside step-function. Moreover, the continuity of traction vector on the line of dislocation requires that

$$\sigma_{zz}(r, 0^+) = \sigma_{zz}(r, 0^-) \quad \text{and} \quad \sigma_{rz}(r, 0^+) = \sigma_{rz}(r, 0^-). \quad (7)$$

For climb edge dislocation the problem is symmetric with respect to the plane $z = 0$, whereas it is antisymmetric for glide dislocation. Therefore, it is convenient to analyze the two problems separately. For the symmetric problem the half-space $z > 0$ is subjected to the boundary conditions

$$u_z(r, 0) = \frac{\delta_z}{2} H(a - r) \quad \text{and} \quad \sigma_{rz}(r, 0) = 0. \quad (8)$$

The boundary conditions for glide dislocation for the region $z > 0$ are

$$u_r(r, 0) = \frac{\delta_r}{2} H(a - r) \quad \text{and} \quad \sigma_{zz}(r, 0) = 0. \quad (9)$$

Consequently, the dislocation solutions for the climb and glide dislocations reduce to the solutions of two harmonic equations

$$\frac{\partial^2 B_i}{\partial r^2} + \frac{1}{r} \frac{\partial B_i}{\partial r} + \frac{\partial^2 B_i}{\partial z^2} = 0 \quad i = 0, 3, \quad z > 0, \quad (10)$$

subjected to boundary conditions (8) and (9), respectively. The solution to (10) is achieved by means of the Hankel transform. The Hankel transform of order ν of a sufficiently regular function $f(r)$ is defined [Sneddon 1972] as

$$F(\xi) = \int_0^\infty r f(r) J_\nu(\xi r) dr, \quad (11)$$

where $J_\nu(\dots)$ is the Bessel function of first kind of order ν . The inversion of Hankel transform yields

$$f(r) = \int_0^\infty \xi F(\xi) J_\nu(\xi r) d\xi. \quad (12)$$

The zero order Hankel transform of (10), assuming that the potentials are $O(r^{-\alpha})$ as $r \rightarrow \infty$ for some $\alpha > 0.5$, leads to two second order ordinary differential equations

$$\frac{d^2 \bar{B}_i(\xi, z)}{dz^2} - \xi^2 \bar{B}_i(\xi, z) = 0 \quad i = 0, 3, \quad z > 0, \quad (13)$$

where $\bar{B}_0(\xi, z)$ and $\bar{B}_3(\xi, z)$ are zero order Hankel transforms of $B_0(r, z)$ and $B_3(r, z)$, respectively. The solution of (13) and (14), which is finite as $z \rightarrow \infty$, is readily known

$$\bar{B}_i(\xi, z) = Q_i(\xi) e^{-\xi z} \quad i = 0, 3. \quad (14)$$

We substitute boundary conditions (8) and (9) into (2) and (4), take the Hankel transform of the resultant equations and utilize (14) to obtain

$$Q_0(\xi) = (2\nu - 1)a \frac{J_1(\xi a)}{\xi^2} \delta_z, \quad Q_3(r, z) = a \frac{J_1(\xi a)}{\xi} \delta_z \quad (15)$$

for climb and

$$Q_0(\xi) = (\nu - 1)a\pi \frac{\eta(\xi, a)}{\xi^2} \delta_r, \quad Q_3(r, z) = \frac{a\pi}{2} \frac{\eta(\xi, a)}{\xi} \delta_r \quad (16)$$

for glide dislocation. In (16) the function $\eta(\xi, a)$ is defined as

$$\eta(\xi, a) = J_0(\xi a)H_1(\xi a) - J_1(\xi a)H_0(\xi a), \quad (17)$$

where $H_\nu(\dots)$ stands for the Struve function of order ν [Abramowitz and Stegun 1964]. The displacement and stress components in view of (14)–(16), (12), (2) and (4) yield

$$\begin{aligned} u_r &= \frac{a}{4(1-\nu)} \int_0^\infty \left[\delta_z(2\nu - 1 + \xi z)J_1(\xi a) + \pi \delta_r \left(\nu - 1 + \frac{\xi z}{2} \right) \eta(\xi, a) \right] J_1(\xi r) e^{-\xi z} d\xi, \\ u_z &= \frac{a}{4(1-\nu)} \int_0^\infty \left[\delta_z(2(1-\nu) + \xi z)J_1(\xi a) + \frac{\pi \delta_r}{2} (1 - 2\nu + \xi z) \eta(\xi, a) \right] J_0(\xi r) e^{-\xi z} d\xi, \\ \sigma_{rr} &= \frac{\mu a}{2(1-\nu)} \left\{ \delta_z \int_0^\infty J_1(\xi a) \left[\xi(\xi z - 1)J_0(\xi r) + \frac{1}{r}(1 - 2\nu - \xi z)J_1(\xi r) \right] e^{-\xi z} d\xi \right. \\ &\quad \left. + \frac{\pi \delta_r}{2} \int_0^\infty \eta(\xi, a) \left[\xi(\xi z - 2)J_0(\xi r) + \frac{1}{r}(2(1-\nu) - \xi z)J_1(\xi r) \right] e^{-\xi z} d\xi \right\}, \\ \sigma_{\theta\theta} &= \frac{\mu a}{2(1-\nu)} \left\{ \delta_z \int_0^\infty J_1(\xi a) \left[-2\nu \xi J_0(\xi r) + \frac{1}{r}(2\nu - 1 + \xi z)J_1(\xi r) \right] e^{-\xi z} d\xi \right. \\ &\quad \left. + \frac{\pi \delta_r}{2} \int_0^\infty \eta(\xi, a) \left[-2\xi \nu J_0(\xi r) + \frac{1}{r}(2(\nu - 1) + \xi z)J_1(\xi r) \right] e^{-\xi z} d\xi \right\}, \\ \sigma_{zz} &= \frac{-\mu a}{2(1-\nu)} \int_0^\infty \left[\delta_z \xi(1 + \xi z)J_1(\xi a) + \frac{\pi \delta_r}{2} \xi^2 z \eta(\xi, a) \right] J_0(\xi r) e^{-\xi z} d\xi, \\ \sigma_{rz} &= \frac{\mu a}{2(1-\nu)} \int_0^\infty \left[-\delta_z \xi^2 z J_1(\xi a) + \frac{\pi \delta_r}{2} \xi(1 - \xi z) \eta(\xi, a) \right] J_1(\xi r) e^{-\xi z} d\xi, \quad z > 0. \end{aligned} \quad (18)$$

The stress and displacement fields for climb ring dislocation were obtained by Kroupa [1960] using the Galerkin solution of linear elasticity theory and solving the ensuing biharmonic equation. The solution in [Kroupa 1960] may be recovered by putting $\delta_r = 0$ in (18). In order to study the asymptotic behavior of stress components σ_{zz} and σ_{rz} at the dislocation location, we set $z = 0$ in the last two equations in (18), and arrive at

$$\sigma_{zz}(r, 0) = -\frac{\mu a \delta_z}{2(1-\nu)} \int_0^\infty \xi J_1(\xi a) J_0(\xi r) d\xi, \quad (19)$$

$$\sigma_{rz}(r, 0) = \frac{\mu a \pi \delta_r}{4(1-\nu)} \int_0^\infty \xi J_1(\xi r) \eta(\xi, a) d\xi, \quad z > 0.$$

These two integrals can be found in [Gradshteyn and Ryzhik 1980], and substituting their values gives

$$\begin{aligned} \sigma_{zz}(r, 0) &= \frac{\mu \delta_z a}{\pi(1-\nu)} \frac{E(r/a)}{r^2 - a^2}, \quad r < a, \\ \sigma_{rz}(r, 0) &= \frac{\mu \pi a \delta_r}{4(1-\nu)} \left\{ \int_0^\infty \xi J_1(\xi r) \left[J_0(\xi a) \left(H_1(\xi a) - \frac{2}{\pi} - Y_1(\xi a) \right) \right. \right. \\ &\quad \left. \left. - J_1(\xi a) \left(H_0(\xi a) - \frac{2}{\pi \xi a} - Y_0(\xi a) \right) \right] d\xi \right. \\ &\quad \left. - \frac{2}{\pi a r} + \frac{4}{\pi^2} E(r/a) \left[\frac{a/r}{r^2 - a^2} + \frac{1}{a r} \right] \right\}, \quad r < a, \\ \sigma_{zz}(r, 0) &= \frac{\mu \delta_z r}{\pi(1-\nu)} \left[\frac{E(a/r)}{r^2 - a^2} - \frac{K(a/r)}{r^2} \right], \quad r > a, \\ \sigma_{rz}(r, 0) &= \frac{\mu \pi a \delta_r}{4(1-\nu)} \left\{ \int_0^\infty \xi J_1(\xi r) \left[J_0(\xi a) \left(H_1(\xi a) - \frac{2}{\pi} - Y_1(\xi a) \right) \right. \right. \\ &\quad \left. \left. - J_1(\xi a) \left(H_0(\xi a) - \frac{2}{\pi \xi a} - Y_0(\xi a) \right) \right] d\xi \right. \\ &\quad \left. - \frac{2}{r a \pi} + \frac{4}{\pi^2} \left[\frac{E(a/r)}{r^2 - a^2} + \frac{E(a/r) - K(a/r)}{a^2} \right] \right\}, \quad r > a. \end{aligned} \tag{20}$$

In (20) $K(\dots)$ and $E(\dots)$ are the complete elliptic integrals of the first and second kind, and $Y_\nu(\dots)$ is the Bessel function of the second kind of order ν . The integrals in (20) are regular; thus, the stress components are Cauchy singular as $r \rightarrow a$, which is a well-known feature of the stress fields caused by Volterra-type dislocations. It is noteworthy to mention that the assumption of axisymmetry of glide dislocation implies the vanishing of Burgers vector δ_r at the origin of coordinates leading to $\sigma_{rz}(0, 0) = 0$. Moreover, the asymptotic expansion of complete elliptic integral shows that $E(r) = \pi/2 + O(r^2)$ as $r \rightarrow 0$. Therefore, the stress fields in (20) are bounded at the origin.

3. Axisymmetric crack formulation

Let climb and glide dislocations with densities $B_z(\rho)$ and $B_r(\rho)$ respectively be distributed on an annular crack situated at $z = z_0$ with inner radius ρ and outer radius $\rho + d\rho$. The axial and shear stress at a point with coordinates (r, z) due to the above distribution of dislocations on the crack surface are

$$\begin{aligned} \sigma_{zz}(r, z) &= -\frac{\mu}{2(1-\nu)} \left[\rho B_z d\rho \int_0^\infty \xi (1 + \xi |z - z_0|) J_1(\xi \rho) J_0(\xi r) e^{-\xi |z - z_0|} d\xi \right. \\ &\quad \left. + \frac{\rho \pi B_r d\rho}{2} \int_0^\infty \xi^2 \operatorname{sgn}(z - z_0) |z - z_0| \eta(\xi, \rho) J_0(\xi r) e^{-\xi |z - z_0|} d\xi \right], \end{aligned}$$

$$\sigma_{rz}(r, z) = \frac{\mu}{2(1-\nu)} \left[-\rho B_z d\rho \int_0^\infty \xi^2 \operatorname{sgn}(z - z_0) |z - z_0| J_1(\xi\rho) J_1(\xi r) e^{-\xi|z-z_0|} d\xi \right. \\ \left. + \frac{\rho\pi B_r d\rho}{2} \int_0^\infty \xi(1 - \xi|z - z_0|) J_1(\xi r) \eta(\xi, \rho) e^{-\xi|z-z_0|} d\xi \right].$$

Let the medium be weakened by N_1 annular and $N - N_1$ penny-shaped coaxial cracks situated at the axial coordinates z_j , $j = 1, 2, \dots, N$. The inner and outer radii of annular cracks are a_j and b_j , $j = 1, 2, \dots, N_1$ respectively and the radii of penny-shaped cracks are b_j , $j = N_1 + 1, \dots, N$. The cracks configurations may be expressed in parametric form as

$$r_j(s) = r_{cj} + L_j s, \quad -1 < s < 1, \quad j = 1, 2, \dots, N, \quad (21)$$

where $r_{cj} = (b_j + a_j)/2$ and $L_j = (b_j - a_j)/2$. The traction components on the surface of i -th crack caused by dislocations distributed on all N cracks surfaces yield

$$\sigma_{zz}(r_i(s), z_i) = \frac{\mu}{2(1-\nu)} \sum_{j=1}^N L_j \int_{-1}^1 \left[K_{zz}(r_i(s), r_j(t)) B_{zj}(t) + K_{zr}(r_i(s), r_j(t)) B_{rj}(t) \right] dt, \quad (22)$$

$$\sigma_{rz}(r_i(s), z_i) = \frac{\mu}{2(1-\nu)} \sum_{j=1}^N L_j \int_{-1}^1 \left[K_{rz}(r_i(s), r_j(t)) B_{zj}(t) + K_{rr}(r_i(s), r_j(t)) B_{rj}(t) \right] dt,$$

where the kernels in the above equations are

$$K_{zz}(r_i(s), r_j(t)) = \int_0^\infty -\xi r_j(t) (1 + \xi|z_i - z_j|) J_1(\xi r_j(t)) J_0(\xi r_i(s)) e^{-\xi|z_i - z_j|} d\xi, \\ K_{zr}(r_i(s), r_j(t)) = \frac{\pi}{2} \int_0^\infty -\xi^2 r_j(t) \operatorname{sgn}(z_i - z_j) |z_i - z_j| \eta(\xi, r_j(t)) J_0(\xi r_i(s)) e^{-\xi|z_i - z_j|} d\xi, \quad (23) \\ K_{rz}(r_i(s), r_j(t)) = \int_0^\infty -\xi^2 r_j(t) \operatorname{sgn}(z_i - z_j) |z_i - z_j| J_1(\xi r_j(t)) J_1(\xi r_i(s)) e^{-\xi|z_i - z_j|} d\xi, \\ K_{rr}(r_i(s), r_j(t)) = \frac{\pi}{2} \int_0^\infty \xi r_j(t) (1 - \xi|z_i - z_j|) \eta(\xi, r_j(t)) J_1(\xi r_i(s)) e^{-\xi|z_i - z_j|} d\xi.$$

Since stress components (20) are Cauchy singular at the dislocation location, the system of integral equations (22) for the density functions are Cauchy singular for $i = j$ as $s \rightarrow t$. Employing the definition of the dislocation density function, the crack opening displacement for an annular crack becomes

$$u_{kj}^+(s) - u_{kj}^-(s) = L_j \int_{-1}^s B_{kj}(t) dt, \quad k = z, r. \quad (24)$$

The displacement field is single-valued away from the crack surfaces. Thus, the dislocation density for the j -th annular crack is subjected to the closure requirement

$$\int_{-1}^1 B_{kj}(t) dt = 0, \quad j = 1, 2, \dots, N_1, \quad k = z, r. \quad (25)$$

To obtain the dislocation density, the integral equations (22) and (25) are to be solved simultaneously. The stress fields exhibit a square-root singularity at the crack tips. Therefore, the dislocation densities

for annular cracks are taken as

$$B_{kj}(t) = \frac{g_{kj}(t)}{\sqrt{1-t^2}}, \quad -1 \leq t \leq 1, \quad j = 1, 2, \dots, N_1, \quad k = z, r. \quad (26)$$

A penny-shaped crack is considered as an annular edge crack. Taking the embedded crack tip at $t = 1$, the dislocation density functions for penny-shaped cracks may be written as

$$B_{kj}(t) = g_{kj}(t) \sqrt{\frac{1+t}{1-t}}, \quad -1 \leq t \leq 1, \quad j = N_1 + 1, \dots, N, \quad k = z, r. \quad (27)$$

The functions $g_{kj}(t)$ in (26)–(27) are continuous in $-1 \leq t \leq 1$. The numerical solution of integral equations (22) and (25) is carried out by the procedure developed in [Faal et al. 2006]. Substituting (26) and (27) into (22) and (25) and discretizing the domain $-1 \leq t \leq 1$ by $n + 1$ segments, the integral equations are reduced to the following system of $N \times n$ linear algebraic equations:

$$\begin{bmatrix} H_{11} & H_{12} & H_{13} & \dots & H_{1N} \\ H_{21} & H_{22} & H_{23} & \dots & H_{2N} \\ H_{31} & H_{32} & H_{33} & \dots & H_{3N} \\ \vdots & \vdots & \vdots & \ddots & \vdots \\ H_{N1} & H_{N2} & H_{N3} & \dots & H_{NN} \end{bmatrix} \begin{bmatrix} \mathbf{g}_1(t_k) \\ \mathbf{g}_2(t_k) \\ \mathbf{g}_3(t_k) \\ \vdots \\ \mathbf{g}_N(t_k) \end{bmatrix} = \begin{bmatrix} \mathbf{q}_1(s_r) \\ \mathbf{q}_2(s_r) \\ \mathbf{q}_3(s_r) \\ \vdots \\ \mathbf{q}_N(s_r) \end{bmatrix}, \quad (28)$$

where the collocation points are

$$s_r = \cos\left(\frac{\pi r}{n}\right), \quad r = 1, \dots, n-1 \quad \text{and} \quad t_k = \cos\left(\pi \frac{2k-1}{2n}\right), \quad k = 1, \dots, n. \quad (29)$$

The components of the matrix and vectors in (28) are

$$H_{ij} = \begin{bmatrix} A_{j1}k_{ij}(s_1, t_1) & A_{j2}k_{ij}(s_1, t_2) & \dots & A_{jn}k_{ij}(s_1, t_n) \\ A_{j1}k_{ij}(s_2, t_1) & A_{j2}k_{ij}(s_2, t_2) & \dots & A_{jn}k_{ij}(s_2, t_n) \\ \vdots & \vdots & \ddots & \vdots \\ A_{j1}k_{ij}(s_{n-1}, t_1) & A_{j2}k_{ij}(s_{n-1}, t_2) & \dots & A_{jn}k_{ij}(s_{n-1}, t_n) \\ A_{j1}B_{ij}(t_1) & A_{j2}B_{ij}(t_2) & \dots & A_{jn}B_{ij}(t_n) \end{bmatrix},$$

$$\mathbf{g}_j(t_k) = \begin{bmatrix} g_{zj}(t_1) & g_{rj}(t_1) & \dots & g_{zj}(t_n) & g_{rj}(t_n) \end{bmatrix}^T, \quad j = 1, \dots, N, \quad (30)$$

$$\mathbf{q}_j(s_r) = \begin{bmatrix} \sigma_{zz}(r_j(s_1), z_j) & \sigma_{rz}(r_j(s_1), z_j) & \dots & \sigma_{zz}(r_j(s_{n-1}), z_j) & \sigma_{rz}(r_j(s_{n-1}), z_j) \end{bmatrix}^T,$$

$$j = 1, 2, \dots, N_1,$$

$$\mathbf{q}_j(s_r) = \begin{bmatrix} \sigma_{zz}(r_j(s_1), z_j) & \sigma_{rz}(r_j(s_1), z_j) & \dots & \sigma_{zz}(r_j(s_{n-1}), z_j) & \sigma_{rz}(r_j(s_{n-1}), z_j) \\ \sigma_{zz}(r_j(-1), z_j) & \sigma_{rz}(r_j(-1), z_j) \end{bmatrix}^T, \quad j = N_1 + 1, \dots, N,$$

where superscript T stands for transposition and

$$\begin{aligned}
 A_{jk} &= \frac{\pi}{n} \begin{cases} 1, & j = 1, 2, \dots, N_1, \\ 1 + t_k, & j = N_1 + 1, \dots, N, \end{cases} \quad k = 1, 2, \dots, n, \\
 B_{ij} &= \frac{\pi}{n} \begin{cases} \delta_{ij} L_i, & j = 1, 2, \dots, N_1, \\ k_{ij}(-1, t_k), & j = N_1 + 1, \dots, N, \end{cases} \quad k = 1, 2, \dots, n, \\
 k_{ij}(s_r, t_k) &= L_j \begin{bmatrix} K_{zz}(r_i(s), r_j(t)) & K_{zr}(r_i(s), r_j(t)) \\ K_{rz}(r_i(s), r_j(t)) & K_{rr}(r_i(s), r_j(t)) \end{bmatrix}.
 \end{aligned} \tag{31}$$

In (31), δ_{ij} in the B_{ij} is the Kronecker delta and the components of matrix $k_{ij}(s_r, t_k)$ are defined in (23). The modes I and II stress intensity factors for an annular crack with inner and outer radii, a and b , respectively, are defined as

$$\begin{Bmatrix} k_{II}^a \\ k_{II}^a \end{Bmatrix} = \lim_{r \rightarrow a^-} \sqrt{2(a-r)} \begin{Bmatrix} \sigma_{zz}(r, 0) \\ \sigma_{rz}(r, 0) \end{Bmatrix} \quad \text{and} \quad \begin{Bmatrix} k_{II}^b \\ k_{II}^b \end{Bmatrix} = \lim_{r \rightarrow b^+} \sqrt{2(r-b)} \begin{Bmatrix} \sigma_{zz}(r, 0) \\ \sigma_{rz}(r, 0) \end{Bmatrix}. \tag{32}$$

Substituting the axial and shear stress components into (32) yields

$$\begin{Bmatrix} k_{II}^{aj} \\ k_{II}^{aj} \end{Bmatrix} = \frac{\sqrt{L_j}}{2(1-\nu)} \begin{Bmatrix} g_{zj}(-1) \\ g_{rj}(-1) \end{Bmatrix} \quad \text{and} \quad \begin{Bmatrix} k_{II}^{bj} \\ k_{II}^{bj} \end{Bmatrix} = -\frac{\sqrt{L_j}}{2(1-\nu)} \begin{Bmatrix} g_{zj}(1) \\ g_{rj}(1) \end{Bmatrix}, \quad j = 1, 2, \dots, N_1. \tag{33}$$

Analogously, for the penny-shaped crack, stress intensity factors becomes

$$\begin{Bmatrix} k_{II}^j \\ k_{II}^j \end{Bmatrix} = -\frac{\sqrt{L_j}}{\sqrt{2}(1-\nu)} \begin{Bmatrix} g_{zj}(1) \\ g_{rj}(1) \end{Bmatrix}, \quad j = N_1 + 1, \dots, N. \tag{34}$$

The solution of the system (28) should be substituted into (33) and (34) to determine stress intensity factors.

4. Numerical results

In what follows, the Poisson's ratio of the medium $\nu = 0.25$ and remote constant tensile traction σ_0 is applied in the axial direction. In the first example, we consider an annular crack with inner and outer radii a and b , respectively. The nondimensional stress intensity factors K/\bar{K} , where $\bar{K} = \sigma_0 \sqrt{(b-a)/2}$ for different crack aspect ratios a/b together with the results obtained in [10, 12], are given in Table 1.

The nondimensional stress intensity factors K_I/K_I^0 and K_{II}/K_I^0 of two parallel penny-shaped cracks with radius a , where $K_I^0 = \sigma_0 \sqrt{a}/\pi$ is the stress intensity factor of a penny-shaped crack with radius a situated in an infinite domain, are presented in Table 2 for different values of distance d between the cracks and compared against those of [Isida et al. 1985; Kachanov and Laures 1989; Zhan and Wang 2006]. The interaction of parallel cracks results in the mode II stress intensity factor which decays by increasing the distance between cracks. As it may be observed, except for K_I/K_I^0 where $d/2a = 0.05$, the results of the above two examples are in excellent agreement with the cited references confirming the validity of the methodology.

The applicability of the procedure is demonstrated by solving two examples with more complicated geometries. Two concentric cracks, a penny-shaped crack surrounded by an annular crack are considered. The dimensions of the annular crack, $b/2$ and b , remain fixed, whereas the radius of the penny-shaped

a/b	Present		[Clements and Ang 1988]		[Nied and Erdogan 1983]	
	K^a/\bar{K}	K^b/\bar{K}	K^a/\bar{K}	K^b/\bar{K}	K^a/\bar{K}	K^b/\bar{K}
0.01	5.7720	0.9013	5.784	0.901	5.922	0.900
0.1	1.9698	0.9091	1.972	0.909	1.972	0.909
0.2	1.5005	0.9180	1.502	0.918	1.502	0.918
0.3	1.3091	0.9270	1.310	0.927	1.310	0.927
0.4	1.2035	0.9363	1.204	0.936	1.204	0.936
0.5	1.1363	0.9461	1.137	0.946	1.137	0.946
0.6	1.0907	0.9559	1.091	0.956	1.089	0.957
0.7	1.0576	0.9662	1.058	0.966	1.057	0.967
0.8	1.0329	0.9768	1.033	0.977	1.032	0.978
0.9	1.0141	0.9880	1.015	0.988	1.014	0.988
0.99	1.0008	0.9983	1.001	0.998	1.001	0.99

Table 1. Stress intensity factors of an annular crack.

$d/2a$	Present		[ZW 2006]		[I+ 1985]		[KL 1989]
	K_I/K_I^0	K_{II}/K_I^0	K_I/K_I^0	K_{II}/K_I^0	K_I/K_I^0	K_{II}/K_I^0	K_I/K_I^0
0.05	0.6966	0.1923	—	—	—	—	0.7386
0.15	0.7351	0.1623	—	—	—	—	—
0.25	0.7671	0.1381	0.7678	0.1382	0.7759	0.1390	0.7678
0.35	0.7950	0.1173	0.7955	0.1173	—	—	0.7898
0.5	0.8313	0.0903	0.8316	0.0903	0.8356	0.0910	0.8249
0.75	0.8810	0.0551	0.8813	0.0551	0.8828	0.0549	0.8781
1	0.9185	0.0322	0.9187	0.0322	0.9189	0.0325	0.9176
1.5	0.9617	0.0114	0.9616	0.0114	0.9613	0.0115	0.9614
2	0.9841	0.0040	0.9802	—	0.9802	0.0041	—
5	1.0000	0.0000	0.9983	—	0.9990	—	—

Table 2. Interaction of two parallel identical penny-shaped cracks under normal loading. [ZW 2006] = [Zhan and Wang 2006]; [I+ 1985] = [Isida et al. 1985]; [KL 1989] = [Kachanov and Laures 1989].

crack, a , changes. Figure 1 shows the nondimensional mode I stress intensity factors K/K_0 of the two cracks, where $K_0 = \sigma_0\sqrt{b}/\pi$. The variation of K/K_0 at the outer edge of the annular crack is negligible, which may be attributed to the large distance between this edge and the penny-shaped crack.

In the last example two interacting identical annular cracks with $a/b = 0.5$ are considered. The dimensionless stress intensity factors at the inner and outer edges are given in Table 3. For $d/b \geq 5$ the interaction vanishes and the problem reduces to an annular crack in infinite medium. It is, however, interesting to note that the mode II stress intensity factor at the inner edge of cracks does not decrease monotonically with increasing distance between cracks. For cracks with the present dimensions, K_{II}^a/\bar{K} has a local maximum at $d/b \simeq 1.5$.

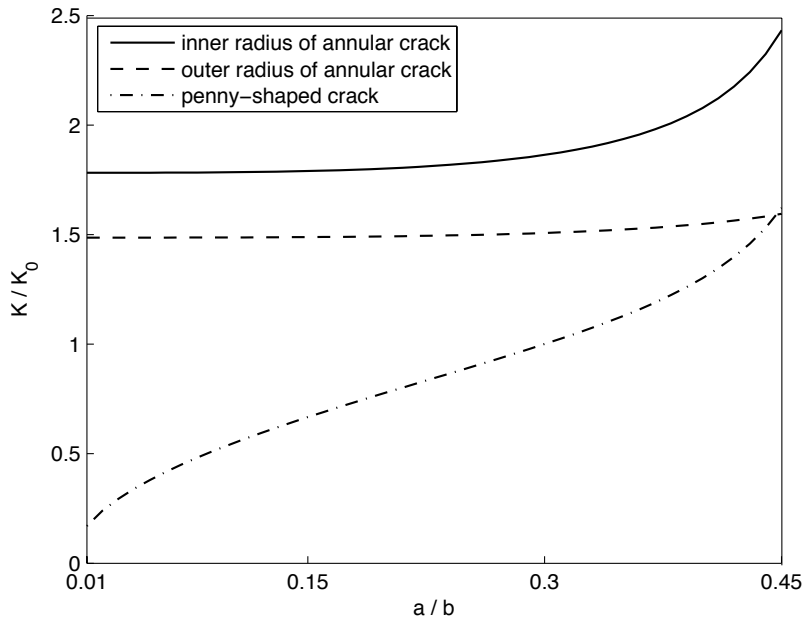


Figure 1. Stress intensity factors of two interacting concentric cracks.

d/b	K_I^a/\bar{K}	K_I^b/\bar{K}	K_{II}^a/\bar{K}	K_{II}^b/\bar{K}
0.05	0.7937	0.6637	0.2049	0.1771
0.15	0.8372	0.7053	0.1566	0.1423
0.25	0.8729	0.7386	0.1179	0.1176
0.35	0.9049	0.7676	0.0842	0.0961
0.5	0.9481	0.8059	0.0427	0.0704
0.75	1.0057	0.8530	0.0025	0.0446
1	1.0414	0.8810	0.0129	0.0315
1.5	1.0790	0.9079	0.0162	0.0191
2	1.0977	0.9230	0.0087	0.0088
5	1.1362	0.9461	0.0000	0.0000

Table 3. Interaction of two parallel identical annular cracks under normal loading for $a/b = 0.5$.

References

- [Abramowitz and Stegun 1964] M. Abramowitz and I. A. Stegun (editors), *Handbook of mathematical functions with formulas, graphs, and mathematical tables*, National Bureau of Standards Applied Mathematics Series **55**, U.S. Government Printing Office, Washington, DC, 1964.
- [Clements and Ang 1988] D. L. Clements and W. T. Ang, “Stress intensity factors for the circular annulus crack”, *Int. J. Eng. Sci.* **26**:4 (1988), 325–329.
- [Collins 1962] W. D. Collins, “Some axially symmetric stress distributions in elastic solids containing penny-shaped cracks, I: Cracks in an infinite solid and a thick plate”, *Proc. R. Soc. Lond. A* **266**:1326 (1962), 359–386.

- [Faal et al. 2006] R. T. Faal, S. J. Fariborz, and H. R. Daghyani, “Antiplane deformation of orthotropic strips with multiple defects”, *J. Mech. Mater. Struct.* **1**:7 (2006), 1097–1114.
- [Fabrikant 1987] V. I. Fabrikant, “Penny-shaped crack revisited: closed-form solutions”, *Philos. Mag. A* **56**:2 (1987), 191–207.
- [Gradshteyn and Ryzhik 1980] I. S. Gradshteyn and I. M. Ryzhik, *Table of integrals, series, and products*, Corr. and enl. ed., edited by A. Jeffrey, Academic Press, New York, 1980.
- [Green and Zerna 1954] A. E. Green and W. Zerna, *Theoretical elasticity*, Clarendon, Oxford, 1954.
- [Guidera and Lardner 1975] J. T. Guidera and R. W. Lardner, “Penny-shaped cracks”, *J. Elasticity* **5**:1 (1975), 59–73.
- [Hills et al. 1996] D. A. Hills, P. A. Kelly, D. N. Dai, and A. M. Korsunsky, *Solution of crack problems: the distributed dislocation technique*, Solid Mechanics and its Applications **44**, Kluwer, Dordrecht, 1996.
- [Isida et al. 1985] M. Isida, K. Hirota, H. Noguchi, and T. Yoshida, “Two parallel elliptical cracks in an infinite solid subjected to tension”, *Int. J. Fract.* **27**:1 (1985), 31–48.
- [Kachanov and Laures 1989] M. Kachanov and J.-P. Laures, “Three-dimensional problems of strongly interacting arbitrarily located penny-shaped cracks”, *Int. J. Fract.* **41**:4 (1989), 289–313.
- [Kassir and Sih 1975] M. K. Kassir and G. C. Sih, *Three-dimensional crack problems: a new selection of crack solutions in three-dimensional elasticity*, Mechanics of Fracture **2**, Noordhoff, Leyden, 1975.
- [Korsunsky 1995] A. M. Korsunsky, “Fundamental eigenstrain solutions for axisymmetric crack problems”, *J. Mech. Phys. Solids* **43**:8 (1995), 1221–1241.
- [Kroupa 1960] F. Kroupa, “Circular edge dislocation loop”, *Czech. J. Phys.* **10**:4 (1960), 284–293.
- [Lur’e 1964] A. I. Lur’e, *Three-dimensional problem of the theory of elasticity*, Interscience, New York, 1964.
- [Nied and Erdogan 1983] H. F. Nied and F. Erdogan, “The elasticity problem for a thick-walled cylinder containing a circumferential crack”, *Int. J. Fract.* **22**:4 (1983), 277–301.
- [Selvadurai and Singh 1985] A. P. S. Selvadurai and B. M. Singh, “The annular crack problem for an isotropic elastic solid”, *Q. J. Mech. Appl. Math.* **38**:2 (1985), 233–243.
- [Sneddon 1946] I. N. Sneddon, “The distribution of stress in the neighbourhood of a crack in an elastic solid”, *Proc. R. Soc. Lond. A* **187**:1009 (1946), 229–260.
- [Sneddon 1972] I. N. Sneddon, *The use of integral transforms*, McGraw-Hill, New York, 1972.
- [Zhan and Wang 2006] S. Zhan and T. Wang, “Interactions of penny-shaped cracks in three-dimensional solids”, *Acta Mech. Sinica* **22**:4 (2006), 341–353.

Received 5 Jul 2008. Revised 1 Nov 2008. Accepted 13 Nov 2008.

EBRAHIM ASADI: [easadi8@yahoo.com](mailto: easadi8@yahoo.com)

Department of Mechanical Engineering, Amirkabir University of Technology (Tehran Polytechnic), Hafez Avenue, 424, Tehran 15875-4413, Iran

SHAHRIAR FARIBORZ: [sjfariborz@yahoo.com](mailto: sjfariborz@yahoo.com)

Department of Mechanical Engineering, Amirkabir University of Technology (Tehran Polytechnic), Hafez Avenue, 424, Tehran 15875-4413, Iran

MOJTABA AYATOLLAHI: [MAyatollahi@yahoo.com](mailto: MAyatollahi@yahoo.com)

Department of Mechanical Engineering, Zanjan University, Zanjan 45195-313, Iran

CLASSICAL AND MIXED ADVANCED MODELS FOR SANDWICH PLATES EMBEDDING FUNCTIONALLY GRADED CORES

SALVATORE BRISCHETTO

This paper analyzes the bending response of several sandwich plates with a functionally graded core, using advanced equivalent single layer (ESL) and layerwise (LW) models with linear to fourth-order expansion in the thickness direction. The functionally graded properties of the core have been approximated by means of Legendre polynomials. The ESL and LW theories have been developed according to the *principle of virtual displacements* and *Reissner's mixed variational theorem*; in the latter case, both displacements and transverse shear/normal stresses have been assumed as primary variables. Closed-form solutions for simply supported sandwich plates loaded by a transverse distribution of harmonic pressure are discussed. Various assessments have been made of the proposed theories with respect to the available results. Our obtained results show that, depending on the chosen functionally graded core, the use of advanced models may turn out to be mandatory with respect to classical theories (for example, first-order shear deformation theory). It has been shown that the use of a core in functionally graded material can offer some advantages with respect to the classical cores that have been widely employed in open literature. A benchmark has been proposed which consists of a sandwich plate with two isotropic faces (ceramic and metallic) and various functionally graded cores. That benchmark could be useful in assessing future refined computational models.

1. Introduction

Functionally graded materials (FGMs) are composite materials made up of two or more constituent phases with a continuously variable composition. FGMs are usually associated with particulate composites where the volume fraction of particles varies in one or several directions. One of the advantages of a monotonous variation of volume fraction of the constituent phases is the elimination of stress discontinuity, which is often encountered in laminated composites and accordingly leads to the avoidance of delamination-related problems. FGMs present a number of advantages that make them attractive in potential future applications, such as a reduction of in-plane and transverse through-the-thickness stresses, an improved residual stress distribution, enhanced thermal properties, higher fracture toughness, and reduced stress intensity factors [Birman and Byrd 2007]. For these reasons, an accurate evaluation of displacements, strains, stresses, and vibrations can be fundamental in the design of such structures.

Several three-dimensional solutions are proposed in the literature for the case of simple problems in one-layered FGM structures. Among these, the three-dimensional elasticity solution proposed by Kashtalyan [2004] for a functionally graded simply supported plate subjected to transverse loading is of particular interest. Young's modulus of the plate is assumed to vary exponentially through the thickness

Keywords: functionally graded materials, sandwich plates with an FGM core, Carrera's unified formulation, classical models, mixed models, equivalent single layer theories, layerwise theories, Legendre polynomials.

and the Poisson's ratio is assumed to be constant. [Reddy and Cheng \[2001\]](#) propose a three-dimensional thermomechanical solution for simply supported functionally graded rectangular plates by means of an asymptotic method. The locally effective material properties are estimated by the scheme from [\[Mori and Tanaka 1973\]](#). [Vel and Batra \[2002; 2003; 2004\]](#) give exact three-dimensional solutions for functionally graded rectangular plates in the case of mechanical and thermal loads on its top and/or bottom surfaces, time-dependent thermal loads, and free and forced vibrations.

Here are some classical and advanced two-dimensional models for these structures made up of one FGM layer: [Zenkour \[2006\]](#) presents the static response for a simply supported functionally graded rectangular plate subjected to a transverse load, where a generalized shear deformation theory is used and the material properties of the plate are assumed to be graded in the thickness direction, according to a simple power-law distribution in terms of the volume fractions of the constituents. [Chi and Chung \[2006\]](#) use the classical plate theory and Fourier series expansion to investigate an elastic, rectangular, and simply supported, FGM plate of medium thickness subjected to transverse loading. [Ramirez et al. \[2006\]](#) obtain a solution for an FGM plate by using a discrete layer theory in combination with the Ritz method in which the plate is divided into an arbitrary number of homogeneous and/or FGM layers. Two types of functionally graded materials are considered: an exponential variation of the mechanical properties through the thickness of the plate, and mechanical properties as a function of the fiber orientation, which varies quadratically through the laminate thickness. Another method used to analyze the static deformations of a simply supported functionally graded plate modeled by a third-order shear deformation theory is the use of the collocation multiquadric radial basis functions proposed by [Ferreira et al. \[2005\]](#). As far as the dynamic analysis is concerned, [Qian et al. \[2004\]](#) investigate the free and forced vibrations of a thick rectangular functionally graded elastic plate using a higher-order shear and normal deformable plate theory and a meshless local Petrov–Galerkin method, [Batra and Jin \[2005\]](#) use first-order shear deformation theory (FSDT) coupled with the finite element method to study free vibrations of a functionally graded anisotropic rectangular plate with the objective of maximizing one of its first five natural frequencies. [Nguyen et al. \[2008\]](#) identify the transverse shear factor by means of energy equivalence for a one-layered FGM plate in the case of first-order shear deformation theory.

All the works mentioned above refer to the case of plates made up of one FGM layer, where the three-dimensional solutions represent very interesting reference solutions and the other two-dimensional models are valuable tools to investigate such problems. The main aim of the present paper is the use of FGMs in multilayer structures. These graded layers can be used as face sheets or as core and its employment can be very efficient to solve some problems usually connected to classical sandwich structures. [Avila \[2007\]](#) considers sandwich beams with a functionally graded core. The proposed failure mode model accurately predicts the failure mechanisms. The best performance is obtained when the core layer with the highest density is located right below the upper face-sheets. [Cheng and Zhong \[2007\]](#) consider a finite crack with constant length propagating in the functionally graded layer. The structure is a functionally graded strip between two dissimilar homogeneous layers. The importance of graded parameters in the dynamic fracture behavior is clearly demonstrated. Considering a functionally graded transition zone between a hard TiC coating and a WC-Co substrate, [Dahan et al. \[2001\]](#) show that the critical load and the wear resistance depend on the concentration profile within the transition layer. The Ti-rich profiles displayed the highest critical load and the lowest wear rate. The transition response of a crack embedded in a functionally graded material layer sandwiched between two dissimilar elastic

layers is analyzed under antiplane shear impact loads by [Li and Fan \[2007\]](#). The effects of crack position, material properties, and the FGM layer thickness are investigated. [Xia and Shen \[2008\]](#) use a high-order shear deformation theory to investigate small and large amplitude vibrations of a compressively and thermally postbuckled sandwich plate with FGM face sheets. When the volume fraction index increases, the fundamental frequency increases in the prebuckling region, but decreases in the postbuckling region. The resulting fracture behavior under impact loading conditions in sandwich structures comprising an FGM core has been illustrated by [Kirugulige et al. \[2005\]](#). These results show a significant reduction in stress intensification in the presence of compositional gradients compared to conventional constructions. The results concerning a sandwich with a homogeneous core and FGM face sheets by [Shen and Li \[2008\]](#) show that the thermal buckling load is modified when using FGM faces. [Zhao et al. \[2008\]](#) investigate the effects of FGM coatings on the thermal shock resistance of a sandwich plate with functionally graded coatings. A two-dimensional solution for the bending analysis, buckling study, and free vibrations of a functionally graded sandwich plate is the sinusoidal shear deformation plate theory by [Zenkour \[2005a; 2005b\]](#). The exact thermoelasticity solution of [Shodja et al. \[2007\]](#) analyzes a thick composite structure consisting of homogeneous and functionally graded layers; stress concentration effects are eliminated and interfacial shear stresses are reduced. The three-dimensional finite element simulations by [Etemadi et al. \[2008\]](#) analyze low velocity impact behavior of sandwich beams with an FGM core. For sandwich beams with functionally graded cores, the maximum contact force increases and the maximum strain decreases compared to those of sandwich beams with a homogeneous core. [Anderson \[2003\]](#) developed an analytical three-dimensional elasticity solution method for a sandwich composite with a functionally graded core subjected to a transverse loading by a rigid spherical indenter. The effects of FGM face sheets and a homogeneous core, or homogeneous face sheets and an FGM core on the free vibrations of sandwich plates with simply supported or clamped edges, are analyzed by [Li et al. \[2008\]](#) by means of a three dimensional linear elasticity theory. The benefits of the use of an FGM core in a sandwich plate for the stresses are analyzed by [Kashtalyan and Menshykova \[2009\]](#) using a three-dimensional solution.

In conclusion, the use of FGM face sheets and/or core in sandwich structures can be very useful to contrast failure mechanisms and crack propagations, to increase critical and buckling loads, to decrease the wear rate, the stress concentration effects and the interfacial shear stresses, and to improve thermal shock resistance. The importance of new accurate plate theories to investigate such types of sandwich structures, as done in [\[Zhu and Sankar 2007\]](#) in the case of a thermal protection system panel with a functionally graded foam core, is therefore clear.

In the present paper, in order to obtain advanced two-dimensional models for sandwich structures with FGM layers, Carrera's unified formulation [\[1995; 2002\]](#), known as CUF, has been extended to materials with properties that are functionally graded through the thickness direction. This extension was made for the classical advanced models in [\[Carrera et al. 2008\]](#) and for the mixed ones in [\[Brischetto and Carrera 2008\]](#). In the first case, the principle of virtual displacements (PVD) was used, while in the second paper, Reissner's mixed variational theorem (RMVT) was employed to model both displacements and transverse shear/ normal stresses. The classical and mixed advanced hierarchical models presented in these two papers were developed for multilayer FGM plates. Applications were only made for single-layered FGM structures. In the present paper, considering sandwich plates with an FGM core, the models obtained in [\[Carrera et al. 2008\]](#) and [\[Brischetto and Carrera 2008\]](#) are validated for multilayer FGM plates. For material properties, only spatial dependence has been considered. These properties have

been considered independent of temperature; the dependence on temperature will be added in future work, where the heat conduction problem will be accounted for. The most important features about the extension of CUF to FGMs have been discussed in [Section 2](#), then [Section 3](#) introduces the employed kinematic models. [Section 4](#) deals with the results and discussion, and the conclusions are given in [Section 5](#).

2. Extension of CUF to FGMs

The application of a two dimensional method for plates allows the unknown variables to be expressed in a set of thickness functions that only depend on the thickness coordinate z and the correspondent variable which depends on the in-plane coordinates (x, y) .

CUF is a technique which handles a large variety of plate/shell modelings in a unified manner [[Carrera 1995; 2002](#)]. According to CUF, the governing equations are written in terms of a few *fundamental nuclei* which do not formally depend on

- the order of expansion N used in the z -direction, and
- the variables description: layerwise (LW) or equivalent single layer (ESL).

The generic variable $\mathbf{a}(x, y, z)$, for instance a displacement, and its variation $\delta\mathbf{a}(x, y, z)$ are therefore written according to the general expansion

$$\mathbf{a}(x, y, z) = F_\tau(z)\mathbf{a}_\tau(x, y), \quad \delta\mathbf{a}(x, y, z) = F_s(z)\delta\mathbf{a}_s(x, y) \quad \text{for } \tau, s = 1, \dots, N, \quad (1)$$

where the bold letters denote arrays, (x, y) are the in-plane coordinates and z the thickness one, and $F_\tau(z)$ and $F_s(z)$ are thickness functions. The summation convention is assumed with repeated indexes τ and s . The order of expansion N goes from first to fourth order, and depending on the used thickness functions $F(z)$, one model could be ESL when the variable is assumed for the whole multilayer and LW when the variable is considered independent in each layer.

A model for the analysis of FGM plates must accurately describe the continuous variations of the material characteristics (mechanical, thermal, or electric) along the thickness. The present section focuses on the procedure that allows the CUF to be expanded to the analysis of FGM layers. These layers could be single or embedded in other classical and/or FGM layers. For the FGM layers, Legendre polynomials have been used to approximate the elastic coefficients in the thickness z .

The variation of the material characteristics is usually given in terms of exponential and/or polynomial functions applied directly to engineering constants such as Young's moduli E_i , shear moduli G_{ij} and/or Poisson's ratio ν_{ij} , or directly to material stiffnesses C_{ij} with $i, j = 1, 6$. Since a relation between the engineering constants and the material stiffnesses holds in each point of the plate, only the second case can actually be treated. The variation of the stiffness matrix is generally given by multiplying it by a function of z

$$\mathbf{C}(z) = \mathbf{C}_0 * g(z), \quad (2)$$

where \mathbf{C}_0 is the reference stiffness matrix and $g(z)$ gives the variation along z . By applying the ideas behind the CUF, the following expansion is made

$$\mathbf{C}(z) = F_b(z)\mathbf{C}_b + F_\gamma(z)\mathbf{C}_\gamma + F_t(z)\mathbf{C}_t = F_r\mathbf{C}_r, \quad (3)$$

where the *thickness functions* F_γ are the same that will be used for the LW expansion in the next section

$$F_t = \frac{P_0 + P_1}{2}, \quad F_b = \frac{P_0 - P_1}{2}, \quad F_\gamma = P_\gamma - P_{\gamma-2} \quad \gamma = 2, \dots, N_r, \quad (4)$$

where $P_j = P_j(\zeta_k)$ is the Legendre polynomial of j -th order defined in the domain $-1 \leq \zeta_k \leq 1$.

The actual \mathbf{C} is then recovered as a weighted summation on the terms \mathbf{C}_r . The weights are given by the thickness functions F_r . The order of the expansion can be arbitrarily chosen. Due to the usual complicated laws used for $g(z)$ in the open literature, the expansion has been in this work extended to $N_r = 10$. Anyway, when a simple polynomial $g(z)$ is applied lower values of N_r could be used.

The procedure to include the varying stiffnesses in the model requires to compute the \mathbf{C}_r matrices. This task can be accomplished solving for each component C_{ijr} a simple algebraic system of order N_r . After that the actual values of C at N_r different locations along the thickness (z_1, \dots, z_{N_r}) have been calculated, leading to the formula

$$\begin{bmatrix} C_{ij}(z_1) \\ \vdots \\ C_{ij}(z_{N_r}) \end{bmatrix} = \begin{bmatrix} F_b(z_1) & \cdots & F_\gamma(z_1) & \cdots & F_t(z_1) \\ \vdots & & \vdots & & \vdots \\ F_b(z_{N_r}) & \cdots & F_\gamma(z_{N_r}) & \cdots & F_t(z_{N_r}) \end{bmatrix} \begin{bmatrix} C_{ijb} \\ \vdots \\ C_{ijr} \\ \vdots \\ C_{ijt} \end{bmatrix}. \quad (5)$$

In the case of classical layers with constant material properties the formula in Equation (3) is not considered and the elastic coefficients are constant in the rigidity matrices.

A detailed description of the CUF extended to FGMs is reported in [Carrera et al. 2008] for the PVD (only the displacements are considered as primary variables) and in [Brischetto and Carrera 2008] for the RMVT (both displacements and transverse shear/normal stresses as primary variables). Further details regarding the assembly procedure (expansion in z for the primary variables and material properties, multilayer assembly procedure) and the governing equations can be found in these same two papers.

3. Description of kinematics

The proposed two-dimensional models have been coded according to the CUF. Details can be found in previous authors' works [Carrera1995; 2002; Brischetto and Carrera 2008; Carrera et al. 2008]. In order to explore how the various kinematic assumptions can affect the response of typical two-dimensional structures, a large variety of plates/shells theories have been considered here.

Plates of constant thickness h are considered. The geometry and reference system are shown in Figure 1. The displacement components u_x , u_y , and u_z are measured with respect to the x , y , and z axes. The latter axis denotes the through-the-thickness direction. Ω is the plate reference surface. Plain-stress/plain-strain conditions have been assumed according to what indicated in the paper concerning the Poisson's locking phenomena for plates [Carrera and Brischetto 2008].

Higher-order theories. Higher-order theories (HOTs) consider the same order of expansion in the thickness direction for the three displacements components (including the transverse one). These theories are obtained in the ESL overview.

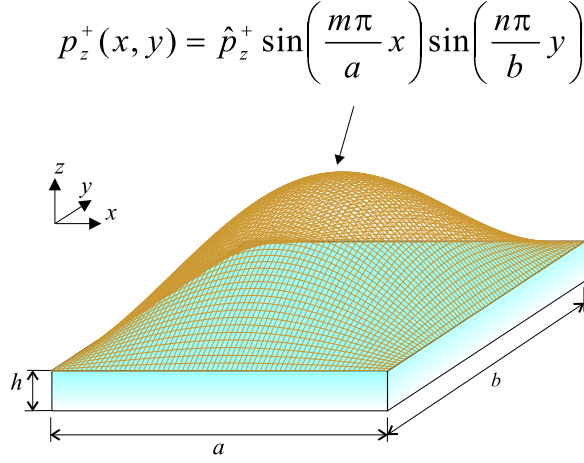


Figure 1. Notations and load configuration for the plates considered.

HOTs including transverse normal strains. Higher-order terms can be introduced in the kinematic assumptions in order to obtain refinements of classical lamination theory (CLT) and FSDT models

$$u_\tau(x, y, z) = u_{0\tau}(x, y) + z^i u_{i\tau}(x, y) \quad \text{with } \tau = x, y, z \text{ and } i = 1, N. \quad (6)$$

The summation convention for the repeated indexes has been adopted. N is the order of expansion, which is taken as a free parameter. In the numerical investigation N is considered to be as low as 1 and as high as 4. According to the acronym system developed within CUF, the related theories are named ED1–ED4. The letter E denotes that the kinematic is preserved for the whole layers, as in the ESL approach, while D denotes that only displacement unknowns are used and the last number states the through-the-thickness expansion order.

HOTs including zigzag effects. The EDN models are not able to describe the discontinuity of the first derivative with correspondence to the layer interfaces, known as the zigzag effects [Carrera 2003] and peculiar of laminates mechanics. It can be introduced via the Murakami's zigzag function (MZZF) [Murakami 1986], which was proposed in the framework of RMVT applications. The dimensionless layer coordinate $\zeta_k = (2z_k)/h_k$ is further introduced, being h_k the thickness of the k -th layer and z_k the layer thickness coordinate. MZZF is defined according to the formula

$$\text{MZZF} = (-1)^k \zeta_k. \quad (7)$$

MZZF has the following properties: it is piecewise linear function of the layer coordinate z_k , it has unit amplitude for the whole layers, and its slope takes opposite sign between two-adjacent layers, since its amplitude layer is independent of thickness. The displacement field accounting for MZZF takes the form

$$u_\tau(x, y, z) = u(x, y)_{0\tau} + z^r u(x, y)_{r\tau} + (-1)^k \zeta_k u(x, y)_{Z\tau} \quad \text{with } \tau = x, y, z \text{ and } r = 1, 2, \dots, N-1. \quad (8)$$

Subscript Z refers to the introduced zigzag term. Higher-order distributions in the z -direction are introduced by polynomials of degree r . Modifications of EDN directed to include MZZF are denoted EDZN.

The classical theories. The classical theory CLT, based on assumptions made by Cauchy [1828], Poisson [1829], and Kirchhoff [1850], discards transverse shear and through-the-thickness deformations. The displacement model related to CLT can be written in the form

$$u_\tau(x, y, z) = u_{0\tau}(x, y) - z \frac{\partial u_{0z}(x, y)}{\partial \tau} \quad \text{with } \tau = x, y \text{ and } u_z(x, y, z) = u_{0z}(x, y), \quad (9)$$

stating that the section remain plane and orthogonal to the plate reference surface Ω . Here u_0 denotes the displacement value relative to the reference surface Ω . Transverse shear stresses are discarded by CLT.

Transverse shear deformation can be introduced according to the Reissner–Mindlin kinematic assumptions [Reissner 1945; Mindlin 1951]:

$$u_\tau(x, y, z) = u_{0\tau}(x, y) + z u_{1\tau}(x, y) \quad \text{with } \tau = x, y \text{ and } u_z(x, y, z) = u_{0z}(x, y). \quad (10)$$

This theory is also called FSDT. Transverse shear stresses show a priori constant piecewise distribution. FSDT can be obtained from ED1 by considering a constant transverse displacement through the thickness. CLT is obtained from FSDT considering an infinite shear correction factor. In both CLT and FSDT, the Poisson locking phenomenon is contrasted by means of the plane-stress conditions, as indicated in [Carrera and Brischetto 2008]. In the proposed analysis of FGM structures, the shear correction factor has not been used for the correction of FSDT because the well-known value $\chi = 5/6$ is calculated for a homogeneous material. The shear correction factor for a general laminate depends on lamina properties and lamination scheme [Reddy 2004].

Layerwise theories. Multilayered plates can be analyzed by kinematic assumptions which are independent in each layer. Following Reddy [2004] these approaches are called here LW theories.

The LW description yields, thus, displacement variables that are independent in each layer. The Taylor expansion of the thickness, adopted in the previous paragraphs for ESL cases, is not convenient for LW description. Displacement interlaminar continuity can be imposed more conveniently by employing interface values as unknown variables. The LW description assumes the form

$$u_\tau^k = F_t u_{\tau t}^k + F_b u_{\tau b}^k + F_r u_{\tau r}^k \quad \text{with } \tau = x, y, z, \quad r = 2, 3, \dots, N, \quad k = 1, 2, \dots, N_l. \quad (11)$$

Subscript t and b denote values related to the top and the bottom of layer, respectively. The thickness functions $F_\tau(\zeta_k)$ have been defined by

$$F_t = \frac{P_0 + P_1}{2}, \quad F_b = \frac{P_0 - P_1}{2}, \quad F_r = P_r - P_{r-2}, \quad r = 2, 3, \dots, N, \quad (12)$$

in which $P_j = P_j(\zeta_k)$ is the j -th order Legendre polynomial defined for $-1 \leq \zeta_k \leq 1$. In the numerical investigations the maximum order is four, and the relevant polynomials are

$$P_0 = 1, \quad P_1 = \zeta_k, \quad P_2 = (3\zeta_k^2 - 1)/2, \quad P_3 = \frac{5\zeta_k^3}{2} - \frac{3\zeta_k}{2}, \quad P_4 = \frac{35\zeta_k^4}{8} - \frac{15\zeta_k^2}{4} + \frac{3}{8}. \quad (13)$$

The preceding functions have the following interesting properties:

$$\text{when } \zeta_k = 1: F_t = 1, F_b = 0, F_r = 0; \quad \text{when } \zeta_k = -1: F_t = 0, F_b = 1, F_r = 0. \quad (14)$$

The top and bottom values have been used as unknown variables. The interlaminar compatibility of displacement can therefore be easily linked:

$$u_{\tau t}^k = u_{\tau b}^{(k+1)}, \quad k = 1, N_l - 1. \quad (15)$$

The acronyms for these theories are LD1–LD4, the L standing for LW.

Mixed theories based on Reissner's mixed variational theorem. The kinematics described previously is not able to furnish interlaminar continuity of transverse shear and normal stresses at the interfaces between two adjacent layers in the case of multilayer structures. RMVT [Reissner 1984] offers the possibility to fulfil a priori the interlaminar continuity. Both displacements and transverse shear/normal stresses can be assumed within the RMVT framework as primary variables.

Layerwise mixed theories. In the LW case the displacement model in (11) is also used for the transverse shear/normal stresses:

$$\sigma_{\tau z}^k = F_t \sigma_{\tau z_t}^k + F_b \sigma_{\tau z_b}^k + F_r \sigma_{\tau z_r}^k \quad \text{with } \tau = x, y, z, \quad r = 2, 3, \dots, N, \quad k = 1, 2, \dots, N_l. \quad (16)$$

The interlaminar transverse shear and normal stresses continuity can be, therefore, easily linked:

$$\sigma_{\tau z_t}^k = \sigma_{\tau z_b}^{(k+1)} \quad \text{with } \tau = x, y, z, \quad k = 1, N_l - 1. \quad (17)$$

These models are denoted as LM1–LM4, where *M* means mixed models based on RMVT.

Equivalent single layer mixed theories. Mixed theories along with an ESL description can be formulated referring to the displacement model in (6) and the LW stress assumptions in (16). These are referred to as EM1–EM4. The theories accounting for the zigzag shape of the displacements are indicated as EMZ1–EMZ3. A further letter C could be added in the acronyms to emphasize the continuity of the transverse shear/normal stresses.

4. Results and discussion

All the examples presented in this section consider a simply supported square plate with a bisinusoidal mechanical load applied to the top surface; see Figure 1. The applied load is

$$p_z(x, y) = \bar{p}_z \sin\left(\frac{m\pi}{a}x\right) \sin\left(\frac{n\pi}{b}y\right), \quad (18)$$

where *a* and *b* are the plate dimensions, *x* and *y* are the in-plane coordinates and *z* is the thickness coordinate. The load amplitude is $\bar{p}_z = 1.0$ Pa and the wavelengths in the *x* and *y* directions are $m = n = 1$.

Assessment 1: one-layered no-FGM plate. The plate is made of aluminum A12024 with Young's modulus $E = 73$ GPa and Poisson's ratio $\nu = 0.34$. The global thickness is $h = 0.001$ m and the thickness ratio is $a/h = 10$. The three-dimensional solution for the dimensionless transverse displacement \bar{w} considered in the middle of the plate is given in [Carrera and Brischetto 2008]. The transverse normal stress σ_{zz} at the top is given by the loading conditions. Table 1 compares a classical theory (FSDT) and advanced classical and mixed models with the three-dimensional solution, to demonstrating how the models for functionally graded materials can degenerate into models for materials with constant properties through thickness *z*. The fictitious layers (Figure 2) have been introduced to validate the multilayer assembly

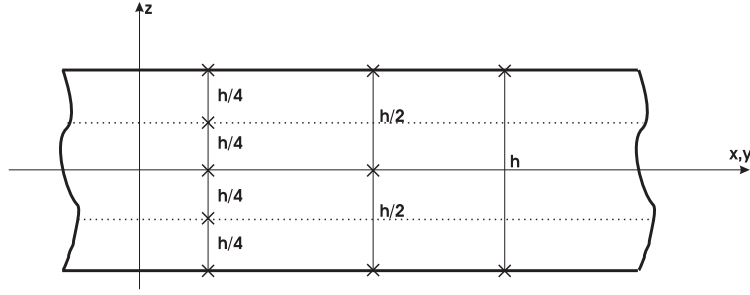


Figure 2. Assessment 1: Isotropic square plate with fictitious layers.

	One layer		Two layers		Four layers	
	$\bar{w}(0)$	$\sigma_{zz}(h/2)$	$\bar{w}(0)$	$\sigma_{zz}(h/2)$	$\bar{w}(0)$	$\sigma_{zz}(h/2)$
3D	2.8655	1.0000	2.8655	1.0000	2.8655	1.0000
FSDT	2.7238	1.5659	2.7238	1.5659	2.7238	1.5659
ED4	2.8655	1.0001	2.8655	1.0001	2.8655	1.0001
EM4	2.8655	1.0001	2.8655	1.0001	2.8655	1.0001
LD4	2.8655	1.0001	2.8655	1.0001	2.8655	1.0000
LM4	2.8655	1.0001	2.8655	1.0000	2.8655	1.0000

Table 1. Assessment 1: Isotropic square plate with thickness ratio $a/h = 10$. The 3D case corresponds to [Carrera and Brischetto 2008]. Results for one layer, two and four fictitious layers. The dimensionless transverse displacement is $\bar{w} = 100Eh^3u_z/(\bar{p}_za^4)$.

procedure. Though a shear correction factor $\chi = 5/6$ could be used for FSDT in case of homogeneous and isotropic plates, $\chi = 1$ has been employed to be consistent with the case of FGM structures.

Assessment 2: one-layered FGM plate. The considered plate is one-layered with Young's modulus $E(z)$ changing in the thickness direction z , according to Zenkour's formula [2006]

$$E(z) = E_m + (E_c - E_m) \left(\frac{2z + h}{2h} \right)^\kappa. \quad (19)$$

The plate is completely metallic at the bottom ($E_m = 70$ GPa) and completely ceramic at the top ($E_c = 380$ GPa). A constant Poisson ratio $\nu = 0.3$ and a thickness ratio $a/h = 10$ are considered. Varying the thickness coordinate z from $-h/2$ to $h/2$, Young's modulus changes with continuity, as illustrated in Figure 3, where the exponential κ varies from 1 to 10. The global thickness is $h = 0.1$ m. A detailed investigation was made in [Carrera et al. 2008] for PVD models and in [Brischetto and Carrera 2008] for RMVT models. The FSDT model is compared in Table 2 with some advanced ones ($\kappa = 1$), with the solution from [Zenkour 2006] (a generalized shear deformation model), and with a discrete layer quasi-three-dimensional solution previously presented in [Carrera et al. 2008]. The fictitious layers, as illustrated in Figure 4, have been considered to demonstrate that the present models are able to carry out the multilayer FGM assembly procedure.

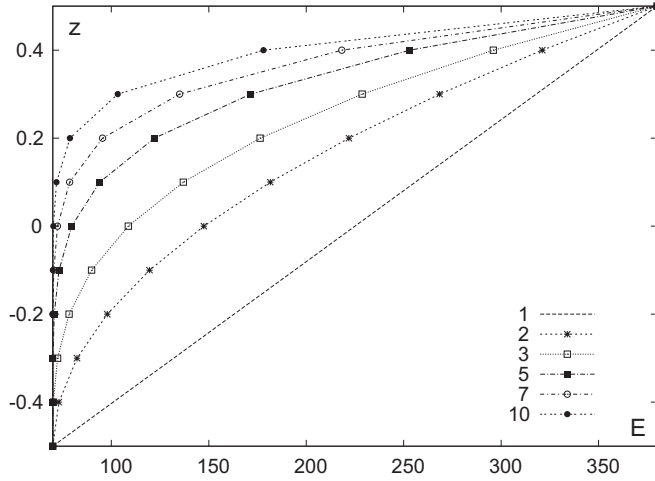


Figure 3. Young's modulus $E(z)$ versus z for different values of the parameter κ considered in the Zenkour's formula (19).

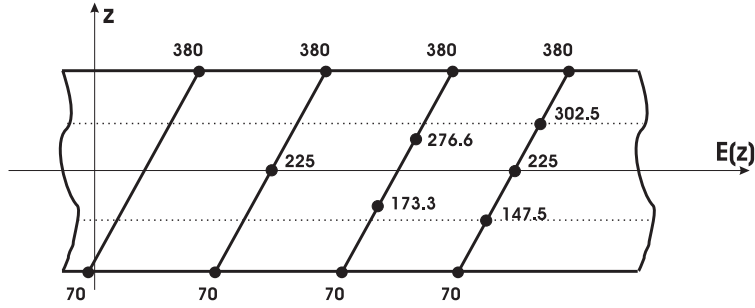


Figure 4. Assessment 2: Functionally graded plate with linear ($\kappa = 1$) Zenkour's law [2006] and fictitious layers.

	One	Two	Three	Four
	$\bar{w}(0)$	$\bar{w}(0)$	$\bar{w}(0)$	$\bar{w}(0)$
Z	0.5889	0.5889	0.5889	0.5889
CBR	0.5875	0.5875	0.5875	0.5875
FSDT	0.4812	0.4812	0.4812	0.4812
ED4	0.5875	0.5875	0.5875	0.5875
EM4	0.5875	0.5875	0.5875	0.5875
LD4	0.5875	0.5875	0.5875	0.5875
LM4	0.5875	0.5875	0.5875	0.5875

Table 2. Assessment 2: Functionally graded square plate with thickness ratio $a/h = 10$ and exponential $\kappa = 1$ for Zenkour's formula [2006] (row marked Z). CBR stands for [Carrera et al. 2008]. Results are shown for one layer and for two, three and four fictitious layers. The dimensionless transverse displacement is $\bar{w} = 10E_c h^3 u_z / (\bar{p}_z a^4)$.

Assessment 3: sandwich FGM plate. A further validation for the employed ESL and LW models, based on PVD and RMVT, is made with the three-dimensional solution proposed by [Kashtalyan and Menshykova \[2009\]](#) for the case of a three-layered plate with a core in FGM; see [Figure 5](#). The global thickness of the plate is $h_0 = 2h$ where h and $-h$ represent the top and bottom coordinates of the plate, respectively. h_c and $-h_c$ are the coordinates of the bottom fourth layer and the top first layer, respectively. The global thickness of the core is $2h_c$. The plate has a global thickness $h_0 = 1.0$ m, the thickness of

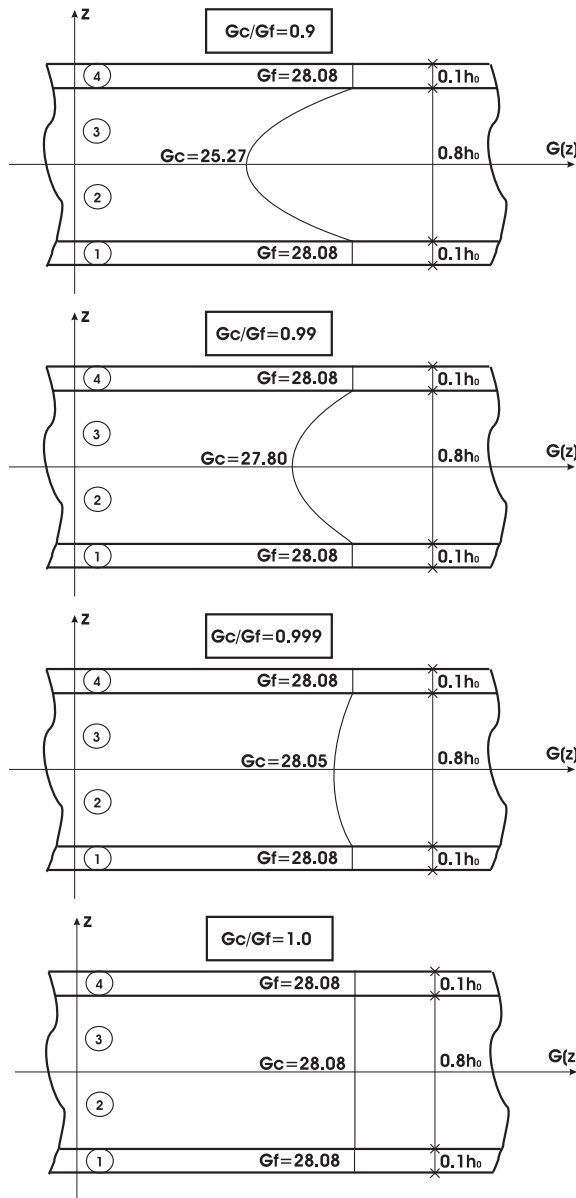


Figure 5. Assessment 3: Examples of different sandwich plates with core in FGM, following [\[Kashtalyan and Menshykova 2009\]](#).

the two faces is $h_f = 0.1h_0$, and the thickness of the core is $2h_c = 0.8h_0$. The considered thickness ratio is $a/h_0 = 3$. The reference Young's modulus is $E_0 = 73$ GPa with Poisson's ratio $\nu = 0.3$, and the two faces consequently have a constant shear modulus $G_f = G_0 = 28.08$ GPa (layers 1 and 4). The core can be divided into parts 2 and 3. The value of the shear modulus in the middle reference surface is indicated with G_c . In layer 2, the exponential law for the shear modulus is $G(z) = G_0 \exp[-\gamma(z/h_c + 1)]$ with $h_c = 0.4$ m and $-0.4 \leq z \leq 0$. For layer 3, the exponential law is $G(z) = G_0 \exp[\gamma(z/h_c - 1)]$ with $h_c = 0.4$ m and $0 \leq z \leq 0.4$. Four different cases will be considered, as illustrated in [Figure 5](#), that correspond to four different shear modulus ratios G_c/G_f (0.9, 0.99, 0.999, 1.0), which means values of the exponential γ equal to 0.105360, 0.010050, 0.001000 and 0.0, respectively. The case $G_c/G_f = 1.0$ means a three-layered plate with the same classical material. [Table 3](#) (page 26) considers the dimensionless transverse displacement \bar{w} in the middle for different values of G_c/G_f ; the transverse normal stress σ_{zz} at the top and bottom of the plate is investigated in [Table 4](#). The three-dimensional reference solution is given by [Kashtalyan and Menshykova \[2009\]](#). For the displacements, when the shear modulus ratio is close to 1.0, both LW and ESL models are able to give the three-dimensional response, but the requested order of expansion in z is lower for the LW models. In the case of $G_c/G_f = 0.9$, the use of LW models and higher orders of expansion is mandatory. The addition of MZZF [[Murakami 1986](#)] to ESL models is not so effective as in the case of classical sandwich structures where the typical zigzag form of the displacement is observable. The comments made for the PVD models in [Table 3](#) are confirmed for the RMVT models on the right-hand side of the same table. To obtain the correct values of the stresses, LW and higher orders of expansions are requested, as suggested by [Table 4](#).

The advantage of RMVT models is clearly demonstrated in the case of LW models with lower orders of expansions and in the case of ESL theories. These conclusions become much clearer if we consider [Figures 6 and 7](#). In [Figure 6](#), where the displacements are plotted along the thickness, it is evident that the use of a higher order of expansion is fundamental. In [Figure 7](#), in the case of transverse shear/normal stresses σ_{xz} and σ_{zz} , for a shear modulus ratio $G_c/G_f = 0.9$, the use of RMVT models is mandatory.

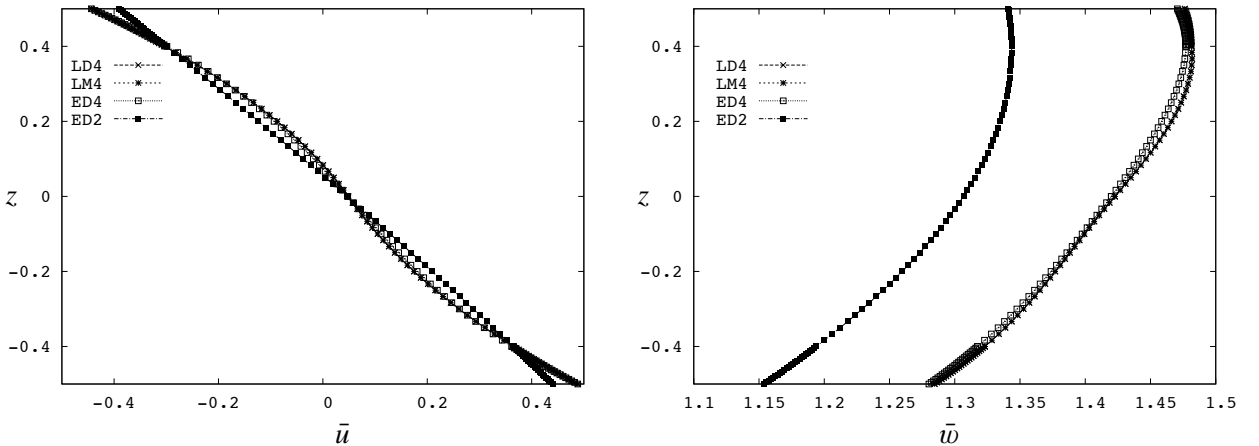


Figure 6. Assessment 3: Displacements $\bar{u} = G_0 u_x / (\bar{p}_z h_0)$ and $\bar{w} = G_0 u_z / (\bar{p}_z h_0)$ vs. z , for the sandwich plate with core in FGM proposed in [[Kashtalyan and Menshykova 2009](#)]. The shear modulus is $G_c/G_f = 0.9$.

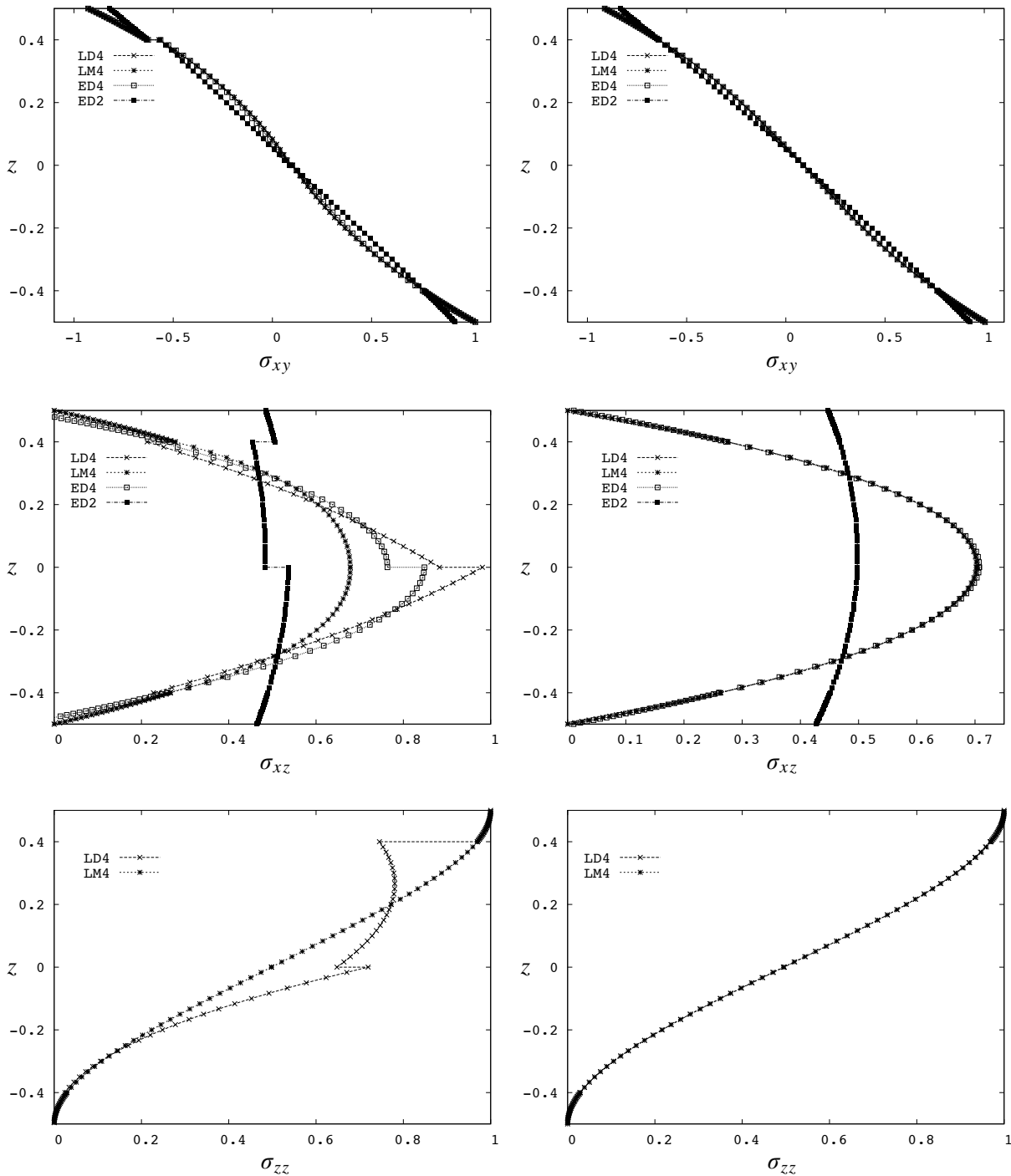


Figure 7. Assessment 3: Sandwich plates with core in FGM according to the solution and formula from [Kashtalyan and Menshykova 2009]. $G_c/G_f = 0.9$ (left column) and $G_c/G_f = 0.999$ (right column). σ_{xy} , σ_{xz} and σ_{zz} versus z .

		G_c/G_f	0.9	0.99	0.999	1.0			G_c/G_f	0.9	0.99	0.999	1.0
		3D	1.4227	1.3500	1.3433	1.3430			3D	1.4227	1.3500	1.3433	1.3430
ESL theories	FSDT	1.1924	1.1714	1.1690	1.1687				EM1	1.1936	1.1714	1.1690	1.1687
	ED1	1.1924	1.1714	1.1690	1.1687				EM2	1.3069	1.2820	1.2792	1.2789
	ED2	1.3067	1.2820	1.2792	1.2789				EM3	1.4224	1.3518	1.3453	1.3446
	ED3	1.4223	1.3518	1.3453	1.3446				EM4	1.4200	1.3496	1.3432	1.3424
	ED4	1.4199	1.3496	1.3432	1.3424								
ESL + MZZF	EDZ1	1.1999	1.1796	1.1772	1.1769				EMZ1	1.2022	1.1808	1.1783	1.1781
	EDZ2	1.3027	1.2728	1.2750	1.2747				EMZ2	1.3023	1.2774	1.2746	1.2742
	EDZ3	1.4179	1.3472	1.3407	1.3400				EMZ3	1.4176	1.3470	1.3405	1.3398
LW theories	LD1	1.3584	1.3190	1.3149	1.3144				LM1	1.4029	1.3498	1.3445	1.3439
	LD2	1.4213	1.3476	1.3413	1.3406				LM2	1.4190	1.3464	1.3402	1.3395
	LD3	1.4227	1.3495	1.3432	1.3425				LM3	1.4228	1.3498	1.3435	1.3428
	LD4	1.4227	1.3496	1.3432	1.3426				LM4	1.4227	1.3495	1.3432	1.3425

Table 3. Assessment 3: Sandwich plate with core in functionally graded material and two external isotropic faces. The three-dimensional solution is from [Kashtalyan and Menshykova 2009]. The thickness ratio is $a/h = 3$ and the dimensionless transverse displacement is $\bar{w} = G_0 u_z / (\bar{p}_z h_0)$ evaluated at $z = 0$. Left: classical model and advanced models based on PVD; right: advanced models based on RMVT.

G_c/G_f	$\sigma_{zz}(h/2)$				$\sigma_{zz}(-h/2)$			
	0.9	0.99	0.999	1.0	0.9	0.99	0.999	1.0
L.C.	1.0000	1.0000	1.0000	1.0000	0.0000	0.0000	0.0000	0.0000
FSDT	1.1536	1.1709	1.1723	1.1724	-1.536	-1.1709	-1.723	-1.1724
ED3	1.1766	1.2226	1.2266	1.2271	-0.3439	-0.2374	-0.2278	-0.2267
ED4	0.9060	0.9940	1.0026	1.0035	-0.0738	-0.0043	0.0016	0.0023
EDZ1	1.2727	1.2496	1.2473	1.2471	-0.2456	-0.2852	-0.2894	-0.2899
EDZ3	0.9060	0.9671	0.9726	0.9732	-0.0738	0.0219	0.0304	0.0313
LD2	1.0119	1.0119	1.0119	1.0119	-0.0105	-0.0104	-0.0104	-0.0104
LD4	1.0000	1.0000	1.0000	1.0000	0.0000	0.0000	0.0000	0.0000
EM3	1.1453	1.2196	1.2263	1.2271	-0.3444	-0.2374	-0.2278	-0.2267
EM4	0.9319	0.9968	1.0028	1.0035	-0.0732	-0.0043	0.0016	0.0023
EMZ1	1.4291	1.3544	1.3472	1.3464	-0.3527	-0.3837	-0.3866	-0.3869
EMZ3	1.0023	1.0334	1.0363	1.0366	-0.1435	-0.0419	-0.0328	-0.0318
LM2	1.0046	1.0071	1.0067	1.0066	-0.0130	0.0036	0.0043	0.0043
LM4	1.0002	1.0001	1.0001	1.0000	0.0000	0.0000	0.0000	0.0000

Table 4. Assessment 3: Values of σ_{zz} on plate surface for the same setup as in Table 3. L.C. means loading condition (expected value of σ_{zz}).

The stresses obtained a priori are in fact continuous in the thickness z direction. The use of ESL models is not effective for the evaluation of such stresses for either cases of $G_c/G_f = 0.9$ or $G_c/G_f = 0.999$. If we consider a value of G_c/G_f close to 1.0, the use of PVD models is sufficient, as illustrated in the right column of [Figure 7](#).

Proposed benchmark. The three proposed assessments have been used to validate the extension of CUF to multilayer functionally graded plates and to highlight the capability of some advanced models with respect to the classical ones. This allows these models to be used with confidence in order to investigate a new benchmark proposed for the first time in this paper. A three-layered plate is considered: the bottom layer is metallic made with Young's modulus $E_m = 70$ GPa and the top layer is in ceramic with $E_c = 380$ GPa. The core consists of an FGM with Young's modulus varying in z according to Zenkour's formula [\[2006\]](#), given here as [Equation \(19\)](#). The proposed plate is given in [Figure 8](#), where the thickness of each face is $h_f = 0.1h$ and the core has $h_c = 0.8h$. In the core, the Young's modulus $E(z)$ changes exponentially in z according to an exponential parameter κ that can assume values of 1, 5 or 10, [Figure 3](#). A fourth case has been added: a core with a constant Young's modulus, that is, an average between E_c and E_m . Poisson's ratio is constant for the three layers ($\nu = 0.3$). Two thickness ratios are investigated, $a/h = 4$ and $a/h = 100$, corresponding to $h = 0.25$ and 0.01 .

[Table 5](#) shows the displacements, [Table 6](#) the in-plane stresses and [Table 7](#) (on page 31) the transverse shear/normal stresses obtained. The results given by advanced models, such as LD4 and LM4, could be considered as reference values for models that will be proposed in the future by other scientists. In the case of a thick plate ($a/h = 4$), the use of LW models is mandatory, if we consider thin plates ($a/h = 100$), ESL models could be used by employing higher-order expansions. The in-plane stress σ_{xx} is considered in [Figure 9](#), top, for κ equal to 1 and 10. Even though the plate is thick, the four theories considered are effective; an ESL model with parabolic expansion in z is enough. In the case of the transverse normal stress σ_{zz} , the use of LW models is mandatory; see [Figure 9](#), bottom. In the case of $\kappa = 10$, the mixed model gives better values of σ_{zz} through the thickness z with respect to the LD4 theory. Some small problems have been pointed out near the top and the bottom of the plate, even though an LM4 theory is employed. This happens because the plate considered is very thick. Such problems disappear in the case of thin plates. In [Figure 10](#), where an advanced model such as LD4 has

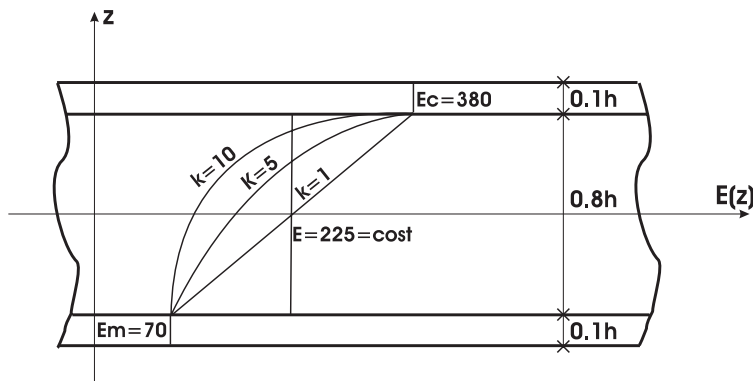


Figure 8. Benchmark: Three-layered plate with core in FGM, either obeying the law [\(19\)](#) proposed in [\[Zenkour 2006\]](#), or made of isotropic material ($E = 225$ GPa).

		$\kappa = 1$		$\kappa = 5$		$\kappa = 10$		$E = 225 \text{ GPa}$	
		$\bar{w}(0)$	$\bar{u}(-2h/5)$	$\bar{w}(0)$	$\bar{u}(-2h/5)$	$\bar{w}(0)$	$\bar{u}(-2h/5)$	$\bar{w}(0)$	$\bar{u}(-2h/5)$
$a/h = 4$	FSDT	0.6346	0.2084	0.8636	0.2937	0.9120	0.2969	0.5441	0.1470
	ED2	0.7520	0.2475	1.0634	0.3530	1.1143	0.3603	0.6274	0.1794
	ED4	0.7627	0.2505	1.1314	0.3504	1.2172	0.3629	0.6504	0.1844
	EMZ1	0.6655	0.2180	0.9513	0.3060	1.0554	0.3134	0.5859	0.1592
	LD4	0.7629	0.2499	1.1327	0.3530	1.2232	0.3663	0.6511	0.1852
	LM4	0.7629	0.2499	1.1329	0.3536	1.2244	0.3667	0.6511	0.1852
$a/h = 100$	FSDT	0.4958	0.0083	0.6441	0.0117	0.6592	0.0119	0.4053	0.0059
	ED2	0.6073	0.0102	0.7891	0.0144	0.8075	0.0145	0.4964	0.0072
	ED4	0.6073	0.0102	0.7892	0.0144	0.8077	0.0145	0.4965	0.0072
	EMZ1	0.5083	0.0085	0.6601	0.0120	0.6801	0.0122	0.4215	0.0061
	LD4	0.6073	0.0102	0.7892	0.0144	0.8077	0.0145	0.4965	0.0072
	LM4	0.6073	0.0102	0.7892	0.0144	0.8077	0.0145	0.4965	0.0072

Table 5. Benchmark: Dimensionless normal displacement $\bar{w} = 10E_c h^3 u_z / (\bar{p}_z a^4)$ and dimensionless in-plane displacement $\bar{u} = 10E_c h^3 u_x / (\bar{p}_z a^4)$ for a sandwich square plate with core in FGM, using Zenkour's formula (19).

		$\kappa = 1$		$\kappa = 5$		$\kappa = 10$		$E = 225 \text{ GPa}$	
		$\bar{\sigma}_{xx}(h/3)$	$\bar{\sigma}_{xy}(h/3)$	$\bar{\sigma}_{xx}(h/3)$	$\bar{\sigma}_{xy}(h/3)$	$\bar{\sigma}_{xx}(h/3)$	$\bar{\sigma}_{xy}(h/3)$	$\bar{\sigma}_{xx}(h/3)$	$\bar{\sigma}_{xy}(h/3)$
$a/h = 4$	FSDT	0.6973	-0.2775	0.5003	-0.2121	0.4198	-0.1679	0.4941	-0.1976
	ED2	0.6636	-0.3094	0.4938	-0.2211	0.3872	-0.1711	0.4742	-0.2179
	ED4	0.6544	-0.3007	0.4834	-0.2022	0.3823	-0.1479	0.4663	-0.2065
	EMZ1	0.7707	-0.2551	0.6303	-0.1799	0.5309	-0.1375	0.5554	-0.1835
	LD4	0.6530	-0.3007	0.4693	-0.1999	0.3627	-0.1412	0.4801	-0.2070
	LM4	0.6531	-0.3007	0.4672	-0.1996	0.3611	-0.1403	0.4801	-0.2070
$a/h = 100$	FSDT	17.344	-6.9375	13.258	-5.3033	10.495	-4.1981	12.352	-4.9408
	ED2	15.784	-8.4972	12.066	-6.4950	9.5510	-5.1413	11.241	-6.0515
	ED4	15.784	-8.4968	12.065	-6.4943	9.5509	-5.1404	11.241	-6.0511
	EMZ1	18.928	-7.1107	15.244	-5.4326	12.597	-4.3287	13.554	-5.1375
	LD4	15.784	-8.4968	12.065	-6.4942	9.5501	-5.1402	11.242	-6.0511
	LM4	15.784	-8.4968	12.065	-6.4942	9.5500	-5.1401	11.242	-6.0511

Table 6. Benchmark: Dimensionless in-plane stresses $\bar{\sigma}_{xx} = h\sigma_{xx}/(a\bar{p}_z)$ and $\bar{\sigma}_{xy} = h\sigma_{xy}/(a\bar{p}_z)$ for a sandwich square plate with core in FGM, using Zenkour's formula (19).

been chosen, the displacements and the stresses are investigated in the thickness z direction for the case of four different cores ($\kappa = 1$, $\kappa = 5$, $\kappa = 10$, and $E_c = \text{constant} = 225 \text{ GPa}$) and for the thickness ratio $a/h = 10$. The displacements in the z direction obtained using a core with a constant Young's modulus

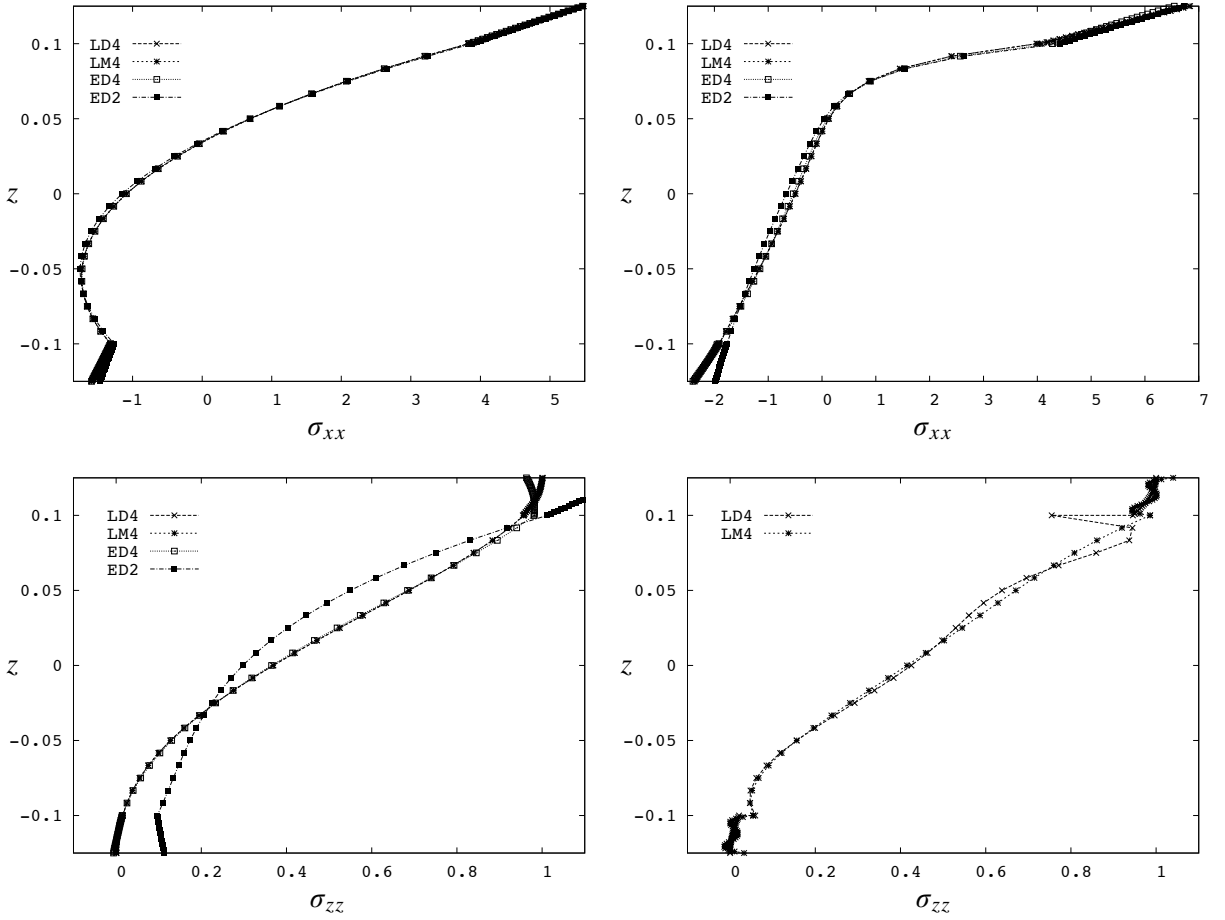


Figure 9. Benchmark: Sandwich plate with core in FGM. In-plane stress σ_{xx} (top row) and transverse-normal stress σ_{zz} (bottom row) versus z for $\kappa = 1$ (left) and $\kappa = 10$ (right). The thickness ratio is $a/h = 4$.

are more conservative than the FGM core cases (top row in Figure 10). On the contrary, the use of an FGM core allows in-plane stresses σ_{xx} and σ_{xy} continuous in the z direction to be obtained, which is not possible with a “classical” core, and the typical discontinuity of in-plane stresses for the sandwich structures is clearly shown (middle row in Figure 10). The discontinuity exhibited by the FGM core in the case of transverse shear and normal stresses σ_{xz} and σ_{zz} in Figure 10 is due to the use of a PVD model. These stresses can actually be obtained continuously in z if we use a mixed model, as already seen in Figure 7.

5. Conclusions

This paper has investigated the static response of several sandwich plates that include different types of functionally graded layers. Conclusions have been outlined, regarding the modeling tools used for these types of structure and the design of sandwich plates including a core in FGM. It has been shown

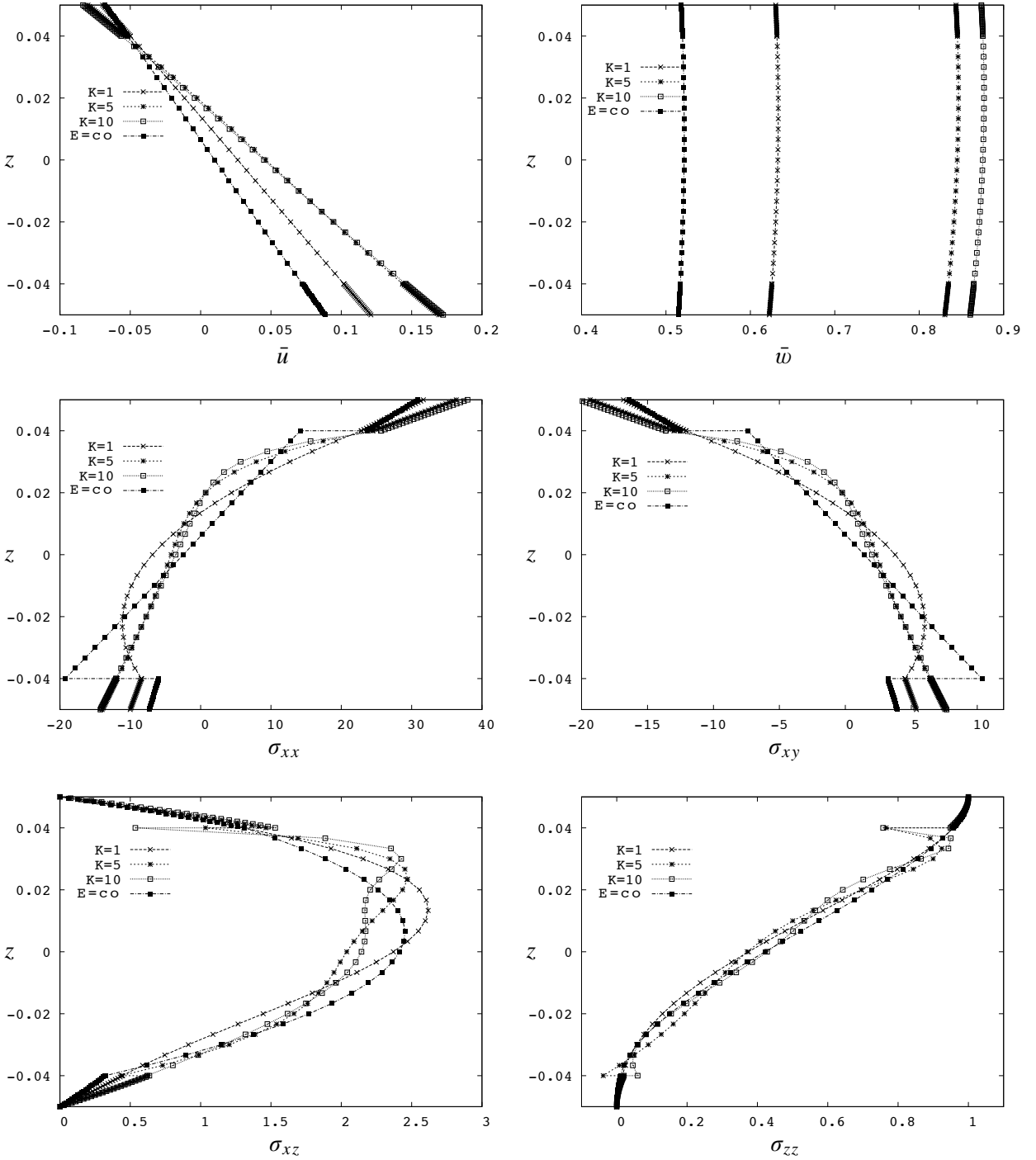


Figure 10. Benchmark: For the sandwich plate with core in FGM, displacements $(\bar{u}, \bar{w}) = 10(u_x, u_z)E_c h^3 / (\bar{p}_z a^4)$ and stresses σ_{xx} , σ_{xy} , σ_{xz} and σ_{zz} versus z for LD4 theory. In addition to the values $\kappa = 1, 5, 10$ in Zenkour’s formula (19), we consider an isotropic material with $E = 225$ GPa for the core (“E = co”). Thickness ratio: $a/h = 10$.

		$\kappa = 1$		$\kappa = 5$		$\kappa = 10$		$E = 225 \text{ GPa}$	
		$\bar{\sigma}_{xz}(0)$	$\bar{\sigma}_{zz}(0)$	$\bar{\sigma}_{xz}(0)$	$\bar{\sigma}_{zz}(0)$	$\bar{\sigma}_{xz}(0)$	$\bar{\sigma}_{zz}(0)$	$\bar{\sigma}_{xz}(0)$	$\bar{\sigma}_{zz}(0)$
$a/h = 4$	FSDT	0.1591	-0.1811	0.0891	-0.1113	0.0906	-0.0965	0.1591	-0.0677
	ED2	0.1913	0.0743	0.1205	0.0429	0.1177	0.0453	0.1704	0.0959
	ED4	0.2374	0.0912	0.1925	0.0833	0.2015	0.0970	0.2400	0.1157
	EMZ1	0.1923	-0.0002	0.1327	0.0051	0.1409	0.0403	0.1950	0.1272
	LD4	0.2345	0.0922	0.1998	0.0911	0.2113	0.1064	0.2405	0.1058
	LM4	0.2345	0.0922	0.2026	0.0924	0.2124	0.1067	0.2403	0.1058
$a/h = 100$	FSDT	0.1591	-4.5270	0.0891	-2.7824	0.0906	-2.4115	0.1591	-1.6935
	ED2	0.1945	0.0084	0.1225	0.0018	0.1192	0.0019	0.1726	0.0039
	ED4	0.2403	0.0037	0.1965	0.0034	0.2043	0.0039	0.2415	0.0046
	EMZ1	0.1950	-2.7104	0.1350	-1.6383	0.1378	-1.2957	0.1955	-0.1044
	LD4	0.2375	0.0038	0.2046	0.0037	0.2149	0.0043	0.2417	0.0042
	LM4	0.2375	0.0038	0.2055	0.0037	0.2122	0.0042	0.2417	0.0042

Table 7. Benchmark: Dimensionless transverse shear stress $\bar{\sigma}_{xz} = h\sigma_{xz}/(a\bar{p}_z)$ and transverse normal stress $\bar{\sigma}_{zz} = h\sigma_{zz}/(a\bar{p}_z)$ for a sandwich square plate with core in FGM, using Zenkour’s formula (19).

that in order to investigate multilayer plates embedding FGM layers, the use of advanced models is mandatory, in particular for thick and moderately thick plates as well as for complicated laws in the z direction given for the material properties. To obtain a quasi-three-dimensional response, LW models and high orders of expansion are necessary. Mixed models are convenient for particular variables such as transverse shear/normal stresses. In the design of sandwich plates, the use of FGM cores can represent a valid alternative to classical materials, because they allow particular features, such as the continuity of in-plane stresses in the thickness direction, that conventional cores do not allow. The discussion about the optimum design of multilayer plates including FGM layers could be the subject of future works. In them the heat conduction problem will be considered and material properties will be dependent on temperature.

References

[Anderson 2003] T. A. Anderson, “A 3-D elasticity solution for a sandwich composite with functionally graded core subjected to transverse loading by a rigid sphere”, *Compos. Struct.* **60**:3 (2003), 265–274.

[Avila 2007] A. F. Avila, “Failure mode investigation of sandwich beams with functionally graded core”, *Compos. Struct.* **81**:3 (2007), 323–330.

[Batra and Jin 2005] R. C. Batra and J. Jin, “Natural frequencies of a functionally graded anisotropic rectangular plate”, *J. Sound Vib.* **282**:2 (2005), 509–516.

[Birman and Byrd 2007] V. Birman and L. W. Byrd, “Modeling and analysis of functionally graded materials and structures”, *Appl. Mech. Rev.* **60**:5 (2007), 195–216.

[Brischetto and Carrera 2008] S. Brischetto and E. Carrera, “Advanced mixed theories for bending analysis of functionally graded plates”, *Comput. Struct.* (2008). In press.

- [Carrera 1995] E. Carrera, “A class of two-dimensional theories for anisotropic multilayered plates analysis”, *Mem. Accad. Sci. Torino Cl. Sci. Fis. Mat. Natur.* **19–20** (1995), 49–87.
- [Carrera 2002] E. Carrera, “Theories and finite elements for multilayered, anisotropic, composite plates and shells”, *Arch. Comput. Methods Eng.* **9:2** (2002), 87–140.
- [Carrera 2003] E. Carrera, “Historical review of zig-zag theories for multilayered plates and shells”, *Appl. Mech. Rev.* **56:3** (2003), 287–308.
- [Carrera and Brischetto 2008] E. Carrera and S. Brischetto, “Analysis of thickness locking in classical, refined and mixed multilayered plate theories”, *Compos. Struct.* **82:4** (2008), 549–562.
- [Carrera et al. 2008] E. Carrera, S. Brischetto, and A. Robaldo, “Variable kinematic model for the analysis of functionally graded material plates”, *AIAA J.* **46:1** (2008), 194–203.
- [Cauchy 1828] A. L. Cauchy, “Sur l’équilibre et le mouvement d’une plaque solide”, pp. 381–411 in *Œuvres complètes d’Augustin Cauchy: exercices de mathématique (anciens exercices)*, vol. 8, Ser. 2, Gauthier-Villars, Paris, 1828.
- [Cheng and Zhong 2007] Z. Cheng and Z. Zhong, “Analysis of a moving crack in a functionally graded strip between two homogeneous layers”, *Int. J. Mech. Sci.* **49:9** (2007), 1038–1046.
- [Chi and Chung 2006] S.-H. Chi and Y.-L. Chung, “Mechanical behavior of functionally graded material plates under transverse load, I: Analysis”, *Int. J. Solids Struct.* **43:13** (2006), 3657–3674.
- [Dahan et al. 2001] I. Dahan, U. Admon, N. Frage, J. Sariel, M. P. Dariel, and J. J. Moore, “The development of a functionally graded TiC-Ti multilayer hard coating”, *Surf. Coat. Technol.* **137:2–3** (2001), 111–115.
- [Etemadi et al. 2008] E. Etemadi, A. Afaghi-Khatibi, and M. Takaffoli, “3D finite element simulation of sandwich panels with a functionally graded core subjected to low velocity impact”, *Compos. Struct.* (2008). In press.
- [Ferreira et al. 2005] A. J. M. Ferreira, R. C. Batra, C. M. C. Roque, L. F. Qian, and P. A. L. S. Martins, “Static analysis of functionally graded plates using third-order shear deformation theory and a meshless method”, *Compos. Struct.* **69:4** (2005), 449–457.
- [Kashtalyan 2004] M. Kashtalyan, “Three-dimensional elasticity solution for bending of functionally graded rectangular plates”, *Eur. J. Mech. A Solids* **23:5** (2004), 853–864.
- .
- [Kashtalyan and Menshykova 2009] M. Kashtalyan and M. Menshykova, “Three-dimensional elasticity solution for sandwich panels with a functionally graded core”, *Compos. Struct.* **87:1** (2009), 36–43.
- [Kirchhoff 1850] G. Kirchhoff, “Über das Gleichgewicht und die Bewegung einer elastischen Scheibe”, *J. Reine Angew. Math.* **40** (1850), 51–88.
- [Kirugulige et al. 2005] M. S. Kirugulige, R. Kitey, and H. V. Tippur, “Dynamic fracture behavior of model sandwich structures with functionally graded core: a feasibility study”, *Compos. Sci. Technol.* **65:7–8** (2005), 1052–1068.
- [Li and Fan 2007] X.-F. Li and T.-Y. Fan, “Dynamic analysis of a crack in a functionally graded material sandwiched between two elastic layers under anti-plane loading”, *Compos. Struct.* **79:2** (2007), 211–219.
- [Li et al. 2008] Q. Li, V. P. Iu, and K. P. Kou, “Three-dimensional vibration analysis of functionally graded material sandwich plates”, *J. Sound Vib.* **311:1–2** (2008), 498–515.
- [Mindlin 1951] R. D. Mindlin, “Influence of rotatory inertia and shear in flexural motions of isotropic elastic plates”, *J. Appl. Mech. (ASME)* **18** (1951), 31–28.
- [Mori and Tanaka 1973] T. Mori and K. Tanaka, “Average stress in matrix and average elastic energy of materials with misfitting inclusions”, *Acta Metall.* **21:5** (1973), 571–574.
- [Murakami 1986] H. Murakami, “Laminated composite plate theory with improved in-plane responses”, *J. Appl. Mech. (ASME)* **53** (1986), 661–666.
- [Nguyen et al. 2008] T.-K. Nguyen, K. Sab, and G. Bonnet, “First-order shear deformation plate models for functionally graded materials”, *Compos. Struct.* **83:1** (2008), 25–36.
- [Poisson 1829] S. D. Poisson, “Mémoire sur l’équilibre et le mouvement des corps élastiques”, *Mém. Acad. Sci. Paris* **8** (1829), 357–570.

- [Qian et al. 2004] L. F. Qian, R. C. Batra, and L. M. Chen, “Static and dynamic deformations of thick functionally graded elastic plates by using higher-order shear and normal deformable plate theory and meshless local Petrov–Galerkin method”, *Compos. B Eng.* **35**:6–8 (2004), 685–697.
- [Ramirez et al. 2006] F. Ramirez, P. R. Heyliger, and E. Pan, “Static analysis of functionally graded elastic anisotropic plates using a discrete layer approach”, *Compos. B Eng.* **37**:1 (2006), 10–20.
- [Reddy 2004] J. N. Reddy, *Mechanics of laminated composite plates: theory and analysis*, CRC Press, New York, 2004.
- [Reddy and Cheng 2001] J. N. Reddy and Z.-Q. Cheng, “Three-dimensional thermomechanical deformations of functionally graded rectangular plates”, *Eur. J. Mech. A Solids* **20**:5 (2001), 841–855.
- [Reissner 1945] E. Reissner, “The effect of transverse shear deformation on the bending of elastic plates”, *J. Appl. Mech. (ASME)* **12** (1945), A–69–A–77.
- [Reissner 1984] E. Reissner, “On a certain mixed variational theorem and a proposed application”, *Int. J. Numer. Methods Eng.* **20**:7 (1984), 1366–1368.
- [Shen and Li 2008] H.-S. Shen and S.-R. Li, “Postbuckling of sandwich plates with FGM face sheets and temperature-dependent properties”, *Compos. B Eng.* **39**:2 (2008), 332–344.
- [Shodja et al. 2007] H. M. Shodja, H. Haftbaradaran, and M. Asghari, “A thermoelasticity solution of sandwich structures with functionally graded coating”, *Compos. Sci. Technol.* **67**:6 (2007), 1073–1080.
- [Vel and Batra 2002] S. S. Vel and R. C. Batra, “Exact solution for thermoelastic deformations of functionally graded thick rectangular plates”, *AIAA J.* **40**:7 (2002), 1421–1433.
- [Vel and Batra 2003] S. S. Vel and R. C. Batra, “Three-dimensional analysis of transient thermal stresses in functionally graded plates”, *Int. J. Solids Struct.* **40**:25 (2003), 7181–7196.
- [Vel and Batra 2004] S. S. Vel and R. C. Batra, “Three-dimensional exact solution for the vibration of functionally graded rectangular plates”, *J. Sound Vib.* **272**:3–5 (2004), 703–730.
- [Xia and Shen 2008] X.-K. Xia and H.-S. Shen, “Vibration of post-buckled sandwich plates with FGM face sheets in a thermal environment”, *J. Sound Vib.* **314**:1–2 (2008), 254–274.
- [Zenkour 2005a] A. M. Zenkour, “A comprehensive analysis of functionally graded sandwich plates, 1: Deflection and stresses”, *Int. J. Solids Struct.* **42**:18–19 (2005), 5224–5242.
- [Zenkour 2005b] A. M. Zenkour, “A comprehensive analysis of functionally graded sandwich plates, 2: Buckling and free vibration”, *Int. J. Solids Struct.* **42**:18–19 (2005), 5243–5258.
- [Zenkour 2006] A. M. Zenkour, “Generalized shear deformation theory for bending analysis of functionally graded plates”, *Appl. Math. Model.* **30**:1 (2006), 67–84.
- [Zhao et al. 2008] J. Zhao, Y. Li, and X. Ai, “Analysis of transient thermal stress in sandwich plate with functionally graded coatings”, *Thin Solid Films* **516**:21 (2008), 7581–7587.
- [Zhu and Sankar 2007] H. Zhu and B. V. Sankar, “Analysis of sandwich TPS panel with functionally graded foam core by Galerkin method”, *Compos. Struct.* **77**:3 (2007), 280–287.

Received 11 Jul 2008. Revised 27 Oct 2008. Accepted 1 Nov 2008.

SALVATORE BRISCHETTO: salvatore.brischetto@polito.it

Politecnico di Torino, Department of Aeronautics and Space Engineering, Corso Duca Degli Abruzzi, 24, 10129 Torino, Italy

VIBRATION SUPPRESSION ANALYSIS OF FGM SHELLS WITH HIGHER ORDER SHEAR DEFORMATION THEORY

SURESH CHANDRA PRADHAN

Analytical solutions of functionally graded material (FGM) shells with embedded magnetostrictive layers are presented in this study. These magnetostrictive layers are used for vibration suppression in the functionally graded shells. Higher order shear deformation theory is employed to study the vibration suppression characteristics. The exact solution for the FGM shell with simply supported boundary conditions is based on the Navier solution procedure. Negative velocity feedback control is used. The parametric effect of the location of the magnetostrictive layers, material properties, and control parameters on the suppression effect are investigated in detail. Higher order shear deformation theory has significant influence on the prediction of the vibration response of thick shells. Further, it is found that the shortest vibration suppression time is achieved by placing the actuating layers farthest from the neutral plane, that the use of thinner smart material layers leads to better vibration attenuation characteristics, and that the vibration suppression time is longer for a smaller value of the feedback control coefficient.

A list of symbols can be found starting on page 54.

1. Introduction

A number of materials have been used in sensor/actuator applications. Piezoelectric materials, magnetostrictive materials, shape memory alloys, and electrorheological fluids have all been integrated with structures to make smart structures. Among these materials piezoelectric, electrostrictive, and magnetostrictive materials have the capability to serve as both sensors and actuators. Piezoelectric materials exhibit a linear relationship between the electric field and strains for low field values (up to 100 V/mm). This relationship is nonlinear for large fields, and the material exhibits hysteresis. Further, piezoelectric materials show dielectric aging and hence lack reproducibility of strains, that is, a drift from zero state of strain is observed under cyclic electric field applications.

An ideal actuator, for distributed embedded application, should have high energy density, negligible weight, and point excitation with a wide frequency bandwidth. Terfenol-D, a magnetostrictive material, has the characteristics of being able to produce strains up to 2000 and an energy density as high as 0.0025 J m^{-3} in response to a magnetic field. Goodfriend and Shoop [1992] reviewed the material properties of Terfenol-D with regard to its use in vibration isolation. Anjanappa and Bi [1994] investigated the feasibility of using embedded magnetostrictive mini actuators for smart structure applications, such as vibration suppression of beams. Bryant et al. [1993] presented experimental results of a magnetostrictive Terfenol-D rod used in dual capacity as a passive structural support element and an active vibration control actuator. Krishna Murty et al. [1997] proposed magnetostrictive actuators that take advantage of the ease with which the actuators can be embedded and the use of the remote excitation capability of

Keywords: functionally graded materials, higher order, shear deformation, vibration, shell.

magnetostrictive particles as new actuators for smart structures. This work is limited to flexible beam theory.

Friedmann et al. [2001] used the magnetostrictive material Terfenol-D in high speed helicopter rotors and studied the vibration reduction characteristics. Vibration and shape control of flexible structures are achieved with the help of actuators and a control law. The response of functionally graded material (FGM) shells is also studied by Loy et al. [1999], Pradhan et al. [2000], Woo and Meguid [2001], and He et al. [2002]. Many modern techniques have been developed in recent years to meet the challenge of designing controllers that suit the function under the required conditions. There have been a number of studies on vibration control of flexible structures using magnetostrictive materials [Bryant et al. 1993; Anjanappa and Bi 1994; Krishna Murty et al. 1997; Giurgiutiu et al. 2001; Pradhan et al. 2001]. Higher order shear deformation theory (HSDT) is discussed in [Reddy 1984a; 1984b]. Kadoli and Ganesan [2006], Haddadpour et al. [2007], Li [2008], Pradyumna and Bandyopadhyay [2008], and Matsunaga [2009] described various vibration analyses of functionally graded materials. Although there have been important research efforts devoted to characterizing the properties of Terfenol-D, fundamental information about the variation in elastomagnetic material properties in a thick functionally graded shell is not available.

In the present work vibration control of functionally graded shells is studied using HSDT. Exact solutions are developed for simply supported doubly curved functionally graded shells with magnetostrictive layers. This closed form solution exists for FGM shells where the coefficients A_{16} , A_{26} , B_{16} , B_{26} , D_{16} , D_{26} , and A_{45} are equal to zero. A simple negative velocity feedback control is used to actively control the dynamic response of the structure through a closed loop control. Numerical results of the vibration suppression effect for various locations of the magnetostrictive layers, material properties, and control parameters are presented. The influence of HSDT on thick FGM shells is also investigated.

2. Theoretical formulation

Kinematic description. Figure 1, left, shows a differential element of a doubly curved shell element with constant curvatures along two coordinate directions (ξ_1, ξ_2) , where (ξ_1, ξ_2, ζ) denote the orthogonal curvilinear coordinates such that the ξ_1 and ξ_2 curves are the lines of curvature on the middle surface ($\zeta = 0$). Thus, in the doubly curved shell panel considered here, the lines of the principal curvature coincide with the coordinate lines. The values of the principal radii of curvature of the middle surface are denoted by R_1 and R_2 . The position vector of a point $(\xi_1, \xi_2, 0)$ on the middle surface is denoted by \mathbf{r} , and the position of an arbitrary point (ξ_1, ξ_2, ζ) is denoted by \mathbf{R} (see Figure 1, top right). The square of the distance ds between points $(\xi_1, \xi_2, 0)$ and $(\xi_1 + d\xi_1, \xi_2 + d\xi_2, 0)$ is determined as [Pradhan 2005]

$$(ds)^2 = d\mathbf{r} \cdot d\mathbf{r} = \alpha_1^2 (d\xi_1)^2 + \alpha_2^2 (d\xi_2)^2, \quad (1)$$

in which $d\mathbf{r} = \mathbf{g}_1 d\xi_1 + \mathbf{g}_2 d\xi_2$, the vectors \mathbf{g}_1 and \mathbf{g}_2 ($\mathbf{g}_i = \partial \mathbf{r} / \partial \xi_i$) are tangent to the ξ_1 and ξ_2 coordinate lines and α_1, α_2 are the surface metrics:

$$\alpha_1^2 = \mathbf{g}_1 \cdot \mathbf{g}_1, \quad \alpha_2^2 = \mathbf{g}_2 \cdot \mathbf{g}_2 \quad (2)$$

The square of the distance dS between (ξ_1, ξ_2, ζ) and $(\xi_1 + d\xi_1, \xi_2 + d\xi_2, \zeta + d\zeta)$ is given by

$$(dS)^2 = d\mathbf{R} \cdot d\mathbf{R} = L_1^2 (d\xi_1)^2 + L_2^2 (d\xi_2)^2 + L_3^2 (d\zeta)^2, \quad (3)$$

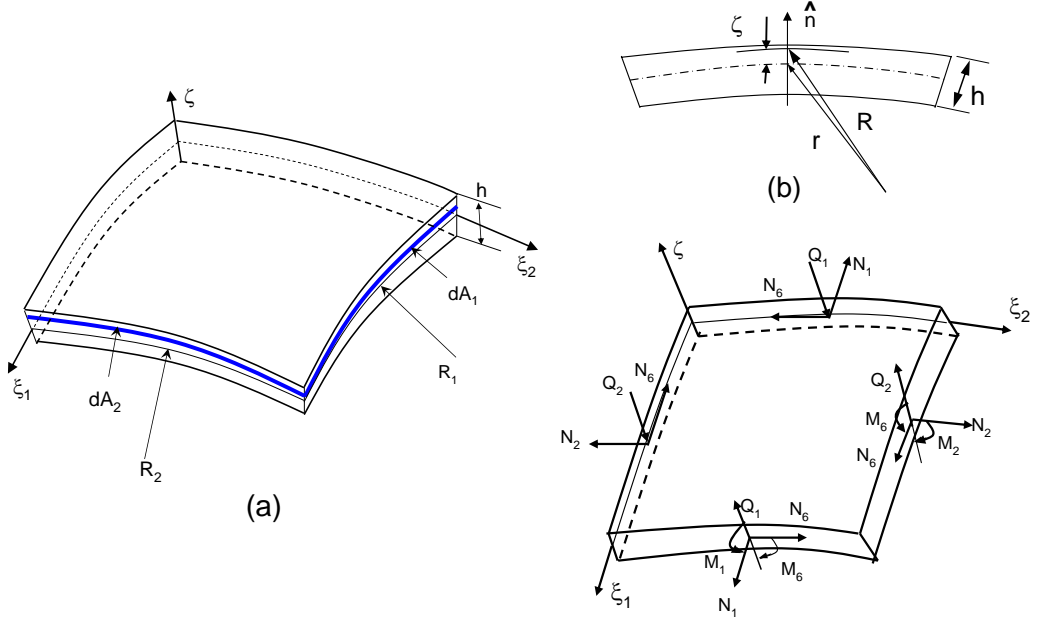


Figure 1. Geometry and stress resultants of a doubly curved shell.

in which $d\mathbf{R} = \frac{\partial \mathbf{R}}{\partial \xi_1} d\xi_1 + \frac{\partial \mathbf{R}}{\partial \xi_2} d\xi_2 + \frac{\partial \mathbf{R}}{\partial \zeta} d\zeta$ and L_1 , L_2 , and L_3 are the Lamé coefficients

$$L_1 = \alpha_1 \left(1 + \frac{\zeta}{R_1} \right), \quad L_2 = \alpha_2 \left(1 + \frac{\zeta}{R_2} \right), \quad L_3 = 1. \quad (4)$$

Displacement field. We assume the following form of the displacement field, consistent with the assumptions of a thick shell theory as explained in [Reddy and Liu 1985]:

$$\begin{aligned} \bar{u}_1(\xi_1, \xi_2, \zeta, t) &= \frac{L_1}{\alpha_1} u_1(\xi_1, \xi_2, t) + \zeta \phi_1(\xi_1, \xi_2, t) - C_1 \zeta^3 \left(\phi_1 + \frac{\partial u_3}{\alpha_1 \partial \xi_1} \right), \\ \bar{u}_2(\xi_1, \xi_2, \zeta, t) &= \frac{L_2}{\alpha_2} u_2(\xi_1, \xi_2, t) + \zeta \phi_2(\xi_1, \xi_2, t) - C_1 \zeta^3 \left(\phi_2 + \frac{\partial u_3}{\alpha_1 \partial \xi_2} \right), \\ \bar{u}_3(\xi_1, \xi_2, \zeta, t) &= u_3(\xi_1, \xi_2, t), \end{aligned} \quad (5)$$

where

$$\frac{1}{\partial x_i} = \frac{1}{\alpha_i} \frac{1}{\partial \xi_i} \quad (i = 1, 2), \quad (6)$$

$(\bar{u}_1, \bar{u}_2, \bar{u}_3)$ are the displacements of a point (ξ_1, ξ_2, ζ) along the (ξ_1, ξ_2, ζ) coordinates, and (u_1, u_2, u_3) are the displacements of a point $(\xi_1, \xi_2, 0)$ on the mid surface of the shell. C_1 is a constant, which depends on shell thickness. The strain-displacement relations are written as

$$\begin{Bmatrix} \varepsilon_1 \\ \varepsilon_2 \\ \varepsilon_6 \end{Bmatrix} = \begin{Bmatrix} \varepsilon_1^0 \\ \varepsilon_2^0 \\ \varepsilon_6^0 \end{Bmatrix} + \zeta \begin{Bmatrix} \varepsilon_1^1 \\ \varepsilon_2^1 \\ \varepsilon_6^1 \end{Bmatrix} + \zeta^3 \begin{Bmatrix} \varepsilon_1^2 \\ \varepsilon_2^2 \\ \varepsilon_6^2 \end{Bmatrix}, \quad \begin{Bmatrix} \gamma_4 \\ \gamma_5 \end{Bmatrix} = \begin{Bmatrix} \gamma_4^0 \\ \gamma_5^0 \end{Bmatrix} + \zeta^2 \begin{Bmatrix} \gamma_4^1 \\ \gamma_5^1 \end{Bmatrix}, \quad (7)$$

where

$$\begin{aligned} \begin{Bmatrix} \varepsilon_1^0 \\ \varepsilon_2^0 \\ \varepsilon_6^0 \end{Bmatrix} &= \begin{Bmatrix} \frac{\partial u_1}{\partial x_1} + \frac{1}{R_1} u_3 \\ \frac{\partial u_2}{\partial x_2} + \frac{1}{R_2} u_3 \\ \frac{\partial u_2}{\partial x_1} + \frac{\partial u_1}{\partial x_2} \end{Bmatrix}, & \begin{Bmatrix} \varepsilon_1^1 \\ \varepsilon_2^1 \\ \varepsilon_6^1 \end{Bmatrix} &= \begin{Bmatrix} \frac{\partial \phi_1}{\partial x_1} \\ \frac{\partial \phi_2}{\partial x_2} \\ \frac{\partial \phi_2}{\partial x_1} + \frac{\partial \phi_1}{\partial x_2} \end{Bmatrix}, & \begin{Bmatrix} \varepsilon_1^2 \\ \varepsilon_2^2 \\ \varepsilon_6^2 \end{Bmatrix} &= -C_1 \begin{Bmatrix} \frac{\partial \phi_1}{\partial x_1} + \frac{\partial^2 u_3}{\partial x_1^2} \\ \frac{\partial \phi_2}{\partial x_2} + \frac{\partial^2 u_3}{\partial x_2^2} \\ \frac{\partial \phi_2}{\partial x_1} + \frac{\partial \phi_1}{\partial x_2} + 2 \frac{\partial^2 u_3}{\partial x_1 \partial x_2} \end{Bmatrix}, \\ \begin{Bmatrix} \gamma_4^0 \\ \gamma_5^0 \end{Bmatrix} &= \begin{Bmatrix} \phi_2 + \frac{\partial u_3}{\partial x_2} \\ \phi_1 + \frac{\partial u_3}{\partial x_1} \end{Bmatrix}, & \begin{Bmatrix} \gamma_4^1 \\ \gamma_5^1 \end{Bmatrix} &= -C_2 \begin{Bmatrix} \phi_2 + \frac{\partial u_3}{\partial x_2} \\ \phi_1 + \frac{\partial u_3}{\partial x_1} \end{Bmatrix}, \end{aligned} \quad (8)$$

and (ϕ_1, ϕ_2) are rotations of a transverse normal line about the ζ_2 and ζ_1 coordinate axes, respectively:

$$\phi_1 = -\frac{\partial u_3}{\partial \zeta_1}, \quad \phi_2 = -\frac{\partial u_3}{\partial \zeta_2}. \quad (9)$$

The constants C_1 and C_2 are defined as

$$C_1 = \frac{4}{3h^2}, \quad C_2 = 3C_1. \quad (10)$$

Constitutive relations. Suppose that the shell is composed of N functionally graded layers. The stress-strain relations of the k -th layer, whether structural layer or actuating/sensing layer, in the shell coordinate system are given as

$$\begin{Bmatrix} \sigma_1 \\ \sigma_2 \\ \sigma_4 \\ \sigma_5 \\ \sigma_6 \end{Bmatrix}^{(k)} = \begin{bmatrix} Q_{11} & Q_{12} & 0 & 0 & 0 \\ Q_{12} & Q_{22} & 0 & 0 & 0 \\ 0 & 0 & Q_{44} & 0 & 0 \\ 0 & 0 & 0 & Q_{55} & 0 \\ 0 & 0 & 0 & 0 & Q_{66} \end{bmatrix}^{(k)} \begin{Bmatrix} \varepsilon_1 \\ \varepsilon_2 \\ \varepsilon_4 \\ \varepsilon_5 \\ \varepsilon_6 \end{Bmatrix} - \zeta \begin{Bmatrix} ce_{31} \\ e_{32} \\ 0 \\ 0 \\ e_{36} \end{Bmatrix}^{(k)} H, \quad (11)$$

where $Q_{ij}^{(k)}$ are the stiffnesses of the k -th layer and

$$Q_{11} = \frac{E_{\text{FGM}}}{1 - \nu_{\text{FGM}}^2}, \quad Q_{12} = \frac{\nu_{\text{FGM}} E_{\text{FGM}}}{1 - \nu_{\text{FGM}}^2}, \quad Q_{22} = Q_{11}, \quad Q_{44} = Q_{55} = Q_{66} = G_{\text{FGM}}. \quad (12)$$

The superscript k on Q_{ij} as well as on the engineering constants E_{FGM} , ν_{FGM} , and so on are omitted for brevity. In Equation (11), H denotes the intensity of the magnetic field. H is applied normal to the thickness of the shell. e_{ij} are the magnetostrictive material coefficients.

Feedback control. A velocity feedback control is used in the present study. In the velocity feedback control, the magnetic field intensity H is expressed in terms of the coil current $I(\zeta_1, \zeta_2, t)$ as

$$H(\zeta_1, \zeta_2, t) = k_c I(\zeta_1, \zeta_2, t). \quad (13)$$

Current I is related to the transverse velocity \dot{u}_3 component as

$$I(\zeta_1, \zeta_2, t) = c(t) \frac{\partial u_3}{\partial t} \quad (14)$$

where k_c is the magnetic coil constant and is related to the number of coil turns n_c , the coil width b_c , and the coil radius r_c by

$$k_c = \frac{n_c}{\sqrt{b_c^2 + 4r_c^2}}. \quad (15)$$

The parameter $c(t)$ is known as the control gain.

Equations of motion. The equations of motion are derived from the dynamic version of the principle of virtual work. By integrating the displacement gradients by parts and setting the coefficients δu_1 , δu_2 , δu_3 , $\delta \phi_1$, and $\delta \phi_2$ to zero separately (the moment terms in the first two equations are omitted) we get

$$\begin{aligned} \frac{\partial N_1}{\partial x_1} + \frac{\partial N_6}{\partial x_2} &= \bar{I}_1 \frac{\partial^2 u_1}{\partial t^2} + \bar{I}_2 \frac{\partial^2 \phi_1}{\partial t^2} - \bar{I}_3 \frac{\partial^2 u_3}{\partial t^2}, & \frac{\partial N_6}{\partial x_1} + \frac{\partial N_2}{\partial x_2} &= \bar{J}_1 \frac{\partial^2 u_2}{\partial t^2} + \bar{J}_2 \frac{\partial^2 \phi_2}{\partial t^2} - \bar{J}_3 \frac{\partial^2 u_3}{\partial t^2}, \\ \frac{\partial Q_1}{\partial x_1} + \frac{\partial Q_2}{\partial x_2} - C_2 \left(\frac{\partial K_1}{\partial x_1} + \frac{\partial K_2}{\partial x_2} \right) + C_1 \left(\frac{\partial^2 P_1}{\partial x_1^2} + 2 \frac{\partial^2 P_6}{\partial x_1 \partial x_2} + \frac{\partial^2 P_2}{\partial x_2^2} \right) - \frac{N_1}{R_1} - \frac{N_2}{R_2} + q \\ &= \bar{I}_3 \frac{\partial^3 u_1}{\partial x_1 \partial t^2} + \bar{I}_5 \frac{\partial^3 \phi_1}{\partial x_1 \partial t^2} + \bar{J}_3 \frac{\partial^3 u_2}{\partial x_2 \partial t^2} + \bar{J}_5 \frac{\partial^3 \phi_2}{\partial x_2 \partial t^2} + I_1 \frac{\partial^2 u_3}{\partial t^2} - C_1^2 I_7 \left(\frac{\partial^4 u_3}{\partial x_1^2 \partial t^2} + \frac{\partial^4 u_3}{\partial x_2^2 \partial t^2} \right), \\ \frac{\partial M_1}{\partial x_1} + \frac{\partial M_6}{\partial x_2} - Q_1 + C_2 K_1 - C_1 \left(\frac{\partial P_1}{\partial x_1} + \frac{\partial P_6}{\partial x_2} \right) &= \bar{I}_2 \frac{\partial^2 u_1}{\partial t^2} + \bar{I}_4 \frac{\partial^2 \phi_1}{\partial t^2} - \bar{I}_5 \frac{\partial^3 u_3}{\partial x_1 \partial t^2}, \\ \frac{\partial M_6}{\partial x_1} + \frac{\partial M_2}{\partial x_2} - Q_2 + C_2 K_2 - C_1 \left(\frac{\partial P_6}{\partial x_1} + \frac{\partial P_2}{\partial x_2} \right) &= \bar{J}_2 \frac{\partial^2 u_2}{\partial t^2} + \bar{J}_4 \frac{\partial^2 \phi_2}{\partial t^2} - \bar{J}_5 \frac{\partial^3 u_3}{\partial x_2 \partial t^2}, \end{aligned} \quad (16)$$

where the forces N_i , the moments M_i , the third-order moments P_i , and the shear forces Q_1 , Q_2 , K_1 , and K_2 are defined as

$$\begin{aligned} (N_i, M_i, P_i) &= \sum_{k=1}^N \int_{\zeta_{k-1}}^{\zeta_k} \sigma_i^{(k)}(1, \zeta, \zeta^3) d\zeta \quad (i = 1, 2, 6), \\ (Q_1, K_1) &= \sum_{k=1}^N \int_{\zeta_{k-1}}^{\zeta_k} \sigma_5^{(k)}(1, \zeta^2) d\zeta, \quad (Q_2, K_2) = \sum_{k=1}^N \int_{\zeta_{k-1}}^{\zeta_k} \sigma_4^{(k)}(1, \zeta^2) d\zeta. \end{aligned} \quad (17)$$

The inertia-driven terms \bar{I}_i and \bar{J}_i are defined as

$$\begin{aligned} \bar{I}_1 &= I_1 + \frac{2}{R_1} I_2, & \bar{I}_2 &= I_3 + \frac{1}{R_1} I_3 - C_1 \left(I_4 + \frac{1}{R_1} I_5 \right), & \bar{I}_3 &= C_1 \left(I_4 + \frac{1}{R_1} I_5 \right), \\ \bar{J}_1 &= I_1 + \frac{2}{R_2} I_2, & \bar{J}_2 &= I_3 + \frac{1}{R_2} I_3 - C_1 \left(I_4 + \frac{1}{R_2} I_5 \right), & \bar{J}_3 &= C_1 \left(I_4 + \frac{1}{R_2} I_5 \right), \\ \bar{I}_4 &= I_3 - C_1 (2I_5 - C_1 I_7), & \bar{I}_5 &= C_1 (2I_5 - C_1 I_7), & \bar{J}_4 &= \bar{I}_4, \quad \bar{J}_5 = \bar{I}_5. \end{aligned} \quad (18)$$

The inertia terms are defined as

$$(I_1, I_2, I_3, I_4, I_5, I_7) = \sum_{k=1}^N \int_{\zeta_{k-1}}^{\zeta_k} \rho^{(k)}(1, \zeta, \zeta^2, \zeta^3, \zeta^4, \zeta^6) d\zeta, \quad (19)$$

where $\rho^{(k)}$ is the density of the k -th layer and N is the number of layers in the laminate.

Shell constitutive equation. Using Equations (7) and (11) in (17) we get the following constitutive equations for the actuator embedded shell:

$$\begin{Bmatrix} \{N\} \\ \{M\} \\ \{P\} \end{Bmatrix} = \begin{bmatrix} [A] & [B] & [E] \\ [B] & [D] & [F] \\ [E] & [F] & [H] \end{bmatrix} \begin{Bmatrix} \{\varepsilon^0\} \\ \{\varepsilon^1\} \\ \{\varepsilon^2\} \end{Bmatrix} - \begin{Bmatrix} \{N\} \\ \{M\} \\ \{P\} \end{Bmatrix}^M, \quad \begin{Bmatrix} \{Q\} \\ \{K\} \end{Bmatrix} = \begin{bmatrix} [A] & [D] \\ [D] & [F] \end{bmatrix} \begin{Bmatrix} \{\gamma^0\} \\ \{\gamma^1\} \end{Bmatrix} - \begin{Bmatrix} \{Q\} \\ \{K\} \end{Bmatrix}^M, \quad (20)$$

where the shell stiffness coefficients (A_{ij} , B_{ij} , D_{ij} , E_{ij} , F_{ij} , and H_{ij} for $i, j = 1, 2, 6$) are defined by

$$(A_{ij}, B_{ij}, D_{ij}, E_{ij}, F_{ij}, H_{ij}) = \sum_{k=1}^N \int_{\zeta_k}^{\zeta_{k+1}} \bar{Q}_{ij}^{(k)}(1, \zeta, \zeta^2, \zeta^3, \zeta^4, \zeta^6) d\zeta \quad (21)$$

and the shell stiffness coefficients (A_{ij} , D_{ij} , and F_{ij} for $i, j = 4, 5$) are defined by

$$(A_{ij}, D_{ij}, F_{ij}) = \sum_{k=1}^N \int_{\zeta_k}^{\zeta_{k+1}} \bar{Q}_{ij}^{(k)}(1, \zeta^2, \zeta^4) d\zeta \quad (i, j = 4, 5). \quad (22)$$

The magnetostrictive stress resultants ($\{N_i^M\}$, $\{M_i^M\}$, and $\{K_i^M\}$ for $i = 1, 2$) are defined by

$$\begin{aligned} \begin{Bmatrix} N_1^M \\ N_2^M \end{Bmatrix} &= \sum_{k=m_1, m_2, \dots}^N \int_{\zeta_k}^{\zeta_{k+1}} \begin{Bmatrix} \bar{e}_{31} \\ \bar{e}_{32} \end{Bmatrix} H_\zeta d\zeta = ck_c \sum_{k=m_1, m_2, \dots}^N \int_{\zeta_k}^{\zeta_{k+1}} \begin{Bmatrix} \bar{e}_{31} \\ \bar{e}_{32} \end{Bmatrix} \frac{\partial u_3}{\partial t} d\zeta \equiv \begin{Bmatrix} \mathcal{A}_{31} \\ \mathcal{A}_{32} \end{Bmatrix} \frac{\partial u_3}{\partial t}, \\ \begin{Bmatrix} M_1^M \\ M_2^M \end{Bmatrix} &= \sum_{k=m_1, m_2, \dots}^N \int_{\zeta_k}^{\zeta_{k+1}} \begin{Bmatrix} \bar{e}_{31} \\ \bar{e}_{32} \end{Bmatrix} \zeta H_\zeta d\zeta = ck_c \sum_{k=m_1, m_2, \dots}^N \int_{\zeta_k}^{\zeta_{k+1}} \begin{Bmatrix} \bar{e}_{31} \\ \bar{e}_{32} \end{Bmatrix} \frac{\partial u_3}{\partial t} \zeta d\zeta \equiv \begin{Bmatrix} \mathcal{B}_{31} \\ \mathcal{B}_{32} \end{Bmatrix} \frac{\partial u_3}{\partial t}, \\ \begin{Bmatrix} K_1^M \\ K_2^M \end{Bmatrix} &= \sum_{k=m_1, m_2, \dots}^N \int_{\zeta_k}^{\zeta_{k+1}} \begin{Bmatrix} \bar{e}_{31} \\ \bar{e}_{32} \end{Bmatrix} \zeta^3 H_\zeta d\zeta = ck_c \sum_{k=m_1, m_2, \dots}^N \int_{\zeta_k}^{\zeta_{k+1}} \begin{Bmatrix} \bar{e}_{31} \\ \bar{e}_{32} \end{Bmatrix} \frac{\partial u_3}{\partial t} \zeta^3 d\zeta \equiv \begin{Bmatrix} \mathcal{C}_{31} \\ \mathcal{C}_{32} \end{Bmatrix} \frac{\partial u_3}{\partial t}, \end{aligned} \quad (23)$$

where

$$\begin{aligned} \mathcal{A}_{ij} &= ck_c \sum_{k=m_1, m_2, \dots} \bar{e}_{ij}^{(k)} (\zeta_{k+1} - \zeta_k), \quad i = 3, \quad j = 1, 2, \\ \mathcal{B}_{ij} &= \frac{1}{2} ck_c \sum_{k=m_1, m_2, \dots} \bar{e}_{ij}^{(k)} (\zeta_{k+1}^2 - \zeta_k^2), \quad i = 3, \quad j = 1, 2, \\ \mathcal{C}_{ij} &= \frac{1}{4} ck_c \sum_{k=m_1, m_2, \dots} \bar{e}_{ij}^{(k)} (\zeta_{k+1}^4 - \zeta_k^4), \quad i = 3, \quad j = 1, 2, \end{aligned} \quad (24)$$

and m_1, m_2, \dots denote the layer numbers of the magnetostrictive (or any actuating/sensing) layers.

Functionally graded material. The material properties P_{FGM} of the FGM are controlled by the volume fractions V_{fi} and the individual material properties P_i of the constituent materials:

$$P_{\text{FGM}} = \sum_{i=1}^{nm} P_i V_{fi}. \quad (25)$$

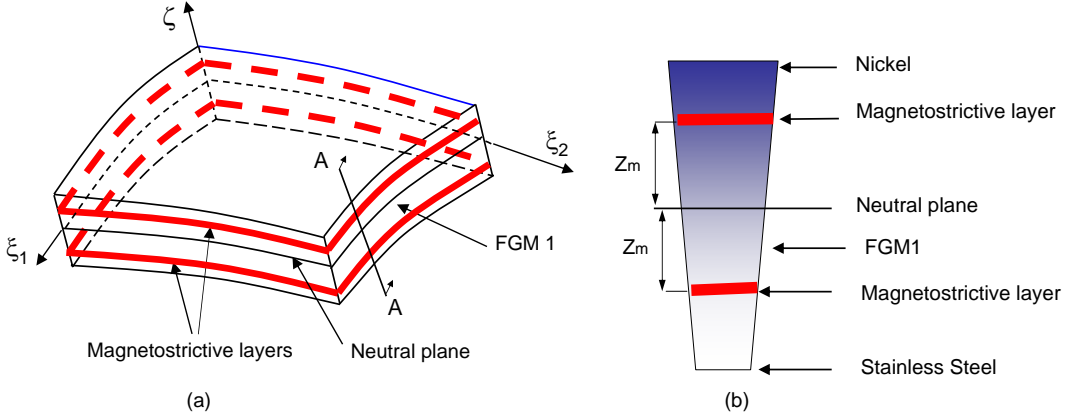


Figure 2. Left: functionally graded shell with embedded magnetostrictive layers. Right: exploded sectional view.

In the present case two different materials are particle mixed to form the FGM material. A schematic of the FGM shell with magnetostrictive layers is shown in Figure 2. The left half of the figure shows two layers of magnetostrictive materials placed symmetrically away from the neutral plane of the FGM shell. A zoomed view of section AA is shown on the right. Assuming there are no defects like voids or foreign particles in the FGM material, the sum of the volume fractions of all the constituent materials is unity:

$$\sum_{i=1}^{nm} V_{fi} = 1. \tag{26}$$

For example, metal and ceramic materials ($nm = 2$) are mixed to form the FGM shell. The volume fractions of the metal and ceramic materials are calculated by simple integration of the distribution over a domain. Different problems of interest have different expressions for the volume fractions. For bending problems of plates and shells the volume fractions of the metal (V_m) and ceramic (V_c) materials are defined as

$$V_m = \left(\frac{h-2z}{2h}\right)^{R_n}, \quad V_c = 1 - V_m, \tag{27}$$

where z is the thickness coordinate ($-h/2 \leq z \leq h/2$) and h represents the shell thickness. R_n is the power law exponent ($0 \leq R_n \leq \infty$). Here V_m varies from 100% to 0% as z varies from $-h/2$ to $h/2$. Similarly V_c varies from 0% to 100% as z varies from $-h/2$ to $h/2$. For various R_n values the average V_m and V_c are depicted in the top and bottom of Figure 3, respectively. The Young’s modulus and Poisson’s ratio of a FGM shell made up of two different materials are expressed as

$$E_{FGM} = (E_2 - E_1) \left(\frac{2z+h}{2h}\right)^{R_n} + E_1, \quad \nu_{FGM} = (\nu_2 - \nu_1) \left(\frac{2z+h}{2h}\right)^{R_n} + \nu_1. \tag{28}$$

E_1 , E_2 , and E_{FGM} are the Young’s moduli of the constituent materials and the FGM material, respectively. ν_1 , ν_2 , and ν_{FGM} are the Poisson’s ratios of the constituent materials and the FGM material, respectively. From Equation (28) we note that at $z = -h/2$, the FGM material properties are the same as those of material 1, while at $z = h/2$, they are the same as those of material 2. Thus, the FGM material properties vary smoothly across the thickness, from material 1 at the inner surface to material 2 at the outer surface.

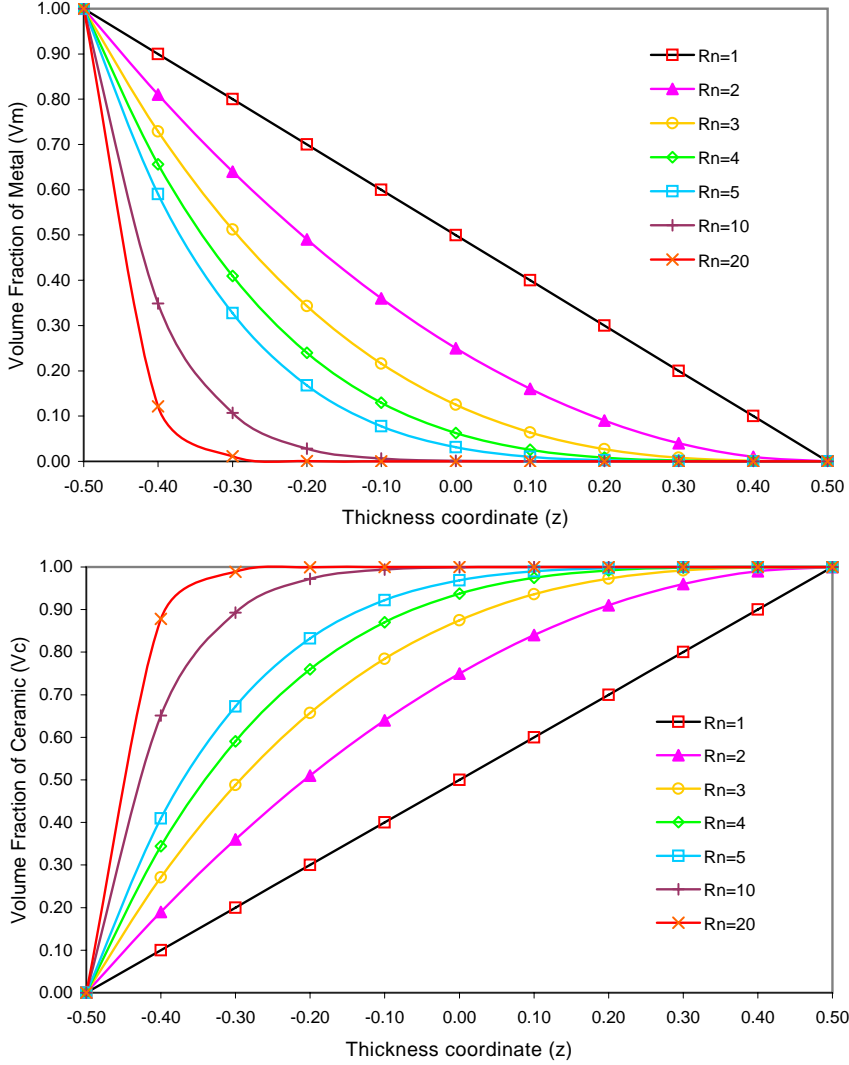


Figure 3. Volume fractions of metal and ceramic materials in the FGM shell.

Two different FGM materials are considered in the present study: FGM1 consists of stainless steel and nickel (Figure 2b), while FGM2 consists of nickel and aluminum oxide. The material properties of stainless steel, nickel, and aluminum oxide are listed in Table 1. The material properties of the FGM shells are calculated at room temperature.

	Young's Modulus E (GPa)	Poisson's ratio	Density (kg m^{-3})
Stainless steel	201.04	0.3262	7900
Nickel	244.27	0.2882	8909
Aluminum oxide	349.55	0.260	3970

Table 1. Material properties of FGM constituent materials.

3. Analytical solution

The equations of motion (16) can be expressed in terms of the displacements ($u_1, u_2, u_3, \phi_1, \phi_2$) by substituting the force and moment resultants from (20). Further, one can derive the equation of motion (16) for homogeneous shells. An exact solution for the partial differential equations (16) on arbitrary domains and for general boundary conditions is not possible. However, for simply supported shells whose projection in the x_1, x_2 -plane is a rectangle and for a lamination scheme of antisymmetric cross-ply or symmetric cross-ply type the equations (16) are solved exactly. The Navier solution exists if $A_{i6} = B_{i6} = D_{i6} = E_{i6} = F_{i6} = H_{i6} = 0$ ($i = 1, 2$), and $A_{45} = D_{45} = F_{45} = 0$ [Reddy 1984a]. The simply-supported boundary conditions for the HSDT are assumed to be

$$\begin{aligned}
 u_1(x_1, 0, t) = 0, & \quad u_1(x_1, b, t) = 0, & \quad u_2(0, x_2, t) = 0, & \quad u_2(a, x_2, t) = 0, \\
 u_3(x_1, 0, t) = 0, & \quad u_3(x_2, b, t) = 0, & \quad u_3(0, x_2, t) = 0, & \quad u_3(a, x_2, t) = 0, \\
 N_1(0, x_2, t) = 0, & \quad N_1(a, x_2, t) = 0, & \quad N_2(x_1, 0, t) = 0, & \quad N_2(x_1, b, t) = 0, \\
 M_1(0, x_2, t) = 0, & \quad M_1(a, x_2, t) = 0, & \quad M_2(x_1, 0, t) = 0, & \quad M_2(x_1, b, t) = 0, \\
 P_1(0, x_2, t) = 0, & \quad P_1(a, x_2, t) = 0, & \quad P_2(x_1, 0, t) = 0, & \quad P_2(x_1, b, t) = 0, \\
 \phi_1(x_1, 0, t) = 0, & \quad \phi_1(x_1, b, t) = 0, & \quad \phi_2(0, x_2, t) = 0, & \quad \phi_2(a, x_2, t) = 0,
 \end{aligned} \tag{29}$$

where a and b denote the lengths along the x_1 and x_2 axes, respectively. The boundary conditions in (29) are satisfied by the following expansions [Reddy 2004]:

$$\begin{aligned}
 u_1(x_1, x_2, t) &= \sum_{n=1}^{\infty} \sum_{m=1}^{\infty} U_{mn}(t) \cos \alpha x_1 \sin \beta x_2, & \quad u_2(x_1, x_2, t) &= \sum_{n=1}^{\infty} \sum_{m=1}^{\infty} V_{mn}(t) \sin \alpha x_1 \cos \beta x_2, \\
 u_3(x_1, x_2, t) &= \sum_{n=1}^{\infty} \sum_{m=1}^{\infty} W_{mn}(t) \sin \alpha x_1 \sin \beta x_2, \\
 \phi_1(x_1, x_2, t) &= \sum_{n=1}^{\infty} \sum_{m=1}^{\infty} X_{mn}(t) \cos \alpha x_1 \sin \beta x_2, & \quad \phi_2(x_1, x_2, t) &= \sum_{n=1}^{\infty} \sum_{m=1}^{\infty} Y_{mn}(t) \sin \alpha x_1 \cos \beta x_2.
 \end{aligned} \tag{30}$$

Substituting (30) into (16), we obtain

$$\begin{aligned}
 \begin{bmatrix} S_{11} & S_{12} & S_{13} & S_{14} & S_{15} \\ S_{21} & S_{22} & S_{23} & S_{24} & S_{25} \\ S_{31} & S_{32} & S_{33} & S_{34} & S_{35} \\ S_{41} & S_{42} & S_{43} & S_{44} & S_{45} \\ S_{51} & S_{52} & S_{53} & S_{54} & S_{55} \end{bmatrix} \begin{Bmatrix} U_{mn} \\ V_{mn} \\ W_{mn} \\ X_{mn} \\ Y_{mn} \end{Bmatrix} + \begin{bmatrix} 0 & 0 & C_{13} & 0 & 0 \\ 0 & 0 & C_{23} & 0 & 0 \\ 0 & 0 & C_{33} & 0 & 0 \\ 0 & 0 & C_{43} & 0 & 0 \\ 0 & 0 & C_{53} & 0 & 0 \end{bmatrix} \begin{Bmatrix} \dot{U}_{mn} \\ \dot{V}_{mn} \\ \dot{W}_{mn} \\ \dot{X}_{mn} \\ \dot{Y}_{mn} \end{Bmatrix} \\
 + \begin{bmatrix} M_{11} & 0 & M_{13} & M_{14} & 0 \\ 0 & M_{22} & M_{23} & 0 & M_{25} \\ M_{31} & M_{32} & M_{33} & M_{34} & M_{35} \\ M_{41} & 0 & M_{43} & M_{44} & 0 \\ 0 & M_{52} & M_{53} & 0 & M_{55} \end{bmatrix} \begin{Bmatrix} \ddot{U}_{mn} \\ \ddot{V}_{mn} \\ \ddot{W}_{mn} \\ \ddot{X}_{mn} \\ \ddot{Y}_{mn} \end{Bmatrix} = \begin{Bmatrix} 0 \\ 0 \\ Q_{mn} \\ 0 \\ 0 \end{Bmatrix}, \tag{31}
 \end{aligned}$$

$$\begin{aligned}
S_{11} &= A_{11}\alpha^2 + A_{66}\beta^2, & S_{12} &= S_{21} = A_{12}\alpha\beta + A_{66}\alpha\beta, \\
S_{13} &= S_{31} = -A_{11}\frac{1}{R_1}\alpha - A_{12}\frac{1}{R_2}\alpha - C_1E_{11}\alpha^3 - C_1E_{12}\alpha\beta^2 - C_1E_{66}2\alpha\beta^2, \\
S_{14} &= S_{41} = B_{11}\alpha^2 - C_1E_{11}\alpha^2 + B_{66}\beta^2 - C_1E_{66}\beta^2, & S_{15} &= S_{51} = B_{12}\alpha\beta - C_1E_{12}\alpha\beta + B_{66}\alpha\beta - C_1E_{66}\alpha\beta, \\
S_{22} &= A_{66}\alpha^2 + A_{22}\beta^2, & S_{23} &= S_{32} = -2C_1E_{66}\alpha^2\beta - A_{12}\frac{1}{R_1}\beta - A_{22}\frac{1}{R_2}\beta - C_1E_{12}\alpha^2\beta - C_1E_{22}\beta^3, \\
S_{24} &= S_{42} = B_{66}\alpha\beta - C_1E_{66}\alpha\beta + B_{12}\alpha\beta - C_1E_{12}\alpha\beta, & S_{25} &= S_{52} = B_{66}\alpha^2 - C_1E_{66}\alpha^2 + B_{22}\beta^2 - C_1E_{22}\beta^2, \\
S_{33} &= A_{55}\alpha^2 - 2C_2D_{55}\alpha^2 + A_{44}\beta^2 - 2C_2D_{44}\beta^2 + C_2^2F_{55}\alpha^2 + C_2^2F_{44}\beta^2 \\
&\quad + 2C_1E_{11}\frac{1}{R_1}\alpha^2 + 2C_1E_{12}\frac{1}{R_2}\alpha^2 + C_1^2H_{11}\alpha^4 + C_1^2H_{12}\alpha^2\beta^2 + 2C_1^2H_{66}\alpha^2\beta^2 + 2C_1E_{12}\frac{1}{R_1}\beta^2 \\
&\quad + 2C_1E_{22}\frac{1}{R_2}\beta^2 + C_1^2H_{12}\alpha^2\beta^2 + C_1^2H_{22}\beta^4 - A_{11}\frac{1}{R_1^2} - 2\frac{1}{R_1R_2}A_{12} - A_{22}\frac{1}{R_2^2}, \\
S_{34} &= S_{43} = A_{55}\alpha - 2C_2D_{55}\alpha + C_2^2F_{55}\alpha - C_1F_{11}\alpha^3 + C_1^2H_{11}\alpha^3 - 2C_1F_{66}\alpha\beta^2 \\
&\quad + 2C_1^2H_{66}\alpha\beta^2 + C_1^2H_{12}\alpha\beta^2 - \frac{1}{R_1}B_{11}\alpha + C_1\frac{1}{R_1}E_{11}\alpha - \frac{1}{R_2}B_{12}\alpha + C_1\frac{1}{R_2}E_{12}\alpha, \\
S_{35} &= S_{53} = A_{44}\beta - 2C_2D_{44}\beta + C_2^2F_{44}\beta - C_1F_{12}\alpha^2\beta + C_1^2H_{12}\alpha^2\beta - 2C_1F_{66}\alpha^2\beta + 2C_1^2H_{66}\alpha^2\beta \\
&\quad - C_1F_{22}\beta^3 + C_1^2H_{22}\beta^3 - \frac{1}{R_1}B_{12}\beta + C_1\frac{1}{R_1}E_{12}\beta - \frac{1}{R_2}B_{22}\beta + C_1\frac{1}{R_2}E_{22}\beta, \\
S_{44} &= D_{11}\alpha^2 - 2C_1F_{11}\alpha^2 + D_{66}\beta^2 - 2C_1F_{66}\beta^2 - A_{55} + 2C_2D_{55} - C_2^2F_{55} + C_1^2H_{11}\alpha^2 + C_1^2H_{66}\beta^2, \\
S_{45} &= S_{54} = D_{66}\alpha\beta + D_{12}\alpha\beta - 2C_1F_{66}\alpha\beta - 2C_1F_{12}\alpha\beta + C_1^2H_{12}\alpha\beta - C_1F_{66}\alpha\beta + C_1^2H_{66}\alpha\beta, \\
S_{55} &= D_{66}\alpha^2 - 2C_1F_{66}\alpha^2 + D_{22}\beta^2 - 2C_1F_{22}\beta^2 - A_{44} + 2C_2D_{44} - C_2^2F_{44} + C_1^2H_{66}\alpha^2 + C_1^2H_{22}\beta^2, \\
C_{13} &= \mathcal{A}_{31}\alpha, & C_{23} &= \mathcal{A}_{32}\beta, & C_{33} &= -\mathcal{C}_{31}\alpha^2 - \mathcal{C}_{32}\beta^2 + \frac{\mathcal{A}_{31}}{R_1} + \frac{\mathcal{A}_{32}}{R_2}, \\
C_{43} &= \mathcal{B}_{31}\alpha - C_1\mathcal{C}_{31}\alpha, & C_{53} &= \mathcal{B}_{32}\beta - C_1\mathcal{C}_{32}\beta, \\
M_{11} &= \bar{I}_1, & M_{12} &= M_{21} = M_{15} = M_{51} = M_{24} = M_{42} = M_{45} = M_{54} = 0, & M_{13} &= M_{31} = \bar{I}_3\alpha, \\
M_{14} &= M_{41} = \bar{I}_2, & M_{22} &= \bar{J}_1, & M_{23} &= M_{32} = \bar{J}_3\beta, & M_{25} &= M_{52} = \bar{J}_2, \\
M_{33} &= \bar{I}_1 + C_1^2I_7(\alpha^2 + \beta^2), & M_{34} &= M_{43} = \bar{I}_5\alpha, & M_{35} &= M_{53} = \bar{J}_5\beta, & M_{44} &= \bar{I}_4, & M_{55} &= \bar{J}_4,
\end{aligned}$$

Table 2. Definition of the variables appearing in Equation (31). The magnetostrictive coefficients \mathcal{A}_{31} , \mathcal{A}_{32} , \mathcal{B}_{31} , \mathcal{B}_{32} , \mathcal{C}_{31} , and \mathcal{C}_{32} are defined in (24).

where S_{ij} , C_{ij} , and M_{ij} ($i, j = 1, 2, \dots, 5$) are defined in Table 2. For vibration control, we assume $q = 0$ and seek the solution of the ordinary differential equations (31) in the form

$$U_{mn}(t) = U_0e^{\lambda t}, \quad V_{mn}(t) = V_0e^{\lambda t}, \quad W_{mn}(t) = W_0e^{\lambda t}, \quad X_{mn}(t) = X_0e^{\lambda t}, \quad Y_{mn}(t) = Y_0e^{\lambda t}. \quad (32)$$

Substituting (32) into (31), and defining

$$\bar{S}_{ij} = S_{ij} + \lambda C_{ij} + \lambda^2 M_{ij} \quad (i, j = 1, 2, 3, 4, 5), \quad (33)$$

we obtain as the condition for a nontrivial solution

$$\begin{vmatrix} \bar{S}_{11} & \bar{S}_{12} & \bar{S}_{13} & \bar{S}_{14} & \bar{S}_{15} \\ \bar{S}_{21} & \bar{S}_{22} & \bar{S}_{23} & \bar{S}_{24} & \bar{S}_{25} \\ \bar{S}_{31} & \bar{S}_{32} & \bar{S}_{33} & \bar{S}_{34} & \bar{S}_{35} \\ \bar{S}_{41} & \bar{S}_{42} & \bar{S}_{43} & \bar{S}_{44} & \bar{S}_{45} \\ \bar{S}_{51} & \bar{S}_{52} & \bar{S}_{53} & \bar{S}_{54} & \bar{S}_{55} \end{vmatrix} = 0. \quad (34)$$

This equation gives five sets of eigenvalues. The lowest one corresponds to the transverse motion. The eigenvalue can be written as $\lambda = -\alpha + i\omega_d$, so that the damped motion is given by

$$u_3(x_1, x_2, t) = \frac{1}{\omega_d} e^{-\alpha t} \sin \omega_d t \sin \frac{n\pi x_1}{a} \sin \frac{n\pi x_2}{b}. \quad (35)$$

In arriving at the last solution, the following boundary conditions are used:

$$\begin{aligned} u_1(x_1, x_2, 0) = 0, \quad \dot{u}_1(x_1, x_2, 0) = 0, \quad u_2(x_1, x_2, 0) = 0, \quad \dot{u}_2(x_1, x_2, 0) = 0, \quad u_3(x_1, x_2, 0) = 0, \\ \dot{u}_3(x_1, x_2, 0) = 1, \quad \phi_1(x_1, x_2, 0) = 0, \quad \dot{\phi}_1(x_1, x_2, 0) = 0, \quad \phi_2(x_1, x_2, 0) = 0, \quad \dot{\phi}_2(x_1, x_2, 0) = 0. \end{aligned} \quad (36)$$

4. Results and discussion

In the present work a theoretical analysis of a functionally graded material (FGM) shell, consisting of layers of magnetostrictive material, is carried out. The magnetostrictive material is assumed to impart vibration control through a velocity dependent feedback law that controls the current to the magnetic coils energizing the magnetostrictive material. Higher order shear deformation theory (HSDT) is used in the derivation. Numerical simulation results are presented. The effect of various parameters on the vibration suppression time is studied. These parameters are: the location of the magnetostrictive layer relative to the neutral plane, the thickness of the magnetostrictive layer, the higher modes of vibration, the material properties of the magnetostrictive material, and the material properties of the FGM material. The influence of HSDT on the vibration response of thick shells is also investigated.

The FGM shell is considered to have dimensions $1 \text{ m} \times 1 \text{ m}$. Two types of FGM shells are considered: FGM1, made up of stainless steel and nickel, and FGM2, made up of nickel and aluminum oxide. The material properties of the constituent materials were listed in Table 1. Two layers of magnetostrictive materials are placed symmetrically away from the neutral plane of the FGM shell, as shown in Figure 2. The magnetostrictive material properties are taken as $E_m = 26.5 \text{ GPa}$, $\nu_m = 0.0$, $\rho_m = 9250 \text{ kg m}^{-3}$, $c(t)r_c = 10^4$. The numerical values of various material and structural constants based on different locations of the magnetostrictive layers and different FGM material properties are listed in Tables 3 and 4. In this study, the vibration suppression time (t_s) is defined as the time required to reduce the uncontrolled vibration amplitude to one-tenth of its initial amplitude. In the present numerical simulations the suppression time and the thickness of the magnetostrictive layer are denoted by t_s and h_m , respectively. Z_m represents the distance between the location of the magnetostrictive layer and the neutral plane.

Effect of magnetostrictive layer location. The effect of the location of the magnetostrictive layers on the vibration suppression is studied. Figure 2 shows the location of the magnetostrictive layers in the FGM shells. Transverse deflection values are plotted as functions of time in Figure 4 for several Z_m values: 3.5 mm, 5.5 mm, 7.5 mm and 9.5 mm. For $Z_m = 9.5 \text{ mm}$ Figure 4d shows the shortest suppression time,

$Z_m/$ m	$F_{11}/$ 10Nm^3	$H_{11}/$ 10^{-3}Nm^5	$D_{11}/$ 10^6Nm	$F_{12}/$ 10Nm^3	$H_{12}/$ 10^{-3}Nm^5	$D_{12}/$ 10^5Nm	$F_{22}/$ 10Nm^3	$H_{22}/$ 10^{-3}Nm^5	$D_{22}/$ 10^6Nm
0.0095	0.624	0.375	0.124	0.178	0.103	0.366	0.624	0.375	0.124
0.0085	0.752	0.534	0.132	0.222	0.157	0.393	0.752	0.534	0.132
0.0075	0.843	0.622	0.139	0.253	0.187	0.417	0.843	0.622	0.139
0.0065	0.904	0.668	0.145	0.274	0.203	0.438	0.904	0.668	0.145
0.0055	0.942	0.689	0.150	0.287	0.210	0.456	0.942	0.689	0.150
0.0045	0.964	0.698	0.155	0.294	0.213	0.471	0.964	0.698	0.155
0.0035	0.976	0.701	0.158	0.298	0.214	0.483	0.976	0.701	0.158
0.0025	0.981	0.702	0.161	0.300	0.215	0.492	0.981	0.702	0.161
0.0015	0.983	0.702	0.163	0.301	0.215	0.498	0.983	0.702	0.163
0.0005	0.983	0.702	0.164	0.301	0.215	0.501	0.983	0.702	0.164
$Z_m/$ m	$F_{66}/$ 10Nm^3	$H_{66}/$ 10^{-3}Nm^5	$D_{66}/$ 10^5Nm	$F_{44}/$ 10Nm^3	$D_{44}/$ 10^5Nm^5	$A_{44}/$ 10^{10}Nm^{-1}	$F_{55}/$ 10Nm^3	$D_{55}/$ 10^5Nm	
0.0095	0.223	0.136	0.438	0.223	0.438	0.156	0.223	0.438	
0.0085	0.265	0.188	0.464	0.265	0.464	0.156	0.265	0.464	
0.0075	0.295	0.217	0.487	0.295	0.487	0.156	0.295	0.487	
0.0065	0.315	0.232	0.507	0.315	0.507	0.156	0.315	0.507	
0.0055	0.328	0.239	0.525	0.328	0.525	0.156	0.328	0.525	
0.0045	0.335	0.242	0.539	0.335	0.539	0.156	0.335	0.539	
0.0035	0.339	0.243	0.551	0.339	0.551	0.156	0.339	0.551	
0.0025	0.340	0.244	0.559	0.340	0.559	0.156	0.340	0.559	
0.0015	0.341	0.244	0.565	0.341	0.565	0.156	0.341	0.565	
0.0005	0.341	0.244	0.568	0.341	0.568	0.156	0.341	0.568	
$Z_m/$ m	$C_1/$ 10^4m^{-2}	$C_2/$ 10^5m^{-2}	$I_1/$ 10^2kgm^{-2}	$I_3/$ 10^{-2}kg	$I_5/$ 10^{-6}kgm^2	$I_7/$ 10^{10}kgm^4	$-\mathcal{B}_{31}/$ 10^2	$-\mathcal{C}_{31}/$ 10^{-2}	
0.0095	0.333	0.100	0.849	0.288	0.175	0.126	0.841	0.761	
0.0085	0.333	0.100	0.849	0.288	0.175	0.126	0.752	0.545	
0.0075	0.333	0.100	0.849	0.285	0.171	0.126	0.664	0.375	
0.0065	0.333	0.100	0.849	0.284	0.170	0.121	0.575	0.244	
0.0055	0.333	0.100	0.849	0.283	0.169	0.120	0.487	0.148	
0.0045	0.333	0.100	0.849	0.282	0.168	0.120	0.398	0.082	
0.0035	0.333	0.100	0.849	0.281	0.168	0.120	0.310	0.039	
0.0025	0.333	0.100	0.849	0.281	0.168	0.120	0.221	0.014	
0.0015	0.333	0.100	0.849	0.280	0.168	0.120	0.133	0.003	
0.0005	0.333	0.100	0.849	0.280	0.168	0.120	0.044	0.000	

Table 3. Coefficients of the FGM1 (stainless steel-nickel) shell.

$Z_m/$ m	$F_{11}/$ 10Nm^3	$H_{11}/$ 10^{-3}Nm^5	$D_{11}/$ 10^6Nm	$F_{12}/$ 10Nm^3	$H_{12}/$ 10^{-3}Nm^5	$D_{12}/$ 10^5Nm	$F_{22}/$ 10Nm^3	$H_{22}/$ 10^{-3}Nm^5	$D_{22}/$ 10^6Nm
0.0095	0.801	0.478	0.161	0.207	0.119	0.426	0.801	0.478	0.161
0.0085	0.974	0.691	0.171	0.258	0.182	0.457	0.974	0.691	0.171
0.0075	1.095	0.809	0.181	0.294	0.218	0.485	1.095	0.809	0.181
0.0065	1.177	0.871	0.189	0.318	0.236	0.509	1.177	0.871	0.189
0.0055	1.228	0.899	0.196	0.333	0.244	0.530	1.228	0.899	0.196
0.0045	1.258	0.911	0.202	0.342	0.248	0.547	1.258	0.911	0.202
0.0035	1.274	0.915	0.207	0.347	0.249	0.561	1.274	0.915	0.207
0.0025	1.281	0.916	0.210	0.349	0.249	0.572	1.281	0.916	0.210
0.0015	1.283	0.916	0.212	0.349	0.249	0.579	1.283	0.916	0.212
0.0005	1.283	0.916	0.214	0.349	0.249	0.583	1.283	0.916	0.214
$Z_m/$ m	$F_{66}/$ 10Nm^3	$H_{66}/$ 10^{-3}Nm^5	$D_{66}/$ 10^5Nm	$F_{44}/$ 10Nm^3	$D_{44}/$ 10^5Nm^5	$A_{44}/$ 10^{10}Nm^{-1}	$F_{55}/$ 10Nm^3	$D_{55}/$ 10^5Nm	
0.0095	0.297	0.179	0.591	0.297	0.591	0.212	0.297	0.591	
0.0085	0.358	0.254	0.628	0.358	0.628	0.212	0.358	0.628	
0.0075	0.401	0.296	0.661	0.401	0.661	0.212	0.401	0.661	
0.0065	0.429	0.317	0.690	0.429	0.690	0.212	0.429	0.690	
0.0055	0.447	0.327	0.715	0.447	0.715	0.212	0.447	0.715	
0.0045	0.458	0.332	0.736	0.458	0.736	0.212	0.458	0.736	
0.0035	0.463	0.333	0.752	0.463	0.752	0.212	0.463	0.752	
0.0025	0.466	0.333	0.765	0.466	0.765	0.212	0.466	0.765	
0.0015	0.467	0.333	0.773	0.467	0.773	0.212	0.467	0.773	
0.0005	0.467	0.333	0.777	0.467	0.777	0.212	0.467	0.777	
$Z_m/$ m	$C_1/$ 10^4m^{-2}	$C_2/$ 10^5m^{-2}	$I_1/$ 10^2kgm^{-2}	$I_3/$ 10^{-2}kg	$I_5/$ 10^{-6}kgm^2	$I_7/$ 10^{10}kgm^4	$-\mathcal{B}_{31}/$ 10^2	$-\mathcal{C}_{31}/$ 10^{-2}	
0.0095	0.333	0.100	0.672	0.240	0.152	0.113	0.841	0.761	
0.0085	0.333	0.100	0.672	0.235	0.144	0.103	0.752	0.545	
0.0075	0.333	0.100	0.672	0.230	0.138	0.097	0.664	0.375	
0.0065	0.333	0.100	0.672	0.226	0.134	0.094	0.575	0.244	
0.0055	0.333	0.100	0.672	0.223	0.131	0.093	0.487	0.148	
0.0045	0.333	0.100	0.672	0.220	0.130	0.092	0.398	0.082	
0.0035	0.333	0.100	0.672	0.218	0.129	0.092	0.310	0.039	
0.0025	0.333	0.100	0.672	0.216	0.129	0.092	0.221	0.014	
0.0015	0.333	0.100	0.672	0.215	0.129	0.092	0.133	0.003	
0.0005	0.333	0.100	0.672	0.215	0.129	0.092	0.044	0.000	

Table 4. Coefficients of the FGM2 (nickel-aluminum oxide) shell.

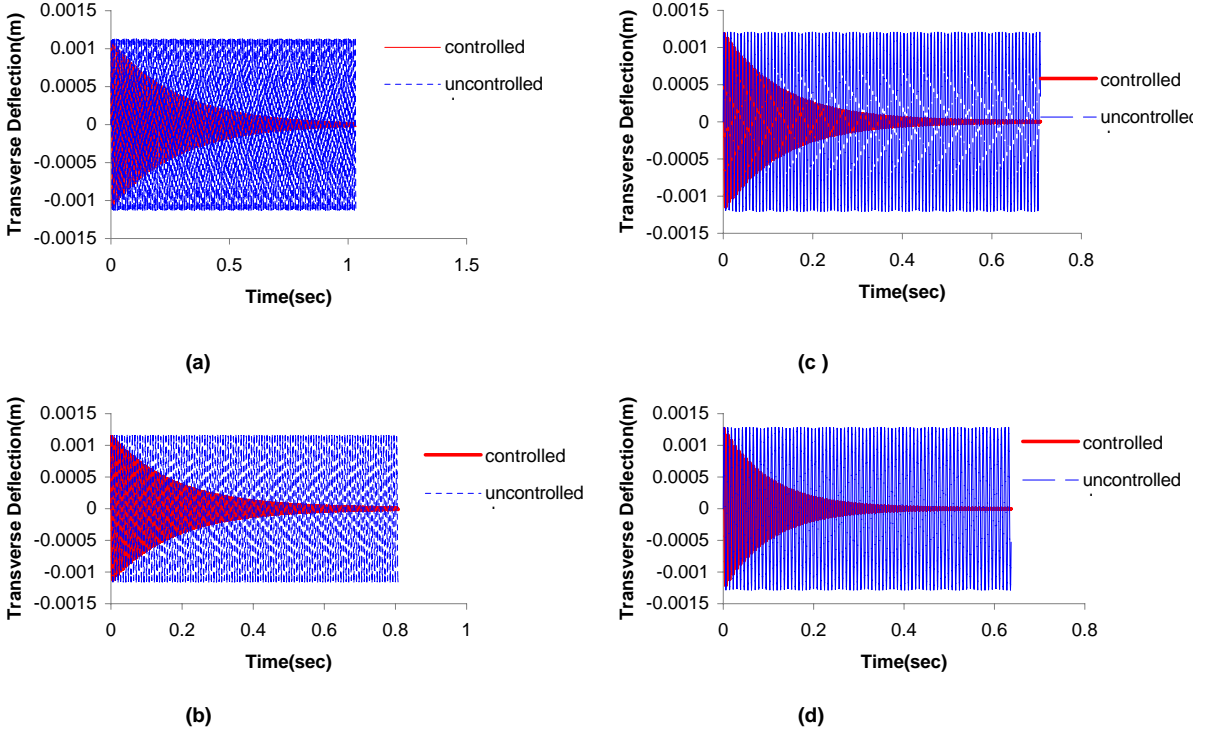


Figure 4. Comparison of uncontrolled (dashed line) and controlled (solid line) motion at the midpoint of the FGM1 shell for various locations of the magnetostrictive layers, (a) $Z_m = 3.5$ mm, (b) $Z_m = 5.5$ mm, (c) $Z_m = 7.5$ mm and (d) $Z_m = 9.5$ mm.

$t_s = 0.22$ s, while for $Z_m = 3.5$ mm [Figure 4a](#) shows the longest suppression time, $t_s = 0.59$ s. From [Figure 4](#), the shortest suppression time is observed when the magnetostrictive layers are placed farther away from the neutral plane. Similarly, from [Figure 4](#) one can observe that the longest suppression time occurs when the magnetostrictive layer is located closest to the neutral plane of the shell.

The influence on the damping of the vibration response of the distance between the magnetostrictive layers and the neutral plane of the shell in the thickness direction is shown in [Tables 5–7](#). In [Tables 5](#) and [6](#), the value of λ_0 increases when the magnetostrictive layer is located farther away from the neutral axis, indicating faster vibration suppression. This is due to the larger bending moment created by the actuating force in the magnetostrictive layers. Further, it is observed that the damping parameter \mathcal{B}_{31} and the associated normalized value of \mathcal{B}_n increase as the magnetostrictive layers are moved away from the neutral plane. These damping parameters are listed in [Tables 3](#) and [4](#). These results agree qualitatively with those presented in [[Pradhan et al. 2001](#); [He et al. 2002](#); [Pradhan 2005](#)].

Effect of thickness of magnetostrictive layers. The vibration response of the FGM1 shell for various thicknesses of the magnetostrictive layers (h_m) is studied. Magnetostrictive damping coefficients and natural frequencies for various thicknesses of the magnetostrictive layers are listed in [Tables 5–6](#). These damping coefficients and natural frequencies refer to the first mode of vibration. The vibration suppression time for h_m values of 1 mm, 2 mm, 3 mm, and 5 mm are listed in [Tables 5](#) and [6](#). These computations

Z_m (m)	$-\lambda_0$	$\pm\omega_d$	W_{\max} (mm)	t_s (s)	t_n
0.0095	9.760	778.57	1.259	0.244	0.055
0.0085	8.731	803.46	1.222	0.268	0.060
0.0075	7.702	828.79	1.184	0.305	0.068
0.0065	6.673	848.44	1.154	0.350	0.078
0.0055	5.645	862.38	1.113	0.410	0.092
0.0045	4.618	873.60	1.116	0.505	0.113
0.0035	3.591	886.54	1.097	0.647	0.145
0.0025	2.564	893.99	1.087	0.909	0.204
0.0015	1.612	892.53	1.091	1.501	0.336
0.0005	0.537	894.26	1.093	4.463	1.000

Z_m (m)	$-\lambda_0$	$\pm\omega_d$	W_{\max} (mm)	t_s (s)	t_n
0.009	18.317	663.54	1.410	0.135	0.118
0.008	16.276	726.37	1.323	0.141	0.124
0.007	14.237	770.68	1.261	0.165	0.145
0.006	12.198	806.39	1.209	0.197	0.173
0.005	10.161	834.35	1.169	0.228	0.200
0.004	8.125	854.79	1.140	0.288	0.252
0.003	6.091	875.41	1.110	0.382	0.335
0.002	4.060	881.40	1.105	0.579	0.507
0.001	2.029	893.62	1.089	1.141	1.000

Z_m (m)	$-\lambda_0$	$\pm\omega_d$	W_{\max} (mm)	t_s (s)	t_n
0.0085	25.702	562.13	1.636	0.092	0.179
0.0075	22.669	661.05	1.401	0.107	0.208
0.0065	19.637	723.98	1.318	0.124	0.241
0.0055	16.607	772.53	1.252	0.140	0.272
0.0045	13.578	812.17	1.196	0.172	0.334
0.0035	10.553	839.35	1.160	0.226	0.439
0.0025	7.533	858.58	1.135	0.309	0.600
0.0015	4.517	881.17	1.104	0.515	1.000

Table 5. Suppression time ratio for various locations of the magnetostrictive layers in the FGM1 shells, for $h_m = 1$ mm (top), $h_m = 2$ mm (middle), and $h_m = 3$ mm (bottom). Z_m is expressed in units of m, W_{\max} in units of mm, and t_s in units of s.

are carried out for various locations (Z_m) of the magnetostrictive layers. The vibration suppression time t_s versus the distance Z_m of the magnetostrictive layers from the neutral plane for various h_m are plotted in Figure 5. This includes magnetostrictive layers with h_m values of 1 mm, 2 mm and 3 mm at various locations. Figure 5 shows that the curve changes more rapidly for a thinner magnetostrictive layer. Further, thin magnetostrictive layers kept away from the neutral plane exhibit better attenuation. The

Z_m	$C(t)r_c = 10^4$					$C(t)r_c = 10^3$				
	$-\lambda_0$	$\pm\omega_d$	W_{\max}	t_s	t_n	$-\lambda_0$	$\pm\omega_d$	W_{\max}	t_s	t_n
0.0075	37.086	414.69	2.071	0.079	0.414	3.709	416.33	2.356	0.623	0.303
0.0065	32.119	565.15	1.594	0.081	0.424	3.212	566.06	1.735	0.724	0.383
0.0055	27.154	669.16	1.377	0.096	0.503	2.715	669.70	1.445	0.856	0.453
0.0045	22.188	743.32	1.282	0.104	0.545	2.219	743.65	1.334	1.024	0.542
0.0035	17.228	792.14	1.219	0.137	0.717	1.723	792.33	1.258	1.303	0.689
0.0025	12.279	831.79	1.168	0.191	1.000	1.228	831.88	1.194	1.890	1.000

Table 6. Suppression time ratio for two values of control gain and various locations of the magnetostrictive layers in the FGM1 shells $h_m = 5$ mm. Z_m is expressed in units of m, W_{\max} in units of mm, and t_s in units of s.

h/a	FSDT		HSDT	
	W_{\max} (mm)	t_s (s)	W_{\max} (mm)	t_s (s)
5	0.085	0.0395	0.129	0.0535
10	0.196	0.0294	0.258	0.0501
100	1.226	0.222	1.259	0.244

Table 7. Vibration suppression using FSDT and HSDT.

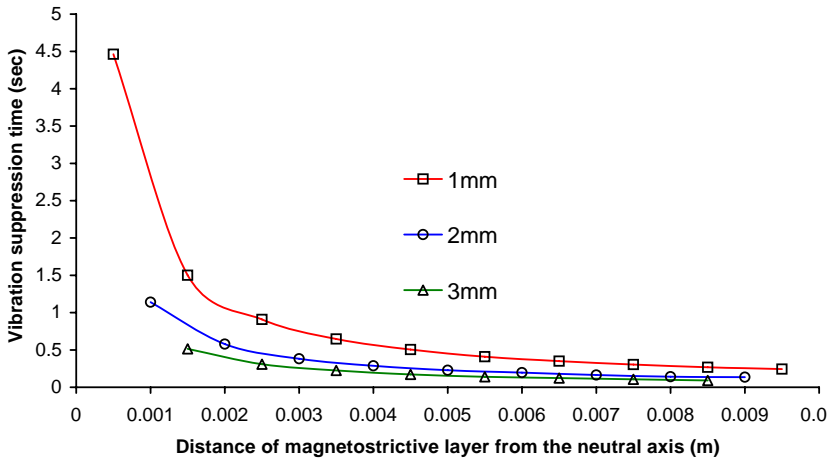


Figure 5. Vibration suppression time (t_s) for various thicknesses of magnetostrictive layers (h_m).

results presented here agree qualitatively with the results presented in [Pradhan et al. 2001; He et al. 2002; Pradhan 2005].

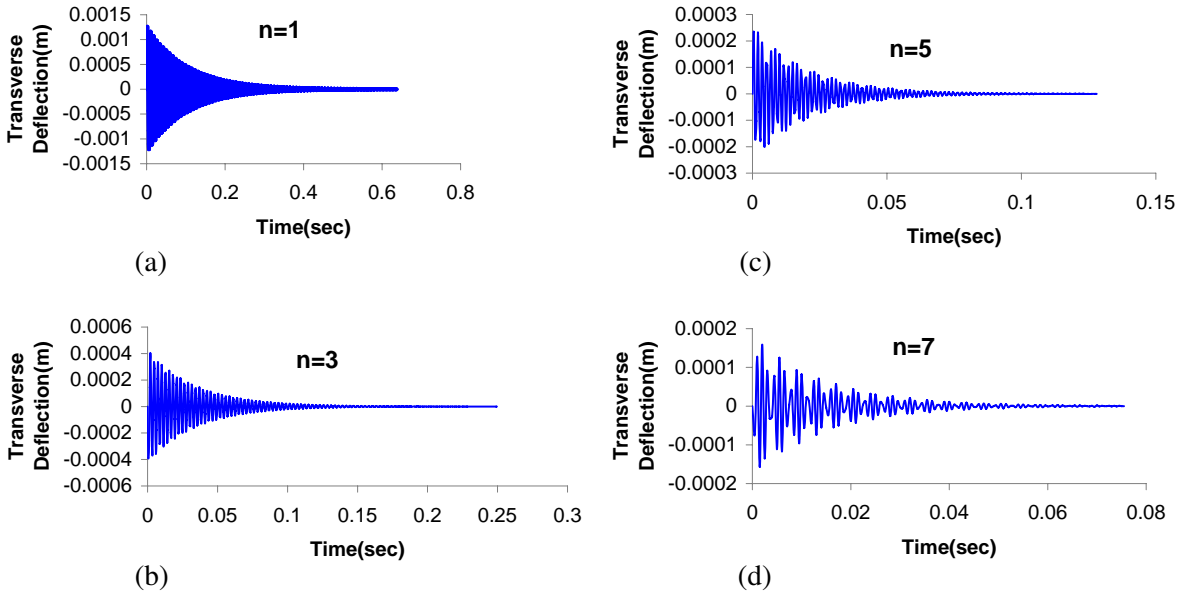


Figure 6. Vibration suppression of higher modes at the midpoint of the FGM1 shell (a) $n = 1$, (b) $n = 3$, (c) $n = 5$, and (d) $n = 7$.

Effect of vibration modes. The effect of higher modes of vibration on the vibration suppression time is studied for the FGM1 shell. Transverse deflection versus time for various cases of the FGM shells are plotted in the next three figures. The parts of Figure 6 show the transient response of modes 1, 3, 5, and 7, respectively. It is observed that attenuation favors the higher modes. This is clearly seen in Figure 7, where modes 1 and 3 are compared for the FGM1 and FGM2 shells. These figures indicate that mode 3 attenuates at a significantly faster rate compared to mode 1. The results in Figure 6 also show that the vibration suppression time decreases very rapidly as the vibration mode number increases. These vibration results for various modes agree qualitatively with the results presented in [Pradhan et al. 2001; Pradhan 2005].

Effect of intensity of control gain. The values of t_s for values of the intensity of control gain $C(t)r_c$ of 1,000 and 10,000 are computed and the results are listed in Table 6. This shows that increase in the intensity of control gain results in a proportional increase in the vibration suppression time. From the results listed in Table 6, it is interesting to note that t_s is directly proportional to the control gain of the applied magnetic field.

Effect of material properties of FGM shell. The effect of the material properties of the FGM shell on the vibration suppression time is studied. Figure 8 displays the vibration suppression for the FGM1 and FGM2 shells. For this comparison study Z_m is assumed to be 9.5 mm. From Figure 8, it is observed that the FGM1 shell has lower frequency compared with the FGM2 shell. This confirms that the FGM1 shell has lower flexural rigidity and thus a lower frequency compared with the FGM2 shell. These results agree qualitatively with the results presented in [Pradhan et al. 2001; Pradhan 2005].

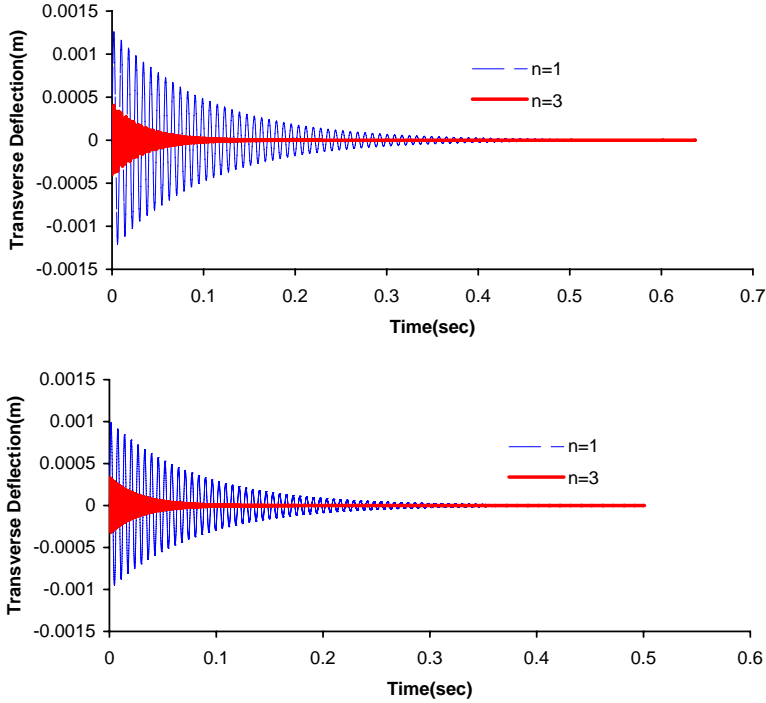


Figure 7. Comparison of controlled motion at the midpoint of the FGM1 (top) and FGM2 (bottom) shells for vibration modes $n = 1$ and $n = 3$.

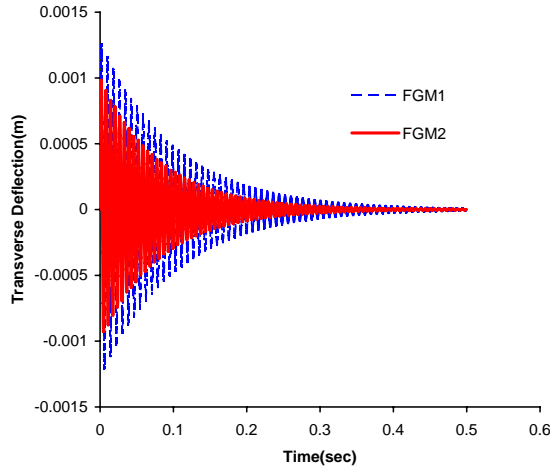


Figure 8. Vibration suppression of the FGM1 and FGM2 shells for $Z_m = 9.5$ mm.

Effect of higher order shear deformation theory. From Table 6, it is observed that when employing HSDT, t_n is dependent on the intensity of the control gain. Under FSDT we observe that t_n is independent of the intensity of the control gain. These results agree qualitatively with the results presented in [Pradhan et al. 2001; Pradhan 2005]. t_n is found to depend on the intensity of the control gain. This reveals that

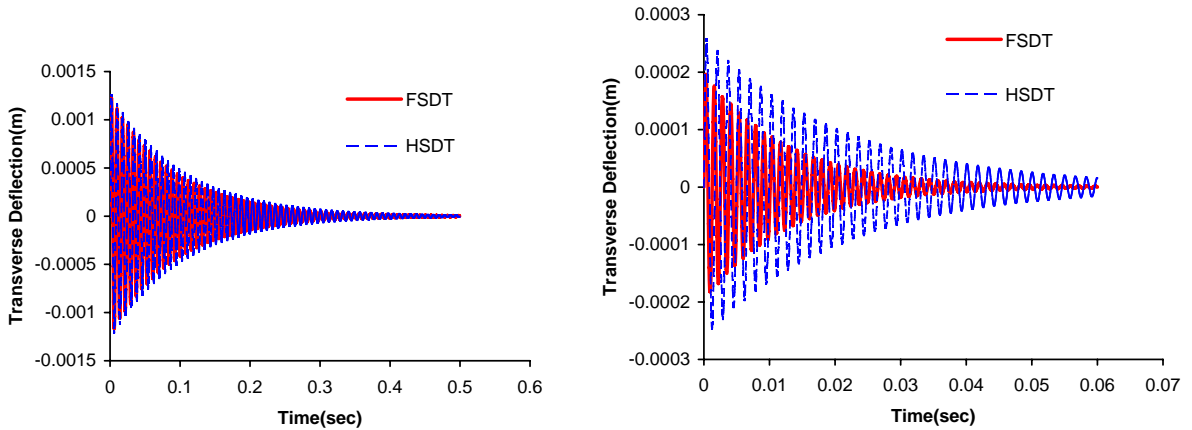


Figure 9. Vibration suppression using FSDT and HSDT for a/h ratios of 100 (left) and 10 (right).

HSDT analysis takes into account the effect of the control gain on the vibration response. Results are obtained for various a/h ratios and listed in Table 7. Here h and a represent the thickness of the shell and the arc length of the shell boundaries. From Table 7 and Figure 9 one could observe that as the thickness of the shell decreases the maximum deflection increases for both FSDT and HSDT. Further maximum deflections predicted by HSDT are larger than those from FSDT. For an a/h ratio of 5 the maximum deflection predicted by HSDT is 51% larger than that from FSDT, while for an a/h ratio of 100 the maximum deflection predicted by HSDT is only 2% larger than that from FSDT. Further, the t_s predicted by HSDT is larger than the corresponding results of FSDT. This is due to the fact that HSDT takes into account the shear forces along the thickness of the thick FGM shell. This study suggests that HSDT should be considered for the analysis of the thick FGM shell.

5. Conclusions

A theoretical formulation for a FGM shell with embedded magnetostrictive layers has been presented. The analytical solutions for the case of simply-supported boundary conditions has been derived, and numerical results are presented. The formulation is based on HSDT, and the analytical solution for the simply-supported shell is based on the Navier solution approach. The effects on the vibration suppression time of the material properties of the FGM shell, the thicknesses of the magnetostrictive layers, and the locations of the magnetostrictive layers have been examined in detail. It was found that attenuation effects were better if the magnetostrictive layers were placed farther away from the neutral plane. Attenuation effects were also better when the magnetostrictive layers were relatively thinner. The suppression time ratio was directly proportional to the control gain of the applied magnetic field. Furthermore, the influence of higher order shear deformation shell theory is significant for thick FGM shells.

Acknowledgement

I am grateful for the technical discussion and suggestions of Professor J. N. Reddy of Texas A&M University.

List of symbols

$A_{31}, A_{32}, B_{31}, B_{32}, C_{31}, C_{32}$	magnetostrictive coefficients
α, β	positive real number
α_1, α_2	surface metrics
$\varepsilon_1, \varepsilon_2, \varepsilon_6, \gamma_4, \gamma_5$	total strains
$\varepsilon_1^0, \varepsilon_2^0, \varepsilon_6^0, \gamma_4^0, \gamma_5^0$	strains from classical shell theory
$\varepsilon_1^1, \varepsilon_2^1, \varepsilon_6^1, \gamma_4^1, \gamma_5^1, \varepsilon_1^2, \varepsilon_2^2, \varepsilon_1^2$	strains from HSDT
ξ_1, ξ_2, ζ	orthogonal curvilinear coordinates
λ	eigenvalue
λ_0	arbitrary constant
ϕ_1, ϕ_2	rotational displacements
ν_1, ν_2	Poisson's ratios of material 1 and material 2
ν_{FGM}	Poisson's ratio of FGM material 1 and material 2
ν_m	Poisson's ratio of magnetostrictive material
$\rho^{(K)}$	density of k -th layer
ρ_m	density of magnetostrictive material
$\sigma_1, \sigma_2, \sigma_4, \sigma_5, \sigma_6$	stress components
ω_d	damping frequency
a	length of the shell
b	breadth of the shell
b_c	coil width
$c(t)$	control gain
dA_1, dA_2	elementary areas across the thickness of the shell
ds	square of the distance on the middle surface
dS	square of the distance
$e_{31}^{(k)}, e_{32}^{(k)}, e_{36}^{(k)}$	magnetostrictive material properties of k -th layer
g_1, g_2	tangents to ξ_1, ξ_2
h	thickness of the shell
h_m	thickness of magnetostrictive layer
k_c	magnetostrictive coil constant
m, m_1, m_2, n	positive integers
n_c	number of coil turns
nm	number of constituent materials in the FGM
q	uniformly distributed load in the transverse direction
r	position vector on the middle surface
r_c	coil radius
t_n	normalized value of t_s
t_s	suppression time ratio
u_1, u_2, u_3	displacements at the middle surface
$\bar{u}_1, \bar{u}_2, \bar{u}_3$	displacements along ξ_1, ξ_2, ζ
z	thickness coordinate

$[\]^0$	contribution due to classical shell theory
$[\]^M$	contribution due to magnetostrictive layer
$A_{ij}, B_{ij}, D_{ij}, E_{ij}, F_{ij}, H_{ij}$	stiffness coefficients of FGM material
C_1, C_2	constants which depend on thickness of the shell
E_1, E_2	Young's moduli of material 1 and material 2
E_{FGM}	Young's modulus of FGM material
E_m	Young's modulus of magnetostrictive material
G_{FGM}	shear modulus of FGM material
H	magnetic field intensity
I	coil current intensity
L_1, L_2, L_3	Lamé coefficients
M^M	moments due to the magnetostrictive layer
N	number of layers assumed for computation
N^M	forces due to the magnetostrictive layer
P_{FGM}	material property of the FGM material
$Q_{ij}^{(k)}$	stiffness coefficients of k -th layer
R	position vector of arbitrary point
R_1, R_2	principal radii of curvature of the middle surface of the shell
R_n	positive real number
S_{ij}, C_{ij}, M_{ij}	coefficients of stiffness, damping and mass matrices
\bar{S}_{ij}	coefficients of solution matrix
V_c	volume fraction of ceramic material
V_{fi}	volume fraction of the constituents of FGM material
V_m	volume fraction of metal material
W_{max}	maximum amplitude in transverse direction
Z_m	transverse location of magnetostrictive layer in the FGM shell

References

[Anjanappa and Bi 1994] M. Anjanappa and J. Bi, "Magnetostrictive mini actuators for smart structure application", *Smart Mater. Struct.* **3**:4 (1994), 383–390.

[Bryant et al. 1993] M. D. Bryant, B. Fernandez, N. Wang, V. V. Murty, V. Vadlamani, and T. S. West, "Active vibration control in structures using magnetostrictive Terfenol with feedback and/or neural network controllers", *J. Intell. Mater. Syst. Struct.* **4**:4 (1993), 484–489.

[Friedmann et al. 2001] P. P. Friedmann, G. P. Carman, and T. A. Millott, "Magnetostrictively actuated control flaps for vibration reduction in helicopter rotors: design considerations for implementation", *Math. Comput. Model.* **33**:10–11 (2001), 1203–1217.

[Giurgiutiu et al. 2001] V. Giurgiutiu, F. Jichi, J. B. Berman, and J. M. Kamphaus, "Theoretical and experimental investigation of magnetostrictive composite beams", *Smart Mater. Struct.* **10**:5 (2001), 934–945.

[Goodfriend and Shoop 1992] M. J. Goodfriend and K. M. Shoop, "Adaptive characteristics of the magnetostrictive alloy, Terfenol-D, for active vibration control", *J. Intell. Mater. Syst. Struct.* **3**:2 (1992), 245–254.

[Haddadpour et al. 2007] H. Haddadpour, S. Mahmoudkhani, and H. M. Navazi, "Free vibration analysis of functionally graded cylindrical shells including thermal effects", *Thin-Walled Struct.* **45**:6 (2007), 591–599.

- [He et al. 2002] X. Q. He, K. M. Liew, T. Y. Ng, and S. Sivashanker, “A FEM model for the active control of curved FGM shells using piezoelectric sensor/actuator layers”, *Int. J. Numer. Methods Eng.* **54**:6 (2002), 853–870.
- [Kadoli and Ganesan 2006] R. Kadoli and N. Ganesan, “Buckling and free vibration analysis of functionally graded cylindrical shells subjected to a temperature-specified boundary condition”, *J. Sound Vib.* **289**:3 (2006), 450–480.
- [Krishna Murty et al. 1997] A. V. Krishna Murty, M. Anjanappa, and Y.-F. Wu, “The use of magnetostrictive particle actuators for vibration attenuation of flexible beams”, *J. Sound Vib.* **206**:2 (1997), 133–149.
- [Li 2008] X.-F. Li, “A unified approach for analyzing static and dynamic behaviors of functionally graded Timoshenko and Euler–Bernoulli beams”, *J. Sound Vib.* **318**:4–5 (2008), 1210–1229.
- [Loy et al. 1999] C. T. Loy, K. Y. Lam, and J. N. Reddy, “Vibration of functionally graded cylindrical shells”, *Int. J. Mech. Sci.* **41**:3 (1999), 309–324.
- [Matsunaga 2009] H. Matsunaga, “Stress analysis of functionally graded plates subjected to thermal and mechanical loadings”, *Compos. Struct.* **87**:4 (2009), 344–357.
- [Pradhan 2005] S. C. Pradhan, “Vibration suppression of FGM shells using embedded magnetostrictive layers”, *Int. J. Solids Struct.* **42**:9–10 (2005), 2465–2488.
- [Pradhan et al. 2000] S. C. Pradhan, C. T. Loy, K. Y. Lam, and J. N. Reddy, “Vibration characteristics of functionally graded cylindrical shells under various boundary conditions”, *Appl. Acoust.* **61**:1 (2000), 111–129.
- [Pradhan et al. 2001] S. C. Pradhan, T. Y. Ng, K. Y. Lam, and J. N. Reddy, “Control of laminated composite plates using magnetostrictive layers”, *Smart Mater. Struct.* **10**:4 (2001), 657–667.
- [Pradyumna and Bandyopadhyay 2008] S. Pradyumna and J. N. Bandyopadhyay, “Free vibration analysis of functionally graded curved panels using a higher-order finite element formulation”, *J. Sound Vib.* **318**:1–2 (2008), 176–192.
- [Reddy 1984a] J. N. Reddy, “A refined nonlinear theory of plates with transverse shear deformation”, *Int. J. Solids Struct.* **20**:9–10 (1984), 881–896.
- [Reddy 1984b] J. N. Reddy, “Exact solutions of moderately thick laminated shells”, *J. Eng. Mech. (ASCE)* **110**:5 (1984), 794–809.
- [Reddy 2004] J. N. Reddy, *Mechanics of laminated composite plates and shells: theory and analysis*, 2nd ed., Chemical Rubber Company, Boca Raton, FL, 2004.
- [Reddy and Liu 1985] J. N. Reddy and C. F. Liu, “A higher-order shear deformation theory of laminated elastic shells”, *Int. J. Eng. Sci.* **23**:3 (1985), 319–330.
- [Woo and Meguid 2001] J. Woo and S. A. Meguid, “Nonlinear analysis of functionally graded plates and shallow shells”, *Int. J. Solids Struct.* **38**:42–43 (2001), 7409–7421.

Received 30 Aug 2008. Revised 7 Jan 2009. Accepted 11 Jan 2009.

SURESH CHANDRA PRADHAN: scp@aero.iitkgp.ernet.in

Department of Aerospace Engineering, IIT Kharagpur, Kharagpur - 721302, West Bengal, India

VISCOELASTIC STATE OF A SEMI-INFINITE MEDIUM WITH MULTIPLE CIRCULAR ELASTIC INHOMOGENEITIES

ANDREY V. PYATIGORETS AND SOFIA G. MOGILEVSKAYA

This paper is concerned with the problem of an isotropic, linear viscoelastic half-plane containing multiple, isotropic, circular elastic inhomogeneities. Three types of loading conditions are allowed at the boundary of the half-plane: a point force, a force uniformly distributed over a segment, and a force uniformly distributed over the whole boundary of the half-plane. The half-plane is subjected to far-field stress that acts parallel to its boundary. The inhomogeneities are perfectly bonded to the material matrix. An inhomogeneity with zero elastic properties is treated as a hole; its boundary can be either traction free or subjected to uniform pressure. The analysis is based on the use of the elastic-viscoelastic correspondence principle. The problem in the Laplace space is reduced to the complementary problems for the bulk material of the perforated half-plane and the bulk material of each circular disc. Each problem is described by the transformed complex Somigliana's traction identity. The transformed complex boundary parameters at each circular boundary are approximated by a truncated complex Fourier series. Numerical inversion of the Laplace transform is used to obtain the time domain solutions everywhere in the half-plane and inside the inhomogeneities. The method allows one to adopt a variety of viscoelastic models. A number of numerical examples demonstrate the accuracy and efficiency of the method.

1. Introduction

The problem of an isotropic, linearly viscoelastic half-plane containing multiple, nonoverlapping circular inhomogeneities is of practical importance in the area of mechanics of composite materials. Analysis of the relevant literature reveals that the problem has not yet received significant attention.

Standard numerical methods such as the finite element method and the boundary element method can be used to solve the problems of viscoelastic media containing inhomogeneities. These methods require very fine meshes to adequately approximate the inhomogeneities or their boundaries and usually employ a time stepping procedure. In addition, the finite element method cannot directly model an infinite or semi-infinite area. As a result, these methods are computational intensive due to their large number of degrees of freedom.

There are few numerical methods custom designed to directly simulate the behavior of viscoelastic composite materials. The problem of an infinite, linear viscoelastic plane containing multiple, nonoverlapping, circular elastic inhomogeneities was considered in [Huang et al. 2005a] for the Kelvin viscoelastic model and in [Huang et al. 2005b] for the Boltzmann viscoelastic model. The numerical approach presented in these papers combines a direct boundary integral method, Fourier series approximations for the boundary unknowns, and a time-stepping algorithm. The method assumes a time-independent

Keywords: viscoelastic half-plane, multiple circular elastic inhomogeneities, correspondence principle, direct boundary integral method, numerical Laplace inversion.

viscoelastic Poisson's ratio. The same assumption was used by [Zatula and Lavrenyuk \[1995\]](#) and [Kaminskii et al. \[2002\]](#), who solved a system of boundary-temporal integral equations with the standard collocation boundary element method to model a viscoelastic half-plane containing circular or rectangular elastic inhomogeneities. The boundary conditions at the surface of the half-plane included a load distributed over a segment. Numerical results were presented for the case of one and two inhomogeneities only.

[Kaloerov and Mironenko \[2007\]](#) considered a linearly viscoelastic plate containing a row of aligned isotropic, elastic, elliptical inhomogeneities or cracks. The authors assumed that the bulk modulus of the plate is constant, while its Poisson's ratio at every moment in time t differs from the instantaneous value at $t = 0$ by a small parameter. Expanding the Kolosov–Muskhelishvili potentials for the problem in infinite series with respect to this parameter and equating the coefficients of the same powers of the parameter, the authors obtain the system of boundary conditions for the unknown functions. These functions themselves were represented by the infinite complex series. The coefficients in these series were determined by the least-squares method. The disadvantage of this technique is that the accuracy of this approach may depend on the choice of the small parameter.

The elastic problems of a piece-wise homogeneous half-plane containing multiple inhomogeneities have been studied extensively. A comprehensive review of the literature related to the elastic case is given by [Legros et al. \[2004\]](#) and [Kushch et al. \[2006\]](#).

This paper is concerned with the problem of an isotropic, linearly viscoelastic half-plane containing multiple, isotropic, circular elastic inhomogeneities. Three types of loading conditions are allowed at the boundary of the half-plane: a point force, a force uniformly distributed over a segment, and a force uniformly distributed over the whole boundary of the half-plane. The half-plane is subjected to far-field stress that acts parallel to its boundary. The analysis in the present paper is based on the use of the elastic-viscoelastic correspondence principle. The problem in Laplace space is reduced to the complementary problems for the bulk material of the perforated half-plane and the bulk material of each circular disc. Each problem is described by the transformed complex Somigliana's traction identity. The transformed complex boundary parameters at each circular boundary are approximated by a truncated complex Fourier series. Numerical inversion of the Laplace transform is used to obtain the time domain solutions everywhere in the half-plane and inside the inhomogeneities. The method does not assume a time-independent viscoelastic Poisson's ratio and allows one to adopt a variety of viscoelastic models. The method described in the present paper is an extension of [\[Pyatigorets et al. 2008\]](#), where the problem of an isotropic, linearly viscoelastic half-plane containing multiple holes was considered. The inversion of the Laplace transform in the latter problem could be performed analytically, which is not the case for the more general problem considered in the present paper.

The paper is organized as follows. After formulating the problem in [Section 2](#), the system of governing boundary integral equations, written in the Laplace domain separately for each inhomogeneity and the viscoelastic matrix, is analyzed in [Section 3](#). In [Section 4](#), the approximations of the unknown displacements and tractions at the boundaries of the inhomogeneities are introduced. Using the Taylor series expansion method one arrives at the system of linear equations, where the vector of unknowns consists of the Fourier coefficients for the boundary parameters. The viscoelastic analogs of the Kolosov–Muskhelishvili potentials are used to obtain the displacements, strains, and stresses in the Laplace domain. The section concludes with a description of the procedure for the numerical inversion of the Laplace transform and discussion of the sources of errors. Three examples, presented in [Section 5](#), show the

accuracy and effectiveness of the method. Two different constitutive models are used in the numerical modeling. The first example is aimed at comparing the results obtained by the present approach with those obtained by the finite element method. The second example investigates the influence of the elastic properties of the inhomogeneity on the behavior of the hoop stress at a point on its boundary. The third example studies the asymptotic behavior of stress state in the viscoelastic half-plane and inside the inhomogeneity for the case when the Burgers model is used to describe the shear response of the bulk material of the half-plane. Several closing remarks conclude the paper.

2. Problem formulation

Consider an isotropic, linearly viscoelastic half-plane ($y \leq 0$) containing an arbitrary number N of nonoverlapping, arbitrarily located, circular, isotropic elastic inhomogeneities, as shown in Figure 1a. The elastic properties of the inhomogeneities (shear moduli μ_k and Poisson's ratios ν_k , $k = 1, \dots, N$) are assumed to be arbitrary. A hole is treated as a particular case of an inhomogeneity with zero elastic properties. Let R_k , z_k , and L_k denote the radius, the center, and the boundary of the k -th inhomogeneity.

Three types of loading conditions are allowed at the surface $y = 0$ of the half-plane. These loads are: a point force $F(t)$ applied at point a , a force $F(t)$ uniformly distributed over the segment (a, b) , a force $F(t)$ uniformly distributed over the whole boundary of the half-plane. The far-field stress $\sigma^\infty(t)$ acts parallel to the boundary of the half-plane. Perfect bonding is assumed between each inhomogeneity and the bulk material of the half-plane. In the case of a hole, its boundary is assumed to be either traction free or subjected to uniform pressure $-p_k(t)$, $k = 1, \dots, N_h$ (where N_h is the number of holes). For practical applications it is sufficient to assume the following time-dependent behavior for the functions $p_k(t)$, $F(t)$, and $\sigma^\infty(t)$:

$$p_k(t) = \tilde{p}_k \cdot f_p(t), \quad k = 1, \dots, N_h, \quad F(t) = \tilde{F} \cdot f_F(t), \quad \sigma^\infty(t) = \tilde{\sigma}^\infty \cdot f_\infty(t), \quad (1)$$

where the constants $\tilde{p}_k, \tilde{\sigma}^\infty$ are real and the constant \tilde{F} is complex ($\tilde{F} = \tilde{F}_x + i\tilde{F}_y$, $i = \sqrt{-1}$). The first expression from (1) implies similar time-dependent behavior for all the functions $p_k(t)$, the second expression implies that the time-dependent behavior of the normal and tangential components of the surface loads is similar, and the third expression is added for consistency.

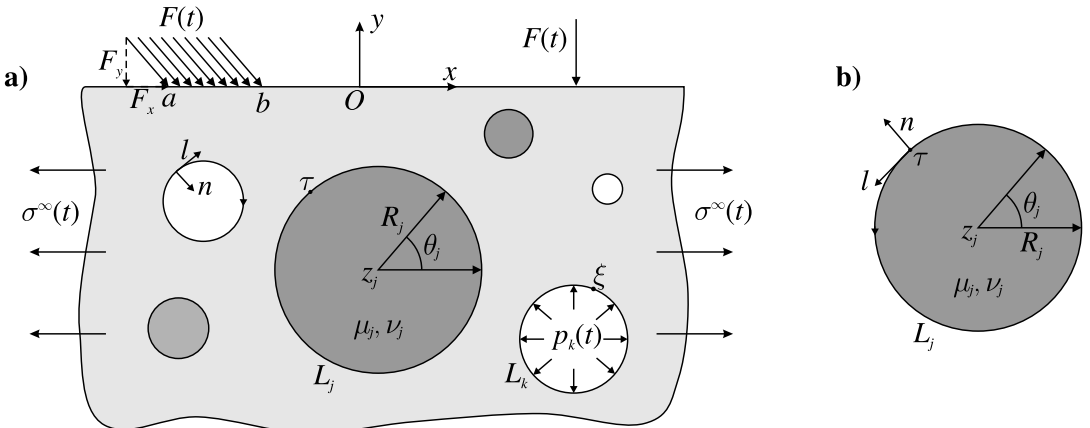


Figure 1. Problem formulation.

The viscoelastic model is not specified at this point, as the method enables the adoption of various models. The evolution of stresses, strains, and displacements in the viscoelastic half-plane and inside the inhomogeneities are to be determined.

3. Basic equations

The problem considered here can be decomposed into $N_d = N - N_h$ problems for each elastic disc and a complementary problem for the half-plane containing N cavities. The problems are interrelated by the condition of perfect bonding between the matrix and the discs.

The analysis is based on the elastic-viscoelastic correspondence principle. According to the principle, the solution of the problem in the time domain can be directly obtained from the solution of the corresponding elastic problem by applying the inverse Laplace transform to s -dependent quantities [Findley et al. 1976], where s is the transform parameter.

The Laplace transform of a real function $f(t)$ is defined as

$$\hat{f}(s) = \mathcal{L}[f(t)] = \int_0^{\infty} f(t)e^{-st} dt, \quad (2)$$

where s in general is a complex number. The inverse Laplace transform is given by the Bromwich integral

$$f(t) = \mathcal{L}^{-1}[\hat{f}(s)] = \frac{1}{2\pi i} \int_{\gamma-i\cdot\infty}^{\gamma+i\cdot\infty} \hat{f}(s)e^{st} ds, \quad (3)$$

where γ is a vertical contour in the complex plane to the right of all singularities of $\hat{f}(s)$.

3.1. The system of boundary integral equations in the Laplace domain. The system of governing equations in the Laplace domain is obtained by using a direct boundary integral method. This formulation is based on the use of the transformed Somigliana's displacement identity, which is a corollary of the reciprocal theorem (the principle of virtual work). The identity expresses the displacements at a point within an elastic region in terms of the integrals of the tractions and displacements over its boundary. Using the strain-displacement relation, Hooke's law, and the stress-traction relation, one can arrive then at the integral identity for the traction at the inner point of the region (Somigliana's traction identity). The tractions at the boundary of the region can be obtained through the limiting process in which the inner point of the region is allowed to approach the boundary of the region [Mogilevskaya and Linkov 1998; Mogilevskaya 2000]. Somigliana's identities can be written either in the time domain [Carini et al. 1991] or in the Laplace domain. In the following we use complex variable identities in the Laplace domain [Huang et al. 2006a]. Thus, the system of governing equations includes the following equations:

(I) The viscoelastic analog of Somigliana's traction identity at the boundary of the k -th disc, $k=1, \dots, N_d$:

$$\begin{aligned} 2\pi i \frac{\kappa_k + 1}{4\mu_k} \hat{\sigma}_k^d(\xi; s) &= \frac{1 - \kappa_k}{2\mu_k} \int_{L_k} \hat{\sigma}_k^d(\tau; s) \frac{d\tau}{\tau - \xi} - \frac{\kappa_k}{2\mu_k} \int_{L_k} \hat{\sigma}_k^d(\tau; s) \frac{\partial}{\partial \xi} K_1(\tau, \xi) d\tau \\ &+ \frac{1}{2\mu_k} \int_{L_k} \overline{\hat{\sigma}_k^d(\tau; s)} \frac{\partial}{\partial \xi} K_2(\tau, \xi) d\bar{\tau} + 2 \int_{L_k} \frac{\hat{u}_k^d(\tau; s)}{(\tau - \xi)^2} d\tau \\ &- \int_{L_k} \hat{u}_k^d(\tau; s) \frac{\partial^2}{\partial \tau \partial \xi} K_1(\tau, \xi) d\tau - \int_{L_k} \overline{\hat{u}_k^d(\tau; s)} \frac{\partial^2}{\partial \bar{\tau} \partial \xi} K_2(\tau, \xi) d\bar{\tau}. \quad (4) \end{aligned}$$

Here $\zeta = \zeta_x + i\zeta_y$, $\tau = \tau_x + i\tau_y$ are complex coordinates of the points $(\zeta_x, \zeta_y) \in L_k$ and $(\tau_x, \tau_y) \in L_k$; s is the Laplace transform parameter; $\hat{\sigma}_k^d(\tau; s) = \hat{\sigma}_{kn}^d(\tau; s) + i\hat{\sigma}_{kl}^d(\tau; s)$ is the unknown transformed complex traction at the point τ in the local coordinate system shown in [Figure 1b](#); $\hat{u}_k^d(\tau; s) = \hat{u}_{kx}^d(\tau; s) + i\hat{u}_{ky}^d(\tau; s)$ is the unknown transformed complex displacement at the point τ in a global coordinate system; κ_k is the Kolosov–Muskhelishvili parameter for the k -th disc, equal to $3 - 4\nu_k$ for plane strain and to $(3 - \nu_k)/(1 + \nu_k)$ for plane stress; a bar over a symbol denotes complex conjugation; and a hat over a symbol denotes the transformed quantity (in the Laplace domain). The direction of travel is counter-clockwise for the boundary L_k .

The kernels K_1 and K_2 in (4) corresponding to the Kelvin fundamental solution are [[Mogilevskaya and Linkov 1998](#)]

$$K_1(\tau, \zeta) = \ln \frac{\tau - \zeta}{\bar{\tau} - \bar{\zeta}}, \quad K_2(\tau, \zeta) = \frac{\tau - \zeta}{\bar{\tau} - \bar{\zeta}}. \quad (5)$$

(II) The viscoelastic analog of Somigliana's traction identity at the boundary of the k -th cavity located in the viscoelastic half-plane, $k = 1, \dots, N$,

$$\begin{aligned} & \sum_{j=1}^N \left\{ 2 \int_{L_j} \frac{\hat{u}_j^h(\tau; s)}{(\tau - \zeta)^2} d\tau - \int_{L_j} \hat{u}_j^h(\tau; s) \frac{\partial^2}{\partial \tau \partial \bar{\zeta}} [K_1(\tau, \zeta) + K_3(\tau, \zeta) + K_4(\tau, \zeta)] d\tau \right. \\ & \quad \left. - \int_{L_j} \overline{\hat{u}_j^h(\tau; s)} \frac{\partial^2}{\partial \bar{\tau} \partial \zeta} [K_2(\tau, \zeta) + K_5(\tau, \zeta) + K_6(\tau, \zeta)] d\bar{\tau} \right\} - \pi i \frac{\hat{\kappa}(s) + 1}{2\hat{\mu}(s)} \hat{\sigma}_k^h(\zeta; s) \\ & - \frac{1}{2\hat{\mu}(s)} \sum_{j=1}^N \left\{ (\hat{\kappa}(s) - 1) \int_{L_j} \frac{\hat{\sigma}_j^h(\tau; s)}{\tau - \zeta} d\tau + \int_{L_j} \hat{\sigma}_j^h(\tau; s) \frac{\partial}{\partial \zeta} [\hat{\kappa}(s)K_1(\tau, \zeta) + \hat{\kappa}(s)K_3(\tau, \zeta) - K_4(\tau, \zeta)] d\tau \right. \\ & \quad \left. - \int_{L_j} \overline{\hat{\sigma}_j^h(\tau; s)} \frac{\partial}{\partial \bar{\zeta}} [K_2(\tau, \zeta) + K_6(\tau, \zeta) - \hat{\kappa}(s)K_5(\tau, \zeta)] d\bar{\tau} \right\} = -2\pi i \frac{\hat{\kappa}(s) + 1}{4\hat{\mu}(s)} \hat{\sigma}_k^{\text{add}}(\zeta; s), \quad (6) \end{aligned}$$

where $\hat{u}_j^h(\tau; s) = \hat{u}_{jx}^h(\tau; s) + i\hat{u}_{jy}^h(\tau; s)$ is the unknown transformed complex displacement at the point $\tau \in L_j$, $\hat{\sigma}_j^h(\tau; s) = \hat{\sigma}_{jn}^h(\tau; s) + i\hat{\sigma}_{jl}^h(\tau; s)$ is the unknown transformed complex traction at the point $\tau \in L_j$ in the local coordinate system shown in [Figure 1a](#), and $\hat{\kappa}(s)$ and $\hat{\mu}(s)$ are the transformed Kolosov–Muskhelishvili parameter and the shear modulus of the bulk material of the half-plane, respectively. The direction of travel is clockwise for the boundary L_j .

In addition to the kernels K_1 and K_2 from (5) the following kernels appear in system (6):

$$\begin{aligned} K_3(\tau, \zeta) &= \ln(\bar{\tau} - \zeta), & K_4(\tau, \zeta) &= \ln(\tau - \bar{\zeta}) + (\zeta - \bar{\zeta}) \frac{\bar{\tau} - \tau}{(\tau - \bar{\zeta})^2}, \\ K_5(\tau, \zeta) &= \frac{\zeta - \bar{\zeta}}{\tau - \bar{\tau}}, & K_6(\tau, \zeta) &= -\frac{\tau - \zeta}{\bar{\tau} - \bar{\zeta}}. \end{aligned} \quad (7)$$

The integral kernels K_3 – K_6 are parts of Melan's fundamental solution [[1932](#)] (a point force applied at an internal point of a half-plane). Due to the use of this fundamental solution, the boundary of the half-plane is not involved in the governing system (6).

The function $\hat{\sigma}_k^{\text{add}}(\zeta; s)$ on the right-hand side of (6) is a complex function that represents the combined influence of the transformed far-field stress $\hat{\sigma}^\infty(s)$ and transformed force $\hat{F}(s)$ applied at the boundary

of the half-plane. It is expressed as

$$\hat{\sigma}_k^{\text{add}}(\zeta; s) = 2\hat{\sigma}_k^\infty(\zeta; s) + \hat{\sigma}_k^F(\zeta; s), \quad (8)$$

where $\hat{\sigma}_k^\infty(\zeta; s)$ is the transformed traction at the trace of the boundary of the k -th cavity ($k = 1, \dots, N$) due to the far-field stress and $\hat{\sigma}_k^F(\zeta; s)$ is the transformed traction at the same boundary due to the force applied at the boundary of the half-plane. Both terms on the right-hand side of (8) are obtained by using s -varying Kolosov–Muskhelishvili potentials $\hat{\phi}(\zeta; s)$ and $\hat{\psi}(\zeta; s)$ (see [Muskhelishvili 1959]) and the formula

$$\hat{\sigma}(\zeta; s) = \frac{\partial}{\partial \bar{\zeta}} \hat{\phi}(\zeta; s) + \overline{\frac{\partial}{\partial \zeta} \hat{\phi}(\zeta; s)} + \frac{d\bar{\zeta}}{d\zeta} \left[\bar{\zeta} \frac{\partial^2}{\partial \bar{\zeta}^2} \hat{\phi}(\zeta; s) + \overline{\frac{\partial}{\partial \zeta} \hat{\psi}(\zeta; s)} \right] \quad (9)$$

(see [Rabotnov 1988]), where $d\bar{\zeta}/d\zeta = \exp(-2i\beta)$, and β is the angle between the axis Ox and the tangent at the point $\zeta \in L_k$. The potentials $\hat{\phi}$ and $\hat{\psi}$ for the far-field stress and the load applied at the boundary of the half-plane are given in [Pyatigorets et al. 2008].

Equations (5) and (6) are complemented by the following boundary conditions. For the case when the k -th inhomogeneity is a hole, the traction $\hat{\sigma}_k^h(\tau; s)$ in (6) is $\hat{\sigma}_k^h(\tau; s) = -\hat{p}_k(s)$. For the case when the k -th inhomogeneity is an elastic disc, the conditions for perfect bonding are

$$\begin{aligned} \hat{u}_k^h(\zeta; s) &= \hat{u}_k^d(\zeta; s) = \hat{u}_k(\zeta; s), & \zeta \in L_k, \\ \hat{\sigma}_k^h(\zeta; s) &= \hat{\sigma}_k^d(\zeta; s) = \hat{\sigma}_k(\zeta; s), & \zeta \in L_k. \end{aligned} \quad (10)$$

3.2. Calculation of the s -dependent fields in the composite system. The transformed stresses and displacements at any point in the viscoelastic half-plane and inside the elastic discs are obtained using the following analogs of the Kolosov–Muskhelishvili formulae:

$$\begin{cases} 2\hat{\mu}(s)\hat{u}(z; s) = \hat{\kappa}(s)\hat{\phi}(z; s) - z \frac{\partial}{\partial z} \hat{\phi}(z; s) - \overline{\hat{\psi}(z; s)}, \\ \hat{\sigma}_{xx}(z; s) + \hat{\sigma}_{yy}(z; s) = 4 \operatorname{Re} \left[\frac{\partial}{\partial z} \hat{\phi}(z; s) \right], \\ \hat{\sigma}_{yy}(z; s) - \hat{\sigma}_{xx}(z; s) + 2i\hat{\sigma}_{xy}(z; s) = 2 \left[\bar{z} \frac{\partial^2}{\partial \bar{z}^2} \hat{\phi}(z; s) + \frac{\partial}{\partial z} \hat{\psi}(z; s) \right]. \end{cases} \quad (11)$$

The strains are expressed through the stresses in the Laplace domain as

$$\begin{cases} \hat{\varepsilon}_{xx} + \hat{\varepsilon}_{yy} = \frac{1 - 2\nu}{2\hat{\mu}} (\hat{\sigma}_{xx} + \hat{\sigma}_{yy}), \\ \hat{\varepsilon}_{yy} - \hat{\varepsilon}_{xx} + 2i\hat{\varepsilon}_{xy} = \frac{1}{2\hat{\mu}} (\hat{\sigma}_{yy} - \hat{\sigma}_{xx} + 2i\hat{\sigma}_{xy}). \end{cases} \quad (12)$$

The corresponding sets of material properties for the inhomogeneities and the matrix should be used in (11) and (12) for the evaluation of viscoelastic fields. The expressions for the potentials involved in (11) and (12) are:

(a) Potentials for the k -th elastic disc ($\hat{\mu}(s) = \mu_k$ and $\hat{\kappa}(s) = \kappa_k$):

$$\begin{aligned}\hat{\phi}_k(z; s) &= -\frac{1}{2\pi i(\kappa_k + 1)} \left[\int_{L_k} \hat{\sigma}_k^d(\tau; s) \ln(\tau - z) d\tau - 2\mu_k \int_{L_k} \frac{\hat{u}_k(\tau; s)}{\tau - z} d\tau \right], \\ \hat{\psi}_k(z; s) &= -\frac{1}{2\pi i(\kappa_k + 1)} \left\{ \left[\int_{L_k} \hat{\sigma}_k^d(\tau; s) \frac{\bar{\tau} d\tau}{\tau - z} + \kappa_k \int_{L_k} \overline{\hat{\sigma}_k^d(\tau; s)} \ln(\tau - z) d\bar{\tau} \right] \right. \\ &\quad \left. + 2\mu_k \left[\int_{L_k} \frac{\overline{\hat{u}_k(\tau; s)}}{\tau - z} d\tau - \int_{L_k} \frac{\hat{u}_k(\tau; s)}{\tau - z} d\bar{\tau} + \int_{L_k} \frac{\hat{u}_k(\tau; s) \bar{\tau}}{(\tau - z)^2} d\tau \right] \right\}.\end{aligned}\quad (13)$$

Expressions (13) are obtained by Laplace transforming the corresponding elastic potentials given in [Mogilevskaya et al. 2008].

(b) Potentials for the bulk material of the viscoelastic half-plane:

$$\begin{aligned}\hat{\phi}(z; s) &= \hat{\phi}_{\text{plane}}(z; s) + \hat{\phi}_{\text{aux}}(z; s) + \hat{\phi}_F(z; s), \\ \hat{\psi}(z; s) &= \hat{\psi}_{\text{plane}}(z; s) + \hat{\psi}_{\text{aux}}(z; s) + \hat{\psi}_F(z; s),\end{aligned}\quad (14)$$

where $\hat{\phi}_{\text{plane}}(z; s)$ and $\hat{\psi}_{\text{plane}}(z; s)$ are the potentials due to Kelvin's fundamental solution and $\hat{\phi}_{\text{aux}}(z; s)$ and $\hat{\psi}_{\text{aux}}(z; s)$ are additional potentials associated with the use of Green's functions specific for a half-plane problem. The potentials $\hat{\phi}_F(z; s)$ and $\hat{\psi}_F(z; s)$ are given in [Pyatigorets et al. 2008] and the rest are obtained by applying the Laplace transform to their elastic analogs [Mogilevskaya 2000]:

$$\begin{aligned}\hat{\phi}_{\text{plane}}(z; s) &= -\frac{1}{2\pi i(\hat{\kappa}(s) + 1)} \sum_{j=1}^N \left[\int_{L_j} \hat{\sigma}_j^h(\tau; s) \ln(\tau - z) d\tau - 2\hat{\mu}(s) \int_{L_j} \frac{\hat{u}_j(\tau; s)}{\tau - z} d\tau \right] + \frac{\hat{\sigma}^\infty(s)}{4} z, \\ \hat{\psi}_{\text{plane}}(z; s) &= -\frac{1}{2\pi i(\hat{\kappa}(s) + 1)} \sum_{j=1}^N \left\{ \left[\int_{L_j} \hat{\sigma}_j^h(\tau; s) \frac{\bar{\tau} d\tau}{\tau - z} + \hat{\kappa}(s) \int_{L_j} \overline{\hat{\sigma}_j^h(\tau; s)} \ln(\tau - z) d\bar{\tau} \right] \right. \\ &\quad \left. + 2\hat{\mu}(s) \left[\int_{L_j} \frac{\overline{\hat{u}_j(\tau; s)}}{\tau - z} d\tau - \int_{L_j} \frac{\hat{u}_j(\tau; s)}{\tau - z} d\bar{\tau} + \int_{L_j} \frac{\hat{u}_j(\tau; s) \bar{\tau}}{(\tau - z)^2} d\tau \right] \right\} - \frac{\hat{\sigma}^\infty(s)}{2} z,\end{aligned}\quad (15)$$

$$\begin{aligned}\hat{\phi}_{\text{aux}}(z; s) &= -\frac{1}{2\pi i(\hat{\kappa}(s) + 1)} \sum_{j=1}^N \left\{ \left[\hat{\kappa}(s) \int_{L_j} \hat{\sigma}_j^h(\tau; s) \ln(\bar{\tau} - z) d\tau + \int_{L_j} \overline{\hat{\sigma}_j^h(\tau; s)} \frac{\tau - z}{\bar{\tau} - z} d\bar{\tau} \right] \right. \\ &\quad \left. + 2\hat{\mu}(s) \left[\int_{L_j} \frac{\hat{u}_j(\tau; s)}{\bar{\tau} - z} d\bar{\tau} - \int_{L_j} \frac{\overline{\hat{u}_j(\tau; s)}}{\bar{\tau} - z} d\tau \right] \right\}, \\ \hat{\psi}_{\text{aux}}(z; s) &= -\frac{1}{2\pi i(\hat{\kappa}(s) + 1)} \sum_{j=1}^N \left\{ z \left[\hat{\kappa}(s) \int_{L_j} \hat{\sigma}_j^h(\tau; s) \frac{d\tau}{\bar{\tau} - z} - \int_{L_j} \overline{\hat{\sigma}_j^h(\tau; s)} \frac{\partial}{\partial z} \frac{\tau - z}{\bar{\tau} - z} d\bar{\tau} \right] \right. \\ &\quad \left. + 2\hat{\mu}(s) \left(\int_{L_j} \overline{\hat{u}_j(\tau; s)} d \frac{\partial}{\partial z} \frac{\tau - z}{\bar{\tau} - z} - \int_{L_j} \hat{u}_j(\tau; s) \frac{d\bar{\tau}}{(\bar{\tau} - z)^2} \right) \right. \\ &\quad \left. + \int_{L_j} \overline{\hat{\sigma}_j^h(\tau; s)} \ln(\bar{\tau} - z) d\bar{\tau} - 2\hat{\mu}(s) \int_{L_j} \frac{\overline{\hat{u}_j(\tau; s)}}{\bar{\tau} - z} d\bar{\tau} \right\}.\end{aligned}\quad (16)$$

4. Numerical solution

4.1. Fourier series approximation of the unknowns at the boundaries. The unknown transformed stresses $\hat{\sigma}_k(\tau; s)$ at each boundary L_k are approximated by the truncated complex Fourier series

$$\hat{\sigma}_k(\tau; s) = \sum_{m=1}^{M_k} \hat{T}_{-mk}(s) g_k^m(\tau) + \hat{T}_{0k}(s) + \sum_{m=1}^{M_k} \hat{T}_{mk}(s) g_k^{-m}(\tau), \quad \tau \in L_k, \quad k = 1, \dots, N_d, \quad (17)$$

where the function $g_k(\tau)$ is defined as

$$g_k(\tau) = \frac{R_k}{\tau - z_k} = \exp(-i\theta_k). \quad (18)$$

The unknown transformed displacements $\hat{u}_k(\tau; s)$ at the boundary L_k are represented by the series

$$\hat{u}_k(\tau; s) = \sum_{m=1}^{M_k-1} \hat{B}_{-mk}(s) g_k^m(\tau) + \hat{B}_{0k}(s) + \sum_{m=1}^{M_k+1} \hat{B}_{mk}(s) g_k^{-m}(\tau), \quad \tau \in L_k, \quad k = 1, \dots, N. \quad (19)$$

Note that the Fourier series in (19) are truncated differently from the series representation (17). The reason for this is explained in [Mogilevskaya et al. 2008].

4.2. System of complex algebraic equations. After substituting (17) and (19) into Somigliana's traction identity (4) and following a procedure similar to the one described in [Mogilevskaya et al. 2008] for the elastic case, one arrives at the expressions

$$\begin{aligned} \hat{T}_{-1k}(s) &= 0, \\ \frac{\kappa_k - 1}{2\mu_k} \hat{T}_{0k}(s) &= \frac{2}{R_k} \operatorname{Re} \hat{B}_{1k}(s), \\ \frac{1}{2\mu_k} \hat{T}_{-mk}(s) &= \frac{m-1}{R_k} \hat{B}_{-(m-1)k}(s), \quad m \geq 2, \\ \frac{\kappa_k}{2\mu_k} \hat{T}_{mk}(s) &= \frac{m+1}{R_k} \hat{B}_{(m+1)k}(s), \quad m \geq 1. \end{aligned} \quad (20)$$

Expression (17) can now be rewritten using (20) as

$$\hat{\sigma}_k(\tau; s) = \frac{2\mu_k}{R_k} \left[\sum_{m=1}^{M_k-1} m \hat{B}_{-mk}(s) g_k^{m+1}(\tau) + \frac{2}{\kappa_k - 1} \operatorname{Re} \hat{B}_{1k}(s) + \frac{1}{\kappa_k} \sum_{m=2}^{M_k+1} m \hat{B}_{mk}(s) g_k^{1-m}(\tau) \right], \quad k = 1, \dots, N_d. \quad (21)$$

After substituting (19) and (21) in Somigliana's traction identity (6), the s -dependent Fourier coefficients $\hat{B}_{mk}(s)$ can be taken out from the integrals, and all the space integrals can be evaluated analytically.

As a result, one arrives at the following system of complex integral equations:

$$\begin{aligned} \hat{\Lambda}_{kk}(\zeta; s) + \sum_{\substack{j=1 \\ j \neq k}}^{N_h} \hat{\Lambda}_{kj}(\zeta; s) + \sum_{r=N_h+1}^N \hat{G}_{kr}(\zeta; s) &= -\frac{\hat{\kappa} + 1}{4\hat{\mu}} (\hat{p}_k + \hat{\sigma}_k^{\text{add}}(\zeta; s)) + \sum_{j=1}^{N_h} \hat{p}_j \hat{\Gamma}_j(\zeta; s), \\ \sum_{j=1}^{N_h} \hat{\Lambda}_{lj}(\zeta; s) + \left[\hat{G}_{ll}(\zeta; s) - \frac{\hat{\kappa} + 1}{2\hat{\mu}} \hat{\sigma}_l(\zeta; s) \right] + \sum_{\substack{r=N_h+1 \\ r \neq l}}^N \hat{G}_{lr}(\zeta; s) &= -\frac{\hat{\kappa} + 1}{4\hat{\mu}} \hat{\sigma}_l^{\text{add}}(\zeta; s) + \sum_{j=1}^{N_h} \hat{p}_j \hat{\Gamma}_j(\zeta; s), \end{aligned} \quad (22)$$

$\zeta \in L_k, k = 1, \dots, N_h,$
 $\zeta \in L_l, l = N_h + 1, \dots, N.$

The left-hand sides of (22) contain the unknown displacements at the boundaries of the cavities, while the right-hand sides contain the known boundary tractions only. The following operators appear in (22):

- operators $\hat{\Lambda}_{kj}(\zeta; s)$ ($k, j = 1, \dots, N_h$) obtained after evaluation of the integrals in (6) containing the unknown Fourier coefficients over the boundaries of the holes;
- operators $\hat{G}_{kj}(\zeta; s)$ ($k, j = N_h, \dots, N$) obtained after evaluation of the integrals in (6) containing the unknown Fourier coefficients over the boundaries of those cavities that later are occupied by the elastic discs;
- operators $\hat{\Gamma}_j(\zeta; s)$ ($j = 1, \dots, N_h$) obtained after evaluation of the integrals in (6) containing the known tractions \hat{p}_j over the boundaries of the holes (\hat{p}_j is factored out in (22)).

The coefficients $\hat{B}_{0k}(s)$ and the imaginary part of $\hat{B}_{1k}(s)$ are not involved in the system of governing equations (22). These coefficients are responsible for the rigid body translation (B_{0k}) and rotation ($\text{Im } B_{1k}$) and can be found from a procedure described in [Wang et al. 2003].

The expressions for the operators $\hat{\Lambda}_{\alpha\beta}$ and $\hat{\Gamma}_j$ can be obtained by applying the Laplace transform to the corresponding expressions used in [Dejoie et al. 2006]. Operators $\hat{G}_{\alpha\beta}$ differ from the expressions for $\hat{\Lambda}_{\alpha\beta}$ by additional s -dependent multipliers in front of the unknown coefficients $\hat{B}_{-mk}(s)$, $\text{Re } \hat{B}_{1k}(s)$, and $\hat{B}_{mk}(s)$ ($m = -(M_k - 1), \dots, M_k + 1, k = N_h + 1, \dots, N$; see Appendix A). These multipliers are

$$\begin{aligned} \hat{\alpha}_{1k} &= -\left(\frac{\mu_k}{\hat{\mu}} - 1\right) && \text{in front of } \hat{B}_{-mk}(s), \\ \hat{\alpha}_{2k} &= -\left(\frac{\mu_k}{\kappa_k - 1} \frac{\hat{\kappa} - 1}{\hat{\mu}} - 1\right) && \text{in front of } \text{Re } \hat{B}_{1k}(s), \\ \hat{\alpha}_{3k} &= -\left(\frac{\mu_k}{\kappa_k} \frac{\hat{\kappa}}{\hat{\mu}} - 1\right) && \text{in front of } \hat{B}_{mk}(s). \end{aligned} \quad (23)$$

4.3. System of real linear algebraic equations. The Taylor expansion method (the so-called addition theorem) described in [Wang et al. 2003] can be used to obtain a system of linear algebraic equations from (22). In this method, all the functions $g_j^m(\zeta)$ involved in the representations of the unknowns at the j -th boundary can be reexpanded in terms of infinite series of functions $g_k(\zeta)$ as

$$g_j^m(\zeta) = g_j^m(z_k) \sum_{q=0}^{\infty} \binom{m+q-1}{q} g_k^q(z_j) g_k^{-q}(\zeta) \quad \text{for all } j \neq k \text{ and } j, k = 1, \dots, N, \quad (24)$$

where $\binom{m+q-1}{q}$ represents a binomial coefficient as usual. The functions $\overline{g_j(\zeta)}$ can similarly be reexpanded in terms of functions $g_k(\zeta)$ due to the fact that

$$\overline{g_j(\zeta)} = g_j^{-1}(\zeta).$$

As a result, all the operators $\hat{\Lambda}_{\alpha\beta}$ and $\hat{G}_{\alpha\beta}$ in the left-hand side of (22) are expressed through the functions $g_k^q(\zeta)$. Similarly, the operators $\hat{\Gamma}_j$ in the right-hand side of (22) can be expressed through the same functions. Using the orthogonality properties of the complex Fourier series, one can equate the coefficients in front of the terms $g_k^q(\zeta)$ with the same powers in both sides of the obtained expressions. A finite system of linear equations with the number of equations equal to the number of unknown coefficients \hat{B}_{mk} , $k = 1, \dots, N$, is obtained if one neglects the terms with powers $q > M_k$ and $q < -M_k$ in the Taylor series for every k .

As a result, one arrives at a system of $\sum_{k=1}^N (2M_k + 1)$ complex linear equations in the Laplace domain; namely, for $k = 1, \dots, N$, we can write

$$\begin{aligned} & \hat{Y}_{kk,q}(\hat{B}_{mk}) + \sum_{\substack{j=1 \\ j \neq k}}^N \hat{Y}_{kj,q}(\hat{B}_{mj}) + \Delta_k \cdot \hat{S}_k(\hat{B}_{qk}) \\ &= \begin{cases} -\frac{\hat{k}+1}{4\hat{\mu}} \hat{\sigma}^\infty - \frac{1-\Delta_k}{\hat{\mu}} \hat{p}_k - \frac{\hat{k}+1}{4\hat{\mu}} \Omega_{k,0}(\hat{F}) + \frac{\hat{k}-1}{2\hat{\mu}} \sum_{j=1}^{N_h} \hat{p}_j \Xi_{kj,0}, & \text{for } q = 0, \\ -\frac{\hat{k}+1}{4\hat{\mu}} \hat{\sigma}^\infty - \frac{\hat{k}+1}{4\hat{\mu}} \Omega_{k,2}(\hat{F}) + \frac{\hat{k}-1}{2\hat{\mu}} \sum_{j=1}^{N_h} \hat{p}_j \Xi_{kj,2}, & \text{for } q = 2, \\ -\frac{\hat{k}+1}{4\hat{\mu}} \Omega_{k,q}(\hat{F}) + \frac{\hat{k}-1}{2\hat{\mu}} \sum_{j=1}^{N_h} \hat{p}_j \Xi_{kj,q}, & \text{for } q \neq 0, 1, 2, \quad -M_k \leq q \leq M_k, \end{cases} \end{aligned} \quad (25)$$

where

$$\hat{S}_k(\hat{B}_{qk}) = \frac{\hat{k}+1}{\hat{\mu}} \frac{\mu_k}{R_k} \cdot \begin{cases} \frac{1-q}{\hat{\alpha}_{3k} \kappa_k} \hat{B}_{(1-q)k}, & \text{if } q \leq -1, \\ \frac{2}{\hat{\alpha}_{2k} (\kappa_k - 1)} \operatorname{Re} \hat{B}_{1k}, & \text{if } q = 0, \\ \frac{q-1}{\hat{\alpha}_{1k}} \hat{B}_{(1-q)k}, & \text{if } q \geq 2, \end{cases} \quad (26)$$

and Δ_k takes the value 0 if L_k is the boundary of a hole and the value 1 if L_k is the boundary of a cavity later occupied by an elastic disc. In general, the coefficients \hat{B}_{mk} are different from the coefficients \hat{B}_{mk} as they may include the multipliers given by (23). The operators $\hat{Y}_{kk,q}$, $\hat{Y}_{kj,q}$, $\Omega_{k,q}$, and $\Xi_{kj,q}$ can be found in [Pyatigorets et al. 2008]¹ if one takes into account the specific method of truncating Fourier series in the present approach.

Separating the real and imaginary parts in complex equations (25) and taking into account that (25) is real for $q = 0$, one arrives at a linear system of $\sum_{k=1}^N (4M_k - 1)$ equations. The resulting system of linear equations can be written in matrix form as

$$[A + \hat{W}(s)] \cdot \hat{B}(s) = \hat{D}(s), \quad (27)$$

¹Due to misprints, all inequalities $q \leq -1$ present in [Pyatigorets et al. 2008, appendices A–C] should be read as $(-q) \leq -1$.

where the s -independent matrix A is

$$A = \left[\begin{array}{c|c} \begin{array}{ccc} \text{block 1} \\ \hline A_{11} & \dots & A_{1N_h} \\ \vdots & \ddots & \vdots \\ A_{N_h 1} & \dots & A_{N_h N_h} \end{array} & \begin{array}{ccc} \text{block 2} \\ \hline A_{1(N_h+1)} & \dots & A_{1(N_h+N_d)} \\ \vdots & \ddots & \vdots \\ A_{N_h(N_h+1)} & \dots & A_{N_h(N_h+N_d)} \end{array} \\ \hline \begin{array}{ccc} A_{(N_h+1)1} & \dots & A_{1N_h} \\ \vdots & \ddots & \vdots \\ \text{block 3} \\ \hline A_{(N_h+N_d)1} & \dots & A_{(N_h+N_d)N_h} \end{array} & \begin{array}{ccc} A_{(N_h+1)(N_h+1)} & \dots & A_{(N_h+1)(N_h+N_d)} \\ \vdots & \ddots & \vdots \\ \text{block 4} \\ \hline A_{(N_h+N_d)(N_h+N_d)} & \dots & A_{(N_h+N_d)(N_h+N_d)} \end{array} \end{array} \right]. \quad (28)$$

The matrix A consists of four blocks:

- block 1, the influence of a hole on another hole;
- block 2, the influence of a hole on a cavity occupied by an elastic disc;
- block 3, the influence of a cavity occupied by an elastic disc on a hole;
- block 4, the influence of a cavity occupied by an elastic disc on another cavity occupied by an elastic disc.

The expressions for submatrices A_{jk} are available in [Pyatigorets et al. 2008] if one takes into account the differing truncation of Fourier series in the present approach. The matrix $\hat{W}(s)$ is deduced from the expression for the operator $\hat{\mathfrak{S}}_k$. This matrix is largely sparse and has the form

$$\hat{W}(s) = \left[\begin{array}{c|ccc} \mathbf{0} & \dots & \mathbf{0} & \\ \vdots & \ddots & \vdots & \\ \mathbf{0} & \dots & \mathbf{0} & \\ \hline \mathbf{0} & \dots & \mathbf{0} & \hat{W}_{(N_h+1)(N_h+1)} \dots \mathbf{0} \\ \vdots & \ddots & \vdots & \\ \mathbf{0} & \dots & \mathbf{0} & \dots \hat{W}_{NN} \end{array} \right], \quad (29)$$

where the only nonzero submatrices $\hat{W}_{kk}(s)$ are of dimension $(4M_k - 1) \times (4M_k - 1)$, $k = N_h + 1, \dots, N$. They have the form

$$\hat{W}_{kk}(s) = -\frac{\hat{\kappa} + 1}{\hat{\mu}} \frac{\mu_k}{R_k} \cdot \left[\begin{array}{c|cc} & m=-(M_k-1) & m=M_k+1 \\ \hline \frac{q-1}{\alpha_{1k}} & \mathbf{0} & \mathbf{0} \\ \hline \mathbf{0} & \frac{2}{\alpha_{2k}(\kappa_k-1)} & \mathbf{0} \\ \hline \mathbf{0} & \mathbf{0} & \frac{q+1}{\alpha_{3k}\kappa_k} \end{array} \right]_{\substack{q=M_k \\ q=-M_k}}. \quad (30)$$

The vector of unknowns $\hat{\mathbb{B}}(s)$ is given as

$$\hat{\mathbb{B}}(s) = \begin{bmatrix} \hat{\mathbb{B}}_1(s) \\ \vdots \\ \hat{\mathbb{B}}_{N_h}(s) \\ \hat{\mathbb{B}}_{N_h+1}(s) \\ \vdots \\ \hat{\mathbb{B}}_N(s) \end{bmatrix}, \quad (31)$$

with the subvectors $\hat{\mathbb{B}}_k(s)$ defined as

$$\hat{\mathbb{B}}_k(s) = \hat{B}_k(s) = \begin{bmatrix} \text{Re } \hat{B}_{-(M_k-1)k} \\ \text{Im } \hat{B}_{-(M_k-1)k} \\ \vdots \\ \text{Re } \hat{B}_{-1k} \\ \text{Im } \hat{B}_{-1k} \\ \text{Re } \hat{B}_{1k} \\ \text{Re } \hat{B}_{2k} \\ \text{Im } \hat{B}_{2k} \\ \vdots \\ \text{Re } \hat{B}_{(M_k+1)k} \\ \text{Im } \hat{B}_{(M_k+1)k} \end{bmatrix}, \quad \hat{\mathbb{B}}_j(s) = \begin{bmatrix} \hat{\alpha}_{1j} \cdot \text{Re } \hat{B}_{-(M_j-1)j} \\ \hat{\alpha}_{1j} \cdot \text{Im } \hat{B}_{-(M_j-1)j} \\ \vdots \\ \hat{\alpha}_{1j} \cdot \text{Re } \hat{B}_{-1j} \\ \hat{\alpha}_{1j} \cdot \text{Im } \hat{B}_{-1j} \\ \hat{\alpha}_{2j} \cdot \text{Re } \hat{B}_{1j} \\ \hat{\alpha}_{3j} \cdot \text{Re } \hat{B}_{2j} \\ \hat{\alpha}_{3j} \cdot \text{Im } \hat{B}_{2j} \\ \vdots \\ \hat{\alpha}_{3j} \cdot \text{Re } \hat{B}_{(M_j+1)j} \\ \hat{\alpha}_{3j} \cdot \text{Im } \hat{B}_{(M_j+1)j} \end{bmatrix}, \quad (32)$$

where $k = 1, \dots, N_h$ and $j = N_h + 1, \dots, N$.

The right-hand vector in (27) can be deduced from the expressions for the operators $\Omega_{k,q}$ and $\Xi_{k,j,q}$ in [Pyatigorets et al. 2008]. It contains N subvectors consisting of $4M_k - 1$, $k = 1, \dots, N$, elements, and its transpose is

$$[\hat{D}(s)]^T = [\hat{D}_1(s), \hat{D}_2(s), \dots, \hat{D}_{N_h}(s), \hat{D}_{N_h+1}(s), \dots, \hat{D}_N(s)]. \quad (33)$$

4.4. Solution in the time domain.

An algorithm for the numerical inversion of the Laplace transform. After the solution of system (27), the potentials involved in expressions (11) and (12) can be written in terms of s -dependent coefficients. Thus, the transformed fields can be expressed explicitly via the coefficients. To obtain the viscoelastic fields in the time domain, one needs to apply the inverse Laplace transform to the s -dependent terms involved in the transformed fields.

In the general case, the system (27) cannot be solved analytically as its both sides depend on the transform parameter s . This fact suggests that a procedure for numerical inversion of the Laplace transform should be used. Most of the methods of numerical Laplace inversion are based on the approximation of the integral (3) by a sum of s -dependent functions evaluated at certain points and multiplied by coefficients specific to a given point. For reviews of some popular methods, see [Davies and Martin 1979; Cheng et al. 1994].

Here we used the numerical Laplace inversion method proposed in [Stehfest 1970]. The series approximation for the Stehfest algorithm is given by

$$f(t) \approx \frac{\ln 2}{t} \sum_{n=1}^{N_{St}} C_n \hat{f}\left(n \frac{\ln 2}{t}\right), \quad (34)$$

where N_{St} is even and the coefficients C_n are

$$C_n = (-1)^{n+N_{St}/2} \sum_{k=(n+1)/2}^{\min(n, N_{St}/2)} \frac{k^{N_{St}/2} (2k)!}{(N_{St}/2 - k)! k! (k-1)! (n-k)! (2k-n)!}. \quad (35)$$

The detailed derivation of expressions (34) and (35) can be found in [Stehfest 1970; Kumar 2000]. The number of terms N_{St} in the series is relatively small and usually varies in the range $2 \leq N_{St} \leq 20$ that makes the calculation procedure fast in comparison with some other methods; see the charts in [Davies and Martin 1979]. Due to its simplicity the algorithm can be easily implemented in various programming languages. In addition, the algorithm does not require knowledge of the poles of the integrand (see (3)). For the case of monotonic smooth functions quite accurate results are reported by Davies and Martin [1979], Cheng et al. [1994], and Stehfest [1970]. However, no accurate results of the inversion should be expected for discontinuous functions or functions containing sharp peaks or rapid oscillations.

As the number of terms in approximation (34) does not change during the calculation of viscoelastic fields, the coefficients C_n are evaluated only once and stored in the computer memory.

Calculation of viscoelastic fields in the time domain. In order to find the viscoelastic potentials in the time domain, one has to solve system (27) for each moment of time t and each point n in the Stehfest algorithm in accordance with expression (34). The Gauss–Seidel iterative algorithm combined with an algorithm based on LU decomposition is adopted to find the explicit solution of system (27). This technique provides a good convergence rate even if the dimension of matrix A is very large. After that all s -dependent terms involved in potentials (13)–(16) have to be evaluated at points $(n \ln 2/t)$. The expressions for the potentials in terms of the Fourier coefficients $\hat{\mathbb{B}}_{mk}(s)$ are given in Appendix B. The final step assumes the summation of expressions (11) and (12) for the viscoelastic fields over all points n in accordance with (34) for each moment of time t .

The stresses and strains in the time domain are uniquely expressed via potentials (13)–(16). However, the displacements in the time domain are defined up to some additional terms that could be found after the rigid body motion is fixed, as in [Mogilevskaya et al. 2008].

Error analysis. Three sources of errors can be identified in the present method:

- (i) the error due to the use of the truncated series in the approximations (19) and (21),
- (ii) the error related to the iterative solution of system (27), and
- (iii) the error due to the use of the numerical inversion of the Laplace transform.

Error (i) can be effectively controlled by using an appropriate number M_k of Fourier terms for the approximations of the displacements and tractions at k -th circular boundary. The value of M_k for this boundary must be determined in the numerical solution process; it depends mostly on the geometry of the problem, and the following procedure is suggested for evaluating it. First, system (27) is solved for

time 0 to find the instantaneous, “elastic” Fourier coefficients. These coefficients are then substituted in the original equation (6), and the normalized difference ε between the left-hand side and the right-hand side of the equation is compared with the predefined accuracy parameter $\varepsilon_{\text{spec}}$. If ε exceeds $\varepsilon_{\text{spec}}$, the number of Fourier terms is increased. The iterations stop when the specified accuracy level is achieved for every circular boundary. The procedure is described in detail in [Mogilevskaya and Crouch 2001].

Error (ii) can be easily controlled by comparing the solution obtained at a current step of iteration with the solution from the previous step. The iterations in the Gauss–Seidel algorithm proceed until the desired degree of accuracy is achieved. In most cases considered in the present work, no more than 30–50 iterations are required for an accuracy around 10^{-8} .

Error (iii) for the Stehfest algorithm of the inversion cannot be controlled automatically, but several indirect means to control it are available:

- The stresses at the boundary of the half-plane obtained numerically by using the present approach can be compared with the prescribed boundary conditions.
- For several linear viscoelastic models (for example, standard solid and Burgers models), the instantaneous ($t = 0$) or large ($t \rightarrow \infty$) time response is the same as for the elastic model. Thus, one can compare the solution obtained by the present approach with the solution of the corresponding elastic problem, which sometimes can be found analytically.
- For the problem of an infinite or semi-infinite perforated viscoelastic plane subjected to constant loading, the stresses in the matrix do not depend on time and are exactly the same as those for the corresponding elastic problem [Huang et al. 2006b; Pyatigorets et al. 2008]. Thus, one may consider the problem in which the inhomogeneities have very small shear moduli so they can simulate the holes in the numerical analysis. The stresses obtained from the solution of this problem should be the same or very close to the stresses obtained from the corresponding elastic problem.
- The viscoelastic stresses, displacements, and strains obtained using the present approach should be consistent with each other. For example, the strains at any time moment can be obtained via transformed Kolosov–Muskhelishvili potentials; see (11) and (12). At the same time, it is easy to find the horizontal strains along a horizontal path or the vertical strains along a vertical path by numerically differentiating the corresponding displacements. In addition, the time-dependent strains inside the elastic inhomogeneities can be found from the stresses by using Hooke’s law. The strains found by using both approaches should be in good agreement with each other.
- The comparison of the selected examples with the finite element analysis can provide an idea about the accuracy of the method and the accuracy of the inverse Laplace transform depending on the number of terms in (34).

An extensive study of the accuracy of the numerical inverse Laplace transform was conducted using the means listed above. It was found that for the case of constant loading and for the constitutive models presented in the next section, the best accuracy is achieved when N_{St} ranges from 8 to 10. However, a smaller number of terms in the Stehfest algorithm should be used ($N_{\text{St}} = 4$ to 6) for the calculation of the stresses near the singular points (where the stresses may be subjected to rapid variations). In such cases, the use of a large number N_{St} may cause the sum in (34) to diverge [Stehfest 1970; Cheng et al. 1994]. This effect is usually observed at small times only, and the error introduced by the reduction of the number of terms in (34) is relatively small. See Section 5.1 for some details.

Time-dependent loading is not considered in the present work. For this case the Stehfest algorithm does not provide accurate results. However, the method described in the present paper is not restricted by the use of any particular procedure in the numerical inversion of the Laplace transform.

5. Examples

Two constitutive models for the material matrix are considered in the following numerical examples. The condition of plane strain is assumed hereafter.

For model I it is assumed that the material of the matrix responds as a standard solid (Boltzmann viscoelastic model) in shear (Figure 2, left), and elastically in bulk. Such behavior is quite realistic as the shear modulus for many polymeric solids relaxes much more than its bulk modulus. The constitutive equations for the model are

$$\frac{E_1 + E_2}{E_1} \sigma_{ij}(t) + \frac{\eta}{E_1} \dot{\sigma}_{ij}(t) = 2E_2 \varepsilon_{ij}(t) + 2\eta \dot{\varepsilon}_{ij}(t), \quad i \neq j \quad \text{and} \quad \sigma_{kk}(t) = 3K \varepsilon_{kk}(t), \quad (36)$$

where σ_{ij} and ε_{ij} , $i \neq j$, are the deviatoric stress and strain, σ_{kk} and ε_{kk} are the volumetric stress and strain, E_1 and E_2 are the elastic moduli of the springs (Figure 2, left), η is the viscosity of the dashpot, K is bulk modulus, and the dot denotes the time derivative. The s -varying analogs of the shear modulus and Kolosov–Muskhelishvili constant are obtained from the procedure described by Wang and Crouch [1982]. They are

$$\hat{\mu}(s) = \frac{E_1(E_2 + \eta s)}{E_1 + E_2 + \eta s}, \quad \hat{\kappa}(s) = 1 + \frac{6E_1(E_2 + \eta s)}{E_1(E_2 + \eta s) + 3K(E_1 + E_2 + \eta s)}. \quad (37)$$

For the sake of simplicity, the following values for the material parameters of the viscoelastic matrix are used for all the examples described by the first constitutive model:

$$E_1 = 8 \times 10^3 \sigma_0, \quad E_2 = 2 \times 10^3 \sigma_0, \quad \eta = 5 \times 10^3 \sigma_0 \cdot \text{sec}, \quad K = 17333.3 \sigma_0. \quad (38)$$

The constant σ_0 serves to normalize all the loads and stresses. All elastic moduli can also be expressed via this parameter.

Model II assumes that the bulk material of the viscoelastic matrix behaves according to Burgers model (Figure 2, right) in shear and elastically in bulk. The constitutive equations for this model are

$$\ddot{\sigma}_{ij}(t) + \left(\frac{E_1}{\eta_1} + \frac{E_1}{\eta_2} + \frac{E_2}{\eta_2} \right) \dot{\sigma}_{ij}(t) + \frac{E_1 E_2}{\eta_1 \eta_2} \sigma_{ij}(t) = 2E_2 \ddot{\varepsilon}_{ij}(t) + 2 \frac{E_1 E_2}{\eta_2} \dot{\varepsilon}_{ij}(t), \quad i \neq j, \quad (39)$$

$$\sigma_{kk}(t) = 3K \varepsilon_{kk}(t).$$

Figure 2, right, explains the meanings of the parameters involved in (39). The expressions for the s -varying shear modulus and the Kolosov–Muskhelishvili parameter can be obtained after applying the

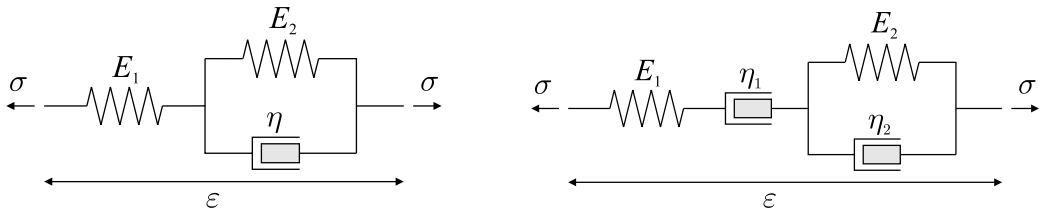


Figure 2. Left: the Boltzmann model. Right: the Burgers model.

Laplace transform to expressions (39). They are

$$\hat{\mu}(s) = \frac{E_1 s \left(s + \frac{E_2}{\eta_2} \right)}{s^2 + s \left(\frac{E_1}{\eta_1} + \frac{E_1}{\eta_2} + \frac{E_2}{\eta_2} \right) + \frac{E_1 E_2}{\eta_1 \eta_2}},$$

$$\hat{\kappa}(s) = 1 + \frac{6E_1 s \left(s + \frac{E_2}{\eta_2} \right)}{E_1 s^2 + \frac{E_1 E_2}{\eta_2} s + 3K \left[s^2 + s \left(\frac{E_1}{\eta_1} + \frac{E_1}{\eta_2} + \frac{E_2}{\eta_2} \right) + \frac{E_1 E_2}{\eta_1 \eta_2} \right]}.$$
(40)

The parameters of the springs and the bulk modulus are taken to be the same as for the first model, and the viscosities of the dashpots are $\eta_1 = 7 \times 10^3 \sigma_0 \cdot \text{sec}$ and $\eta_2 = \eta$; see (38).

It is worth noting that the Poisson's ratio $\nu(t)$ of the viscoelastic matrix is time-dependent for both constitutive models.

In all the examples presented below it is assumed that the loads applied to the boundaries of half-plane do not vary in time. Thus, the functions in (1) are taken as $f_\infty(t) = 1$, $f_p(t) = 1$, $f_F(t) = 1$, the Laplace transform of which gives

$$\hat{f}_\infty(s) = \frac{1}{s}, \quad \hat{f}_p(s) = \frac{1}{s}, \quad \hat{f}_F(s) = \frac{1}{s}.$$
(41)

5.1. Verification with finite element software ANSYS (model I). Consider the problem of a viscoelastic half-plane containing two holes and one rigid inhomogeneity as shown in Figure 3. The problem is solved using the present approach and the finite element software ANSYS.

A rectangular domain of size $600R_1 \times 500R_1$ (width \times height) is used for the finite element analysis. In order to achieve a high degree of accuracy, the rigid disc is meshed with approximately 23100 quadrilateral 8-node elements, while 131400 elements of the same type are used for the viscoelastic matrix.

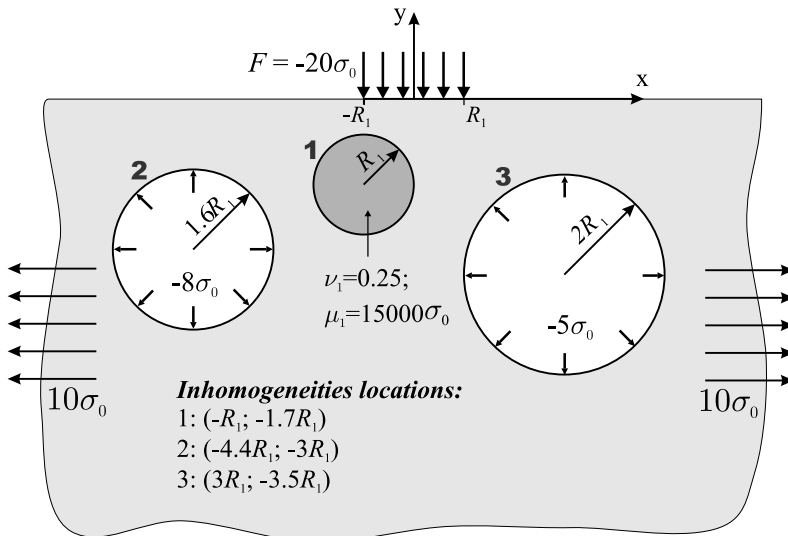


Figure 3. Problem geometry for Example 1.

The use of such a large number of elements is not dictated by any factor; possibly a smaller number of elements can be used to achieve satisfactory accuracy in the results (however, it was found that the use of a mesh with a total of about 35000 elements results in a significantly less accurate solution). The Prony series is adopted to approximate the relaxation of the shear modulus of the matrix. A time stepping algorithm is applied to obtain the time domain solution from the time $t = 0$ till time $t = 10$ sec with time step $\delta t = 0.5$ sec.

The stresses and strains obtained by both approaches can be compared directly. To compare the displacements it is necessary to introduce proper constraints in the finite element model and to constrain rigid body motion in the present approach. The procedure is described in detail in [Pyatigorets et al. 2008].

In the present method, the accuracy parameter $\varepsilon_{\text{spec}}$ is specified at the level $\varepsilon_{\text{spec}} = 10^{-5}$. The number of Fourier terms M_k used in the approximation of the boundary displacements is as follows:

	Left hole	Elastic disc	Right hole
$M_k =$	18	23	20

Using ten terms in sum (34) provides quite accurate results for the numerical Laplace inversion. The calculations with the present method take 8–10 seconds on a Dell computer workstation (Intel P4 3.6 GHz, 2 GB RAM), while the finite element calculations require about 7 hours at the same computer workstation (no special optimization technique is used).

Some illustrative examples are given in Figures 4–7. Figures 4 and 5 show very good agreement between the results for the displacements and strains calculated with both approaches. The graphs in Figures 4 and 5 are plotted for several time instances only (0, 8, and 10 sec), however, good agreement is found for all time moments for which the solution is found. The comparison of the time-dependent stresses, obtained by the present approach for two values of $N_{\text{St}} = 10$ and $N_{\text{St}} = 2$, with the results from the finite element analysis is illustrated in Figures 6 and 7. One can see that for $N_{\text{St}} = 10$, the stresses exhibit very good agreement with those obtained by ANSYS (see Figure 6). For the case of $N_{\text{St}} = 2$ some discrepancy in the results given in Figure 7 is observed at small time values only; at larger time the error reduces greatly. Similar behavior is observed for all the examples considered in the paper. As the discrepancy is sufficiently small it seems reasonable to use a smaller number of terms in the Stehfest algorithm when large N_{St} causes the sum (34) to diverge.

The same procedure was performed to compare the viscoelastic fields for the case of a point force and a force distributed over the whole boundary of the half-plane. The results for these cases also reveal good agreement with the results from the finite element analysis.

5.2. Example with a single inhomogeneity (model I). Consider a viscoelastic half-plane containing a single inhomogeneity. The material properties of the half-plane are described by constitutive model I. Four types of loading conditions are considered:

- (i) a far-field stress $\sigma^\infty = \sigma_0$ acting parallel to the boundary of the half-plane;
- (ii) a point force $F = -\sigma_0$ acting perpendicular to the boundary of the half-plane along the axis of symmetry;
- (iii) a force $F = -\sigma_0$ acting perpendicular to the boundary of the half-plane and distributed over the interval of length $2R$ whose center is located on the axis of symmetry;

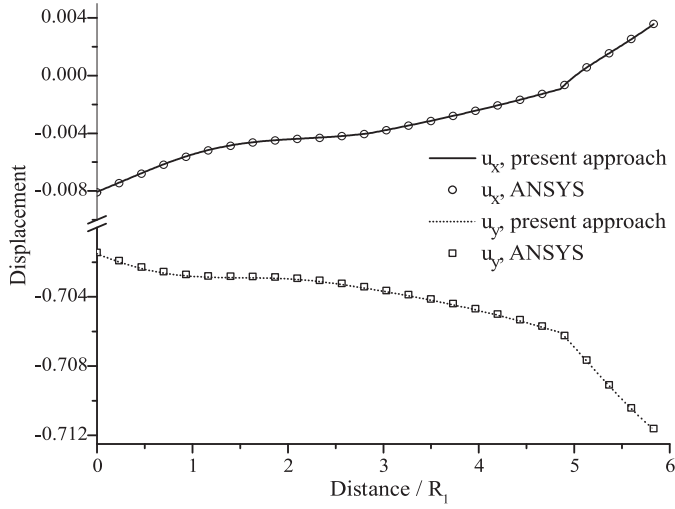


Figure 4. Variation of the displacements along the path $(-3R_1, -5R_1) \div (0, 0)$ at time $t = 8$ sec.

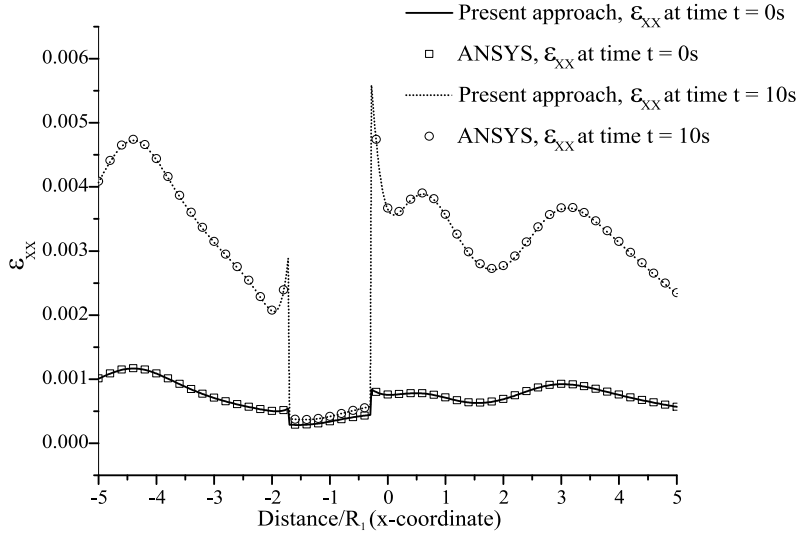


Figure 5. Variation of the horizontal strain along the path $(-5R_1, -R_1) \div (5R_1, -R_1)$.

(iv) a normal force $F = -\sigma_0$ uniformly distributed over the whole boundary of the half-plane.

In this example we study the influence of the shear modulus of the inhomogeneity on the hoop stress at point A (the closest point to the boundary of the half-plane that is located on the intersection of the boundary of the inhomogeneity and the axis of symmetry).

The Poisson's ratio of elastic inhomogeneity is set to $\nu = 0.35$, while the shear modulus is varied from $\mu_{\text{inh}} = 10^{-3}\sigma_0$ to $\mu_{\text{inh}} = 8 \cdot 10^5\sigma_0$. It is convenient to normalize μ_{inh} by the instantaneous shear modulus of the viscoelastic matrix $\mu|_{t=0} = 8000\sigma_0$. This value is equal to the elastic modulus E_1 in constitutive model I, as the dashpot does not exhibit instantaneous deformation (see [Figure 2](#), left). Ten terms are

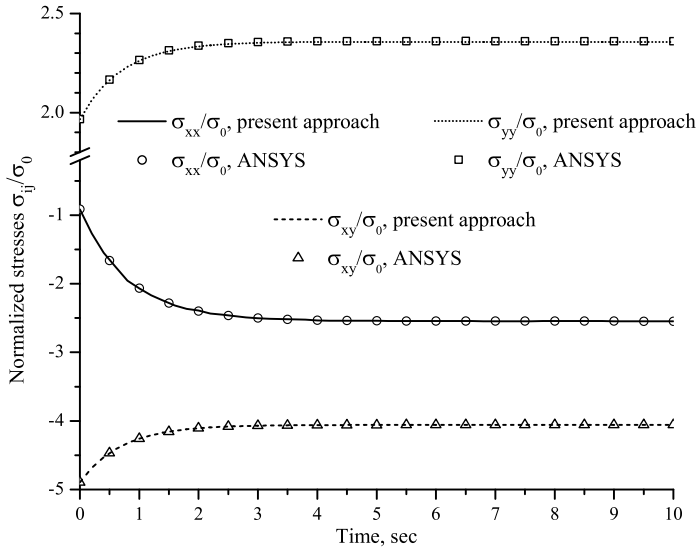


Figure 6. Variation of the normalized stresses at the point $(-2.28R_1, -2.3R_1)$ located inside the viscoelastic matrix ($N_{St} = 10$).

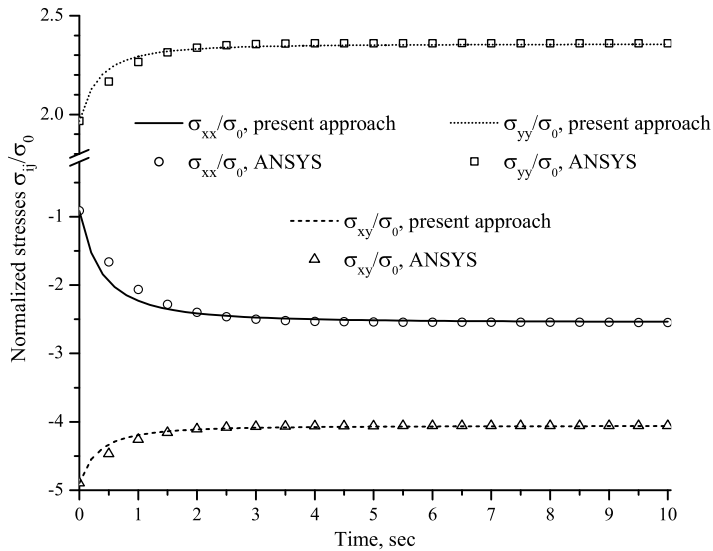


Figure 7. Variation of the normalized stresses at the point $(-2.28R_1, -2.3R_1)$ located in the viscoelastic matrix ($N_{St} = 2$).

used in the procedure of numerical inversion of the Laplace transform, (34), and the number of Fourier terms M_k required to achieve the accuracy level $\varepsilon_{spec} = 10^{-5}$ is the following:

Type of load	Far-field stress	Concentrated force	Force over a segment	Force over the boundary
M_k	37	209	34	22

The fact that the hoop stress at point A is equal to the stress $\sigma_{xx}(t)$ allows for additional verification of the method and the computer code. Consider the case when the shear modulus of the inhomogeneity is close to zero and far-field stress is applied parallel to the boundary of the half-plane. For the inhomogeneity located far away from the boundary of the half-plane, the stresses in the vicinity of the inhomogeneity will not be affected by that boundary and will be the same as in the case of a full plane. In addition, the stresses for this case do not depend on time, and are exactly the same as the stresses in the corresponding “elastic” problem: $\sigma_{xx}/\sigma^\infty = 3$. The hoop stress found by the present method for $\mu_{\text{inh}} = 10^{-3}\sigma_0$ and $z_{\text{center}} = (0, -2000R)$ agrees with the elastic solution up to 6 significant digits for any moment in time.

The variation of hoop stress at point A versus the shear modulus of the inhomogeneity is shown in Figures 8–11 for all types of loading. The plots reveal that the hoop stresses vary greatly with the variation of the shear modulus of the inhomogeneity. However, in all four cases, the hoop stresses exhibit an asymptotic behavior when $\mu_{\text{inh}}/\mu \rightarrow 0$ (the case of a hole) or $\mu_{\text{inh}}/\mu \rightarrow \infty$ (the case of a stiff inhomogeneity). In case (i), the hoop stress is tensile (Figure 8), while in case (iv) it is compressive (Figure 11). The hoop stress changes sign for two remaining cases of loading (Figures 9 and 10).

The hoop stress at point A depends greatly on the separation distance between the inhomogeneity and the boundary of the half-plane. The investigation of this dependency for the case of a hole located in a viscoelastic half-plane is given in [Pyatigorets et al. 2008]. It is interesting to compare the results obtained by the present approach with the results presented in the latter paper. It has been found that the hoop stresses obtained by the present method for $\mu_{\text{inh}} = 10^{-3}\sigma_0$ match with the results provided by Pyatigorets et al. [2008] up to the third decimal number for any moment in time.

5.3. Example with two inhomogeneities (model II). Two inhomogeneities with different elastic properties are considered in this example. The geometry of the problem is shown in Figure 12. Both inhomogeneities have the same radii R and their centers are located on the same horizontal line $y = -1.4R$.

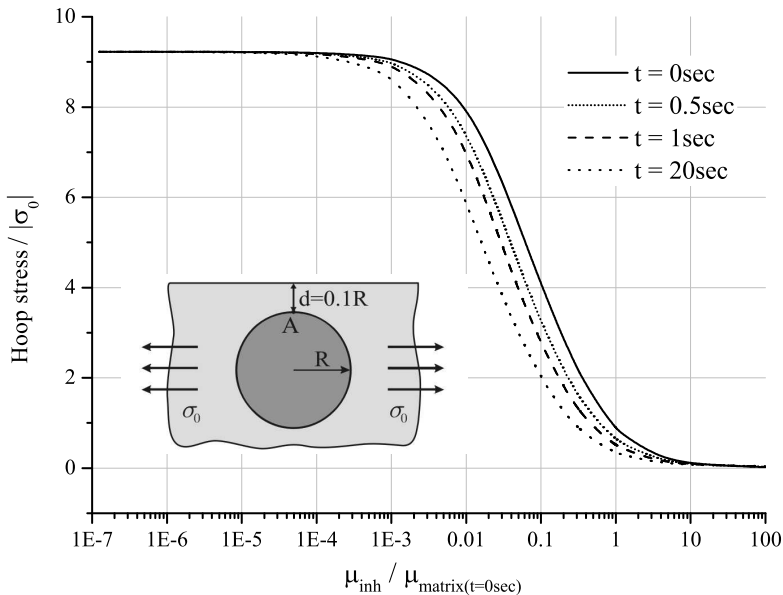


Figure 8. Variation of the normalized hoop stress at point A for loading case (i).

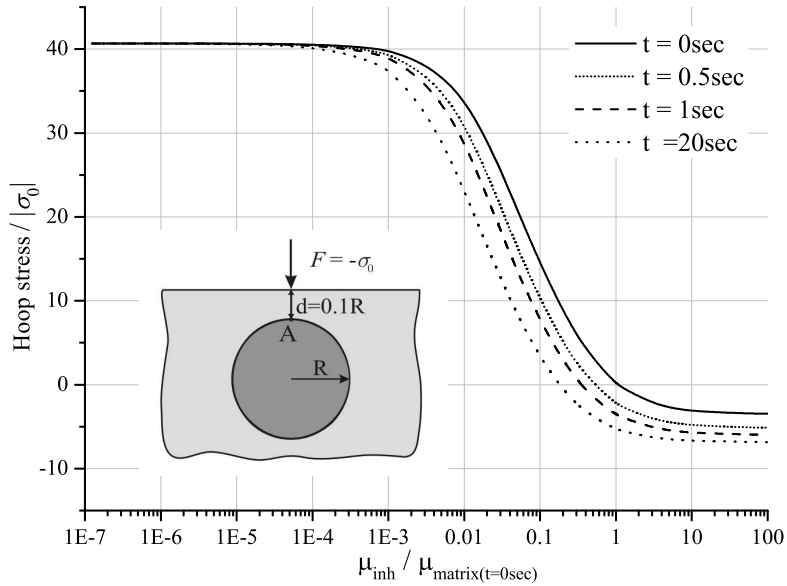


Figure 9. Variation of the normalized hoop stress at point A for loading case (ii).

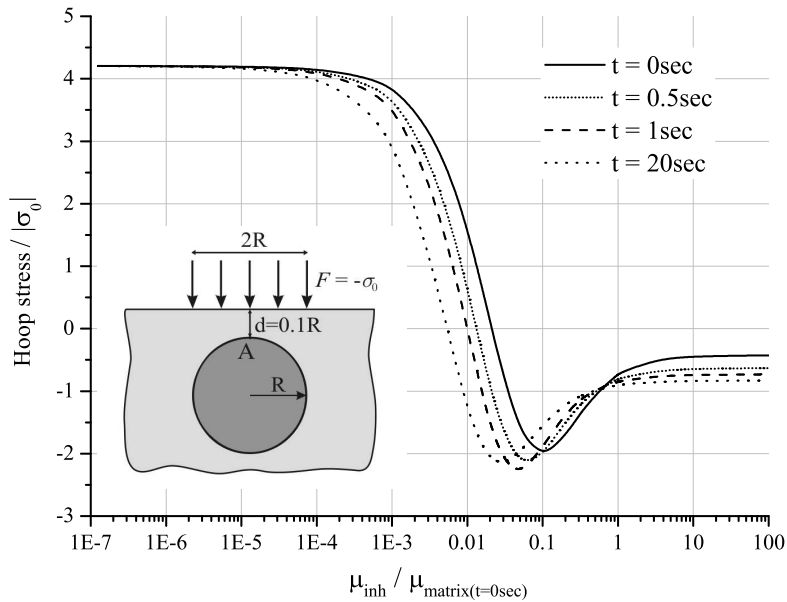


Figure 10. Variation of the normalized hoop stress at point A for loading case (iii).

The separation distance between the inhomogeneities is $0.4R$. The far-field stress σ_0 acts parallel to the boundary of the half-plane. The bulk material of the half-plane behaves according to constitutive model II. The properties of the elastic inhomogeneities are as follows:

- Left inhomogeneity: $\nu = 0.35$, $\mu = 32000\sigma_0$ (very rigid inhomogeneity);
- Right inhomogeneity: $\nu = 0.35$, $\mu = 400\sigma_0$ (very soft inhomogeneity).

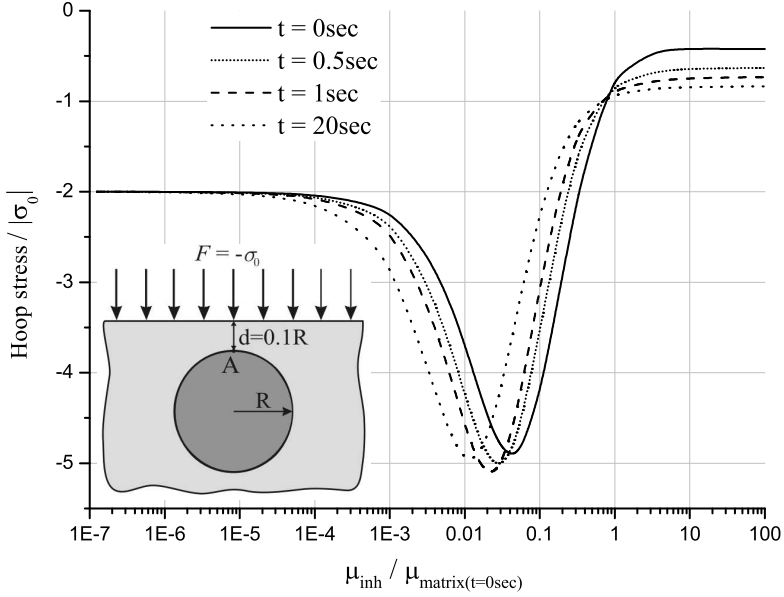


Figure 11. Variation of the normalized hoop stress at point A for loading case (iv).

The distribution of maximum shear stresses is found for different moments in time. The maximum shear stress at a point is given by the expression

$$\tau_{\max}(z, t) = \frac{1}{2}(\sigma_1(z, t) - \sigma_2(z, t)),$$

where $\sigma_1(z, t)$ is the major in-plane principal stress and $\sigma_2(z, t)$ is the minor in-plane principal stress. The location of maximum shear stress can provide valuable information about the initiation and propagation of cracks.

The accuracy parameter $\varepsilon_{\text{spec}}$ is set to 10^{-5} . To achieve this accuracy 51 terms in Fourier series ($M_k = 25$) are required for each inhomogeneity. The number of terms N_{St} used in the algorithm for the numerical inverse Laplace transform is set to 8. It was found that when one uses 10 terms in approximation (34), the results of the approximation begin to diverge at certain points of the space domain. For additional verification of the results obtained in this example a finite element model was built. The solution found using our approach (for $N_{\text{St}} = 8$) shows very good agreement with the one obtained via finite elements.

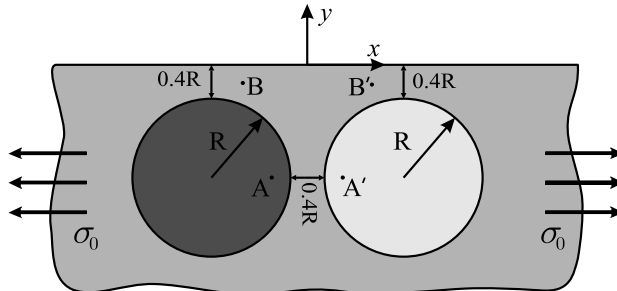


Figure 12. Problem geometry for Example 3.

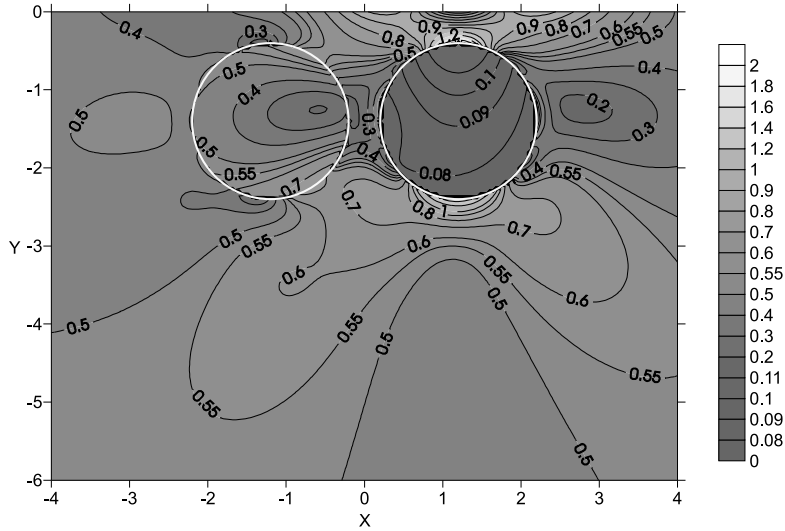


Figure 13. Contours of $\tau_{\max}(z, t)/\sigma_0$ at time $t = 0$ sec.

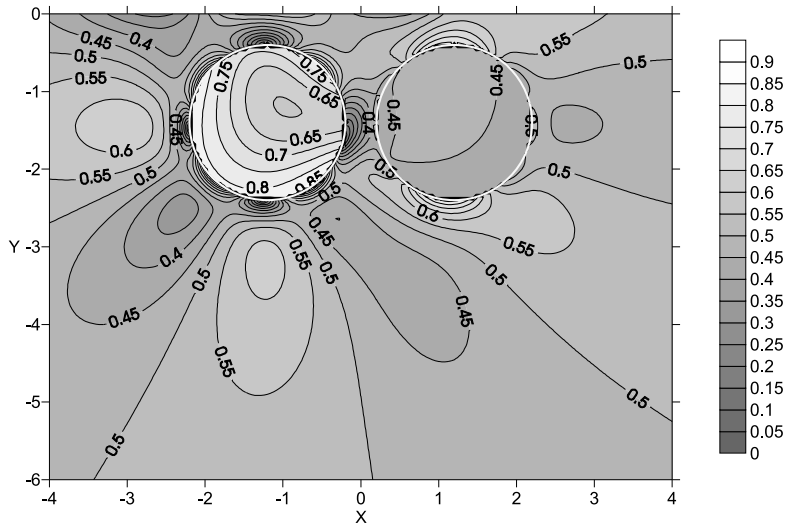


Figure 14. Contours of $\tau_{\max}(z, t)/\sigma_0$ at time $t = 5$ sec.

The contour plots of $\tau_{\max}(z, t)/\sigma_0$ are given in the next three figures for three moments in time: $t = 0$ sec, $t = 5$ sec, and $t = 300$ sec. At the start (Figure 13), the highest shear stress concentration is seen to be localized between the soft inhomogeneity and the boundary of the half-plane. At the same time the stresses inside the inhomogeneity are much lower than in the surrounding bulk material. These results are expected as the distribution of stresses is similar to the one observed for the problem of the perforated half-plane. The stresses inside the stiff inhomogeneity are about the same magnitude as in the surrounding matrix. The next snapshot (Figure 14) reveals that stresses inside the inhomogeneities increase rapidly approaching the magnitude of the far-field stress σ_0 inside the stiff inhomogeneity. The distribution of the stresses in the matrix also changes considerably, but the maximum magnitude of τ_{\max}

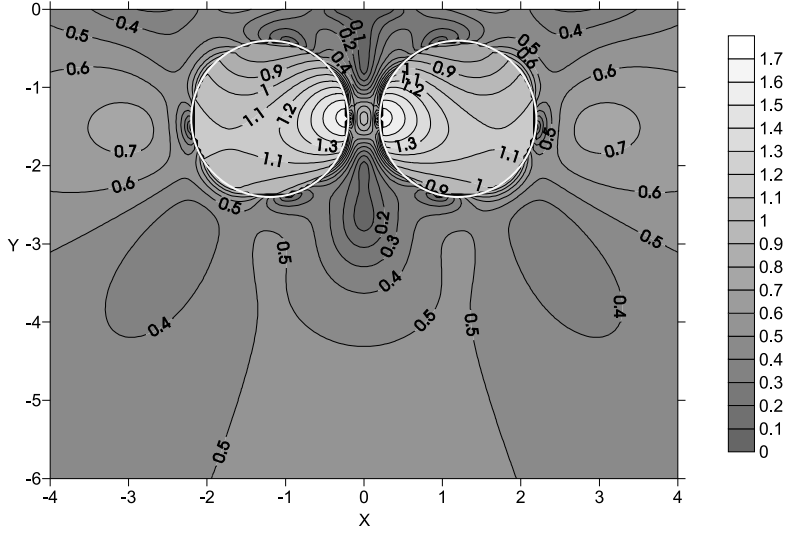


Figure 15. Contours of $\tau_{\max}(z, t)/\sigma_0$ at time $t = 300$ sec.

decreases from the level of $2\sigma_0$ to the level of σ_0 . The distribution of stresses at large times (exemplified by Figure 15) becomes symmetric relative to the line $x = 0$. At time $t = 300$ sec the magnitude of the maximum shear stress almost reaches the level of $2\sigma_0$ again, but the maximum stresses are localized inside the inhomogeneities.

The symmetric distribution of maximum shear stresses observed at large times (despite the fact that the material properties of the inhomogeneities are very different) allows one to suggest that for the case of constitutive model II and constant loading, the stresses at large times do not depend on the material properties of the viscoelastic matrix and elastic inhomogeneities. To support this conclusion, stress components are found at a number of points inside the half-plane for several different sets of material properties of the matrix and inhomogeneities. The illustrative results for the case of vertical stress σ_{yy} are presented in Figures 16 and 17. The first set of material properties corresponds to that stated above in the current example. The second set is

$$\begin{aligned}
 E_1 &= 1000\sigma_0, & E_2 &= 6000\sigma_0, & \eta_1 &= 3000\sigma_0 \cdot \text{sec}, & \eta_2 &= 9000\sigma_0 \cdot \text{sec}, & K &= 24999\sigma_0, \\
 \text{Left inhomogeneity:} & & \nu &= 0.4, & \mu &= 1200\sigma_0, \\
 \text{Right inhomogeneity:} & & \nu &= 0.2, & \mu &= 16000\sigma_0.
 \end{aligned}$$

The stresses are found at the points $A = (-0.4R, -1.4R)$ and $A' = (0.4R, -1.4R)$ located inside the left and right inhomogeneities, respectively, and at the points $B = (-0.8R, -0.2R)$ and $B' = (0.8R, -0.2R)$ located inside the matrix. The results, presented in Figures 16 and 17, reveal that the stresses at large times, indeed, do not depend on the material properties, although they depend on the geometry of the problem and on the loading, meaning stresses are statically determined. Similar behavior of stresses is observed for other types of loading considered in the present paper. As a hole can be treated as inhomogeneity with zero elastic properties the same conclusion can be made for the case of more complicated geometries including multiple holes and elastic inhomogeneities. We emphasize that the strains and

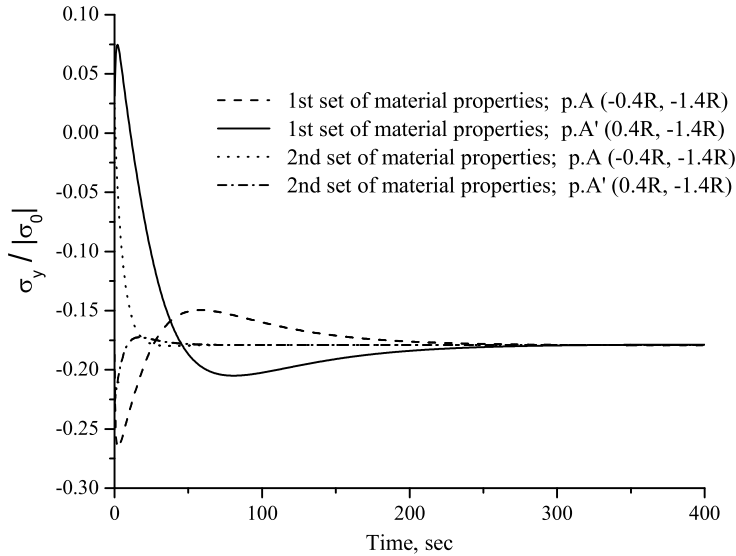


Figure 16. Variation of the normalized vertical stress at points A and A'.

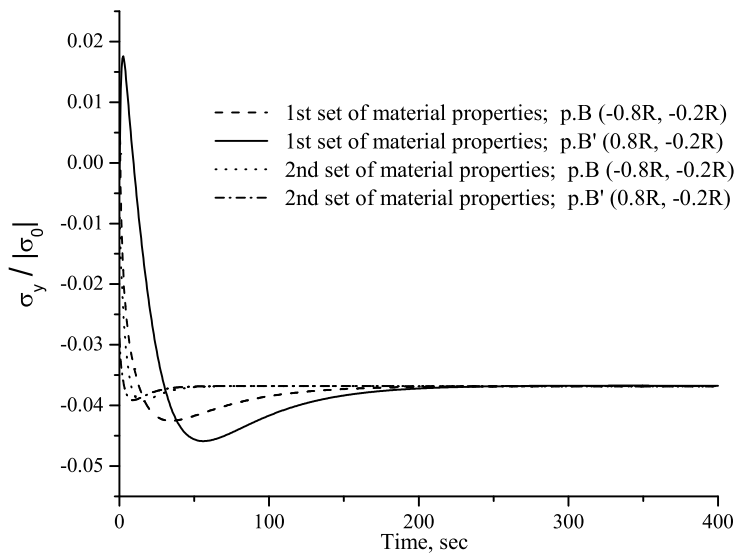


Figure 17. Variation of the normalized vertical stress at points B and B'.

displacements depend on the material properties even when time is large. These results are supported by the results from the finite element analysis.

Note that the numerical analysis for the case when the viscoelastic matrix is described by constitutive model I reveals that the stresses do not exhibit asymptotic behavior at large times. It is the viscous flow introduced by the combination of dashpots in the Burger model that is responsible for the steady solution at large times.

5.4. Asymptotic behavior at large times (model II). In some cases, it is possible to find analytically the behavior of the time-dependent stresses at large times. To illustrate this, we consider the case of a single inhomogeneity in the full plane. For this problem system (6) reduces to the single equation

$$\begin{aligned}
& -2 \int_L \frac{\hat{u}^h(\tau; s)}{(\tau - \xi)^2} d\tau + \int_L \hat{u}^h(\tau; s) \frac{\partial^2 K_1(\tau, \xi)}{\partial \tau \partial \xi} d\tau + \int_L \overline{\hat{u}^h(\tau; s)} \frac{\partial^2 K_2(\tau, \xi)}{\partial \bar{\tau} \partial \bar{\xi}} d\bar{\tau} \\
& + \frac{\hat{\kappa}(s)}{2\hat{\mu}(s)} \left[\int_L \hat{\sigma}^h(\tau; s) \frac{\partial K_1(\tau, \xi)}{\partial \xi} d\tau - \int_L \overline{\hat{\sigma}^h(\tau; s)} \frac{\partial K_2(\tau, \xi)}{\partial \bar{\xi}} d\bar{\tau} \right] \\
& + \frac{\hat{\kappa}(s) - 1}{2\hat{\mu}(s)} \int_L \frac{\hat{\sigma}^h(\tau; s)}{\tau - \xi} d\tau + \pi i \frac{\hat{\kappa}(s) + 1}{2\hat{\mu}(s)} \hat{\sigma}^h(\xi; s) = 2\pi i \frac{\hat{\kappa}(s) + 1}{4\hat{\mu}(s)} (1 + g^2(\xi)) \hat{\sigma}^\infty(s), \quad (42)
\end{aligned}$$

where L is the boundary of the hole occupied by the inhomogeneity. As there are only two terms $g^0(\xi) \equiv 1$ and $g^2(\xi)$ on the right-hand side of Equation (42), the only nonzero Fourier coefficients $\hat{B}_m(s)$ present in approximations (19) are $\hat{B}_{-1}(s)$ and $\hat{B}_1(s)$. These coefficients are found from the solution of (42) and can be expressed as

$$\hat{B}_{-1}(s) = \frac{\hat{\sigma}^\infty(s)}{4} \frac{\hat{\kappa}(s) + 1}{\hat{\mu}(s) + \hat{\kappa}(s)\mu_d} R, \quad \text{Re } \hat{B}_1(s) = \frac{\hat{\sigma}^\infty(s)}{8} \frac{\hat{\kappa}(s) + 1}{\hat{\mu}(s) + 2\mu_d/(\kappa_d - 1)} R, \quad (43)$$

where R is the radius of the inhomogeneity, and μ_d and κ_d are its shear modulus and Kolosov–Muskhelishvili parameter, respectively.

As an illustration, we investigate the behavior of the Kolosov–Muskhelishvili potential $\varphi(z, t)$ at $t \rightarrow \infty$. It follows from (15) that

$$\begin{aligned}
\hat{\varphi}(z, s) &= -\frac{\mu_d - \hat{\mu}(s)}{\hat{\mu}(s) + \hat{\kappa}(s)\mu_d} \frac{R^2}{z - z_c} \frac{\hat{\sigma}^\infty(s)}{2} + \frac{\hat{\sigma}^\infty(s)}{4} z, \quad z \in \text{matrix}, \\
\hat{\varphi}(z, s) &= \frac{\mu_d}{\kappa_d - 1} \frac{\hat{\kappa}(s) + 1}{\hat{\mu}(s) + 2\mu_d/(\kappa_d - 1)} (z - z_c) \frac{\hat{\sigma}^\infty(s)}{4}, \quad z \in \text{elastic disc},
\end{aligned} \quad (44)$$

where z_c is the complex coordinate of the center of the inhomogeneity.

The behavior of the potential in the time domain at the time $t \rightarrow \infty$ corresponds to the behavior of its Laplace transform at $s \rightarrow 0$. Equations (40) give

$$\hat{\mu}(s) \rightarrow 0, \quad \hat{\kappa}(s) \rightarrow 1 \quad \text{when } s \rightarrow 0. \quad (45)$$

Using (44) and (45) and not accounting for the behavior of $\hat{\sigma}_{xx}^\infty(s)$ at $s \rightarrow 0$ (this quantity should be transformed back in the time domain), we get

$$\begin{aligned}
\hat{\varphi}(z, s) &= \frac{\hat{\sigma}^\infty(s)}{4} \left[z - \frac{2R^2}{z - z_c} \right], \quad z \in \text{matrix}, \quad s \rightarrow 0, \\
\hat{\varphi}(z, s) &= (z - z_c) \frac{\hat{\sigma}^\infty(s)}{4}, \quad z \in \text{elastic disc}, \quad s \rightarrow 0.
\end{aligned} \quad (46)$$

Angle, deg	$t = 0$ sec	$t = 5$ sec	$t = 500$ sec	Equation (47)
Circular contour located inside the matrix ($r = 1.1R$)				
0	1.359325	2.511734	2.652893	2.652893
15	1.311184	2.3092	2.431448	2.431447
30	1.179662	1.755867	1.826447	1.826446
45	0.99999999	1.00000011	1.00000012	1
60	0.820338	0.244133	0.173554	0.173554
75	0.688816	-0.3092	-0.431447	-0.431447
90	0.640676	-0.511733	-0.652893	-0.652893
Circular contour located inside the inhomogeneity ($r = 0.8R$)				
0-360	1.076923	1.006881	1.00000006	1

Table 1. The values of $\sigma_{xx}(z) + \sigma_{yy}(z)$ found numerically and from (47).

Finally using (11) and (46) one arrives at

$$\sigma_{xx}(z) + \sigma_{yy}(z) = \sigma^\infty \left[1 + 2 \operatorname{Re} \left(\frac{R}{z - z_c} \right)^2 \right], \quad z \in \text{matrix}, \quad t \rightarrow \infty, \quad (47)$$

$$\sigma_{xx}(z) + \sigma_{yy}(z) = \sigma^\infty, \quad z \in \text{elastic disc}, \quad t \rightarrow \infty.$$

It follows from expressions (47) that, at large times, the sum of the horizontal and vertical stresses inside the inhomogeneity is constant and equal to the value of the far-field stress. The results given by (47) can be used as the benchmark solution. Consider a single inhomogeneity located far from the boundary of the viscoelastic half-plane subjected to far-field stress σ^∞ . Let $R = 1$ and $z_c = (5R, -2000R)$. We assume that the viscoelastic matrix obeys constitutive model II, $\nu_d = 0.2$, and $\mu_d = 16000\sigma^\infty$. Table 1 shows the results for the combination $\sigma_{xx}(z) + \sigma_{yy}(z)$ calculated at several points located on two circular contours cocentrical with the boundary of the inhomogeneity. The first contour is located inside the inhomogeneity and its radius is $r = 0.8R$; the radius of the contour located outside the inhomogeneity is $r = 1.1R$. For both contours the angle is defined similarly to the angle shown in Figure 1b. Due to the symmetry of the problem the values of $\sigma_{xx}(z) + \sigma_{yy}(z)$ are given for the first quarter of the complex plane only. As one can see from Table 1, the combination $\sigma_{xx}(z) + \sigma_{yy}(z)$ tends to the results prescribed by (47) when time is sufficiently large.

6. Conclusion

We have shown that the proposed method of solution of the problem of a semi-infinite, isotropic, linear viscoelastic half-plane containing multiple, nonoverlapping circular inhomogeneities is efficient and accurate. As the upper boundary of the half-plane may be subjected to different loading conditions, the method can be successfully used in the modeling of indentation processes.

An important feature of the algorithm is that most of the derivation, including space integration and the Laplace transform, is performed analytically. In the case of the perforated half-plane, when the method reduces to the one presented in [Pyatigorets et al. 2008], the inversion of the Laplace transform can be

also performed analytically. However, in the general case of the inhomogeneities, it has to be performed numerically.

An algorithm for numerical inversion of the Laplace transform proposed by Stehfest is used in the present work. It is found that for the case of constant boundary conditions and for the constitutive models presented in the paper, the algorithm provides accurate results. The results of the numerical simulations indicate that the Stehfest algorithm does not provide accurate results for those problems where time-dependent boundary conditions are prescribed. However, the method described in the present paper is not restricted by the use of any particular procedure for the numerical inversion of the Laplace transform.

The major advantage of the algorithm is its time efficiency: problems containing large arrays of inhomogeneities (tens/hundreds) can be accurately solved in a relatively small time on a standard single-processor PC (seconds or minutes if the solution is found at a few spatial points and several hours if the number of points is tens or hundreds of thousands). The calculation of viscoelastic fields can be effectively parallelized on multiprocessor/multicore machines. A multithreading architecture is implemented in the current version of the computer code that allows one to additionally speed up calculations on multiprocessor machines. The present method allows one to easily modify constitutive viscoelastic models in the computer code if the expressions for the transformed shear modulus and the Kolosov–Muskhelishvili parameter are known.

Several numerical examples are considered in the paper. Interesting results are obtained from the study of the hoop stress at a point on the boundary of a single inhomogeneity located in the vicinity of the boundary of the half-plane. The study reveals that the hoop stress greatly depends on the material properties of the inhomogeneity and can be tensile or compressive depending on the time moment and shear modulus of the inhomogeneity. The results obtained for constitutive model II (Example 3) show that the state of the stresses is statically determined at large times, with an asymptotic behavior as $t \rightarrow \infty$ determined only by the geometry of the problem. Nevertheless, the value of t when the stresses approach the asymptotic behavior depends on the material parameters.

One of the future developments of the approach may include the consideration of imperfect interfaces between the inhomogeneities and the matrix. Cracks or inhomogeneities of more general geometry can also be incorporated, although the method would have to employ the boundary element technique.

Appendix A

The operator $\hat{\Lambda}_{kk}$ is the Laplace transform of the corresponding operator presented in [Dejoie et al. 2006]:

$$\hat{\Lambda}_{kk}(\xi; s) = -\frac{1}{R_k} \left\{ 2 \operatorname{Re} \hat{B}_{1k} + \sum_{m=1}^{M_k-1} m \hat{B}_{-mk} g_k^{m+1}(\xi) + \sum_{m=2}^{M_k+1} \hat{B}_{mk} g_k^{1-m}(\xi) \right\}. \quad (\text{A.1})$$

The operator \hat{G}_{kk} is given by

$$\begin{aligned} \hat{G}_{kk}(\xi; s) &= \frac{1}{R_k} \left\{ 2 \left(\frac{\mu_k}{\kappa_k - 1} \frac{\hat{\kappa} - 1}{\hat{\mu}} - 1 \right) \operatorname{Re} \hat{B}_{1k} \right. \\ &\quad \left. + \left(\frac{\mu_k}{\hat{\mu}} - 1 \right) \sum_{m=1}^{M_k-1} m \hat{B}_{-mk} g_k^{m+1}(\xi) + \left(\frac{\mu_k}{\kappa_k} \frac{\hat{\kappa}}{\hat{\mu}} - 1 \right) \sum_{m=2}^{M_k+1} \hat{B}_{mk} g_k^{1-m}(\xi) \right\} \\ &= -\frac{1}{R_k} \left\{ 2 \hat{\alpha}_{2k} \operatorname{Re} \hat{B}_{1k} + \hat{\alpha}_{1k} \sum_{m=1}^{M_k-1} m \hat{B}_{-mk} g_k^{m+1}(\xi) + \hat{\alpha}_{3k} \sum_{m=2}^{M_k+1} \hat{B}_{mk} g_k^{1-m}(\xi) \right\}. \quad (\text{A.2}) \end{aligned}$$

Expression (A.2) differs from (A.1) by the presence of additional terms in front of unknown Fourier coefficients \hat{B}_{-mk} , $\text{Re } \hat{B}_{1k}$, and \hat{B}_{mk} only. All other operators \hat{G}_{jk} can be obtained in a similar way from the corresponding expressions given in [Dejoie et al. 2006].

Appendix B

Potentials for the k-th elastic disc derived from (13):

$$\begin{aligned}\hat{\varphi}(z, s) &= \frac{2\mu_k}{\kappa_k - 1} \text{Re } \hat{B}_{1k} g_k^{-1}(z) + \frac{2\mu_k}{\kappa_k} \sum_{m=2}^{M_k+1} \hat{B}_{mk} g_k^{-m}(z) \\ &= \frac{2\mu_k}{\kappa_k - 1} \frac{1}{\hat{\alpha}_{2k}} \text{Re } \hat{\mathbb{B}}_{1k} g_k^{-1}(z) + \frac{2\mu_k}{\kappa_k} \frac{1}{\hat{\alpha}_{3k}} \sum_{m=2}^{M_k+1} \hat{\mathbb{B}}_{mk} g_k^{-m}(z),\end{aligned}\quad (\text{B.1})$$

$$\begin{aligned}\hat{\psi}(z, s) &= -\frac{2\mu_k}{\kappa_k - 1} \frac{\bar{z}_k}{R_k} \text{Re } \hat{B}_{1k} - \frac{2\mu_k}{\kappa_k} \left[\frac{\bar{z}_k}{R_k} + g_k(z) \right] \sum_{m=2}^{M_k+1} m \hat{B}_{mk} g_k^{-(m-1)}(z) - 2\mu_k \sum_{m=1}^{M_k-1} \hat{B}_{-mk} g_k^{-m}(z) \\ &= -\frac{2\mu_k}{\kappa_k - 1} \frac{\bar{z}_k}{\hat{\alpha}_{2k} R_k} \text{Re } \hat{\mathbb{B}}_{1k} \\ &\quad - \frac{2\mu_k}{\hat{\alpha}_{3k} \kappa_k} \left[\frac{\bar{z}_k}{R_k} + g_k(z) \right] \sum_{m=2}^{M_k+1} m \hat{\mathbb{B}}_{mk} g_k^{-(m-1)}(z) - \frac{2\mu_k}{\hat{\alpha}_{1k}} \sum_{m=1}^{M_k-1} \hat{\mathbb{B}}_{-mk} g_k^{-m}(z).\end{aligned}\quad (\text{B.2})$$

Similar expressions are used in [Mogilevskaya et al. 2008] for the calculation of elastic potentials.

Potentials for the matrix derived from (15) and (16):

$$\hat{\varphi}_{\text{plane}}(z; s) = \frac{2\hat{\mu}}{\hat{\kappa} + 1} \sum_{k=1}^N \sum_{m=1}^{M_k-1} \hat{\mathbb{B}}_{-mk} g_k^m(z) + \frac{\hat{\sigma}^\infty(s)}{4} z, \quad (\text{B.3})$$

$$\begin{aligned}\hat{\psi}_{\text{plane}}(z; s) &= -\frac{\hat{\kappa} - 1}{\hat{\kappa} + 1} \sum_{k=1}^{N_h} \hat{p}_k R_k g_k(z) + \frac{2\hat{\mu}}{\hat{\kappa} + 1} \sum_{k=1}^N \left[-2 \text{Re } \hat{\mathbb{B}}_{1k} g_k(z) \right. \\ &\quad \left. + \sum_{m=1}^{M_k-1} m \hat{\mathbb{B}}_{-mk} g_k^{m+1}(z) \left(\frac{\bar{z}_k}{R_k} + g_k(z) \right) - \sum_{m=1}^{M_k+1} \hat{\mathbb{B}}_{mk} g_k^m(z) \right] - \frac{\hat{\sigma}^\infty(s)}{2} z,\end{aligned}\quad (\text{B.4})$$

$$\begin{aligned}\hat{\varphi}_{\text{aux}}(z; s) &= \frac{\hat{\kappa} - 1}{\hat{\kappa} + 1} \sum_{j=1}^{N_h} \hat{p}_j R_j h_j(z) + \frac{2\hat{\mu}}{\hat{\kappa} + 1} \sum_{j=1}^N \left[2 \text{Re } \hat{\mathbb{B}}_{1j} h_j(z) \right. \\ &\quad \left. + \sum_{m=1}^{M_j-1} m \hat{\mathbb{B}}_{-mj} h_j^{m+1}(z) (g_j^{-1}(z) - h_j(z)) + \sum_{m=2}^{M_j+1} \hat{\mathbb{B}}_{mj} h_j^m(z) \right],\end{aligned}\quad (\text{B.5})$$

$$\begin{aligned}\hat{\psi}_{\text{aux}}(z; s) &= \frac{\hat{\kappa} - 1}{\hat{\kappa} + 1} z \sum_{j=1}^{N_h} \hat{p}_j h_j^2(z) + \frac{2\hat{\mu}}{\hat{\kappa} + 1} \frac{z}{R_j} \sum_{j=1}^N \left\{ 2 \text{Re } \hat{\mathbb{B}}_{1j} h_j^2(z) + \sum_{m=2}^{M_j+1} m \hat{\mathbb{B}}_{mj} h_j^{m+1}(z) \right. \\ &\quad \left. - \sum_{m=1}^{M_j-1} m \hat{\mathbb{B}}_{-mj} h_j^{m+1}(z) \left[1 - (m+1) g_j^{-1}(z) h_j(z) + (m+2) h_j^2(z) + \frac{1}{m} \frac{R_j}{z} h_j^{-1}(z) \right] \right\},\end{aligned}\quad (\text{B.6})$$

where

$$h_j(z) = \frac{R_j}{z - \bar{z}_j}. \quad (\text{B.7})$$

The potentials $\hat{\varphi}_F(z; s)$ and $\hat{\psi}_F(z; s)$ are due to the use of Flamant's fundamental solution, and they do not depend on the displacements or stresses at the boundaries of the holes. The expressions for these potentials are given in [Pyatigorets et al. 2008].

References

- [Carini et al. 1991] A. Carini, M. Diligenti, and G. Maier, “Boundary integral equation analysis in linear viscoelasticity: variational and saddle point formulations”, *Comput. Mech.* **8**:2 (1991), 87–98.
- [Cheng et al. 1994] A. Cheng, P. Sidauruk, and Y. Abousleiman, “Approximate inversion of the Laplace transform”, *Math. J.* **4**:2 (1994), 76–82.
- [Davies and Martin 1979] B. Davies and B. Martin, “Numerical inversion of the Laplace transform: a survey and comparison of methods”, *J. Comput. Phys.* **33**:1 (1979), 1–32.
- [Dejoie et al. 2006] A. Dejoie, S. G. Mogilevskaya, and S. L. Crouch, “A boundary integral method for multiple circular holes in an elastic half-plane”, *Eng. Anal. Bound. Elem.* **30**:6 (2006), 450–464.
- [Findley et al. 1976] W. N. Findley, J. S. Lai, and K. Onaran, *Creep and relaxation of nonlinear viscoelastic materials*, North-Holland Series in Applied Mathematics and Mechanics **18**, North-Holland, Amsterdam, 1976. Reprinted Dover, New York, 1989.
- [Huang et al. 2005a] Y. Huang, S. L. Crouch, and S. G. Mogilevskaya, “A time domain direct boundary integral method for a viscoelastic plane with circular holes and elastic inclusions”, *Eng. Anal. Bound. Elem.* **29**:7 (2005), 725–737.
- [Huang et al. 2005b] Y. Huang, S. L. Crouch, and S. G. Mogilevskaya, “Direct boundary integral procedure for a Boltzmann viscoelastic plane with circular holes and elastic inclusions”, *Comput. Mech.* **37**:1 (2005), 110–118.
- [Huang et al. 2006a] Y. Huang, S. G. Mogilevskaya, and S. L. Crouch, “Complex variable boundary integral method for linear viscoelasticity, I: Basic formulation”, *Eng. Anal. Bound. Elem.* **30**:12 (2006), 1049–1056.
- [Huang et al. 2006b] Y. Huang, S. G. Mogilevskaya, and S. L. Crouch, “Semi-analytical solution for a viscoelastic plane containing multiple circular holes”, *J. Mech. Mater. Struct.* **1**:3 (2006), 471–501.
- [Kaloerov and Mironenko 2007] S. A. Kaloerov and A. B. Mironenko, “Analyzing the viscoelastic state of a plate with elliptic or linear elastic inclusions”, *Int. Appl. Mech.* **43**:2 (2007), 198–208.
- [Kaminskii et al. 2002] A. A. Kaminskii, N. I. Zatula, and V. N. Dyakon, “Investigation of the stress-strain state of viscoelastic piecewise-homogeneous bodies by the method of boundary integral equations”, *Mech. Compos. Mater.* **38**:3 (2002), 209–214.
- [Kumar 2000] U. Kumar, “Computer-aided numerical inversion of Laplace transform”, *Active and Passive Elec. Comp.* **22**:3 (2000), 189–213.
- [Kushch et al. 2006] V. I. Kushch, S. V. Shmegeera, and V. A. Buryachenko, “Elastic equilibrium of a half plane containing a finite array of elliptic inclusions”, *Int. J. Solids Struct.* **43**:11–12 (2006), 3459–3483.
- [Legros et al. 2004] B. Legros, S. G. Mogilevskaya, and S. L. Crouch, “A boundary integral method for multiple circular inclusions in an elastic half-plane”, *Eng. Anal. Bound. Elem.* **28**:9 (2004), 1083–1098.
- [Melan 1932] E. Melan, “Der Spannungszustand der durch eine Einzelkraft im Innern beanspruchten Halbscheibe”, *Z. Angew. Math. Mech.* **12** (1932), 343–346.
- [Mogilevskaya 2000] S. G. Mogilevskaya, “Complex hypersingular integral equation for the piece-wise homogeneous half-plane with cracks”, *Int. J. Fract.* **102**:2 (2000), 177–204.
- [Mogilevskaya and Crouch 2001] S. G. Mogilevskaya and S. L. Crouch, “A Galerkin boundary integral method for multiple circular elastic inclusions”, *Int. J. Numer. Methods Eng.* **52**:10 (2001), 1069–1106.
- [Mogilevskaya and Linkov 1998] S. G. Mogilevskaya and A. M. Linkov, “Complex fundamental solutions and complex variables boundary element method in elasticity”, *Comput. Mech.* **22**:1 (1998), 88–92.
- [Mogilevskaya et al. 2008] S. G. Mogilevskaya, S. L. Crouch, and H. K. Stolarski, “Multiple interacting circular nano-inhomogeneities with surface/interface effects”, *J. Mech. Phys. Solids* **56**:6 (2008), 2298–2327.
- [Muskhelishvili 1959] N. I. Muskhelishvili, *Some basic problems of the mathematical theory of elasticity*, Noordhoff, Groningen, 1959.

- [Pyatigorets et al. 2008] A. V. Pyatigorets, S. G. Mogilevskaya, and M. O. Marasteanu, “[Linear viscoelastic analysis of a semi-infinite porous medium](#)”, *Int. J. Solids Struct.* **45**:5 (2008), 1458–1482.
- [Rabotnov 1988] Y. N. Rabotnov, *Механика деформируемого твердого тела*, Nauka, Moscow, 1988.
- [Stehfest 1970] H. Stehfest, “[Algorithm 368: Numerical inversion of Laplace transforms](#)”, *Commun. ACM* **13**:1 (1970), 47–49.
- [Wang and Crouch 1982] Y. Wang and S. L. Crouch, “[Boundary element methods for viscoelastic media](#)”, Chapter 73, pp. 705–711 in *Issues in rock mechanics: Proceedings of the Twenty-Third Symposium on Rock Mechanics* (Berkeley, CA, 1982), edited by R. E. Goodman and F. E. Heuze, The Society of Mining Engineers of the American Institute of Mining, Metallurgical and Petroleum Engineers, New York, 1982.
- [Wang et al. 2003] J. Wang, S. L. Crouch, and S. G. Mogilevskaya, “[A complex boundary integral method for multiple circular holes in an infinite plane](#)”, *Eng. Anal. Bound. Elem.* **27**:8 (2003), 789–802.
- [Zatula and Lavrenyuk 1995] N. I. Zatula and V. I. Lavrenyuk, “[Stressed-strained state of a viscous half-plane with circular inclusions](#)”, *Int. Appl. Mech.* **31**:9 (1995), 754–760.

Received 2 Sep 2008. Accepted 20 Nov 2008.

ANDREY V. PYATIGORETS: pyati002@umn.edu

Department of Civil Engineering, University of Minnesota, 500 Pillsbury Drive SE, Minneapolis, MN 55455, United States

SOFIA G. MOGILEVSKAYA: mogil003@umn.edu

Department of Civil Engineering, University of Minnesota, 500 Pillsbury Drive SE, Minneapolis, MN 55455, United States

<http://www.ce.umn.edu/people/faculty/mogilevs/>

COMPARATIVE STUDY OF SYMMETRIC AND ASYMMETRIC DEFORMATION OF AL SINGLE CRYSTAL UNDER MICROSCALE LASER SHOCK PEENING

SINIŠA VUKELIĆ, YOUNENG WANG, JEFFREY W. KYSAR AND Y. LAWRENCE YAO

The process of laser shock peening induces compressive residual stresses in a material to improve material fatigue life. For micron sized laser beams, the size of the laser-target interaction zone is of the same order of magnitude as the target material grains and, thus, the target material must be considered anisotropic and inhomogeneous. Single crystals are chosen to study the effects of the anisotropic mechanical properties. It is of further interest to investigate the response of symmetric and asymmetric slip systems with respect to the shocked surface. In the present study, analytic, numerical, and experimental aspects of laser shock peening on two different crystal surfaces, (110) and (1 $\bar{1}$ 4), of aluminum single crystals are studied. Anisotropic slip line theory is employed for the construction of slip line fields for both orientations and compared with numerical results. Lattice rotations of the cross section are measured using Electron Backscatter Diffraction (EBSD).

1. Introduction

Laser shock peening (LSP) is a surface treatment introduced in the 1960s [Clauer and Holbrook 1981; Fabbro et al. 1990; Clauer and Lahrman 2001] as a potential replacement for shot peening, which has the same goal of inducing compressive residual stresses on the surface of a material to improve fatigue behavior and wear resistance of the target material. Shocks induced by a laser induce compressive residual stresses of the same order of magnitude as those created by conventional shock peening, however, the residual stresses generated by LSP penetrate deeper into the material resulting in the significant improvement of material response to the cyclic loading [Hammersley et al. 2000]. Moreover, it is much easier to control the position of laser beams, and the process as a whole is much more flexible.

More recently, microscale laser shock peening (μ LSP) has been employed as a means to improve reliability of various micro devices, such as MEMS (microelectromechanical systems). The process is performed by coating the specimen with an ablative layer and submerging it into water, after which a high intensity laser is directed at the ablative layer for 50 ns. The result is a plasma confined by the surrounding fluid so that much of the energy is directed into the material as a shock pulse. The process is considered to be primarily mechanical without any thermal effects that modify the microstructure. Most of the initial work in this field was on polycrystalline materials [Zhang and Yao 2002; Fan et al. 2005].

Keywords: laser shock peening, single crystal, micromechanics, anisotropic slip line theory.

This work is supported by National Science Foundation under grant DMII-0500239. Dr. Jean Jordan Sweet of IBM Watson Research Center provided help with usage of X-ray microdiffraction equipment at the National Synchrotron Light Source at Brookhaven National Laboratory. This work has used the shared experimental facilities that are supported primarily by the MRSEC Program of the National Science Foundation under Award Number DMR – 0213574 by the New York State Office of Science, Technology and Academic Research (NYSTAR). Dr. Paul van der Wilt generously assisted during EBSD measurements.

However, since the laser beam spot size, usually several microns, is comparable to the average grain size of most polycrystalline materials used in the fabrication of microdevices (aluminum, copper, etc.), at most a few grains are affected by a single laser pulse. Thus the effects of anisotropy and heterogeneity have to be taken into account to properly understand this process. This was the motivation for previous studies [Chen et al. 2004a] in which the response of single crystals of aluminum and copper were examined after laser treatment. Two different orientations of aluminum and copper single crystals were examined, a numerical model was established, and the results were compared to experimental findings.

Anisotropic properties of single crystal materials have been studied extensively. One of the early efforts was presented by Hill [1998], who extended the classical slip line theory [Hencky 1923] developed for isotropic materials by substituting a circular yield surface with an elliptic one. Rice [1973] and Booker and Davis [1972] went further in the generalization of slip line theory by expanding it to materials with arbitrary anisotropy. Asaro [1983] summarized the principles of single crystal plasticity. Anisotropic slip line theory as well as plasticity theory was applied to the problem of a flat punch impinged onto the surface of a plastic medium of arbitrary anisotropy [Rice 1973]. The same theory was used by Rice [1987] and Dragan [2001] for derivation of the asymptotic crack tip stress field solutions for elastic ideally-plastic single crystals. An analytic solution for the stress distribution and deformation state around a cylindrical void has been found in [Kysar 1997; 2001a; 2001b].

Single crystal plasticity and anisotropic slip line theory have also been employed to study the response of single crystals under laser shock peening. The approach taken by Wang et al. [2008] was to approximate the Gaussian pressure loading from laser shocks as a punch problem with nonuniform pressure. An aluminum single crystal of a nonsymmetric ($\bar{1}\bar{1}4$) orientation was used in the study because only one slip system was predicted to be active directly under the applied loading. The size of the deformed region was estimated, and an approximate analytic solution was obtained and compared with findings acquired from numerical analysis.

A symmetric orientation of the crystal is of interest because multiple slip systems are activated under a Gaussian pressure distribution. This complicates the analytic derivation and raises issues of the difference in material response and stress field distributions between nonsymmetric and symmetric cases. In the present study, the (110) orientation is chosen because two slip systems are activated under loading, since the symmetry of the yield surface simplifies the derivation of the deformation field. Furthermore, in real applications, polycrystalline materials with textures involving mostly low Miller index grains are quite common.

Thus, the objective of this work is a comparative study of aluminum single crystal behavior under a Gaussian pressure distribution induced by μ LSP for two different crystallographic surfaces, one nonsymmetric with high Miller index ($\bar{1}\bar{1}4$) and the other symmetric with low Miller index (110). A line of μ LSP shocks exists in the ($\bar{1}\bar{1}0$) on the respective surfaces in order to introduce an approximate two-dimensional deformation state. The effects of anisotropy are emphasized, neglecting inertial terms present due to the dynamic nature of the process, terms which are taken into account in [Vukelic et al. \geq 2009]. The deformation state is characterized experimentally, and anisotropic slip line theory is used to investigate the stress distribution and deformation state induced by laser shock peening of a single crystal surface under plane strain conditions. In addition, the finite element method (FEM) is used for the detailed analysis of single crystal plasticity as another perspective of the study. The results are clearly approximate because inertia is neglected, however, the results give insight into the role of anisotropy.

2. Experimental setup and characterization

Twelve dislocation-mediated plastic slip systems exist in the face-centered cubic aluminum, denoted as $\{111\} \langle 110 \rangle$, where $\{111\}$ corresponds to the family of slip planes and $\langle 110 \rangle$ denotes the family of slip directions. If a line loading is applied parallel to the $(\bar{1}10)$ direction, the twelve physical slip systems reduce to three effective in-plane slip systems resulting in an approximate plane strain deformation [Rice 1973; 1987; Kysar et al. 2005]. Lines of laser shocks applied parallel to the $(\bar{1}10)$ direction on the (110) and $(1\bar{1}4)$ planes are called, respectively, the symmetric and asymmetric deformations. The symmetric case admits slip on two effective in-plane slip systems in the region immediately below the laser shock. The asymmetric case admits slip only on one effective slip system. The two experimental setups with effective in-plane slip systems are shown in Figure 1. A detailed discussion about the formation of the approximate two-dimensional deformation can be found in [Rice 1987; Kysar 2001a; Kysar et al. 2005]. The geometric conditions needed for plane strain conditions to be achieved are summarize in [Crone et al. 2004].

Aluminum single crystals are used in this study grown via the Bridgeman method. The sample is mounted on a three circle goniometer and its orientation is determined by Laue diffraction. The specimen is cut to size with a wire electrical discharge machine (EDM) to within $\pm 1^\circ$ of the desired orientation, and the resulting heat affected zone (HAZ) is removed via mechanical polishing. Finally, electropolishing is used in order to remove any residual deformed material.

A frequency tripled Q-switched Nd:YAG laser with wavelength $\lambda = 355$ nm in TEM₀₀ mode is used for the μ LSP experiments, with a beam diameter of $12 \mu\text{m}$, pulse duration of 50 ns, and laser intensity of about 4 GW/cm^2 . A thin polycrystalline aluminum foil is used as an ablative coating applied tightly over an evenly spread layer (approximately $10 \mu\text{m}$ thick) of high vacuum grease. The specimen is placed into a shallow container filled with distilled water to about two millimeters above the sample's top surface as shown in Figure 1. More details about laser shocking can be found in [Zhang and Yao 2002; Chen et al. 2004b]. To obtain an approximate two-dimensional deformation state, laser shocks are applied with a $25 \mu\text{m}$ spacing along the $(1\bar{1}0)$ direction.

μ LSP induces deformation into the single crystal that can be characterized experimentally through lattice rotation which is measured by comparing the as-deformed crystallographic orientation [Kysar 2001a; Wang et al. 2008] relative to the known undeformed state. Lattice orientation is measured using Electron Backscatter Diffraction (EBSD) as a function of micrometer scale spatial position. In order to get information about the depth of the affected region and magnitude of lattice rotation under the surface, EBSD mapping is employed on a cross section of the sample. For these measurements, an HKL Technology system attached to a JEOL JSM 5600LV scanning electron microscope (SEM) is used with a scan area of $200 \mu\text{m} \times 200 \mu\text{m}$ and $120 \mu\text{m} \times 120 \mu\text{m}$ on the shocked surface and cross section, respectively, with $3 \mu\text{m}$ step size.

3. Numerical simulation conditions of single crystals

Finite element analysis is performed based on single crystal plasticity theory described by [Asaro 1983]. For the purpose of this analysis, a plane strain model is established based upon results of prior experiments [Chen et al. 2004a; Wang et al. 2008; Vukelic et al. \geq 2009] which demonstrate that the deformation is approximately two-dimensional at any cross section along a shock line parallel to a $\langle 110 \rangle$ crystallographic

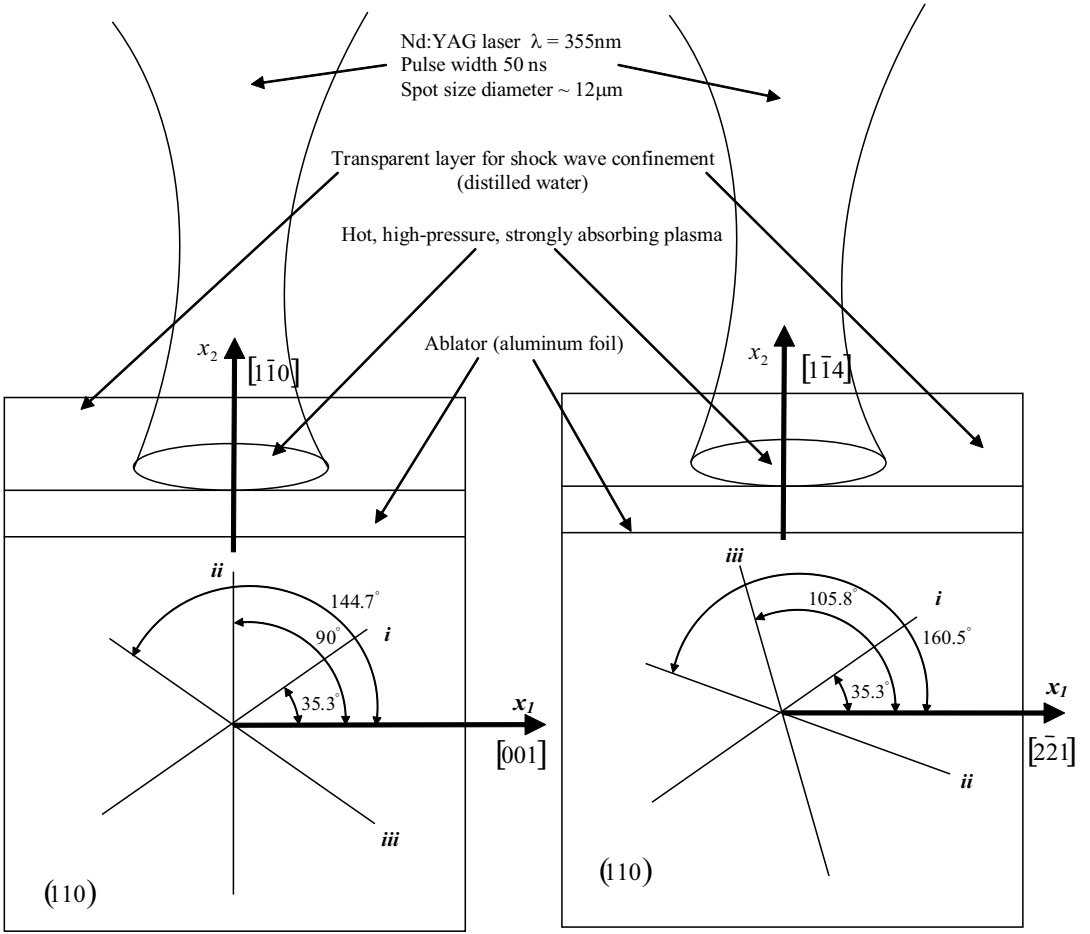


Figure 1. Experimental setup: effective in-plane strain slip systems active corresponding to the (110) orientation (left) and the $(1\bar{1}4)$ orientation (right).

direction. The simulation assumes quasistatic conditions, which, although a gross oversimplification in comparison to the highly dynamic character of μ LSP, still gives insight into the role of the anisotropy, especially in comparison to the analytic solution. Boundary conditions are specified, with reference to the configuration in Figure 1, as follows: zero traction on the side edges; zero vertical displacement on the bottom; and a Gaussian pressure distribution on the upper surface, given by

$$P(x) = P_0 \exp\left(-\frac{x^2}{2R^2}\right), \quad (1)$$

where R is the plasma radius, x is the distance from the center of the Gaussian pressure distribution and P_0 is the peak pressure. The analysis is performed with the commercial finite element (FEM) program ABAQUS/Standard with a user-defined material subroutine (UMAT) written by Huang [1991] and modified by Kysar [1997]. The aluminum slip systems are assumed to have a critical shear strength of $\tau \approx 1$ MPa; the peak pressure is taken to be $P_0/\tau = 7$.

4. Single crystal micromechanics

According to [Asaro 1983], plastic deformation of a single crystal can be conceptually broken down into three steps which, when combined, determine the overall deformation gradient F : first, plastic slip through the undeformed crystal F^P ; second, rigid body rotation F^R ; finally, elastic stretching of the lattice F^e . Therefore, the deformation gradient tensor can be multiplicatively decomposed as

$$F = F^e \cdot F^R \cdot F^P. \quad (2)$$

The first two terms of (2) can be combined together, and the general expression for the deformation gradient becomes $F = F^* \cdot F^P$, where F^P is the deformation related to the plastic shear and F^* represents the stretching and rotation of the crystal lattice. The velocity gradient, L , which is the sum of the spin rate tensor, Ω , and deformation rate tensor, D , can also be calculated as $L = \dot{F} \cdot F^{-1}$. Furthermore, D and Ω can be decomposed into $D = D^* + D^P$ and $\Omega = \Omega^* + \Omega^P$. It can then be shown that the constitutive equation in rate form is

$$\tau^\nabla = L : D - \sum_{\alpha=1}^n [L : P^{(\alpha)} + \beta^{(\alpha)}]_{\lambda}^{(\alpha)}, \quad (3)$$

where L is the tensor of elastic moduli, τ^∇ is the Jaumann rate of the Kirchhoff stress tensor, $\beta^{(\alpha)} = W^{(\alpha)} \dot{\tau} - \dot{\tau} W^{(\alpha)}$, and $\dot{\gamma}^{(\alpha)}$ is the shear strain rate on the slip system α . Another important issue is the definition of the Schmid stress, also known as resolved shear stress, which is responsible for producing an effective force on dislocations. From the general expression of the rate of work,

$$\tau : D^P = \sum_{\alpha=1}^n \tau : P_{\lambda}^{\alpha.(\alpha)}, \quad (4)$$

the Schmid stress on a particular slip system α is

$$\tau^{(\alpha)} = P^{(\alpha)} : \tau, \quad (5)$$

with the Schmid tensor defined as $P^{(\alpha)} = (n^{(\alpha)} \otimes s^{(\alpha)} + s^{(\alpha)} \otimes n^{(\alpha)})/2$, where $n^{(\alpha)}$ is the unit normal of the α -th {111} plane and $s^{(\alpha)}$ is the unit vector corresponding to the α -th <110> slip direction.

5. Anisotropic slip line theory

Slip line theory for isotropic rigid-ideally plastic materials experiencing plane strain deformation has been originally developed by Hencky [1923] and Prandtl [1923]. The stress distribution under a flat punch with a constant pressure was first derived by Hill [1998] for anisotropic materials with an elliptic yield surface using slip line theory and was solved with the generalized theory for arbitrary anisotropic yield surface by Rice [1973] and Booker and Davis [1972]. Wang et al. [2008] employed anisotropic slip line theory to investigate stress and deformation fields for the case of a Gaussian pressure distribution on a single crystal surface for the asymmetric case. In essence, they assumed that the deformation from μ LSP can be thought of as being induced by a punch with a Gaussian pressure distribution, rather than a constant pressure across the width of the punch.

Anisotropic slip line theory is employed to investigate the deformation field of a single face-centered cubic crystal under μ LSP for the symmetric case. Slip line theory treats incipient plane flow and it

is assumed that plastic deformation occurs simultaneously over the domain of interest. The governing equations are a set of equilibrium equations that have the form of hyperbolic partial differential equations; the two families of characteristics, referred to as α and β lines, correspond, respectively, to slip directions and slip plane normals in the case of anisotropic slip line theory applied to single crystals. More details about anisotropic slip line theory can be found in [Rice 1973] and [Kysar et al. 2005].

6. Analytic treatment of deformation and stress field

6.1. Gaussian pressure distribution on a (110) crystallographic orientation. The stress and deformation states associated with a Gaussian pressure loading are derived by assuming that the pressure is applied by a punch with a nonuniform pressure distribution. By this formulation, flat punch kinematics is employed, but the distribution of the stresses under the punch is deformed by a Gaussian distribution. The stress state in the triangular region immediately below the punch is at yield for both problems. Under these conditions, one expects there to be a singular point associated with the edges of the punch about which exist constant stress angular sectors. The only ambiguity in the derivation is to determine the precise positions of the singular points relative to the Gaussian pressure distribution. Therefore, the following procedure is employed to determine a scaling relationship for the positions of the singular points, and a detailed numerical simulation is performed to locate the precise position. The derivation for the (1 $\bar{1}$ 4) case can be found in [Wang et al. 2008].

We first assume that a uniaxial stress state consisting of uniform pressure, P^* , is applied to the surface to be shocked such that plastic deformation is incipient. Schmid's law for a plane strain deformation state with effective in-plane slip systems can be expressed as [Kysar et al. 2005]

$$\sigma_{12} = \tan \phi^{(\alpha)} \left(\frac{\sigma_{11} - \sigma_{22}}{2} \right) \pm \frac{\beta^{(\alpha)} \tau^{(\alpha)}}{\cos 2\phi^{(\alpha)}}, \quad (6)$$

where the superscript α denotes the active slip system, $\phi^{(\alpha)}$ represents the angle between the slip system and the x_1 -axis, $\tau^{(\alpha)}$ is the critical resolved shear stress which can be experimentally determined, and $\beta^{(\alpha)}$ is a geometric ratio ($\beta^{(1)} = \beta^{(3)} = 2/\sqrt{3}$, $\beta^{(2)} = \sqrt{3}$), defined by [Rice 1987]. As seen in Figure 1, for both cases considered, there are three effective slip systems denoted by i , ii , and iii , which can be activated, as in Table 1. In order to find a scaling relation for the approximate position of the singular point, we find the uniaxial stress at which plastic deformation initiates by solving (6) for P^* with $\sigma_{22} = -P^*$, $\sigma_{12} = 0$ and $\sigma_{11} = 0$ to obtain

$$P^* = \pm \frac{2\beta^{(\alpha)} \tau^{(\alpha)}}{\sin 2\phi^{(\alpha)}} \quad (7)$$

as the approximate pressure at which plastic deformation will initiate. This value of P^* is equated to $P(x)$ in (1), and the corresponding value of x , denoted as x_p , is

$$x_p = R \sqrt{\ln \frac{P_0^2 \sin^2 \phi}{(2\beta\tau)^2}}. \quad (8)$$

This result is a scaling relation for the approximate position of the singular point. We further define $x'_p = cx_p$, where c is a dimensionless constant of order unity to be determined by detailed numerical simulation to specify the precise location, x'_p , of the singular point.

Active slip system	ϕ for (110) case	ϕ for ($\bar{1}\bar{1}4$) case	β
<i>i</i>	144.7°	35.3°	$2/\sqrt{3}$
<i>ii</i>	90.0°	160.5°	$\sqrt{3}$
<i>iii</i>	35.3°	105.8°	$2/\sqrt{3}$

Table 1. Values of ϕ and β for active slip systems.

6.2. Analytic prediction of slip sectors for (110) and ($\bar{1}\bar{1}4$) orientations. For a Gaussian pressure distribution applied to the (110) surface, the surface tractions are given by $\sigma_{22} = -P(x)$ and $\sigma_{12} = 0$. If one assumes incipient plastic deformation, it is evident that the stress state will coincide with vertex *F* of the yield locus in Figure 2, left (see also Table 2 on page 97), so that both slip systems *i* and *iii* are activated under the pressure loading. From (7), the values of P^* for the slip systems *i* and *iii* are

$$(P^*)^i = \mp \frac{2\beta^{(1)}\tau^{(1)}}{\sin 2\phi^{(1)}}, \quad (P^*)^{iii} = \mp \frac{2\beta^{(3)}\tau^{(3)}}{\sin 2\phi^{(3)}},$$

where the superscripts on P^* denote the active slip system. Since $\phi^{(3)} = -\phi^{(1)}$, as indicated in Figure 2, we have $|P_*^{(1)}| = |P_*^{(3)}|$ so that both slip systems *i* and *iii* are expected to be activated under the Gaussian pressure distribution on the (110) surface, as expected. The approximate punch radius can then be estimated for the (110) orientation from (8) based upon the values of ϕ_1 and β_1 in Table 1.

The slip line field is then constructed based upon the concepts of [Rice 1973; 1987], as shown in Figure 3. There are constant stress angular sectors centered at each of the singular points; the boundaries of these sectors are slip directions and slip normals which pass through the singular point. In addition,

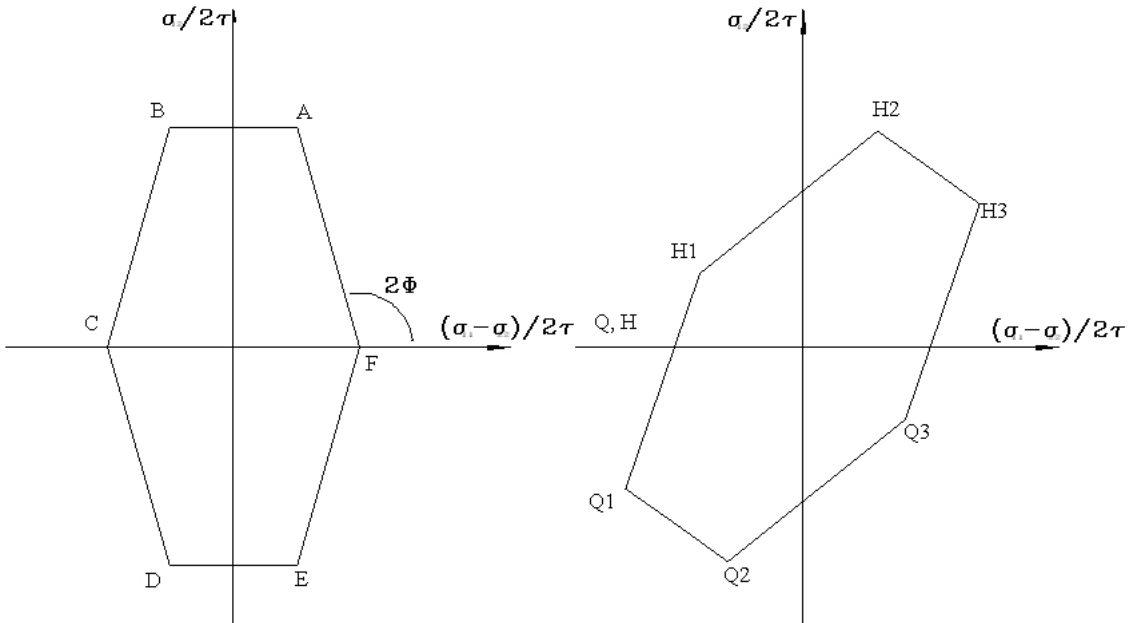


Figure 2. Yield locus for the (110) orientation (left) and for the ($\bar{1}\bar{1}4$) orientation (right).

there are constant stress triangular regions at the periphery of the slip line field. Within the center triangular region, the stress state corresponds to position F on the yield locus in Figure 2, right. From Figure 3, top it can be seen that the symmetric yield locus gives rise to a symmetric slip line field. On the other hand, the slip line field on the $(1\bar{1}4)$ surface, shown in Figure 3, bottom, as constructed by Wang et al. [2008] is asymmetric, reflecting the asymmetry of the yield locus for that orientation in Figure 2, right. From both parts of Figure 3, the geometry of the slip line field also provides an estimate for the

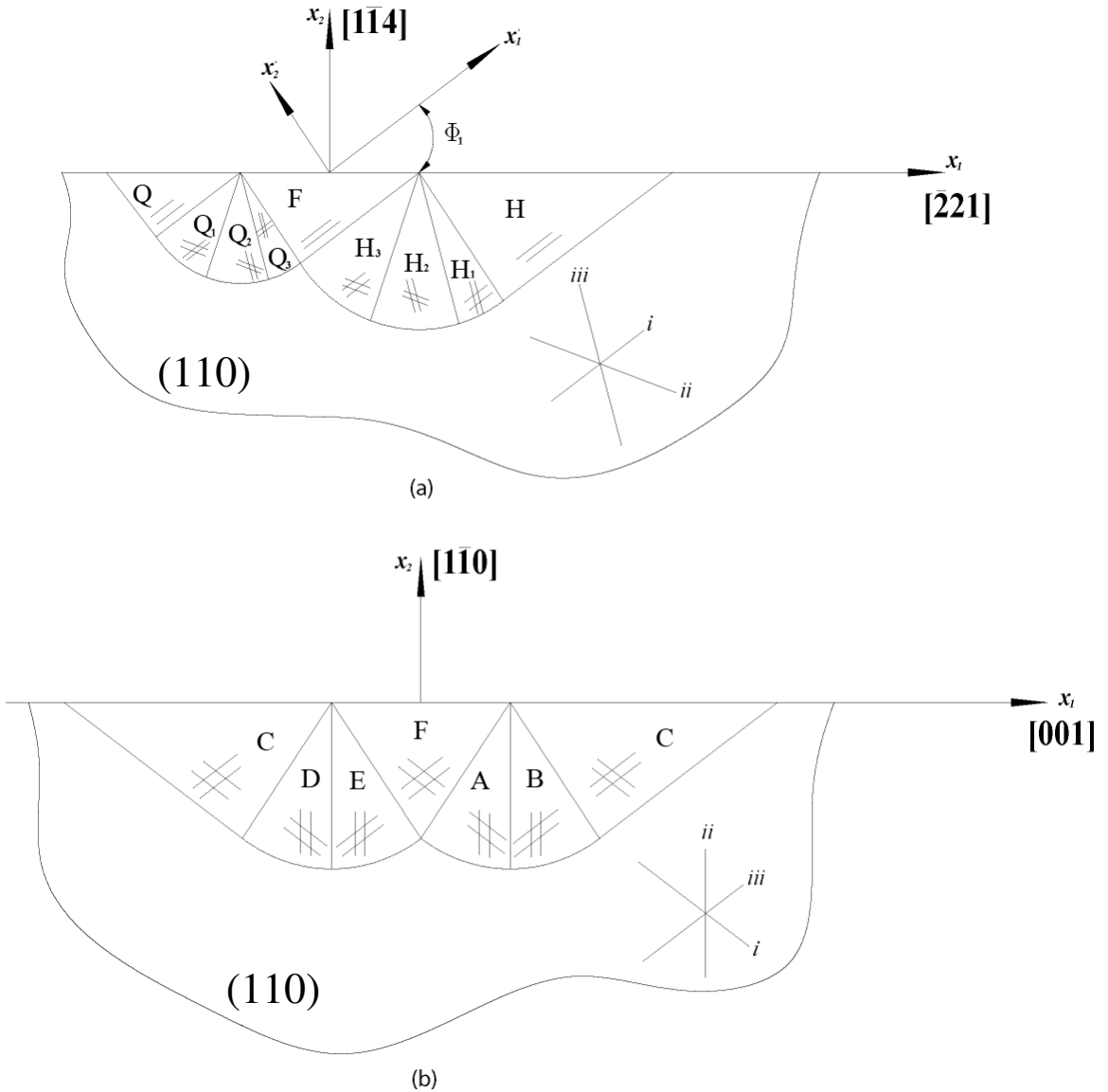


Figure 3. Geometry of slip line field under Gaussian loading for the $(1\bar{1}4)$ orientation (top) and the (110) orientation (bottom).

Vertex	$(\sigma_{11} + \sigma_{22})/2\tau$	σ_{12}/τ	Vertex	$(\sigma_{11} + \sigma_{22})/2\tau$	σ_{12}/τ
A	$\frac{1}{2}\sqrt{\frac{3}{2}}$	$\sqrt{3}$	H ₁	$-\frac{7}{8}\sqrt{6}$	$\frac{4}{9}\sqrt{3}$
B	$-\frac{1}{2}\sqrt{\frac{3}{2}}$	$\sqrt{3}$	H ₂	$\frac{1}{4}\sqrt{6}$	$\sqrt{3}$
C	$-\sqrt{\frac{3}{2}}$	0	H ₃	$\frac{23}{36}\sqrt{6}$	$\frac{5}{9}\sqrt{3}$
D	$-\frac{1}{2}\sqrt{\frac{3}{2}}$	$-\sqrt{3}$	F	$\frac{1}{2}\sqrt{6}$	0
E	$\frac{1}{2}\sqrt{\frac{3}{2}}$	$-\sqrt{3}$	Q ₃	$\frac{7}{18}\sqrt{6}$	$-\frac{4}{9}\sqrt{3}$
F	$\sqrt{\frac{3}{2}}$	0	Q ₂	$-\frac{1}{4}\sqrt{6}$	$-\sqrt{3}$
			Q ₁	$-\frac{23}{36}\sqrt{6}$	$-\frac{5}{9}\sqrt{3}$
			Q	$-\frac{1}{2}\sqrt{6}$	0

Table 2. Yield locus vertices for the (110) case (left) and the (1 $\bar{1}$ 4) case (right).

size of the plastically deformed region for the (110) and (1 $\bar{1}$ 4) cases, respectively:

$$L = 2x_p \left(1 + \frac{1}{\cos^2 \phi}\right) = 2cR \sqrt{\ln \frac{P_0^2 \sin^2 \phi}{(2\beta\theta)^2}} \left(1 + \frac{1}{\cos^2 \phi}\right), \quad (9)$$

$$L = 2x_p(1 + \cot \phi + \tan \phi) = 2\sqrt{2}cR(1 + \cot \phi + \tan \phi) \sqrt{\ln \left(\frac{P_0}{2A}\right) + \ln \sin 2\phi}.$$

6.3. Analytic prediction of stresses within slip systems. Rice [1987] derived for the asymptotic deformation and stress fields under plane strain conditions in elastic-ideally plastic single crystals. By satisfying equilibrium and assuming that a particular angular sector is at yield, he showed that as $r \rightarrow 0$ the stress state must be of a “constant stress type”. Furthermore, since the stress states along the crack flanks and the prolongation of the crack are different, the stress field has to be divided into several constant stress sectors separated by either elastic sectors or lines of discontinuity. For the case of a stationary crack, if the entire domain is at yield, the stress state will necessarily follow the yield locus in stress space; each vertex corresponds to the stress state in a constant angle sector. In the transition region between sectors there is a discontinuity corresponding to the edge on the yield locus which connects two adjacent vertices. These stress discontinuities are constrained to lie at certain angles and coincide with families of slip lines and slip plane normals. Rice [1982] stated that an analogous approach can be used for punch problems. The analytic prediction of the stress distribution under a Gaussian pressure distribution based on anisotropic slip line theory in aluminum with (1 $\bar{1}$ 4) orientation is discussed in detail in [Wang et al. 2008]. Although the (110) orientation is more complex because of double slip, a similar conclusion about stress distribution can be drawn for it; see [Rice 1987].

The solution can be derived by assuming a Gaussian pressure distribution for $x \leq x'_p$, and zero traction boundary conditions for $x > x'_p$. Then, following established procedures [Rice 1973; 1987; Wang et al. 2008], the relationship between the change of average stress $\Delta\sigma = \frac{1}{2}\Delta(\sigma_{11} + \sigma_{22})$ and arc length ΔL , which has units of stress, around the yield locus is

$$\frac{1}{2}\Delta(\sigma_{11} + \sigma_{22}) = -\Delta L. \quad (10)$$

Sector	σ_{11}/τ_{cr}	σ_{22}/τ_{cr}	σ_{12}/τ_{cr}	Active slip systems
A	$-\frac{3}{2}\sqrt{6}$	$-2\sqrt{6}$	$\sqrt{3}$	<i>i, ii</i>
B	$-\frac{3}{2}\sqrt{6}$	$-\sqrt{6}$	$\sqrt{3}$	<i>ii, iii</i>
C	$-\sqrt{6}$	0	0	<i>i, iii</i>
D	$-\frac{3}{2}\sqrt{6}$	$-\sqrt{6}$	$-\sqrt{3}$	<i>i, ii</i>
E	$-\frac{3}{2}\sqrt{6}$	$-2\sqrt{6}$	$-\sqrt{3}$	<i>ii, iii</i>

Sector	σ_{11}/τ_{cr}	σ_{22}/τ_{cr}	σ_{12}/τ_{cr}	Active slip systems
H	$-\sqrt{6}$	0	0	<i>i</i>
H ₁	$-\frac{11}{9}\sqrt{6}$	$-\frac{4}{9}\sqrt{6}$	$\frac{4}{9}\sqrt{3}$	<i>i, iii</i>
H ₂	$-\frac{4}{3}\sqrt{6}$	$-\frac{11}{6}\sqrt{6}$	$\sqrt{3}$	<i>ii, iii</i>
H ₃	$-\frac{13}{9}\sqrt{6}$	$-\frac{49}{18}\sqrt{6}$	$\frac{5}{9}\sqrt{3}$	<i>i, ii</i>
Q ₃	$-\frac{16}{9}\sqrt{6}$	$-\frac{23}{9}\sqrt{6}$	$-\frac{4}{9}\sqrt{3}$	<i>i, iii</i>
Q ₂	$-\frac{5}{3}\sqrt{6}$	$-\frac{7}{6}\sqrt{6}$	$-\sqrt{3}$	<i>ii, iii</i>
Q ₁	$-\frac{14}{9}\sqrt{6}$	$-\frac{5}{18}\sqrt{6}$	$-\frac{5}{9}\sqrt{3}$	<i>i, ii</i>
Q	$-\sqrt{6}$	0	0	<i>i</i>

Table 3. Stresses within sectors for the (110) case (top) and the (1 $\bar{1}$ 4) case (bottom).

Yield locus vertices can be found from geometry, and thus the arc length L can be calculated so that stresses in each of the regions in Figure 3 can be derived. Table 3 shows the normalized values of stress components in each sector for both the (110) and (1 $\bar{1}$ 4) case. More detailed solutions for cracks and cylindrical voids in single crystals case can be found in [Rice 1987; Kysar et al. 2005].

6.4. Analytic prediction of lattice rotation for (110) and (1 $\bar{1}$ 4) orientations. As seen in Section 4, the spin tensor Ω consists of Ω^* , which corresponds to lattice rotation, and Ω^P , associated with plastic slip. Following [Asaro 1983], the plastic part of Ω^P is

$$\Omega^P = \sum_{\alpha=1}^N W^{(\alpha)} \cdot \dot{\lambda}^\alpha, \quad (11)$$

where α represents active slip systems, $\dot{\gamma}$ is the rate of shear, and the tensor W is defined by

$$W^{(\alpha)} = \frac{1}{2}(s^{(\alpha)} \otimes n^{(\alpha)} - n^{(\alpha)} \otimes s^{(\alpha)}). \quad (12)$$

Therefore, Ω^* can be rewritten as

$$\Omega^* = \Omega - \frac{1}{2} \sum_{\alpha=1}^N \dot{\gamma} (s^{(\alpha)} \otimes n^{(\alpha)} - n^{(\alpha)} \otimes s^{(\alpha)}) \quad (13)$$

which gives a relation between the spin tensor responsible for lattice rotation and the slip rate of each active slip system. If \mathbf{n} and \mathbf{s} are projected onto the x_1, x_2 plane and rescaled as unit vectors \mathbf{N} and \mathbf{S} , taking into account the plane strain condition, (8) can be expressed as

$$\Omega^* = \Omega - \frac{1}{2} \sum_{\alpha=1}^N \dot{\gamma} (S^{(\alpha)} \otimes N^{(\alpha)} - N^{(\alpha)} \otimes S^{(\alpha)}) \beta^{(\alpha)} \quad (14)$$

From [Rice 1987] it follows that $S_1 = N_2, S_2 = -N_1$, so the term in parentheses reduces to a constant. The only factors left under the summation are the strain rate and the β term, which is different for each slip system, as discussed by Rice.

Unlike the (1 $\bar{1}$ 4) case, in which only one slip system is active in the triangular regions, in the (110) orientation there are two active slip systems. From the solution for the stresses, it can be shown that the shear strain on each slip system has the same sign, so that the lattice spin induced by both slip systems also has the same sign, which leads to the conclusion that the deformation associated with each slip system adds to the total rotation. Furthermore, the (110) orientation is symmetric, and therefore each active slip system equally contributes to the magnitude of the lattice deformation. On the other hand, only one slip system is active for the (1 $\bar{1}$ 4) case, which suggests that the overall lattice rotation might be less than that in the symmetric case. A more detailed discussion about the numerical and experimental results is given below.

7. Numerical results and comparison with experiments and analytic solutions

7.1. Slip sectors and shear strain increments. According to the analytic solution, the entire deformation field is divided into sectors. In each of those sectors one or two slips are active. As discussed by [Rice 1987], boundaries of sectors are slip directions and slip normals which represent lines of stress discontinuity. The numerical model agrees well with the analytic solution as shown by [Wang et al. 2008] for (1 $\bar{1}$ 4) case. In the case of the (110) orientation, the analytic results derived in the previous section and superimposed on the numerical findings are in good agreement as well, as seen in Figure 4. However, here, emphasis is placed on comparison between the deformation states of the symmetric and asymmetric orientations. Both total shear as well as shear increments for each slip system are of interest. Figure 4 depicts antisymmetry of shear strain increments associated with slips i and iii . At the same time, shear strain increment on slip system ii is symmetric about the center of the shock. The extent of the shear strain increment of all slip systems agrees well with the deformation field derived analytically, if one chooses the consistent c to determine x'_p . Likewise, the (1 $\bar{1}$ 4) calculations agree well with the analytic solution (see Figure 5). The distribution of the shear strain increments is larger on the right side of the deformation field.

7.2. Lattice rotation. Plastic deformation induced by μ LSP causes crystallographic lattice rotation that was characterized via Electron Backscatter Diffraction (EBSD). The region of interest is mapped after laser treatment and its crystallographic orientation compared with the known initial state which serves as a reference. More details about this method can be found in [Kysar and Briant 2002]. Results shown here were reported elsewhere [Wang et al. 2008; Vukelic et al. \geq 2009], and in this study they serve as a comparison with the numerical model.

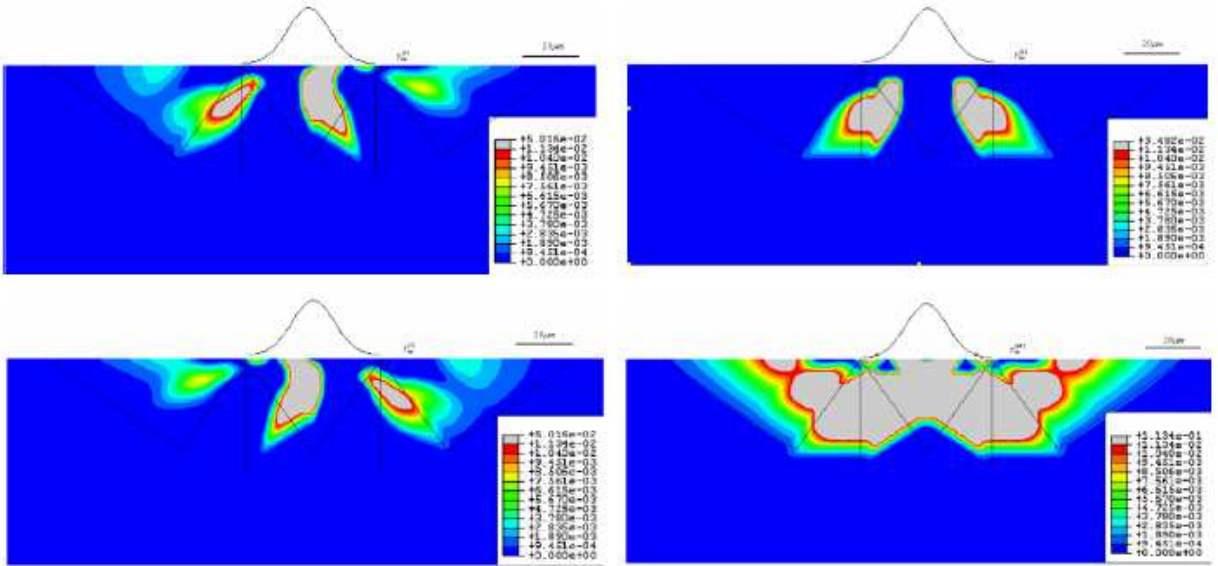


Figure 4. Shear strain increment in each slip system at the end of the loading step for the (110) orientation. Top left, increment in slip system i ; top right, slip system ii ; bottom left, slip system iii ; bottom right, total shear strain increment.

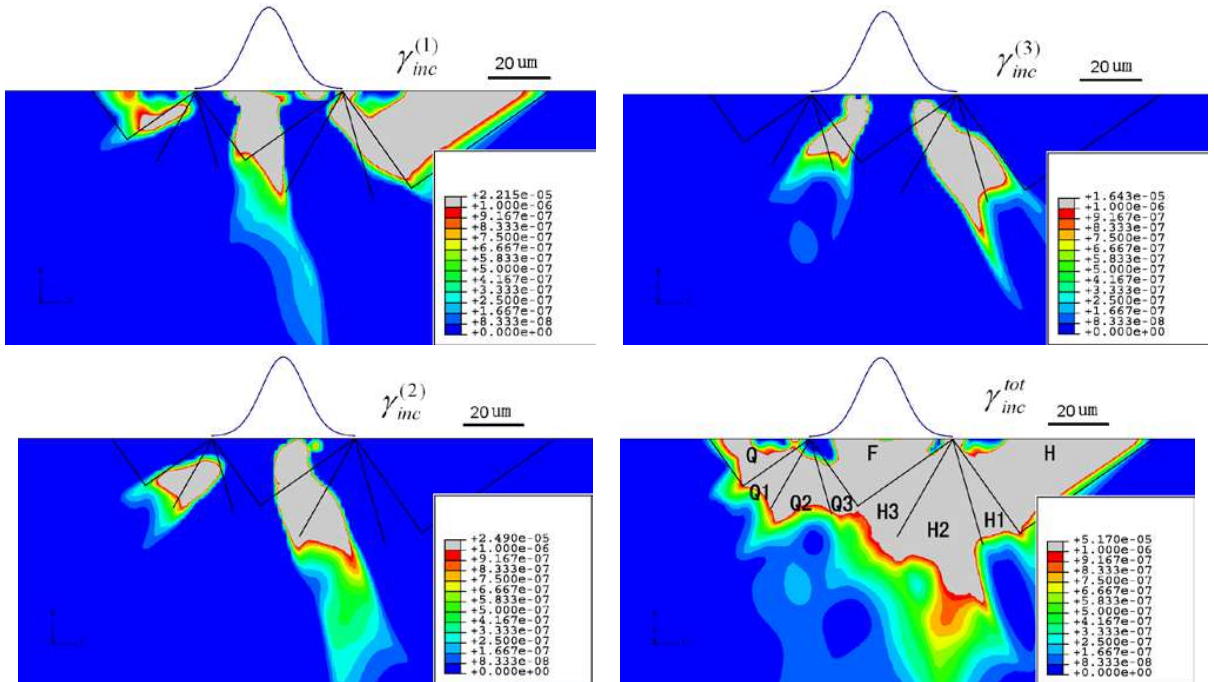


Figure 5. Shear strain increment in each slip system in the end of loading step for the (114) orientation. Top left, increment in slip system i ; top right, slip system ii ; bottom left, slip system iii ; bottom right, total shear strain increment.

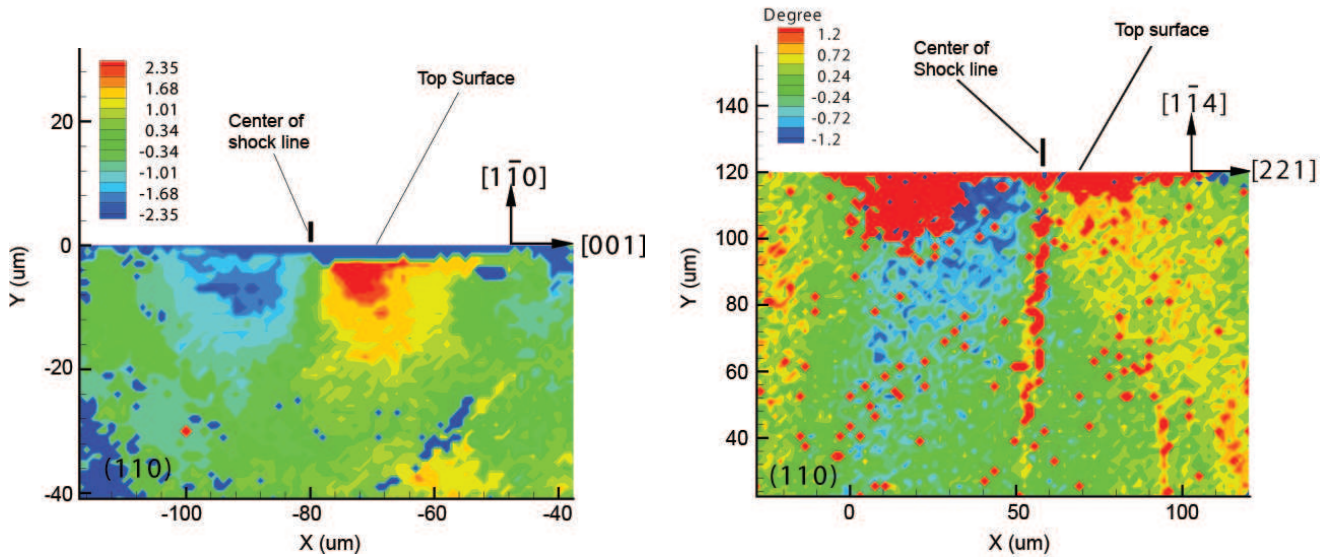


Figure 6. Lattice rotation contour map on the (110) cross section. Positive rotation is counterclockwise about the z -axis.

Lattice rotation results obtained from EBSD measurements of the cross-section are shown in Figure 6. Antisymmetric rotation about the center of the shock line can be observed with blue regions corresponding to counterclockwise rotation and red regions depicting clockwise rotation. Green areas in the field represent unrotated parts of the crystal. From Figure 6a it can be seen that deformation of the (110) crystal is approximately symmetric and slightly narrower than in the (114) case. The magnitude of deformation is largest close to the surface of the specimen and about 15 μm away from the center of the shock line. It can also be seen that directly under the center of the shock line is a region of unrotated crystal. The magnitude of deformation is different for the symmetric and asymmetric cases; for the (110) orientation, the lattice rotates between $\pm 2.4^\circ$, almost double of the rotation of the (114) orientation which is about $\pm 1.2^\circ$. These results are consistent with analytic predictions derived in the previous section that the double slip will cause a larger increase in the lattice rotation than the case of a single slip corresponding to the (114) orientation.

Numerical results of the in-plane lattice rotation are shown in Figure 7. One sees there good agreement between simulation and experimental findings. The main trend for the case of counterclockwise and clockwise rotations located directly under the center of the loading is apparent. The (110) orientation gives a symmetric response as opposed to the asymmetric case of (114). Also, the magnitude of the lattice rotation is larger for the double slip case. However, there is a discrepancy between experimental results and simulation, mainly seen in the magnitude of rotation. This arises from the limitations of the FEM model in which the effects of inertia and work hardening are being neglected.

7.3. Stress distribution. The FEM results of residual stress, σ_{11} , after unloading are shown in Figure 8. It can be seen that the stress field is symmetric in the (110) case and asymmetric in the (114) case. A region of compressive residual stress exists in the center region, whereas self-equilibrating regions of

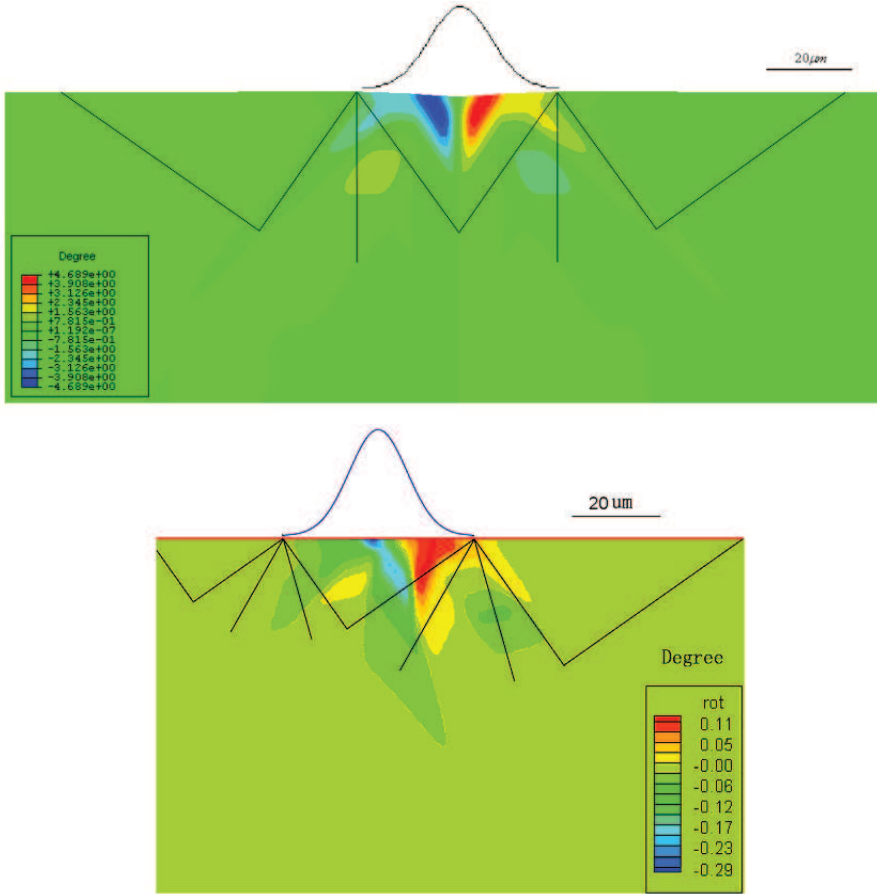


Figure 7. Lattice deformation contour by FEM for the (110) orientation (top) and the (114) orientation (bottom).

tensile residual stress is located far from the center, with the exception of two small regions of tensile residual stress located at the tips of the assumed ends of the punch. The trend shown in Figure 8 suggests that the process of μ LSP is beneficial to the fatigue life and wear resistance of micro components experiencing cyclic loading. Also, it should be noted that in previous studies [Wang et al. 2008], the surface displacement after applying laser shocks onto the top surface has been measured by atomic force microscopy (AFM) and optical profilometry [Vukelic et al. \geq 2009], and the trend coincides with the results captured by finite element simulation.

8. Conclusion

We presented a comparison between laser shock peening of two different orientations of aluminum single crystals, one symmetric and one asymmetric. Anisotropic slip line theory was employed for the construction of slip line fields for both orientations and compared with numerical results. In addition, the stress distribution in angular sectors has been calculated. For the double slip symmetric case, plastic deformation caused by two slip systems adds to the total deformation as characterized by the lattice rotations

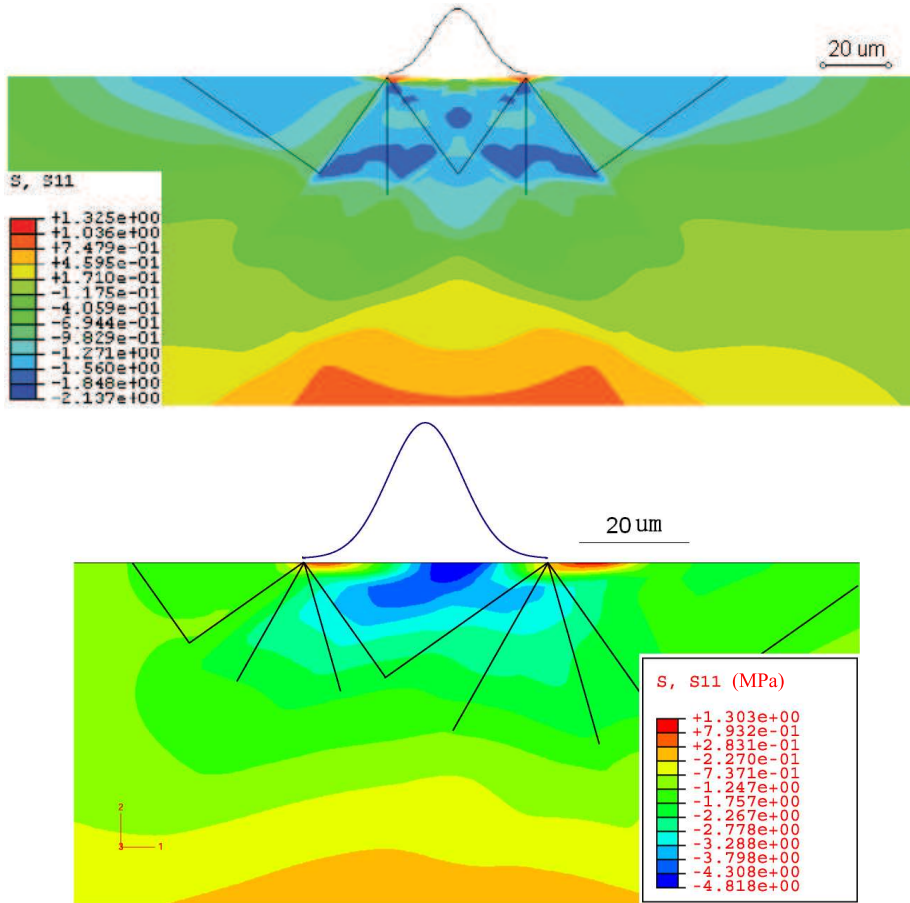


Figure 8. FEM simulation of residual stress distribution for the (110) orientation (top) and the (1 $\bar{1}$ 4) orientation (bottom).

which suggests that deformation in the symmetric orientation will be greater than in the asymmetric case. A numerical model is established for a more detailed investigation of the μ LSP process and compared to experiments. Experimental measurement of lattice rotation via EBSD in the double slip case shows that lattice rotation is twice as large as in the single slip case, which is consistent with the analytic work. Future work will include the effect of heterogeneity through the study of the grain boundary response to μ LSP, which will be achieved by examination of bicrystals.

References

- [Asaro 1983] R. J. Asaro, “Micromechanics of crystals and polycrystals”, *Adv. Appl. Mech.* **23** (1983), 1–115.
- [Booker and Davis 1972] J. R. Booker and E. H. Davis, “A general treatment of plastic anisotropy under conditions of plane strain”, *J. Mech. Phys. Solids* **20**:4 (1972), 239–250.
- [Chen et al. 2004a] H. Q. Chen, J. W. Kysar, and Y. L. Yao, “Characterization of plastic deformation induced by microscale laser shock peening”, *J. Appl. Mech. (ASME)* **71**:5 (2004), 713–723.

- [Chen et al. 2004b] H. Q. Chen, Y. L. Yao, and J. W. Kysar, “Spatially resolved characterization of residual stress induced by micro scale laser shock peening”, *J. Manuf. Sci. Eng. (ASME)* **126**:2 (2004), 226–236.
- [Clauer and Holbrook 1981] A. H. Clauer and J. H. Holbrook, “Effects of laser induced shock waves on metals”, Chapter 38, pp. 675–703 in *Shock waves and high-strain-rate phenomena in metals: concepts and applications* (Albuquerque, NM, 1980), edited by M. A. Meyers and L. E. Murr, Plenum, New York, 1981.
- [Clauer and Lahrman 2001] A. H. Clauer and D. F. Lahrman, “Laser shock processing as a surface enhancement process”, *Key Eng. Mat.* **197** (2001), 121–142.
- [Crone et al. 2004] W. C. Crone, T. W. Shield, A. Creuziger, and B. Henneman, “Orientation dependence of the plastic slip near notches in ductile FCC single crystals”, *J. Mech. Phys. Solids* **52**:1 (2004), 85–112.
- [Drugan 2001] W. J. Drugan, “Asymptotic solutions for tensile crack tip fields without kink-type shear bands in elastic-ideally plastic single crystals”, *J. Mech. Phys. Solids* **49**:9 (2001), 2155–2176.
- [Fabbro et al. 1990] R. Fabbro, J. Fournier, P. Ballard, and D. Devaux, “Physical study of laser-produced plasma in confined geometry”, *J. Appl. Phys.* **68**:2 (1990), 775–784.
- [Fan et al. 2005] Y. Fan, Y. Wang, S. Vukelic, and Y. L. Yao, “Wave-solid interactions in laser-shock-induced deformation processes”, *J. Appl. Phys.* **98**:10 (2005), 104904–104904–11.
- [Hammersley et al. 2000] G. Hammersley, L. A. Hackel, and F. Harris, “Surface prestressing to improve fatigue strength of components by laser shot peening”, *Opt. Lasers Eng.* **34**:4–6 (2000), 327–337.
- [Hencky 1923] H. Hencky, “Über einige statisch bestimmte Fälle des Gleichgewichts in plastischen Körpern”, *Z. Angew. Math. Mech.* **3**:4 (1923), 241–251.
- [Hill 1998] R. Hill, *The mathematical theory of plasticity*, Oxford University Press, New York, 1998.
- [Huang 1991] Y. Huang, “A user-material subroutine incorporating single crystal plasticity in the ABAQUS finite element program”, Division of Applied Sciences, Harvard University, Cambridge, MA, 1991, Available at http://www.columbia.edu/~jk2079/fem/umat_documentation.pdf.
- [Kysar 1997] J. W. Kysar, “Addendum to ‘A user-material subroutine incorporating single crystal plasticity in the ABAQUS finite element program, Mech Report 178’”, Division of Applied Sciences, Harvard University, Cambridge, MA, 1997, Available at <http://www.columbia.edu/~jk2079/fem/Addendum%20to%20umat.pdf>.
- [Kysar 2001a] J. W. Kysar, “Continuum simulations of directional dependence of crack growth along a copper/sapphire bicrystal interface, I: Experiments and crystal plasticity background”, *J. Mech. Phys. Solids* **49**:5 (2001), 1099–1128.
- [Kysar 2001b] J. W. Kysar, “Continuum simulations of directional dependence of crack growth along a copper/sapphire bicrystal interface, II: Crack tip stress/deformation analysis”, *J. Mech. Phys. Solids* **49**:5 (2001), 1129–1153.
- [Kysar and Briant 2002] J. W. Kysar and C. L. Briant, “Crack tip deformation fields in ductile single crystals”, *Acta Mater.* **50**:9 (2002), 2367–2380.
- [Kysar et al. 2005] J. W. Kysar, Y. X. Gan, and G. Mendez-Arzuza, “Cylindrical void in a rigid-ideally plastic single crystal, I: Anisotropic slip line theory solution for face-centered cubic crystals”, *Int. J. Plast.* **21**:8 (2005), 1481–1520.
- [Prandtl 1923] L. Prandtl, “Anwendungsbeispiele zu einem Henckyschen Satz über das plastische Gleichgewicht”, *Z. Angew. Math. Mech.* **3**:6 (1923), 401–406.
- [Rice 1973] J. R. Rice, “Plane strain slip line theory for anisotropic rigid/plastic materials”, *J. Mech. Phys. Solids* **21**:2 (1973), 63–74.
- [Rice 1982] J. R. Rice, “Elastic-plastic crack growth”, pp. 539–562 in *Mechanics of solids: The Rodney Hill 60th anniversary volume*, edited by H. G. Hopkins and M. J. Sewell, Pergamon, Oxford, 1982.
- [Rice 1987] J. R. Rice, “Tensile crack tip fields in elastic-ideally plastic crystals”, *Mech. Mater.* **6**:4 (1987), 317–335.
- [Vukelic et al. ≥ 2009] S. Vukelic, Y. Wang, J. W. Kysar, and Y. L. Yao, “Dynamic material response of aluminum single crystal under micro scale laser shock peening”. Submitted to *J. Manuf. Sci. Eng. (ASME)*.
- [Wang et al. 2008] Y. Wang, J. W. Kysar, and Y. L. Yao, “Analytical solution of anisotropic plastic deformation induced by micro-scale laser shock peening”, *Mech. Mater.* **40**:3 (2008), 100–114.
- [Zhang and Yao 2002] W. Zhang and Y. L. Yao, “Microscale laser shock processing of metallic components”, *J. Manuf. Sci. Eng. (ASME)* **124**:2 (2002), 369–378.

Received 17 Sep 2008. Revised 10 Nov 2008. Accepted 13 Nov 2008.

SINIŠA VUKELIĆ: sv2147@columbia.edu

Columbia University, Mechanical Engineering Department, 500 W 120th Street, S. W. Mudd Building Room 220, MC 4703, New York, NY 10027, United States

YOUNENG WANG: yw2119@columbia.edu

Columbia University, Mechanical Engineering Department, 500 W 120th Street, S. W. Mudd Building Room 220, MC 4703, New York, NY 10027, United States

JEFFREY W. KYSAR: jk2079@columbia.edu

Columbia University, Mechanical Engineering Department, 500 W 120th Street, S. W. Mudd Building Room 220, MC 4703, New York, NY 10027, United States

Y. LAWRENCE YAO: yly1@columbia.edu

Columbia University, Mechanical Engineering Department, 500 W 120th Street, S. W. Mudd Building Room 220, MC 4703, New York, NY 10027, United States

NONUNIFORM INTERFACIAL SLIP IN FIBROUS COMPOSITES

XU WANG

We consider a solitary circular elastic inclusion bonded to an infinite elastic matrix through a linear viscous interface. Here the viscous interface with vanishing thickness can simulate the Nabarro–Herring or Coble creep of a thin interphase layer between the fiber and the matrix. The interface drag parameter is varied along the interface to reflect the real thickening and thinning of the interphase layer. In particular, we consider a special form of the interface function that yields closed-form solutions in terms of elementary functions under four loading conditions: the matrix is subjected to remote uniform antiplane shearing; a screw dislocation is located in the matrix; a screw dislocation is located inside the inclusion; and uniform eigenstrains are imposed on the inclusion.

Our results show that a nonuniform interface parameter will induce an intrinsically nonuniform stress field inside the inclusion when the matrix is subjected to remote uniform shearing or when uniform eigenstrains are imposed on the inclusion, and will also result in a noncentral image force acting on the screw dislocation. In addition, the nonuniformity of the interface will increase the characteristic time of the composite. More interestingly our results show that there coexist at the same time a transient stable and another transient unstable equilibrium positions for a screw dislocation in the matrix when the viscous interface is extremely nonuniform and when the inclusion is stiffer than the matrix. Also discussed is the overall time-dependent shear modulus of the fibrous composite by using the Mori–Tanaka mean-field method.

Notation

w	Out-of-plane displacement
σ_{zx}, σ_{zy}	Stress components in the Cartesian coordinate system
$\sigma_{zr}, \sigma_{z\theta}$	Stress components in the polar coordinate system
γ_{zx}, γ_{zy}	Engineering shear strains
μ	Shear modulus
R	Radius of the circular inclusion
$\beta(\theta)$	Nonuniform interface drag parameter
t	Time
z	Complex variable
c	Volume fraction of the fiber
b	Burgers vector
F_r, F_θ	Image force components on the dislocation in polar coordinates

Superscript ⁽¹⁾ and ⁽²⁾ denote, respectively, the physical quantities in the inclusion and matrix.

Keywords: fibrous composites, creep, interface, nonuniform interface drag parameter.

1. Introduction

In fibrous composites an interphase layer is often introduced between the inclusion (fiber) and the matrix to improve the attachment between the inclusion and the matrix, and to reduce the material mismatch induced stress concentration at the interface (see [Ru 1999] and the references cited therein). Under some conditions (for example at high temperatures), the creep behavior of the interphase layer should be considered [Kim and McMeeking 1995; Fan and Wang 2003]. It is further assumed that the interphase layer is creeping in the linear region controlled by Nabarro–Herring or Coble creep which is diffusion-controlled [Frost and Ashby 1982; Kim and McMeeking 1995]. The creep behavior of the interphase layer can be described by $\tau = \eta\dot{\gamma}$, where τ is the shear stress, η is the viscosity and $\dot{\gamma}$ is the shear strain rate. In this research it is assumed that the thickness h of the interphase layer is much smaller than the radius R of the fiber, that is, $h \ll R$. As a result, $\dot{\gamma} = \dot{\delta}/h$, where $\dot{\delta}$ is the sliding velocity (the differentiation of the relative sliding with respect to the time t). Consequently the slip boundary condition on the interface can be written as $\tau = \beta\dot{\delta}$, with $\beta = \eta/h \geq 0$ being the interface drag parameter, which is identical to the constitutive law for a viscous interface. If we take into consideration the fact that the thickening and thinning of the interphase layer is quite possible during creep flow [Kim and McMeeking 1995], then $\beta = \beta(\theta)$, with θ being the polar angle, is nonuniform along the interface. The aim of this research is to investigate the influence of the nonuniformity of $\beta = \beta(\theta)$ on the response of the fibrous composite with a viscous (or time-dependent sliding) interface. In general it is only possible to derive series form solutions when $\beta(\theta)$ takes an arbitrary form. Here we focus on the special form $1/\beta(\theta) = a_0 + a_1 e^{i\theta} + \bar{a}_1 e^{-i\theta}$, with $a_0 \geq 2|a_1|$, for which closed-form solutions in terms of elementary functions still exist.

2. Basic formulae

We consider a domain in \mathbb{R}^2 , infinite in extent, containing a solitary circular elastic inclusion of radius R with elastic properties different from those of the surrounding matrix (Figure 1). The linearly elastic materials occupying the inclusion and the matrix are assumed to be homogeneous and isotropic with associated shear moduli μ_1 and μ_2 . In this research we ignore the inertia effect for both the inclusion and the matrix, and the two-phase composite is under antiplane shear deformations. Consequently the

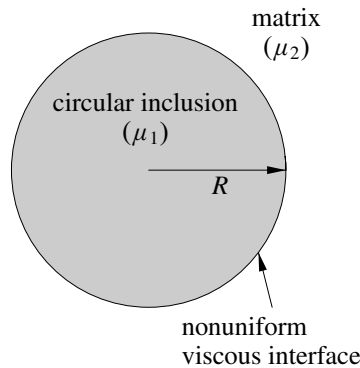


Figure 1. A circular elastic inclusion bonded to an infinite elastic matrix through a nonuniform viscous interface.

out-of-plane displacement w , the stress components σ_{zx} , σ_{zy} in the Cartesian coordinate system, and the stress components σ_{zr} , $\sigma_{z\theta}$ in the polar coordinate system can be expressed in terms of a single analytic function $f(z, t)$ as

$$w = \text{Im } f(z, t), \quad (1)$$

$$\sigma_{zy} + i\sigma_{zx} = \mu f'(z, t), \quad (2)$$

$$\sigma_{z\theta} + i\sigma_{zr} = \mu \frac{z}{|z|} f'(z, t), \quad (3)$$

where t is the real time variable, whilst $z = x + iy = re^{i\theta}$ is the complex variable, and $f'(z, t) = \partial f(z, t)/\partial z$. The appearance of the real time variable t in the analytic function f is due to the influence of the viscous interface between the inclusion and the surrounding matrix.

3. General solutions

In this section we will derive general solutions for the loading case in which the matrix is subjected to an arbitrary type singularity (for example, remote uniform loading or a screw dislocation in the matrix). It follows from the Introduction that the boundary conditions on the interface can be expressed as

$$\sigma_{zr}^{(1)} = \sigma_{zr}^{(2)} = \beta(\theta)(\dot{w}^{(2)} - \dot{w}^{(1)}), \quad r = R \text{ and } t > 0, \quad (4)$$

where the interface drag parameter $\beta(\theta) (\geq 0)$ is a periodic function of the polar angle θ . In this research it is further assumed that $\beta(\theta)$ takes the following special form:

$$\frac{1}{\beta(\theta)} = a_0 + a_1 e^{i\theta} + \bar{a}_1 e^{-i\theta}, \quad (5)$$

where $a_0 \geq 2|a_1|$ to ensure a nonnegative value of $\beta(\theta)$.

The boundary conditions in (4) can also be equivalently expressed in terms of $f_1(z, t)$ defined in the circular inclusion and $f_2(z, t)$ defined in the matrix as

$$\begin{aligned} \mu_1 f_1^+(z, t) + \mu_1 \bar{f}_1^-\left(\frac{R^2}{z}, t\right) &= \mu_2 f_2^-(z, t) + \mu_2 \bar{f}_2^+\left(\frac{R^2}{z}, t\right), \\ \dot{f}_2^-(z, t) - \dot{\bar{f}}_2^+\left(\frac{R^2}{z}, t\right) - \dot{f}_1^+(z, t) + \dot{\bar{f}}_1^-\left(\frac{R^2}{z}, t\right) &= \frac{\mu_1}{\beta(\theta)R} \left(z f_1'^+(z, t) - \frac{R^2}{z} \bar{f}_1'^-\left(\frac{R^2}{z}, t\right) \right) \quad (|z| = R). \end{aligned} \quad (6)$$

It follows from (6)₁ that

$$f_2(z, t) = \frac{\mu_1}{\mu_2} \bar{f}_1^-\left(\frac{R^2}{z}, t\right) + f_0(z) - \bar{f}_0\left(\frac{R^2}{z}\right), \quad \bar{f}_2\left(\frac{R^2}{z}, t\right) = \frac{\mu_1}{\mu_2} f_1(z, t) + \bar{f}_0\left(\frac{R^2}{z}\right) - f_0(z), \quad (7)$$

where $f_0(z)$, which is time-independent, is the complex potential for a singularity in an infinite homogeneous material with shear modulus μ_2 . For example, when the matrix is subjected to uniform loading at infinity, $f_0(z)$ is given by

$$f_0(z) = \frac{\sigma_{zy}^\infty + i\sigma_{zx}^\infty}{\mu_2} z. \quad (8)$$

When the matrix is only subjected to a screw dislocation with Burgers vector b at $z = z_0 = x_0 + iy_0$, then $f_0(z)$ is

$$f_0(z) = \frac{b}{2\pi} \ln(z - z_0). \quad (9)$$

Substituting (7) into (6)₂ and eliminating $f_2^-(z)$ and $\bar{f}_2^+(R^2/z)$, we finally arrive at

$$\dot{f}_1^+(z, t) + \frac{\mu_1\mu_2}{R\eta(\theta)(\mu_1 + \mu_2)} z f_1^+(z, t) = \dot{f}_1^-\left(\frac{R^2}{z}, t\right) + \frac{\mu_1\mu_2}{R\beta(\theta)(\mu_1 + \mu_2)} \frac{R^2}{z} \bar{f}_1^-\left(\frac{R^2}{z}, t\right) \quad (|z| = R). \quad (10)$$

In view of the expression (5) for $\beta(\theta)$, it follows that the left-hand side of (10) is analytic within the circle $|z| = R$, while the right-hand side of (10) is analytic outside the circle, including the point at infinity. By applying Liouville's theorem, we arrive at the following partial differential equation for $f_1(z, t)$:

$$\dot{f}_1(z, t) + \frac{\mu_1\mu_2}{R\beta(\theta)(\mu_1 + \mu_2)} z f_1'(z, t) = 0, \quad (|z| < R). \quad (11)$$

The above equation is still difficult to solve in its present form in view of the fact that $\beta(\theta)$ is varied along the circular interface. In order to solve the above equation, we introduce the following conformal mapping function

$$z = m(\zeta) = \frac{\zeta - \rho}{(\bar{\rho}/R^2)\zeta - 1}, \quad (12)$$

where

$$\rho = -\frac{2\bar{a}_1}{a_0 + \sqrt{a_0^2 - 4|a_1|^2}} R \quad (|\rho| < R). \quad (13)$$

Now (11) can be simplified in the ζ -domain as

$$\dot{f}_1(\zeta, t) + \lambda \zeta f_1'(\zeta, t) = 0 \quad (|\zeta| < R), \quad (14)$$

where

$$\lambda = \frac{\sqrt{a_0^2 - 4|a_1|^2} \mu_1 \mu_2}{R(\mu_1 + \mu_2)}. \quad (15)$$

In writing (14), for convenience $f_1(z, t) = f_1(m(\zeta), t) = f_1(\zeta, t)$ has been adopted. It is observed that not only a_0 but also a_1 , which characterizes the nonuniformity of the interface, enters the expression of λ , which is the inverse of the characteristic time t_0 . The nonuniformity of the interface will increase the characteristic time. The general solution to (14) can be easily obtained as $f_1(\zeta, t) = f_1(\exp(-\lambda t)\zeta, 0)$. Finally, the general solution in the original z -plane can be given as

$$f_1(z, t) = f_1\left(\frac{z(R^2 \exp(-\lambda t) - \rho\bar{\rho}) + \rho R^2(1 - \exp(-\lambda t))}{z\bar{\rho}(\exp(-\lambda t) - 1) + R^2 - \rho\bar{\rho} \exp(-\lambda t)}, 0\right) \quad (|z| < R), \quad (16)$$

which indicates that once the initial value $f_1(z, 0)$ is known, it is enough to replace the complex variable z by

$$\frac{z(R^2 \exp(-\lambda t) - \rho\bar{\rho}) + \rho R^2 - \rho R^2 \exp(-\lambda t)}{z\bar{\rho}(\exp(-\lambda t) - 1) + R^2 - \rho\bar{\rho} \exp(-\lambda t)}$$

to arrive at $f_1(z, t)$.

At the initial time $t = 0$ the interface is a perfect one due to the fact that at $t = 0$ the displacement across the interface has no time to experience any jump [Fan and Wang 2003]. As a result we can obtain the initial value $f_1(z, 0)$ as

$$f_1(z, 0) = \frac{2\mu_2}{\mu_1 + \mu_2} f_0(z). \quad (17)$$

Then $f_1(z, t)$ in (16) can be more specifically expressed as

$$f_1(z, t) = \frac{2\mu_2}{\mu_1 + \mu_2} f_0 \left(\frac{z(R^2 \exp(-\lambda t) - \rho\bar{\rho}) + \rho R^2(1 - \exp(-\lambda t))}{z\bar{\rho}(\exp(-\lambda t) - 1) + R^2 - \rho\bar{\rho} \exp(-\lambda t)} \right) \quad (|z| < R). \quad (18)$$

Substituting this into (7)₁, we arrive at the expression of $f_2(z, t)$ as

$$f_2(z, t) = \frac{2\mu_1}{\mu_1 + \mu_2} \overline{f_0 \left(\frac{\bar{z}\rho R^2(1 - \exp(-\lambda t)) + R^2(R^2 \exp(-\lambda t) - \rho\bar{\rho})}{\bar{z}(R^2 - \rho\bar{\rho} \exp(-\lambda t)) + \bar{\rho} R^2(\exp(-\lambda t) - 1)} \right)} + f_0(z) - \bar{f}_0 \left(\frac{R^2}{z} \right) \quad (|z| > R). \quad (19)$$

4. Specific results for an arbitrary singularity in the matrix

We now address some specific loadings to demonstrate the general solutions obtained.

4.1. Remote uniform loading. When the matrix is subjected to uniform loading, it follows from (8) for the specific expression of $f_0(z)$ and the general solutions (18) and (19) that

$$f_1(z, t) = \frac{2(\sigma_{zy}^\infty + i\sigma_{zx}^\infty)}{\mu_1 + \mu_2} \frac{z(R^2 \exp(-\lambda t) - \rho\bar{\rho}) + \rho R^2(1 - \exp(-\lambda t))}{z\bar{\rho}(\exp(-\lambda t) - 1) + R^2 - \rho\bar{\rho} \exp(-\lambda t)} \quad (|z| < R), \quad (20)$$

$$f_2(z, t) = \frac{2\mu_1(\sigma_{zy}^\infty - i\sigma_{zx}^\infty)}{\mu_2(\mu_1 + \mu_2)} \frac{z\bar{\rho} R^2(1 - \exp(-\lambda t)) + R^2(R^2 \exp(-\lambda t) - \rho\bar{\rho})}{z(R^2 - \rho\bar{\rho} \exp(-\lambda t)) + \rho R^2(\exp(-\lambda t) - 1)} - \frac{\sigma_{zy}^\infty - i\sigma_{zx}^\infty}{\mu_2} \frac{R^2}{z} + \frac{\sigma_{zy}^\infty + i\sigma_{zx}^\infty}{\mu_2} z \quad (|z| > R). \quad (21)$$

Thus the time-dependent stresses in the two-phase composite can be easily obtained as

$$\sigma_{zy}^{(1)} + i\sigma_{zx}^{(1)} = \frac{2\mu_1(\sigma_{zy}^\infty + i\sigma_{zx}^\infty)}{\mu_1 + \mu_2} \frac{(R^2 - \rho\bar{\rho})^2 \exp(-\lambda t)}{(z\bar{\rho}(\exp(-\lambda t) - 1) + R^2 - \rho\bar{\rho} \exp(-\lambda t))^2} \quad (|z| < R), \quad (22)$$

$$\sigma_{zy}^{(2)} + i\sigma_{zx}^{(2)} = (\sigma_{zy}^\infty - i\sigma_{zx}^\infty) \left(\frac{R^2}{z^2} - \frac{2\mu_1}{(\mu_1 + \mu_2)} \frac{R^2(R^2 - \rho\bar{\rho})^2 \exp(-\lambda t)}{(z(R^2 - \rho\bar{\rho} \exp(-\lambda t)) + \rho R^2(\exp(-\lambda t) - 1))^2} \right) + \sigma_{zy}^\infty + i\sigma_{zx}^\infty \quad (|z| > R). \quad (23)$$

Clearly the internal stress field is intrinsically nonuniform when $t > 0$ due to the nonuniformity of the sliding interface ($\rho \neq 0$). To highlight this, we show in Figure 2 the nonuniform distributions of the internal stress components

$$\tilde{\sigma}_{zy} = \frac{\mu_1 + \mu_2}{2\mu_1} \frac{\sigma_{zy}^{(1)}}{\sigma_{zy}^\infty} \quad \text{and} \quad \tilde{\sigma}_{zx} = \frac{\mu_1 + \mu_2}{2\mu_1} \frac{\sigma_{zx}^{(1)}}{\sigma_{zy}^\infty}$$

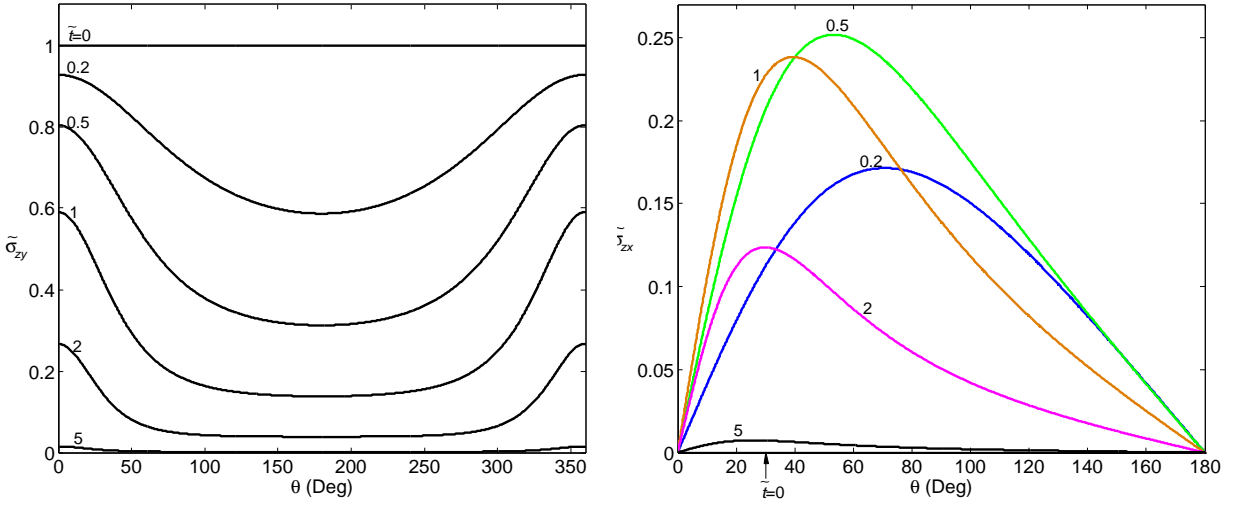


Figure 2. Nonuniform distribution of the internal stress components $\tilde{\sigma}_{zy}$ and $\tilde{\sigma}_{zx}$ along the circular interface $z = Re^{i\theta}$ at times $\tilde{t} = \lambda t = 0, 0.2, 0.5, 1, 2, 5$, with $\rho = 0.5R$, when the matrix is only subjected to σ_{zy}^∞ .

along the circular interface $z = Re^{i\theta}$ at six different times $\tilde{t} = \lambda t = 0, 0.2, 0.5, 1, 2, 5$ with $\rho = 0.5R$ when the matrix is only subjected to σ_{zy}^∞ . It is clearly observed that the internal stresses are nonuniformly distributed along the interface when $t > 0$ and that nonzero $\sigma_{zx}^{(1)}$ will also be induced by σ_{zy}^∞ when $t > 0$ (notice that σ_{zy}^∞ will not induce the stress component $\sigma_{zx}^{(1)}$ when the interface is uniform). In addition the internal stress level of $\tilde{\sigma}_{zy}$ will monotonically decrease as the time evolves, whilst that of $\tilde{\sigma}_{zx}$ attains a maximum value at a certain moment. When $t \rightarrow \infty$ the internal stresses approach zero since the fact that the viscous interface will finally become a free-sliding one which does not sustain any shear force.

The time-dependent average stresses $\overline{\sigma_{zy}^{(1)}}$ and $\overline{\sigma_{zx}^{(1)}}$ within the circular inclusion, which are equivalent to the stresses at the center of the circular inclusion [Ru and Schiavone 1997], can be obtained as

$$\sigma = \frac{\overline{\sigma_{zy}^{(1)}} + i\overline{\sigma_{zx}^{(1)}}}{\sigma_{zy}^\infty + i\sigma_{zx}^\infty} = \frac{2\mu_1}{\mu_1 + \mu_2} \frac{(R^2 - \rho\bar{\rho})^2 \exp(-\lambda t)}{(R^2 - \rho\bar{\rho} \exp(-\lambda t))^2}, \quad (24)$$

which is a monotonically decreasing function of the time t .

The displacement jump across the circular interface can be obtained as

$$\begin{aligned} \Delta w &= w^{(2)} - w^{(1)} \\ &= \frac{2R|Re^{i\theta} - \rho|^2(1 - \exp(-\lambda t))}{\mu_2} \text{Im} \frac{\sigma_{zy}^\infty + i\sigma_{zx}^\infty}{e^{-i\theta}(R^2 - \rho\bar{\rho} \exp(-\lambda t)) - R\bar{\rho}(1 - \exp(-\lambda t))}. \end{aligned} \quad (25)$$

The obtained results for an isolated inclusion can be further employed to predict the effective properties of a two-phase composite consisting of equal-sized circular isotropic cylinders (with shear modulus μ_1) of radius R randomly dispersed in a homogeneous isotropic matrix of shear modulus μ_2 . Here we adopt the Mori–Tanaka mean field method [Mori and Tanaka 1973; He and Lim 2001] to derive the effective

properties of the composite. Somewhat to our surprise, we find that the overall behavior of the fibrous composite under longitudinal shearing is still *isotropic* even though the interface drag parameter $\beta(\theta)$ is varied along the interface. In addition the overall constitutive law for the fibrous composite can be represented by

$$\langle \sigma_{zy} \rangle = \mu_c \langle \gamma_{zy} \rangle, \quad \langle \sigma_{zx} \rangle = \mu_c \langle \gamma_{zx} \rangle, \quad (26)$$

where $\langle * \rangle$ stands for the average value, μ_c stands for the time-dependent effective shear modulus. Here $\gamma_{zy} = \partial w / \partial y$ and $\gamma_{zx} = \partial w / \partial x$ are the engineering shear strains in view of the fact that the in-plane displacements are zero.

In order to describe the overall behavior of the composite, we focus on a representative volume element (RVE). In addition we assume that the RVE is subjected to the antiplane shearing σ_{zy}^∞ . The volume-averaged values within the RVE can be proved to be [He and Lim 2001]

$$\begin{aligned} \langle \sigma_{zy} \rangle &= c \langle \sigma_{zy} \rangle_f + (1 - c) \langle \sigma_{zy} \rangle_m, \\ \langle \gamma_{zy} \rangle &= c \langle \gamma_{zy} \rangle_f + (1 - c) \langle \gamma_{zy} \rangle_m + \frac{c}{\pi R^2} \int_l \Delta w \hat{n}_2 dl, \end{aligned} \quad (27)$$

where c is the volume fraction of the fiber, $\langle \rangle_f$ and $\langle \rangle_m$ refer to the averages over volumes of the fiber and matrix respectively, the line integral is taken along the perimeter l of a typical fiber, Δw is the displacement jump across the interface, and \hat{n}_2 is the y -component of the unit normal vector on the interface in the outward direction with respect to the fiber. In addition $\langle \sigma_{zy} \rangle = \sigma_{zy}^\infty$. Here the Mori–Tanaka mean-field approximation is adopted to evaluate $\langle \sigma_{zy} \rangle_f$. Under this approximation $\langle \sigma_{zy} \rangle_f$ is equal to the average value of σ_{zy} in an isolated fiber embedded in an infinitely extended matrix that is subjected to the shear stress $\langle \sigma_{zy} \rangle_m$ at infinity. Then it follows from (24) and (27)₁ that

$$\langle \sigma_{zy} \rangle_m = \frac{\sigma_{zy}^\infty}{1 - \left(c - c \frac{2\mu_1}{\mu_1 + \mu_2} \frac{(R^2 - \rho\bar{\rho})^2 \exp(-\lambda t)}{(R^2 - |\rho|^2 \exp(-\lambda t))^2} \right)}. \quad (28)$$

The average shear strain in the fiber and in the matrix can be found as

$$\langle \gamma_{zy} \rangle_f = \frac{\langle \sigma_{zy} \rangle_f}{\mu_1}, \quad \langle \gamma_{zy} \rangle_m = \frac{\langle \sigma_{zy} \rangle_m}{\mu_2}, \quad (29)$$

and the surface integral in (27)₂ can be finally carried out as follows

$$\frac{1}{\pi R^2} \int_l \Delta w n_2 dl = 2 \langle \sigma_{zy} \rangle_m \frac{(1 - \exp(-\lambda t))}{\mu_2} \frac{R^4 - |\rho|^4 \exp(-\lambda t)}{(R^2 - |\rho|^2 \exp(-\lambda t))^2}. \quad (30)$$

Equation (25) and the residue theorem have been utilized to derive (30). By using (28), (29) and (30), Equation (27)₂ can be finally expressed as

$$\langle \gamma_{zy} \rangle = \frac{1 + c \left(1 - \frac{2\mu_1}{\mu_1 + \mu_2} \frac{(R^2 - |\rho|^2)^2 \exp(-\lambda t)}{(R^2 - |\rho|^2 \exp(-\lambda t))^2} \right) \sigma_{zy}^\infty}{1 - c \left(1 - \frac{2\mu_1}{\mu_1 + \mu_2} \frac{(R^2 - |\rho|^2)^2 \exp(-\lambda t)}{(R^2 - |\rho|^2 \exp(-\lambda t))^2} \right) \mu_2}, \quad (31)$$

Comparison of (26) with (31) will immediately lead to the time-dependent effective modulus as

$$\mu_c = \mu_2 \frac{1 - c \left(1 - \frac{2\mu_1}{\mu_1 + \mu_2} \frac{(R^2 - |\rho|^2)^2 \exp(-\lambda t)}{(R^2 - |\rho|^2 \exp(-\lambda t))^2} \right)}{1 + c \left(1 - \frac{2\mu_1}{\mu_1 + \mu_2} \frac{(R^2 - |\rho|^2)^2 \exp(-\lambda t)}{(R^2 - |\rho|^2 \exp(-\lambda t))^2} \right)}, \quad (32)$$

which will reduce to the value obtained by [He and Lim 2001] when $\rho = 0$ for a homogeneous interface.

4.2. A screw dislocation in the matrix. When the matrix is only subjected to a screw dislocation with Burgers vector b at $z = z_0$, it follows from (9) for the specific expression of $f_0(z)$ and the general solutions (18) and (19) that

$$f_1(z, t) = \frac{\mu_2 b}{\pi(\mu_1 + \mu_2)} \ln \left(\frac{z(R^2 \exp(-\lambda t) - \rho \bar{\rho}) + \rho R^2(1 - \exp(-\lambda t))}{z \bar{\rho}(\exp(-\lambda t) - 1) + R^2 - \rho \bar{\rho} \exp(-\lambda t)} - z_0 \right) \quad (|z| < R), \quad (33)$$

$$f_2(z, t) = \frac{\mu_1 b}{\pi(\mu_1 + \mu_2)} \ln \left(\frac{z \bar{\rho} R^2(1 - \exp(-\lambda t)) + R^2(R^2 \exp(-\lambda t) - \rho \bar{\rho})}{z(R^2 - \rho \bar{\rho} \exp(-\lambda t)) + \rho R^2(\exp(-\lambda t) - 1)} - \bar{z}_0 \right) + \frac{b}{2\pi} \ln \frac{z(z - z_0)}{\bar{z}_0 z - R^2} \quad (|z| > R). \quad (34)$$

Equation (33) implies that the solution in the inclusion can be considered as the superposition of the following two moving dislocations in a homogeneous infinite elastic plane with the shear modulus μ_1 :

- (i) a dislocation $\frac{2\mu_2}{\mu_1 + \mu_2} b$ located at the moving singular point

$$z = \frac{z_0(R^2 - \rho \bar{\rho} \exp(-\lambda t)) - \rho R^2(1 - \exp(-\lambda t))}{(R^2 \exp(-\lambda t) - \rho \bar{\rho}) - z_0 \bar{\rho}(\exp(-\lambda t) - 1)},$$

which originates from $z = z_0$ and moves toward $z = R^2/\bar{\rho}$;

- (ii) a dislocation $-\frac{2\mu_2}{\mu_1 + \mu_2} b$ located at the moving singular point

$$z = \frac{R^2 - \rho \bar{\rho} \exp(-\lambda t)}{\bar{\rho}(1 - \exp(-\lambda t))},$$

which originates from $z = \infty$ and moves toward $z = R^2/\bar{\rho}$.

The two moving image dislocations (or more precisely a moving dislocation dipole), both of which are located outside the inclusion, will finally converge to the same point $z = R^2/\bar{\rho}$, as seen in Figure 3. The sum of the two moving dislocations is always zero.

Equation (34) implies that the solution in the matrix can be considered as the superposition of the following three static dislocations and two moving dislocations in a homogeneous infinite elastic plane with the shear modulus μ_2 :

- (i) a dislocation b located at the original static singular point $z = z_0$;
- (ii) a dislocation $-b$ located at the static singular point $z = R^2/\bar{z}_0$;
- (iii) a dislocation b located at the static singular point $z = 0$;

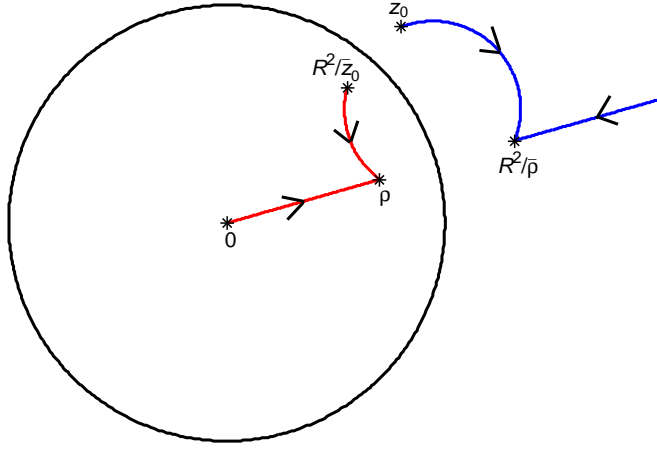


Figure 3. Loci of the moving image dislocations when the original dislocation is located in the matrix. The image dislocations outside the circle $r = R$ are those for the inclusion; those within the circle $r = R$ are for the matrix.

(iv) a dislocation $\frac{2\mu_1}{\mu_1 + \mu_2}b$ located at the moving singular point

$$z = \frac{\bar{z}_0 \rho R^2 (\exp(-\lambda t) - 1) - R^2 (R^2 \exp(-\lambda t) - \rho \bar{\rho})}{\bar{\rho} R^2 (1 - \exp(-\lambda t)) - \bar{z}_0 (R^2 - \rho \bar{\rho} \exp(-\lambda t))},$$

which originates from $z = R^2/\bar{z}_0$ and moves toward $z = \rho$;

(v) a dislocation $-\frac{2\mu_1}{\mu_1 + \mu_2}b$ located at the moving singular point

$$z = \frac{\rho R^2 (1 - \exp(-\lambda t))}{R^2 - \rho \bar{\rho} \exp(-\lambda t)},$$

which originates from $z = 0$ and moves toward $z = \rho$.

Except for the original dislocation at $z = z_0$, all the other four image dislocations are located within the inclusion. The two moving dislocations (or more precisely a moving dislocation dipole) will finally converge to the same point $z = \rho$, as also illustrated in Figure 3. The sum of these five dislocations is b .

In the polar coordinate system, the time-dependent image force acting on the screw dislocation is (see [Lazar 2007])

$$\begin{aligned} & F_r - iF_\theta \\ &= \frac{\mu_1 \mu_2 b^2}{\pi (\mu_1 + \mu_2)} \frac{R^2 (R^2 - |\rho|^2)^2 \exp(-\lambda t)}{|z_0|^2 (R^2 - |\rho|^2 \exp(-\lambda t)) - 2 \operatorname{Re}(z_0 \bar{\rho}) R^2 (1 - \exp(-\lambda t)) - R^2 (R^2 \exp(-\lambda t) - |\rho|^2)} \\ & \quad \times \frac{1}{|z_0| ((R^2 - |\rho|^2 \exp(-\lambda t)) + z_0^{-1} \rho R^2 (\exp(-\lambda t) - 1))} - \frac{\mu_2 b^2}{2\pi} \frac{R^2}{|z_0| (|z_0|^2 - R^2)}, \quad (35) \end{aligned}$$

where F_r and F_θ are respectively the radial and tangential components of the image force. When $\rho = 0$ for a homogeneous viscous interface, this reduces to that derived in [Wang et al. 2008]. On the other hand, when $t = 0$, the expression above reduces to Dundurs' classical solution [1967] for a perfect interface.

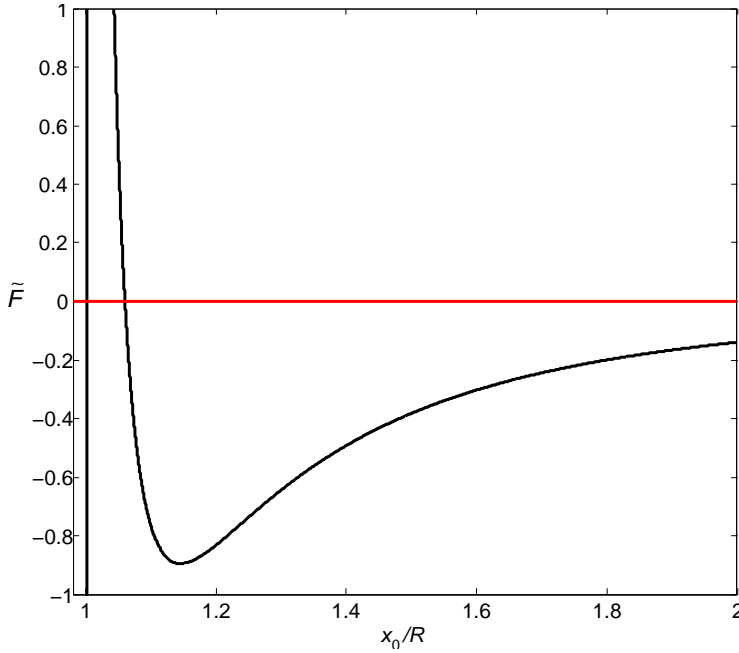


Figure 4. Distribution of the image force \tilde{F} on a screw dislocation located on the positive x -axis in the matrix when $\mu_1 = 3\mu_2$, $\rho = 0.98R$ and $\lambda t = 0.2$.

It is observed that in general the image force is not a central force due to the existence of the nonzero tangential component F_θ . This noncentral image force is solely caused by the nonuniformity of the viscous interface (that is, $\rho \neq 0$). Only when $\text{Arg}(z_0) = \text{Arg}(\rho)$ or $\text{Arg}(z_0) = \text{Arg}(\rho) - \pi$ will the image force be a central one with $F_\theta = 0$.

It has been found that there exists a transient unstable equilibrium position ($F_r = F_\theta = 0$) for a screw dislocation interacting with a homogeneous viscous interface when the inclusion is stiffer than the matrix [Wang et al. 2008]. Our present results show that when the nonuniformity of the interface is extremely serious ($|\rho| \rightarrow R$) and when the inclusion is stiffer than the matrix, a transient stable equilibrium position and another transient unstable equilibrium position may exist at the same time. To highlight this unique feature, we show in Figure 4 the distribution of the image force $\tilde{F} = (2\pi R/\mu_2 b^2)F_r$, on a screw dislocation located on the positive x -axis in the matrix when $\mu_1 = 3\mu_2$, $\rho = 0.98R$ and $\lambda t = 0.2$. It is observed from (35) that $F_\theta = 0$ when ρ and z_0 are both real. It can be seen in Figure 4 that $x_0 = 1.0022R$, which is extremely close to the interface, is a transient unstable equilibrium position, whilst $x_0 = 1.0598R$, which is further away from the interface, is a transient stable equilibrium position.

5. Other loading conditions

The general solutions derived in Section 3 are only valid for an arbitrary type singularity located in the matrix. In fact the method in Section 3 can be extended to other loading conditions. In the following we will address two other type loading conditions: (i) a screw dislocation inside the inclusion; (ii) uniform eigenstrains imposed on the inclusion.

5.1. A screw dislocation inside the inclusion. The analysis of a screw dislocation inside the inclusion is similar to, but a little bit more difficult than, the above analysis of a screw dislocation in the matrix. Here the specific intermediate procedure will be suppressed. When the screw dislocation is located at $z = z_0$ in the inclusion, the two analytic functions can be finally obtained as

$$f_1(z, t) = \frac{\mu_2 b}{\pi(\mu_1 + \mu_2)} \ln \left(\frac{z \bar{\rho} R^2 (1 - \exp(\lambda t)) + R^2 (R^2 \exp(\lambda t) - \rho \bar{\rho})}{z (R^2 - \rho \bar{\rho} \exp(\lambda t)) + \rho R^2 (\exp(\lambda t) - 1)} - \bar{z}_0 \right) - \frac{\mu_2 b}{\pi(\mu_1 + \mu_2)} \ln \frac{z \bar{\rho} R^2 (1 - \exp(\lambda t)) + R^2 (R^2 \exp(\lambda t) - \rho \bar{\rho})}{z (R^2 - \rho \bar{\rho} \exp(\lambda t)) + \rho R^2 (\exp(\lambda t) - 1)} + \frac{b}{2\pi} \ln \frac{z - z_0}{\bar{z}_0 z - R^2} \quad (|z| < R), \quad (36)$$

$$f_2(z, t) = \frac{\mu_1 b}{\pi(\mu_1 + \mu_2)} \ln \left(\frac{z (R^2 \exp(\lambda t) - \rho \bar{\rho}) + \rho R^2 (1 - \exp(\lambda t))}{z \bar{\rho} (\exp(\lambda t) - 1) + R^2 - \rho \bar{\rho} \exp(\lambda t)} - z_0 \right) - \frac{\mu_1 b}{\pi(\mu_1 + \mu_2)} \ln \frac{z (R^2 \exp(\lambda t) - \rho \bar{\rho}) + \rho R^2 (1 - \exp(\lambda t))}{z \bar{\rho} (\exp(\lambda t) - 1) + R^2 - \rho \bar{\rho} \exp(\lambda t)} + \frac{b}{2\pi} \ln z \quad (|z| > R). \quad (37)$$

Equation (36) implies that the solution in the inclusion can be considered as the superposition of the following two static dislocations and two moving dislocations in a homogeneous infinite elastic plane with the shear modulus μ_1 :

- (i) a dislocation b located at the original static singular point $z = z_0$;
- (ii) a dislocation $-b$ located at the static singular point $z = R^2/\bar{z}_0$;
- (iii) a dislocation $\frac{2\mu_2}{\mu_1 + \mu_2} b$ located at the moving singular point
$$z = \frac{\bar{z}_0 \rho R^2 (\exp(\lambda t) - 1) - R^2 (R^2 \exp(\lambda t) - \rho \bar{\rho})}{\bar{\rho} R^2 (1 - \exp(\lambda t)) - \bar{z}_0 (R^2 - \rho \bar{\rho} \exp(\lambda t))},$$

which originates from $z = R^2/\bar{z}_0$ and moves toward $z = (R^2/\bar{\rho})$;

- (iv) a dislocation $-\frac{2\mu_2}{\mu_1 + \mu_2} b$ located at the moving singular point

$$z = \frac{R^2 (R^2 \exp(\lambda t) - \rho \bar{\rho})}{\bar{\rho} R^2 (\exp(\lambda t) - 1)},$$

which originates from $z = \infty$ and moves toward $z = R^2/\bar{\rho}$.

Except for the original dislocation at $z = z_0$, all other image dislocations are located outside the inclusion. The two moving dislocations (or more precisely a moving dislocation dipole) will finally converge to the same point $z = R^2/\bar{\rho}$, as seen in Figure 5. The sum of these four dislocations is zero.

Equation (37) implies that the solution in the matrix can be considered as the superposition of the following one static dislocation and two moving dislocations in a homogeneous infinite elastic plane with shear modulus μ_2 :

- (i) a dislocation b located at the static singular point $z = 0$;
- (ii) a dislocation $\frac{2\mu_1}{\mu_1 + \mu_2} b$ located at the moving singular point
$$z = \frac{z_0 (R^2 - \rho \bar{\rho} \exp(\lambda t)) - \rho R^2 (1 - \exp(\lambda t))}{(R^2 \exp(\lambda t) - \rho \bar{\rho}) - z_0 \bar{\rho} (\exp(\lambda t) - 1)},$$

which originates from $z = z_0$ and moves toward $z = \rho$;

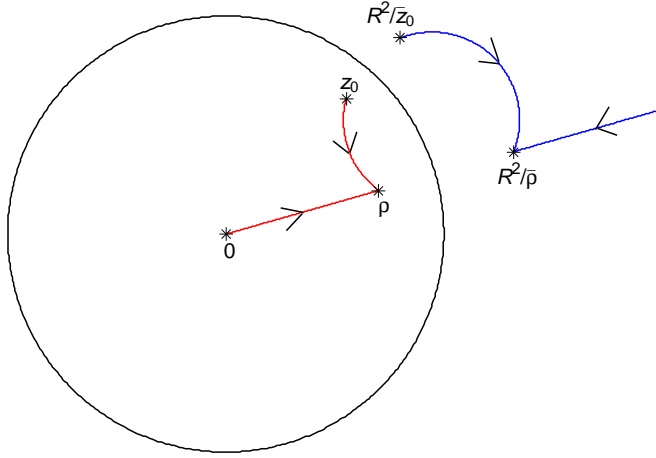


Figure 5. Loci of the moving image dislocations when the original dislocation is located inside the inclusion. The image dislocations outside the circle $r = R$ are those for the inclusion; those within the circle $r = R$ are for the matrix.

(iii) a dislocation $-\frac{2\mu_1}{\mu_1+\mu_2}b$ located at the moving singular point

$$z = \frac{\rho R^2(\exp(\lambda t) - 1)}{R^2 \exp(\lambda t) - \rho \bar{\rho}},$$

which originates from $z = 0$ and moves toward $z = \rho$.

All four image dislocations are located within the inclusion. The two moving dislocations (or more precisely a moving dislocation dipole) will finally converge to the same point $z = \rho$, as also illustrated in Figure 5. The sum of these three dislocations is b .

5.2. Uniform eigenstrains imposed on the inclusion. When only uniform eigenstrains ε_{zx}^* and ε_{zy}^* are imposed on the circular inclusion, the two analytic functions can be finally derived as

$$f_1(z, t) = -\frac{2\mu_2(\varepsilon_{zy}^* + i\varepsilon_{zx}^*)}{\mu_1 + \mu_2} \frac{z(R^2 \exp(-\lambda t) - \rho \bar{\rho}) + \rho R^2(1 - \exp(-\lambda t))}{z\bar{\rho}(\exp(-\lambda t) - 1) + R^2 - \rho \bar{\rho} \exp(-\lambda t)} \quad (|z| < R), \quad (38)$$

$$f_2(z, t) = -\frac{2\mu_1(\varepsilon_{zy}^* - i\varepsilon_{zx}^*)}{\mu_1 + \mu_2} \frac{z\bar{\rho}R^2(1 - \exp(-\lambda t)) + R^2(R^2 \exp(-\lambda t) - \rho \bar{\rho})}{z(R^2 - \rho \bar{\rho} \exp(-\lambda t)) + R^2\rho(\exp(-\lambda t) - 1)} \quad (|z| > R). \quad (39)$$

It is observed that the internal stress field is also nonuniform when uniform eigenstrains are imposed on the inclusion with a nonuniform viscous interface.

6. Conclusions

We obtained closed-form solutions in terms of elementary functions for a circular elastic inclusion bonded to an infinite elastic matrix through a circumferentially inhomogeneous viscous interface. Here the interface drag parameter takes the special form $1/\beta(\theta) = a_0 + a_1 e^{i\theta} + \bar{a}_1 e^{-i\theta}$, which can grasp the main feature of the nonuniformity of the interface.

We first obtained the general solutions for an arbitrary type singularity located in the matrix. Then the general solutions were applied to two specific loading cases: when the matrix is subjected to remote uniform shearing, and when a screw dislocation is located in the matrix. The effective shear modulus was obtained using the Mori–Tanaka method. We also interpreted the obtained dislocation solution in terms of image moving and static dislocations.

We then discussed other two loading conditions: a screw dislocation inside the inclusion, and uniform eigenstrains imposed on the inclusion.

The dislocation solutions obtained in this research can be easily applied to study a curved or a straight crack interacting with the inclusion [Cheeseman and Santare 2000; 2001].

Acknowledgement

This research was supported by the United States Army Research Laboratory through the Composite Materials Technology cooperative agreement with the Center for Composite Materials at the University of Delaware.

References

- [Cheeseman and Santare 2000] B. A. Cheeseman and M. H. Santare, “The interaction of a curved crack with a circular elastic inclusion”, *Int. J. Fract.* **103**:3 (2000), 259–277.
- [Cheeseman and Santare 2001] B. A. Cheeseman and M. H. Santare, “The effect of the interphase on crack-inclusion interactions”, *Int. J. Fract.* **109**:3 (2001), 303–323.
- [Dundurs 1967] J. Dundurs, “On the interaction of a screw dislocation with inhomogeneities”, pp. 223–233 in *Recent advances in engineering science*, vol. 2, edited by A. C. Eringen, Gordon and Breach, 1967.
- [Fan and Wang 2003] H. Fan and G. F. Wang, “Interaction between a screw dislocation and viscoelastic interfaces”, *Int. J. Solids Struct.* **40**:4 (2003), 763–776.
- [Frost and Ashby 1982] H. J. Frost and M. F. Ashby, *Deformation-mechanism maps*, Pergamon Press, Oxford, 1982.
- [He and Lim 2001] L. H. He and C. W. Lim, “Time-dependent interfacial sliding in fiber composites under longitudinal shear”, *Compos. Sci. Technol.* **61**:4 (2001), 579–584.
- [Kim and McMeeking 1995] K. T. Kim and R. M. McMeeking, “Power law creep with interface slip and diffusion in a composite material”, *Mech. Mater.* **20**:2 (1995), 153–164.
- [Lazar 2007] M. Lazar, “On the screw dislocation in a functionally graded material”, *Mech. Res. Commun.* **34**:3 (2007), 305–311.
- [Mori and Tanaka 1973] T. Mori and K. Tanaka, “Average stress in matrix and average elastic energy of materials with misfitting inclusions”, *Acta Metall.* **21**:5 (1973), 571–574.
- [Ru 1999] C. Q. Ru, “Three-phase elliptical inclusions with internal uniform hydrostatic stresses”, *J. Mech. Phys. Solids* **47**:2 (1999), 259–273.
- [Ru and Schiavone 1997] C. Q. Ru and P. Schiavone, “A circular inclusion with circumferentially inhomogeneous interface in antiplane shear”, *Proc. R. Soc. Lond. A* **453** (1997), 2551–2572.
- [Wang et al. 2008] X. Wang, E. Pan, and A. K. Roy, “Interaction between a screw dislocation and a piezoelectric circular inclusion with viscous interface”, *J. Mech. Mater. Struct.* **3**:4 (2008), 761–773.

Received 6 Oct 2008. Revised 5 Feb 2009. Accepted 12 Feb 2009.

XU WANG: xuwang@uakron.edu

University of Delaware, Center for Composite Materials, 202 Composites Manufacturing Science Laboratory, Newark, DE 19716, United States

INVESTIGATING THE SECONDARY BUCKLING OF THIN FILMS WITH A MODEL BASED ON ELASTIC RODS WITH HINGES

GUILLAUME PARRY, CHRISTOPHE COUPEAU, JÉRÔME COLIN AND ALAIN CIMETIÈRE

Thin films are usually submitted to high residual compression stresses which cause them to delaminate and buckle. We focus on the case in which delaminated areas take the form of long rectangular strips. The most commonly observed buckling equilibria that develop on such strip-delaminated areas are the straight-sided wrinkle, the row of bubbles, and the telephone cord wrinkle. An analytical model, based on elastic rods with hinges and taking into account the contact between film and substrate, is set up for the study of the post-buckling regime of the transition from straight-sided wrinkles to bubbles. The existence of snap-through is investigated; previous numerical studies revealed that this phenomenon can sometimes occur. The present analytical approach excludes numerical artifacts that can easily arise due to the high sensitivity of this problem to initial imperfections. The model reveals a critical bubble aspect ratio associated with the snap-through, and the existence of several simultaneous bubble equilibria.

1. The thin film secondary buckling problem and its mechanical description

The mechanical behavior of stressed multilayers and thin films has been the object of several investigations over the past twenty years in the fields of solid mechanics [Hutchinson and Suo 1991; Moon et al. 2004; Evans and Hutchinson 2007; Tvergaard and Hutchinson 2008] and materials sciences [Gille and Rau 1984; Abdallah et al. 2008]. Coatings are involved in a wide range of technological applications from microelectronic devices to thermal barrier coatings used in aero-engines.

High residual compressive stresses tend to arise in thin films deposited on substrates. The stress levels can be high and can reach, for instance, a few GPa in the case of thin metallic films prepared by sputtering deposition methods. The films may consequently delaminate and buckle spontaneously under the effects of high stress. Delamination and buckling are closely related; buckling occurs on the delaminated areas of the film where the flat equilibrium shape is no longer stable. Many buckling shapes can be observed on a delaminated area depending on the area's shape and on the stresses present in the film.

In the present text, we shall focus our attention on equilibria developing on rectangular areas of infinite length, which we shall refer to as "strip-delaminated" areas. The most common buckling equilibria on such domains are the straight-sided wrinkle, the row of bubbles, and the telephone cord wrinkle. Evidence from experiment [George et al. 2002] and analytical theory [Audoly 1999] suggests that both the bubbles and the telephone cord equilibria can result from the buckling of the straight-sided wrinkle. In those studies the delaminated strip was modeled as a von Karman plate and the perturbation method was used on the straight-sided wrinkle. Since the straight-sided wrinkle is itself a post-buckling state of the flat film (a primary buckling), the two other equilibria are often referred to as "secondary buckling" equilibria. A

Keywords: mechanical properties of thin films, static buckling, instability, variational and optimizational methods, elastic rods with hinges models.

stability diagram of the different secondary buckling equilibria has been recently determined [Parry et al. 2006]. The boundaries of the stability domains of the different equilibria are associated with critical values of some nondimensional loading parameters, stress level, elastic properties, delaminated strip width, and film thickness. The delaminated strip was also modeled as a plate, and the stability domains have been obtained through finite element calculations, taking into account large displacements and the contact between film and substrate. This allows one to follow the buckled structure in the advanced post-critical regime. Investigation of these secondary buckling equilibria is still active [Jagla 2007; Gruttmann and Pham 2008; Song et al. 2008].

Numerical exploration by means of the finite element method has proved to be valuable for gaining a better understanding of thin film secondary buckling phenomena. It has enabled us to follow the post-critical paths far from the straight-sided wrinkle equilibrium [Parry et al. 2006]. Nevertheless, because it consists in following along equilibrium branches, using initial imperfections with shapes designed to guide the solution toward the desired equilibrium branch in the neighborhood of the bifurcation point, this type of exploration is “local” in the sense of the loading space: it does not offer a global vision and understanding of the whole equilibrium branch structure. For a given loading and for a chosen set of parameters, the exact number of possible branches (that is, of possible buckling states) is not known *a priori*. It is consequently possible to miss a bifurcation point or snap-through.

In this context, a simplified model based on elastic rods with hinges has been developed in order to study *analytically* the secondary buckling of the strip-delaminated structure, especially the transition from straight-sided wrinkle to bubbles. A two-parameter model, capable of characterizing the straight-sided buckle to bubbles transition, has been set up. Such simplified models have proved to be valuable in analyzing post-critical buckling phenomena [Thompson and Hunt 1973; Arboez et al. 1987]. The idea is to provide intrinsic characteristics of the transition, explicitly investigating the parameters’ dependence and avoiding numerical artifacts.

The equations derived from the simplified model have to be simple enough to be solved by analytical methods, or at least to involve only very basic numerical tools. In the meantime, the model has to be realistic enough to conserve the post-critical behavior of the original structure. As we will show, the simplified model fulfills the above requirements.

Although the model is simplified compared to the original thin film, it shows behavior similar to thin films, and, therefore, can help by giving some explanation of the buckling behavior for such films. The phenomena are qualitatively well reproduced, and the critical values (critical a/b ratio, critical load) can also be predicted quantitatively with good accuracy.

2. Experimental results for the strip-delaminated thin films buckling problem

In this section, we present experimental results for the uniaxial compression of nickel thin films on polycarbonate substrates leading to strip buckling patterns. A summary of the experimental observations related to secondary buckling patterns is made.

Recent experiments [Coupeau et al. 1998] have been carried out on nickel thin films deposited on polycarbonate substrates using *in situ* atomic force microscopy (AFM) imaging together with a compression device. Uniaxial compression of the substrate is performed, with two purposes (Figure 1).

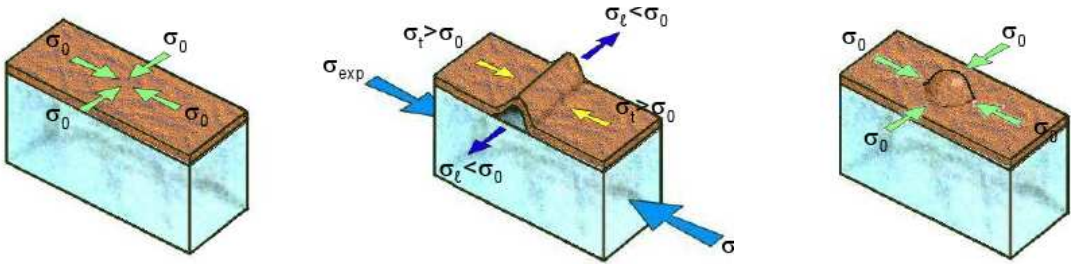


Figure 1. Uniaxial compression of a nickel thin film on a polycarbonate substrate. Left: Nickel thin film on polycarbonate substrate. Equibiaxial stress of magnitude σ_0 in the film. Middle: An uniaxial compression is applied to the substrate leading to strip-shaped delamination and straight-sided wrinkle formation. This structure is stable because of the high transversal compression. The small arrows indicate the stress variations in the film. Right: As the external compression is released, the straight wrinkle bifurcates into a row of bubbles. The stress state is back to the initial equibiaxial stress of magnitude σ_0 in the adherent parts of the film.

- The first purpose is to induce the strip-delamination pattern on the film; a network of parallel strips develops perpendicularly to the compression axis (Figure 1, middle; σ_{exp} is the stress induced in the substrate by the experimental device).
- The second purpose is to modify the initially equibiaxial stress state in the film (Figure 1, left), and hence the loading applied to the delaminated strips. The variation of the stress state in the film due to external compression is depicted in the middle part of the same figure.

Denote by σ_t and σ_l the stress components in the adherent part of the film, taken in the transversal and longitudinal directions of the strip, respectively (these are principal values, as the compression direction is perpendicular to the strips). The loading applied to the delaminated part of the film is in fact a displacement prescribed by the substrate along the boundaries of the delaminated area. The values σ_t and σ_l are directly related to this imposed displacement.

Before applying external compression, the film is only submitted to an equibiaxial compression state due to the internal stress ($\sigma_t = \sigma_l \equiv \sigma_0$) (first and left parts of Figure 1). During the uniaxial compression of the substrate, the stress component in the film becomes more compressive in the compression direction (that is, in the transversal direction of the strip) whereas the stress component perpendicular to the compression direction (that is, in the longitudinal direction of the strip) becomes *less* compressive (middle part of same figure). This behavior results from the difference between the Poisson's coefficients of the two materials ($\nu_{\text{film}} < \nu_{\text{substrate}}$). The ratio of stress components in the longitudinal and transversal directions of the strip (σ_l/σ_t) is a critical parameter which triggers the transition between the straight-sided equilibrium and the secondary buckling equilibria (bubbles or telephone cord).

Secondary buckling occurs while the external compression is released (Figure 1, right). As a matter of fact, a large external compression promotes a transversal stress component higher than the longitudinal one, leading to a stable straight-sided wrinkle (Figure 1, middle). While the external compression is released, the σ_l/σ_t ratio increases, destabilizing the straight-sided wrinkle and a bubble or telephone cord equilibrium then arises.

The only irreversible step of the experiment is the delamination of the interface, which determines the width of the strips during the first compression. The buckling itself is purely elastic (reversible) and the experiment can be repeated with multiple cycles. It is worth noting that the delaminated strip width does not evolve during the successive loading/unloading. The interaction of debonding with buckling of the film is not studied in this article. Many studies on this topic have been published (for example see [Thouless et al. 1992; Faulhaber et al. 2006]).

The reversibility of buckling in the above described experiment allows one to observe, in-situ, different areas of the film and to follow the different equilibria in their post-critical regime while the external compression is modified. Remarkable observations are:

- (a) both bubbles and telephone cords can be found on the same sample;
- (b) the transition from straight-sided wrinkle to bubbles is characterized by snap-through under particular conditions;
- (c) some bubbles are rather shallow, remaining on top of the straight-sided wrinkle, whereas others are much deeper, settling down to the substrate level, as observed in Figure 2.

These experimental observations reveal the strong nonlinear character of the problem. Transitions occur in configurations where large out-of-plane displacements are involved. The film-substrate contact is a source of nonlinearity as well. The wrinkle-to-bubbles transition is thus particularly complex.

The questions arising in point (a) were addressed in [Parry et al. 2006]. It was found that, for a given loading, bubbles tend to appear on the narrowest strips whereas telephone cords develop on wider ones.

The question pointed out in point (b), the snap-through in the wrinkle-to-bubbles transition, has been explored in [Parry et al. 2005] by means of the finite element method. The length-over-width ratio for the bubbles turns out to be a critical parameter for the nature of the transition.

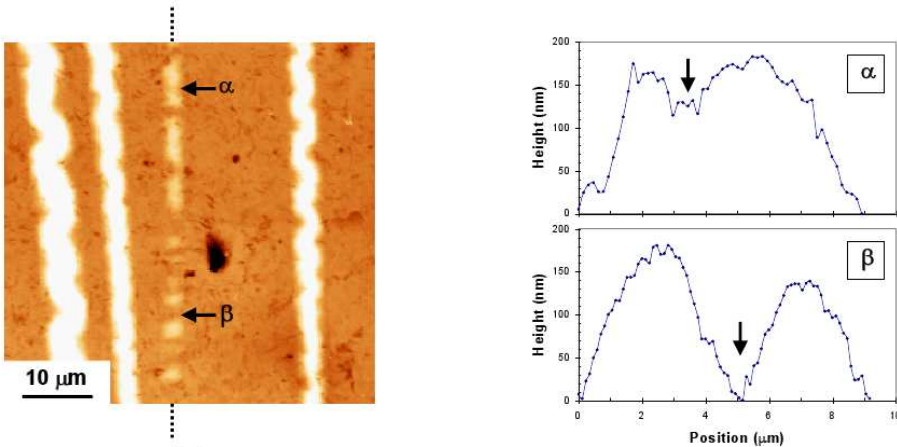


Figure 2. AFM image of a row of bubbles. Left: Detail of a row formed after the collapse of a straight-sided wrinkle. The other wrinkles in the neighborhood have a telephone cord buckling pattern. Two points are spotted, both located between two successive bubbles. Right: A slight depression is observed at point α , whereas the film is completely redeposited on the substrate at point β .

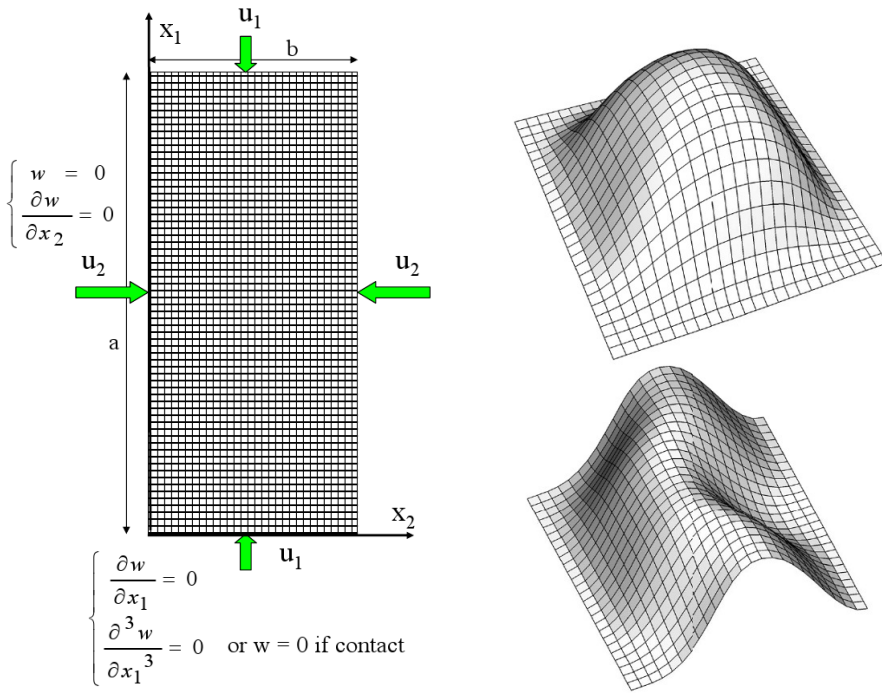


Figure 3. Structure sensibility to initial imperfections. Left: Mechanical model used in finite element computations. One unit cell (length a , width b) of the delaminated strip is modeled as a plate, with prescribed displacements at edges. Initial shape imperfection is on the order of $b/1500$. The straight-sided wrinkle bifurcates into a bubble structure (top right), or into a telephone cord structure (bottom right).

The two principal aims of the simplified model are to investigate point (c), which has not been addressed previously, and to explore further point (b). The latter point is difficult to address using plate theory and numerical methods because of the multiplicity of parameters and sensitivity of the secondary buckling to initial imperfections.

An example of this sensitivity is illustrated in Figure 3. In this example, a plate of length a and width b relies on a rigid support (Figure 3, left). The plate is submitted to displacements along its boundaries. The displacement components are normal to the plate edges. This plate represents one unit cell of the buckling mode: b is the strip width and a is the length of one bubble or the telephone cord spatial period. Two buckling calculations are carried out using two different initial geometric imperfections. The imperfections are very small, their amplitude being on the order of $b/1500$. In the first calculation (Figure 3, right top), the imperfection shape is “symmetric”, imitating a bubble. As the amplitude of the prescribed displacement increases, the plane structure first bifurcates in a straight-sided wrinkle; the secondary buckling under a bubble shape then occurs. In the second case (Figure 3, right bottom), an “antisymmetric” imperfection inspired by the telephone cord shape is introduced; the structure follows the same evolution as the process just described, from the plane structure to the straight-sided buckle,

but it finally bifurcates into a telephone cord shape as the loading is increased. These calculations show the key dependence of the numerical results on the initial imperfection used to carry out the calculation.

3. The simplified rod and spring model for buckling and post-buckling

The simplified system is composed of elastic rods, connected by hinges (Figure 4). The bending stiffness is obtained by introducing rotational springs between the rods. The arrows represent the prescribed load or displacement applied perpendicularly to the edges.

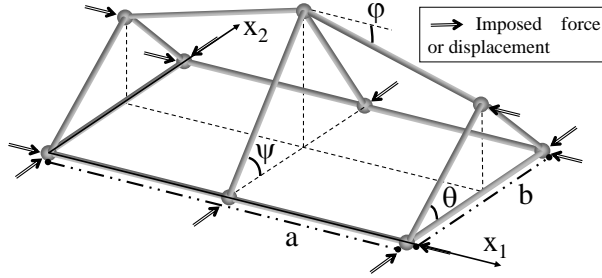


Figure 4. Rods and springs structure. The variables ψ , ϕ , and θ are the rotations of the rods with respect to the horizontal plane. The arrows stand for imposed forces or displacements.

The structure depicted in Figure 4 is one unit cell of width b and length a of the buckled structure that arises during secondary buckling. It represents a structure of spatial periodicity a , a straight-sided wrinkle, or a flat structure.

A state of deformation is characterized by two angular parameters ϕ and ψ . For convenience, a third parameter θ is introduced which is a function of the two degrees of freedom ϕ and ψ ($\theta \equiv \theta(\phi, \psi)$). When $\phi = 0$ and $\theta = \psi$, the straight-sided wrinkle can be recognized. The value $\theta = 0$ indicates the point at which the post-critical regime is advanced enough such that the bubble edges come in contact with the substrate. All the other values ϕ , ψ , and θ describe states that are in the post-critical secondary buckling regime. It is worth noting here that the telephone cord buckle cannot be described by this model. In order to do so, the introduction of one additional parameter is necessary which would not allow us to preserve the simplicity and the clarity of our statements. The present study focuses on the wrinkle-to-bubbles transition.

The potential energy V of the structure is defined as

$$V = E_{\text{el}}^{\text{b}} + E_{\text{el}}^{\text{s}} - W_{\text{ext}}, \quad (1)$$

where E_{el}^{b} is the bending elastic deformation energy, E_{el}^{s} the stretching elastic deformation energy, and W_{ext} the work of external forces. The bending part of the elastic deformation energy is composed of the following terms:

$$E_{\text{el}}^{\text{b}} = \frac{1}{2}C_1\psi^2 + \frac{1}{2}C_1\theta^2 + \frac{1}{2}C_2\phi^2 + C_3\phi(\psi - \theta), \quad (2)$$

where C_1 and C_2 are the pure bending stiffness coefficients associated with bending around the Ox_1 and Ox_2 axes, respectively, and C_3 is the shear stiffness coefficient. The shear energy is chosen to be the simplest polynomial that vanishes for $\varphi = 0$ and $\psi - \theta = 0$.

It is necessary to carefully choose these three coefficients to obtain a realistic behavior of the simplified model. In order to find the coefficients, the behavior of the bars system is identified with the behavior of a rectangular plate of same dimensions (length a and width b) at the onset of buckling. The identification of the critical loads, for a well chosen set of buckling modes, allows for the determination of the coefficients.

For this identification step, the structure is loaded in its initial (flat) plane by forces applied normal to the edges (see Figure 5). Denote by f the force per unit length of the structure edge, so the total load applied on an edge parallel to the x_1 direction is fa . This load is distributed on the four hinges, with $fa/4$ at the extremities and $fa/2$ in the middle (as suggested by the periodicity conditions). The same argument holds for the load applied along the edges parallel to the x_2 direction.

The two chosen buckling modes that we wish to use for identification are:

- The straight-sided wrinkle (Figure 5, left), characterized by $\varphi = 0$ (hence $\theta = \psi$), arising from the flat equilibrium. This buckling mode does not activate shear, and makes it possible to identify coefficients C_1 and C_2 .
- The bubble mode (Figure 5, right), arising from the flat equilibrium. This mode activates shear, and allows for the determination of C_3 .

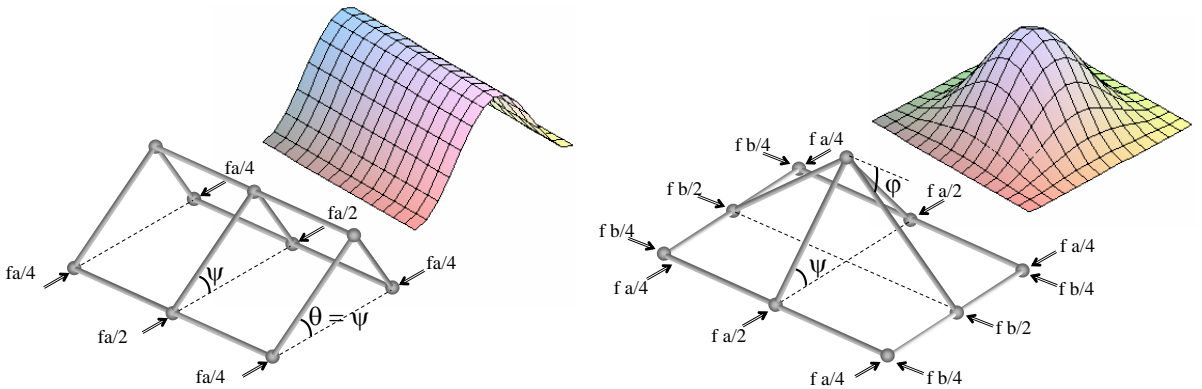


Figure 5. Buckling modes used for bending stiffness identification. Left: Straight-sided wrinkle mode. Right: Four times clamped plate or “deposited bubble” structure.

As the identification is made for incipient buckling, it is assumed that the deformation occurs without stretching of the middle plane. In this case, the potential energy of the bars structure is written as

$$V = \frac{1}{2}C_1\theta^2(\varphi, \psi) + \frac{1}{2}C_1\psi^2 + \frac{1}{2}C_2\varphi^2 + C_3\varphi(\psi - \theta(\varphi, \psi)) - 2\left(f\frac{a}{2}(1 - \cos\varphi)\frac{b}{2}\right) - 2\left(f\frac{b}{2}(1 - \cos\theta(\varphi, \psi))\frac{a}{2}\right) - 2\left(f\frac{b}{2}(1 - \cos\psi)\frac{a}{2}\right). \quad (3)$$

We now describe the first step of the identification process, that is, the determination of C_1 using the straight-sided wrinkle equilibrium (Figure 5, left). It is possible to find an exact solution of the von

Karman equation for this straight-sided wrinkle problem, for example, [Hutchinson and Suo 1991]. The critical value f_c of the force per unit length associated with this buckling mode is $f_c = 4\pi^2 D/b^2$ (with D the flexural stiffness of the plate). As far as the bars structure is concerned, this equilibrium is characterized by $\varphi = 0$ and $\theta = \psi$. The critical value of the load is $f_c = 2C_1/(ba)$. We deduce that

$$C_1 = 2\pi^2 D \frac{a}{b}, \quad C_2 = 2\pi^2 D \frac{b}{a}. \quad (4)$$

We next describe the second step of the identification process, that is, the determination of C_3 using the bubble equilibrium (Figure 5, right). There is no exact solution for the buckling problem of a rectangular plate clamped along all edges. Nonetheless, a good approximation for the solution to this problem is

$$w(x, y) = \frac{w_m}{4} \left(1 - \cos \frac{2\pi}{a} x\right) \left(1 - \cos \frac{2\pi}{b} y\right). \quad (5)$$

An approximate critical buckling load is obtained by setting the work of external forces ΔW equal to the bending energy ΔU_b of the plate for any amplitude w_m of the lateral deflection. These two expressions ΔW and ΔU_b can be written as

$$\begin{aligned} \Delta W &= \frac{1}{2} \int_0^a \int_0^b \left(f \left(\frac{\partial w}{\partial x} \right)^2 + f \left(\frac{\partial w}{\partial y} \right)^2 \right) dx dy, \\ \Delta U_b &= \frac{D}{2} \int_0^a \int_0^b \left(\left(\frac{\partial^2 w}{\partial x^2} + \frac{\partial^2 w}{\partial y^2} \right)^2 - 2(1-\nu) \left(\frac{\partial^2 w}{\partial x^2} \frac{\partial^2 w}{\partial y^2} - \left(\frac{\partial^2 w}{\partial x \partial y} \right)^2 \right) \right) dx dy, \end{aligned}$$

which provides the value for the approximate critical buckling load,

$$f_c = \frac{4\pi^2 D}{b^2} \frac{2\tilde{a}^2 + 3 + 3\tilde{a}^4}{3\tilde{a}^2(1 + \tilde{a}^2)}, \quad (6)$$

with $\tilde{a} = a/b$. Finite-element parametric studies show that this analytical formula for the bubble buckling load is quite accurate.

We now calculate the critical load associated with the system of bars. The potential energy given by equation (3) is used here. The relationship between the angles is $\sin \theta = \sin \psi - (a/b) \sin \varphi$, which under the small displacement hypothesis becomes $\theta = \psi - (a/b)\varphi$. The bubble equilibrium is characterized by $\theta = 0$. Taking into account these equalities yields

$$f_c = \frac{4\pi^2 D}{b^2} \frac{3C_3/(D\pi^2)\tilde{a}^2 + 3 + 3\tilde{a}^4}{3\tilde{a}^2(1 + \tilde{a}^2)}, \quad (7)$$

from which $C_3 = \frac{2}{3}\pi^2 D$ is identified.

4. The unilateral buckling problem with two degrees of freedom

The displacements along the delaminated areas of the film are in fact imposed by the substrate. Let us call u_1 and u_2 the two components of the displacement imposed on the edges of the strip (Figure 6, left). We introduce the notation $u_1 = \frac{1}{2}a\varepsilon_1$ and $u_2 = \frac{1}{2}b\varepsilon_2$, where ε_1 and ε_2 are the biaxial strains in the adherent part of the film, due to the substrate action. During loading, the lengths of the rods change as

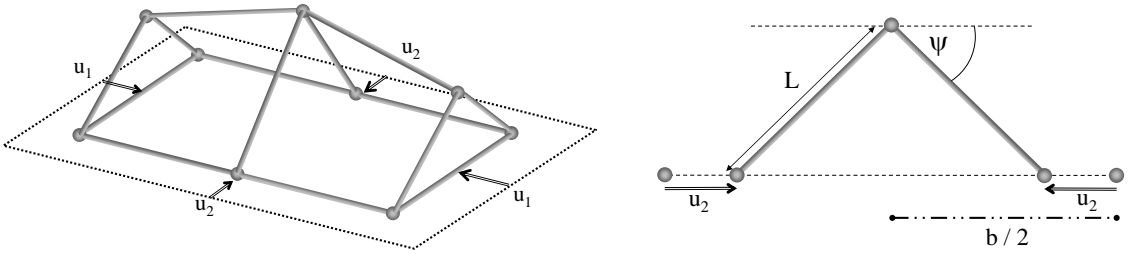


Figure 6. System of elastic rods under prescribed displacement. Left: Displacements u_1 and u_2 prescribed on the edges of the structure. Right: Relationships between displacement and current rod length.

illustrated in the case of the transversal rods, with rotation identified by the angular variable ψ in Figure 6, right.

In order to introduce the stretching energy component into the rod system, we have to identify an equivalent compression stiffness for each rod. This is done by matching the uniaxial compression stiffness of the rod system with that of a plate with the same dimensions. An illustration is given in Figure 7. The total compression force acting on the edge parallel to direction x_1 is $F = \sigma ha$. For a displacement ΔL of the edge, the stiffness of the plate is denoted K , with $F = K \Delta L$. Since $\sigma = E(2\Delta L/b)$, we identify $K = 2E(a/b)h$. This stiffness is distributed between the middle rod ($k' = E(a/b)h$) and the side rods ($k'' = \frac{1}{2}E(a/b)h$ for each rod, for symmetry reasons).

The same arguments hold for compression in the other direction (x_2 direction). The global stiffness is then $K = 2E(b/a)h$. It is distributed among the different rods as well.

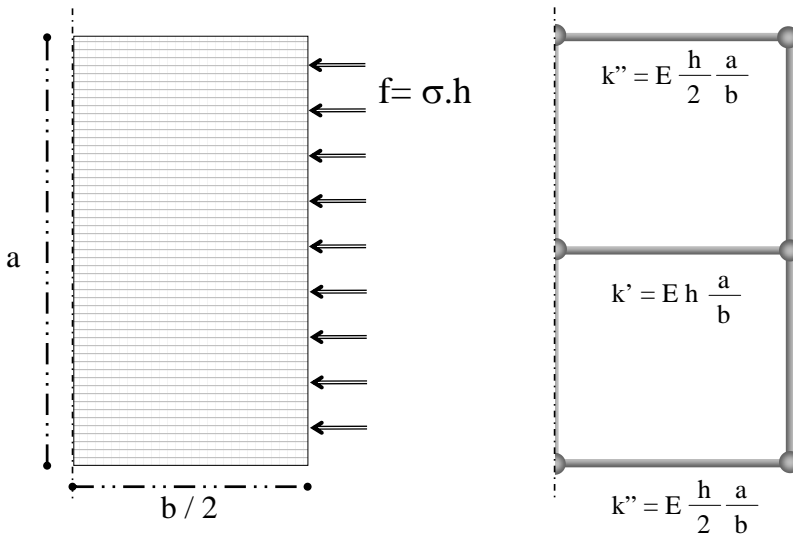


Figure 7. Rod-and-spring structure. The variables ψ , φ and θ are the rotations of the rods with respect to the horizontal plane. The arrows stand for imposed forces or displacements.

The next step is to express the length variation for each rod as a function of the angular variables. An example is depicted in [Figure 6](#), right, for the middle transversal rod which is associated with the rotation parameter ψ . The initial length for this rod is $b/2$. For a given value of ψ , the length L of the rod is given by $\frac{1}{2}b = L \cos \psi + u_2$. The length variation of the rod is

$$\Delta L = \frac{b}{2} \left(1 - \frac{1 - \varepsilon_2}{\cos \psi} \right).$$

The contact between the structure and the support, assumed to be rigid, is managed by the introduction of a reaction force, denoted R , exerted “upwards” by the support on the mobile lateral hinges ([Figure 8](#)).

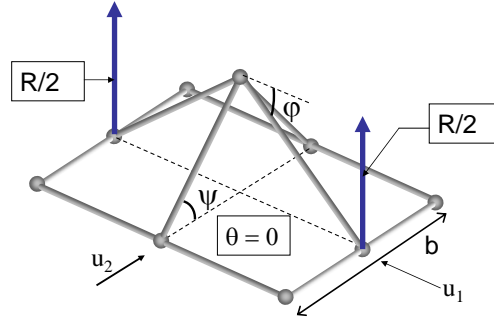


Figure 8. Contact force R due to the rigid support, applied to the central hinges when they come into contact with the support.

The vertical displacement d of a lateral hinge is linked to the lateral displacement and to θ by

$$d = \left(\frac{b}{2} - u_2 \right) \tan \theta = \frac{b}{2} (1 - \varepsilon_2) \tan \theta. \quad (8)$$

The displacement d and the reaction R satisfy the conditions

$$d \geq 0, \quad R \geq 0, \quad Rd = 0.$$

In order to take into account the unilateral contact, we introduce the potential energy of the system, which reads, in a nondimensional form $\tilde{V} = V/(\pi^2 D)$,

$$\begin{aligned} \tilde{V} = & \tilde{a}\theta^2 + \tilde{a}\psi^2 + \frac{1}{\tilde{a}}\varphi^2 + \frac{2}{3}\varphi(\psi - \theta) + \tilde{k}\tilde{a}\varepsilon_1^2 \\ & + \tilde{k}\tilde{a}\left(1 - \frac{1 - \varepsilon_1}{\cos \varphi}\right)^2 + \tilde{k}\tilde{a}\left(1 - \frac{1 - \varepsilon_2}{\cos \theta}\right)^2 + \tilde{k}\tilde{a}\left(1 - \frac{1 - \varepsilon_2}{\cos \psi}\right)^2 - \lambda d(\theta), \end{aligned} \quad (9)$$

where

$$\tilde{k} = \frac{Ehb^2}{4\pi^2 D}, \quad \tilde{a} = \frac{a}{b}, \quad \lambda = \frac{Rb}{2\pi^2 D}.$$

At equilibrium, λ and $d(\theta)$ satisfy the complementary conditions

$$\lambda \geq 0, \quad \lambda d(\theta) = 0.$$

In the following, we will omit the symbol \sim and handle only nondimensional values. Note that \tilde{k} expresses the competition between the stretching stiffness and the bending stiffness. Also note that the cosine terms account for the geometric nonlinearities. The notation $\varepsilon_1 = \rho\varepsilon$, $\varepsilon_2 = \varepsilon$ is introduced for the prescribed strains, with ρ , the biaxial prescribed displacement ratio.

5. Analysis of the equilibria

The rod system has two angular degrees of freedom, φ and ψ . The shape of the potential energy indicates that the underlying equilibrium equations of the systems are nonlinear. The equilibrium equations are solved for the rod system subjected to displacements $U = (u_1, u_2)$ as a simplified model for the delaminated film strip subjected to biaxial deformation $\varepsilon = (\varepsilon_1, \varepsilon_2)$. A sensitivity study of equilibrium stability with respect to the various parameters is carried out in order to characterize the transition from straight-sided wrinkle to bubbles.

The model experiment to which the results of this study can be compared is the previously described case of a 50 nm nickel thin film on a Polycarbonate substrate. A Young's modulus of 160 GPa has been experimentally determined for the film by using nano-indentation. The Poisson ratio is $\nu = 0.31$. The width b of the delaminated area is around $3 \mu\text{m}$. Using these data, a value of approximately 1000 is found for the parameter \tilde{k} .

Due to the fact that the substrate is relatively compliant compared to the film, the boundaries of the delaminated film can move slightly toward each other during delamination, leading to a relaxation in the direction x_2 (along the width of the delaminated strip). Hence ε_2 is smaller than ε_1 in the experimental case. The parameter ρ is set to 1.2 here in order to fit the non-equibiaxial loading conditions of the experiment.

The two variable parameters of the study are the aspect ratio of the unit cell a/b , accounting for the spatial periodicity of the bubble distribution, and the loading parameter ε , representing the level of compressive deformation prescribed by the substrate.

For each pair of parameters $(\varepsilon, a/b)$ a two-step procedure is carried out. The first step is the search of equilibria for which the system does not come into contact with the rigid support ($\theta > 0$, $\lambda = 0$). We will describe such equilibria as "contact-free". The second step is to check the existence of a contact equilibrium ($\theta = 0$, $\lambda > 0$). The potential energy can be computed for the different equilibria, and stability of the contact-free equilibria can be studied.

5.1. Search for contact-free equilibria ($\theta > 0$, $\lambda = 0$). We set $V_1(\varphi, \psi, \varepsilon) = V(\varphi, \psi, \lambda = 0, \varepsilon)$. The equilibrium equations for the contact-free equilibria are given by

$$\begin{aligned} \frac{\partial V_1}{\partial \psi} &= f_1(\varphi, \psi, \varepsilon) = 0, \\ \frac{\partial V_1}{\partial \varphi} &= f_2(\varphi, \psi, \varepsilon) = 0. \end{aligned} \tag{10}$$

The method consists in plotting the curves \mathcal{C}_1 and \mathcal{C}_2 representing $f_1 = 0$ and $f_2 = 0$, respectively, in the (φ, ψ) plane limited to the $(\psi \geq 0, \theta(\varphi, \psi) > 0)$ area for a given value of the loading parameter ε . Each couple of coordinates (ψ, φ) at an intersection point of the two curves corresponds to an equilibrium state.

Once a particular equilibrium (φ_1, ψ_1) has been identified, the Hessian matrix for the potential energy ($\partial^2 V / \partial u_i \partial u_j$ for $1 \leq i \leq 2, 1 \leq j \leq 2$) is computed with $u = (\varphi, \psi)$ in order to determine the shape of the potential energy in the neighborhood of equilibrium. The two eigenvalues, λ_1 and λ_2 , of this Hessian matrix are computed and their sign is analyzed.

- (a) If λ_1 and λ_2 are both strictly positive, the equilibrium is at a local strict minimum of the potential energy.
- (b) If λ_1 and λ_2 are both negative, the equilibrium is at a maximum of the potential energy.
- (c) If λ_1 and λ_2 have different signs, the equilibrium is at a saddle point of the potential energy.

Following the second variation stability criterion, only case (a) is associated with a stable equilibrium. As we shall see, two types of equilibria are discovered this way. The first one is the expected straight sided wrinkle (SSW) equilibrium, with $\varphi = 0$ and $\psi > 0$. The second one is a shallow-bubble (SB) equilibrium, with $\psi > \theta > 0$. This last equilibrium can represent experimentally observed equilibria that are characterized by shallow undulations at the top of SSW.

5.2. Search for contact equilibria ($\theta = 0, \lambda \geq 0$). Our model allows for the existence of a contact equilibrium subjected to a nonzero reaction force from the support ($\lambda > 0$). This is the representation of the deep-bubble (DB) equilibrium, experimentally observed when the film comes into contact with the substrate as bubbles form from the SSW equilibrium.

Write $V_2(\psi, \lambda, \varepsilon) = V(\varphi = (b/a)\psi, \psi, \lambda, \varepsilon)$. The equilibrium equations in the case of contact yield

$$\begin{aligned} \frac{\partial V_2}{\partial \psi} &= g_1(\psi, \lambda, \varepsilon) = 0, \\ \frac{\partial V_2}{\partial \lambda} &= g_2(\psi, \lambda, \varepsilon) = 0. \end{aligned} \tag{11}$$

For a particular set of values for $(a/b, \varepsilon)$, the solution to the above system indicates if a contact equilibrium exists (solution with $\psi > 0$ and $\lambda > 0$), as well as the value of ψ for the given equilibrium (that is, the bubble height).

5.3. Results. Three different post-critical behaviors can be identified, depending on the a/b ratio. We will address the problem of the equilibrium transition in light of three cases corresponding to the ratios $a/b = 0.9, 1$, and 1.1 . These cases are in the range of those observed experimentally. For each case, deformation levels from low to high are considered. Increasing the deformation level gives rise to new equilibria and can also trigger a change in the stability of those equilibria. The results are depicted in Figures 9, 10, and 11. Curves \mathcal{C}_1 and \mathcal{C}_2 have been drawn in solid and dashed lines, respectively. Each intersection point of the curves indicates the existence of an equilibrium. The trivial planar equilibrium ($\varphi = 0, \psi = 0$) and the SSW equilibrium ($\varphi = 0, \psi \neq 0$) are easily identified.

The potential V has also been plotted in each case in order to observe its shape in the neighborhood of each equilibrium. It is possible to see whether the equilibrium is a minimum, a maximum, or a saddle point of the potential, and hence to indicate its stability. Only the part where $\psi > \frac{a}{b}\varphi$ (that is, $\theta \geq 0$) is relevant. The other part shows the existence of a bilateral equilibrium, which is not possible here because of the rigid support.

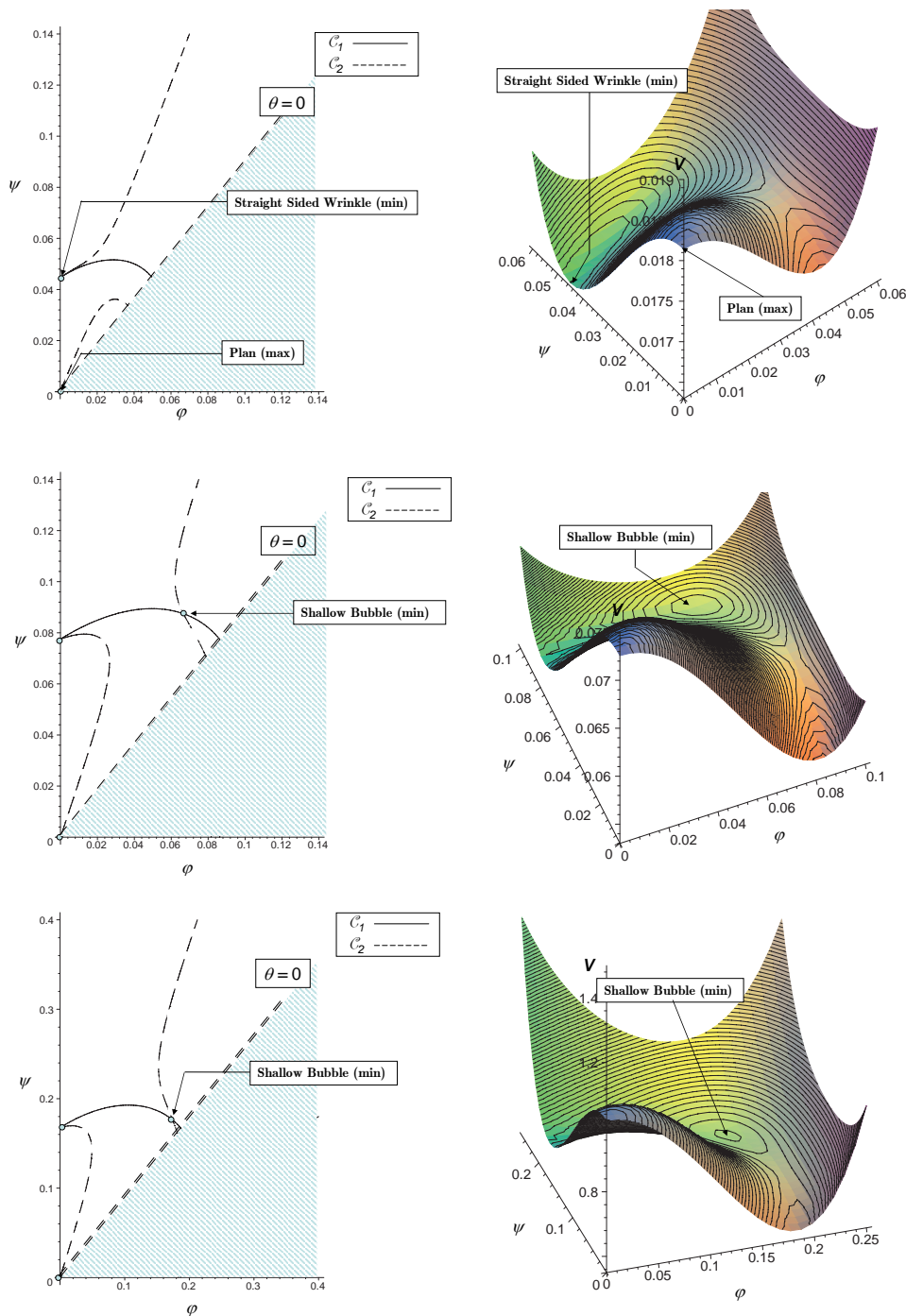


Figure 9. Equilibria for $a/b = 0.9$. Top: $\varepsilon = 0.002$; planar equilibrium ($\varphi = 0, \psi = 0$) and straight-sided equilibrium $\varphi = 0$ can be identified on the vertical axis. Middle: $\varepsilon = 0.004$; a stable shallow-bubble equilibrium arises, and the straight-sided equilibrium is unstable. Bottom: $\varepsilon = 0.015$; same equilibria as for $\varepsilon = 0.004$.

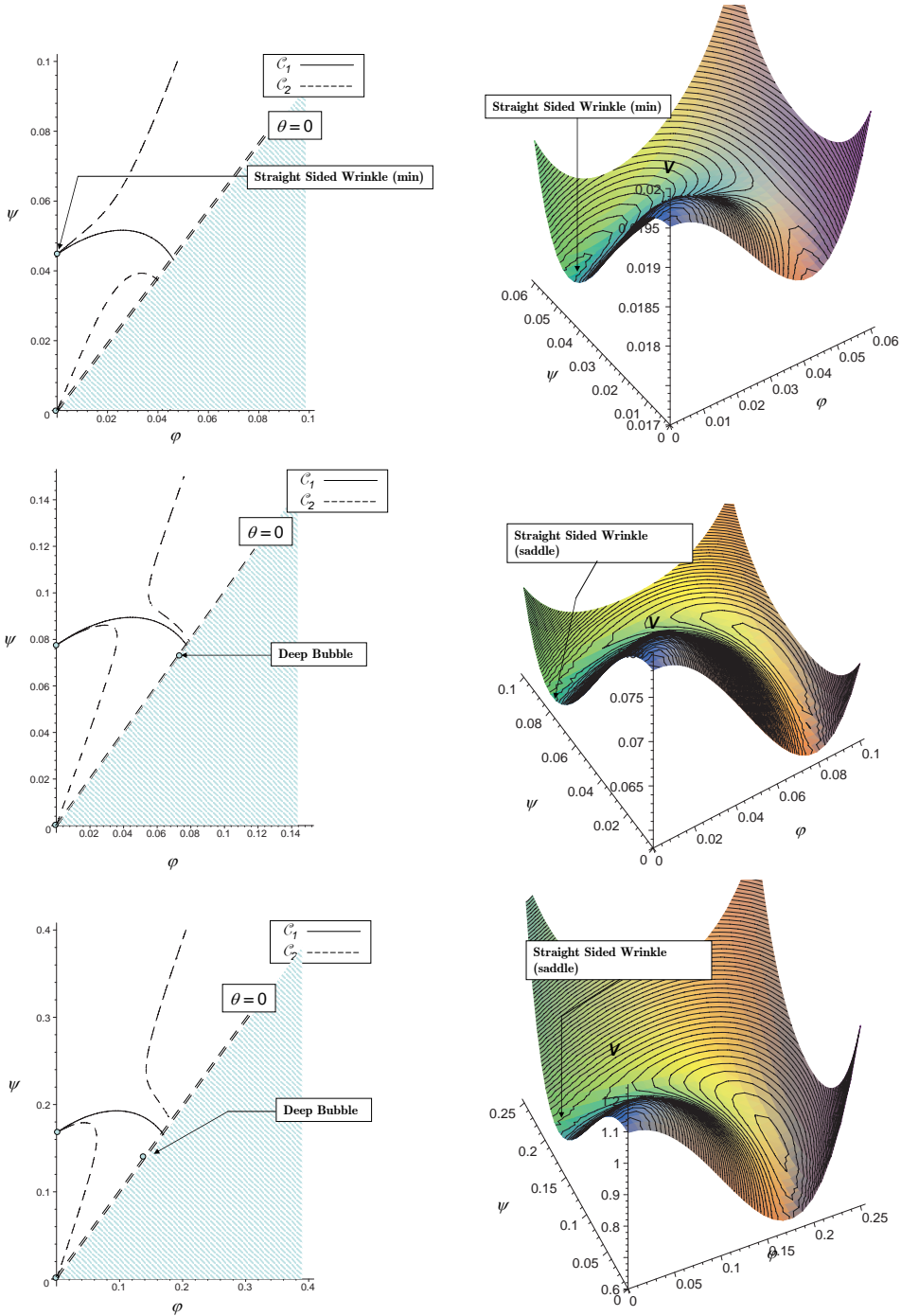


Figure 10. Equilibria for $a/b = 1$. Top: $\varepsilon = 0.002$; planar equilibrium ($\varphi = 0$, $\psi = 0$) and straight-sided equilibrium $\varphi = 0$ can be identified on the vertical axis. Middle: $\varepsilon = 0.004$; deep-bubble equilibrium is arising, and the other equilibria are unstable. Bottom: $\varepsilon = 0.015$; same observation as for $\varepsilon = 0.004$.

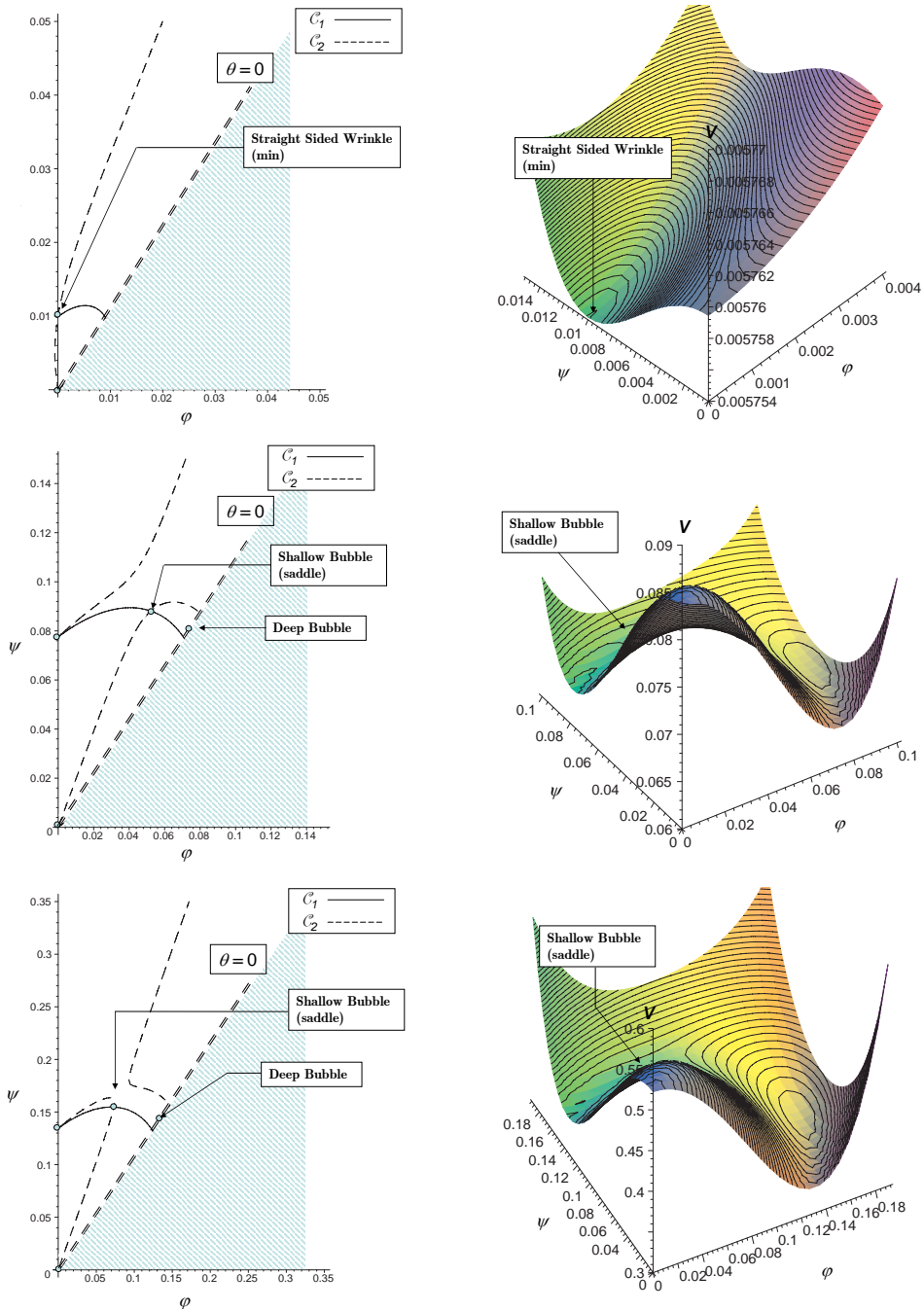


Figure 11. Equilibria for $a/b = 1.1$. Top: $\varepsilon = 0.001$; planar equilibrium ($\varphi = 0, \psi = 0$) and straight-sided equilibrium $\varphi = 0$ can be identified on the vertical axis. Middle: $\varepsilon = 0.004$; A shallow bubble equilibrium (unstable) and a deep bubble equilibrium are identified. Bottom: $\varepsilon = 0.010$. The same equilibria can be identified for higher deformation levels.

Short bubbles ($a/b = 0.9$). The case of short bubbles is illustrated in [Figure 9](#) for $a/b = 0.9$. A stable SB (shallow-bubble) equilibrium rapidly arises as the deformation level is raised. This buckling mode, characterized by values of φ that are rather small compared to ψ can be connected to experimental observations of small undulations (or incipient bubbles) on top of straight-sided wrinkles. It is experimentally observed that these undulations are short. As the deformation level ε increases, these undulations become deeper.

There is no deep-bubble equilibrium for this a/b ratio (no solution for the contact equilibrium problem). It is interesting to note that there are no experimental observations of short deep bubbles. We expect these to arise for higher levels of a/b .

Intermediate case ($a/b = 1$). For small values of the deformation ε ([Figure 10](#), top), the SSW (straight-sided wrinkle) equilibrium is stable. There is no other equilibrium, except the trivial flat equilibrium, which is unstable.

Over a critical value of the deformation, the SSW becomes unstable. The existence of a deep-bubble equilibrium arises simultaneously with this loss of stability ([Figure 10](#), middle and bottom). The potential energy of the DB (deep-bubble) equilibrium is lower than that of the SSW equilibrium, and in fact occupies the potential energy minimum. When losing its stability, the SSW will hence evolve toward a DB equilibrium. It is interesting to see, from the shape of the curves, that the transition cannot evolve smoothly. Because of the absence of a SB equilibrium, the structure cannot continuously evolve from SSW to DB. Snap-through is to be expected.

Longer bubbles ($a/b = 1.1$). The case $a/b \geq 1.1$ is illustrated in [Figure 11](#). For small values of ε , the SSW is the only nonplanar equilibrium (top) and is stable (at a potential energy minimum). As ε increases, an SB and a DB equilibria arise (middle and bottom), and the SSW loses its stability. The SB equilibrium is unstable and the system evolves to the DB equilibrium at the potential energy minimum.

It is worth noting that the SSW and the SB equilibria are close to each other in the (ψ, φ) space. Some defects on the wrinkle could trigger the shallow-bubble saddle-point mode in a transient way, which would lead to a snap-through to the deep-bubble equilibrium. This phenomenon has been observed both numerically and experimentally over a critical a/b ratio of the bubbles [[Parry et al. 2005](#)].

6. Conclusion

The results of this study clarify and give an explanation for various experimental observations of the post-critical buckling of delaminated films. First of all, some undulations are sometimes experimentally observed on the top of the straight-sided wrinkles ([Figure 2](#)). These undulations are short and shallow and neighbor areas with deep bubbles that are obviously longer. This is in agreement with the conclusion that the shallow bubbles equilibrium is stable for small values of a/b .

Experimental observations show that above a given length of the bubbles there is a transition between the straight-sided wrinkle and a bubble equilibrium where the edges of the bubbles are touching the substrate. It is also observed that for a critical value of a/b , between 1.1 and 1.2, the transition is subcritical [[Parry et al. 2005](#)]. This is in good agreement with the results of the rod model, both qualitatively and quantitatively, because it has been shown that for a critical value of the a/b ratio the shallow-bubble equilibrium becomes unstable and that the deep-bubble equilibrium is stable. If some undulations are

present on the top of the straight-sided wrinkle, due to defects or imperfections, the saddle-point shallow-bubble equilibrium can be briefly met immediately preceding the deep-bubble equilibrium with an abrupt transition.

The ability of this model to accurately represent the transitions in the post-critical regime of this buckling film system (qualitatively but also quantitatively, and with only a few variables) encourages further exploration and motivates work that will model the trigger behavior of plates and films for various post-critical regimes.

References

- [Abdallah et al. 2008] A. A. Abdallah, P. C. P. Bouten, J. M. J. Den Toonder, and G. de With, “The effect of moisture on buckle delamination of thin inorganic layers on a polymer substrate”, *Thin Solid Films* **516**:6 (January 2008), 1063–1073.
- [Arbocz et al. 1987] J. Arbocz, M. Potier-Ferry, J. Singer, and V. Tvergaard, *Buckling and post-buckling: four lectures in experimental, numerical and theoretical solid mechanics based on talks given at the CISM-Meeting held in Udine, Italy, September 29–October 3, 1985*, Lecture notes in physics **288**, Springer-Verlag, Berlin, 1987.
- [Audoly 1999] B. Audoly, “Stability of straight delamination blisters”, *Phys. Rev. Lett.* **83**:20 (1999), 4124–4127.
- [Coupeau et al. 1998] C. Coupeau, J. C. Girard, and J. Grilhe, “Plasticity study of deformed materials by in situ atomic force microscopy”, *J. Vac. Sci. Technol. B* **16**:4 (July 1998), 1964–1970.
- [Evans and Hutchinson 2007] A. G. Evans and J. W. Hutchinson, “The mechanics of coating delamination in thermal gradients”, *Surf. Coat. Technol.* **201**:18 (June 2007), 7905–7916.
- [Faulhaber et al. 2006] S. Faulhaber, C. Mercer, M.-W. Moon, J. W. Hutchinson, and A. Evans, “Buckling delamination in compressed multilayers on curved substrates with accompanying ridge cracks”, *J. Mech. Phys. Solids* **54**:5 (2006), 1004–1028.
- [George et al. 2002] M. George, C. Coupeau, J. Colin, F. Cleymand, and J. Grilhe, “Delamination of metal thin films on polymer substrates: from straight-sided blisters to varicose structures”, *Philos. Mag. A* **82**:3 (2002), 633–641.
- [Gille and Rau 1984] G. Gille and B. Rau, “Buckling instability and adhesion of carbon layers”, *Thin Solid Films* **120**:2 (1984), 109–121.
- [Gruttmann and Pham 2008] F. Gruttmann and V. D. Pham, “A finite element model for the analysis of buckling driven delaminations of thin films on rigid substrates”, *Comput. Mech.* **41**:3 (2008), 361–370.
- [Hutchinson and Suo 1991] J. W. Hutchinson and Z. Suo, “Mixed mode cracking in layered materials”, *Adv. Appl. Mech.* **29** (1991), 63–191.
- [Jagla 2007] E. A. Jagla, “Modeling the buckling and delamination of thin films”, *Phys. Rev. B* **75**:8 (2007), 085405.
- [Moon et al. 2004] M. W. Moon, K. R. Lee, K. H. Oh, and J. W. Hutchinson, “Buckle delamination on patterned substrates”, *Acta Mater.* **52**:10 (2004), 3151–3159.
- [Parry et al. 2005] G. Parry, J. Colin, C. Coupeau, F. Foucher, A. Cimetiere, and J. Grilhe, “Snapthrough occurring in the postbuckling of thin films”, *Appl. Phys. Lett.* **86**:8 (2005), 081905.
- [Parry et al. 2006] G. Parry, A. Cimetiere, C. Coupeau, J. Colin, and J. Grilhe, “Stability diagram of unilateral buckling patterns of strip-delaminated films”, *Phys. Rev. E* **74**:6 Pt 2 (2006), 066601.
- [Song et al. 2008] J. Song, H. Jiang, W. M. Choi, and D. Y. Khang, “An analytical study of two-dimensional buckling of thin films on compliant substrates”, *J. Appl. Phys.* **103**:1 (2008), 014303.
- [Thompson and Hunt 1973] J. M. T. Thompson and G. W. Hunt, *A general theory of elastic stability*, John Wiley, London, 1973.
- [Thouless et al. 1992] M. D. Thouless, J. W. Hutchinson, and E. G. Liniger, “Plane-strain, buckling-driven delamination of thin films: model experiments and mode-II fracture”, *Acta Metall. Mater.* **40**:10 (1992), 2639–2649.
- [Tvergaard and Hutchinson 2008] V. Tvergaard and J. W. Hutchinson, “Mode III effects on interface delamination”, *J. Mech. Phys. Solids* **56**:1 (January 2008), 215–229.

Received 8 Oct 2008. Revised 4 Dec 2008. Accepted 4 Dec 2008.

GUILLAUME PARRY: guillaume.parry@simap.grenoble-inp.fr

Laboratoire SIMaP/LTPCM, CNRS UMR 5266-INPG-UJF, 1130 Rue de la Piscine, 38402 Saint Martin d'Hères, France

CHRISTOPHE COUPEAU: christophe.coupeau@univ-poitiers.fr

Laboratoire de Metallurgie Physique (LMP), UMR 6630 du CNRS, Université de Poitiers, BP 30179, 86962 Futuroscope Cedex, France

JÉRÔME COLIN: jerome.colin@univ-poitiers.fr

Laboratoire de Metallurgie Physique (LMP), UMR 6630 du CNRS, Université de Poitiers, BP 30179, 86962 Futuroscope Cedex, France

ALAIN CIMETIÈRE: alain.cimetiere@univ-poitiers.fr

Laboratoire de Metallurgie Physique (LMP), UMR 6630 du CNRS, Université de Poitiers, BP 30179, 86962 Futuroscope Cedex, France

FUNDAMENTAL SOLUTION IN THE THEORY OF VISCOELASTIC MIXTURES

SIMONA DE CICCO AND MERAB SVANADZE

In the first part of the paper, we derive a linear theory of thermoviscoelastic binary mixtures. Then, the fundamental solution of the system of linear coupled partial differential equations of steady oscillations (steady vibrations) of the theory of viscoelastic binary mixtures is constructed in terms of elementary functions, and basic properties are established.

1. Introduction

The theory of mixtures was introduced to describe the mechanics of materials in which two or more constituents coexist. The crucial factor that differentiates this theory from other classical approaches is the matter of scale. The theory of mixtures is intended to study the behavior of a material at the small scale of its inhomogeneities and the states of its individual constituents. The great abstraction that a material can be modeled as a single homogeneous continuum is avoided. In contrast with approaches that use averaging procedures, the theory of mixtures permits to define the motion, mass density, stress tensor, internal energy, temperature, entropy and other relevant physical quantities, for every single constituent of the continuum. In the case of the diffusion of a fluid through a porous solid or of one solid through another, this information is critical. The theory of mixtures overcomes the inadequacy of classical theories which cannot predict the stresses in the solid in a diffusion process. Moreover, the theory allows for the possibility of studying another two distinct physical phenomena: chemical reactions and multiple temperatures. These issues are important in the mechanics of geological and biological materials. For the history of the problem and the analysis of the results we refer to [Bowen 1976; Atkin and Craine 1976b; 1976a; Bedford and Drumheller 1983; Samohyl 1987; Rajagopal and Tao 1995]. Starting from the origin of the modern formulation of the theory a variety of mathematical models have been developed in order to study mixtures exhibiting complex mechanical behaviors.

In the last three decades there has been interest in the formulation of thermomechanical theories of viscoelastic mixtures. There exist various continuum theories of viscoelastic composites [Marinov 1978; McCarthy and Tiersten 1983; Hills and Roberts 1987; 1988; Aboudi 2000; Iesan and Quintanilla 2002]. A nonlinear theory of heat-conducting viscoelastic mixtures in a Lagrangian description was presented by Iesan [2004]. In this theory the mixture consists of two constituents: a porous elastic solid and a viscous fluid. A linear variant of this theory was developed by Quintanilla [2005], and the existence and exponential decay of solutions are proved.

Iesan and Nappa [2008] introduced a nonlinear theory of heat-conducting mixtures where the individual components are modelled as Kelvin–Voigt viscoelastic materials. The basic equations are obtained using a Lagrangian description (in contrast with mixtures of fluids), which naturally yields an Eulerian

Keywords: mixtures, thermoviscoelasticity, constitutive equations, fundamental solution.

description. We remark that material and spatial descriptions lead to different theories with different meaning of displacement vector field. Moreover the latter does not allow us to consider boundary conditions in the reference configuration.

For investigating boundary value problems of the theory of elasticity and thermoelasticity with the potential method (boundary integral method) it is necessary to construct fundamental solutions of systems of partial differential equations and establish their basic properties [Kupradze 1965; Kupradze et al. 1979].

Several methods are known for constructing fundamental solutions of differential equations of the classical theory of elasticity and thermoelasticity [Gurtin 1972, Chapter 9; Hetnarski and Ignaczak 2004, Chapter 7; Kupradze et al. 1979, Chapter 2]. The fundamental solutions of equations of the linear theory of binary mixtures for elastic solids have been constructed by Svanadze [1988; 1990]. Useful information on fundamental solutions of differential equations is contained in [Hörmander 1983, Chapters 10 and 12; Lopatinsky 1951].

In the first part of this paper (Sections 2 and 3), we derive a linear theory of thermoviscoelastic mixtures, assuming that the constituents have a common temperature and that the mixture is subjected to a thermodynamical process that satisfies the Clausius–Duhem inequality. The intended applications of the theory are to viscoelastic composite materials, to viscoelastic mixtures of two compatible polymers, or to cortical bone. For a review of the literature on viscoelastic properties of cortical bone the reader is referred to [Lakes 2001]. As in [Jesan and Nappa 2008], with the aim to specify the boundary conditions in the reference configuration, a Lagrangian description is adopted. The constitutive equations are derived independently from nonlinear theory. In contrast with the theory of mixtures of fluids we find that the diffusive force depends on both relative displacement and relative velocity. This constitutive relation generalizes Darcy’s law and is frame-independent. We recall that, as observed by Wilmanski [2003], Darcy’s law is frame-dependent.

In the second part of this paper (Sections 4 and 5), the fundamental solution of the system of linear coupled partial differential equations of steady vibrations of the theory of viscoelastic binary mixtures is constructed in terms of elementary functions, and basic properties are established.

2. Basic equations

The mixtures under consideration consist of two interacting continua s_1 and s_2 . We assume that at time t_0 the body occupies the region B of Euclidean three-dimensional space E^3 and is bounded by piecewise smooth surface ∂B . In describing the motion of the body, we refer to the configuration at time t_0 and to a fixed system of rectangular Cartesian axes. We use vector and Cartesian tensor notation with Latin indices having the values 1, 2, 3. Greek indices are understood to range over the integers 1, 2 and a summation convention is not used for these indices. Bold letters denote vectors and tensors.

In the following \mathbf{X} and \mathbf{Y} are the positions of typical particles of s_1 and s_2 in the reference positions. Following Bedford and Stern [1972], we assume that $\mathbf{X} = \mathbf{Y}$, so that the particles occupy the same position in the reference configuration. The motion of the mixture is given by

$$\mathbf{x} = \mathbf{x}(\mathbf{X}, t), \quad \mathbf{y} = \mathbf{y}(\mathbf{X}, t), \quad (\mathbf{X}, t) \in B \times I, \quad (2-1)$$

where $I = [t_0, \infty)$.

We consider arbitrary material regions P_α of each constituent which coincide at time t_0 with a region P . We postulate an energy balance in the form [Green and Naghdi 1965; 1969; 1972]

$$\frac{d}{dt} \sum_{\alpha=1}^2 \int_P \rho_\alpha (e + \frac{1}{2} \mathbf{v}^{(\alpha)} \cdot \mathbf{v}^{(\alpha)}) dv = \sum_{\alpha=1}^2 \left(\int_P \rho_\alpha (\mathbf{f}^{(\alpha)} \cdot \mathbf{v}^{(\alpha)} + r) dv - \int_{\partial P} (\tilde{\mathbf{t}}^{(\alpha)} \cdot \mathbf{v}^{(\alpha)} + q^{(\alpha)}) da \right), \quad (2-2)$$

where e is the internal energy of the mixture per unit mass, $\mathbf{v}^{(\alpha)}$ is the velocity vector field associated with the constituent s_α , $\mathbf{f}^{(\alpha)}$ is the body force per unit mass acting on the constituent s_α , $\tilde{\mathbf{t}}^{(\alpha)}$ is the partial stress vector, r is the external volume supply per unit mass per unit time, $q^{(\alpha)}$ is the heat flux per unit area per unit time associated with the constituent s_α , and ρ_α is the mass density of the constituent s_α .

Let $\mathbf{u}^{(\alpha)}$ be the displacement vector field associated with the constituent s_α . In the linear theory we assume that $\mathbf{u}^{(\alpha)} = \varepsilon \mathbf{u}'^{(\alpha)}$, with ε being a constant small enough for squares and higher powers to be neglected, and with $\mathbf{u}'^{(\alpha)}$ independent of ε . The functions (2-1) can be expressed in the form

$$\mathbf{x} = \mathbf{X} + \mathbf{u}^{(1)}, \quad \mathbf{y} = \mathbf{X} + \mathbf{u}^{(2)}. \quad (2-3)$$

By (2-2) and (2-3) we get

$$\sum_{\alpha=1}^2 \int_P (\rho_\alpha \dot{e} + \rho_\alpha \dot{\mathbf{u}}^{(\alpha)} \cdot \ddot{\mathbf{u}}^{(\alpha)}) dv = \sum_{\alpha=1}^2 \left(\int_P (\rho_\alpha \mathbf{f}^{(\alpha)} \cdot \dot{\mathbf{u}}^{(\alpha)} + \rho r) dv - \int_{\partial P} (\tilde{\mathbf{t}}^{(\alpha)} \cdot \dot{\mathbf{u}}^{(\alpha)} + q^{(\alpha)}) da \right). \quad (2-4)$$

Following Green and Naghdi [1965], (2-4) is also true when $\dot{\mathbf{u}}^{(\alpha)}$ is replaced by $\mathbf{u}^{(\alpha)} + \mathbf{c}$, with \mathbf{c} an arbitrary constant vector, so that by subtraction we have

$$\sum_{\alpha=1}^2 \left(\int_P \rho_\alpha (\ddot{\mathbf{u}}^{(\alpha)} - \mathbf{f}^{(\alpha)}) dv - \int_{\partial P} \tilde{\mathbf{t}}^{(\alpha)} da \right) = \mathbf{0}. \quad (2-5)$$

From (2-5) we obtain

$$\tilde{\mathbf{t}}^{(1)} + \tilde{\mathbf{t}}^{(2)} = (\mathbf{t}^{(1)} + \mathbf{t}^{(2)})^T \mathbf{n}, \quad (2-6)$$

where $\mathbf{t}^{(\alpha)T}$ is the transpose of the stress tensor $\mathbf{t}^{(\alpha)}$ associated with the constituent s_α , and \mathbf{n} is the unit outward normal vector to the surface ∂P . It follows from (2-5) and (2-6) that

$$\sum_{\alpha=1}^2 (\text{div } \mathbf{t}^{(\alpha)T} + \rho_\alpha \mathbf{f}^{(\alpha)} - \rho_\alpha \ddot{\mathbf{u}}^{(\alpha)}) = \mathbf{0}. \quad (2-7)$$

On taking into account (2-6) and (2-7), (2-4) can be written in the form

$$\int_P \left(\rho \dot{e} + \frac{1}{2} (\rho_1 \ddot{\mathbf{u}}^{(1)} - \rho_2 \ddot{\mathbf{u}}^{(2)}) \cdot (\dot{\mathbf{u}}^{(1)} - \dot{\mathbf{u}}^{(2)}) - \frac{1}{2} (\rho_1 \mathbf{f}^{(1)} - \rho_2 \mathbf{f}^{(2)}) \cdot (\dot{\mathbf{u}}^{(1)} - \dot{\mathbf{u}}^{(2)}) \right. \\ \left. - \frac{1}{2} (\mathbf{t}^{(1)} + \mathbf{t}^{(2)})^T \cdot (\dot{\mathbf{H}}^{(1)} + \dot{\mathbf{H}}^{(2)}) - \rho r \right) dv = \int_{\partial P} \left(\frac{1}{2} (\tilde{\mathbf{t}}^{(1)} - \tilde{\mathbf{t}}^{(2)}) \cdot (\dot{\mathbf{u}}^{(1)} - \dot{\mathbf{u}}^{(2)}) + q \right) da, \quad (2-8)$$

where

$$\mathbf{H}^{(\alpha)} = \nabla \mathbf{u}^{(\alpha)}, \quad q = q^{(1)} + q^{(2)}, \quad \rho = \rho_1 + \rho_2.$$

With an argument similar to that used in obtaining (2-6) from (2-5), we obtain

$$\frac{1}{2}(\tilde{\mathbf{t}}^{(1)} - \tilde{\mathbf{t}}^{(2)} - (\mathbf{t}^{(1)} - \mathbf{t}^{(2)})^T \mathbf{n}) \cdot (\dot{\mathbf{u}}^{(1)} - \dot{\mathbf{u}}^{(2)}) + \mathbf{q} - \mathbf{q} \cdot \mathbf{n} = 0, \quad (2-9)$$

where \mathbf{q} is the heat flux vector. We introduce the notation

$$\mathbf{p} = \frac{1}{2}(\text{div}(\mathbf{t}^{(1)} - \mathbf{t}^{(2)})^T + \rho_1 \mathbf{f}^{(1)} - \rho_2 \mathbf{f}^{(2)} - (\rho_1 \ddot{\mathbf{u}}^{(1)} - \rho_2 \ddot{\mathbf{u}}^{(2)})). \quad (2-10)$$

Introducing (2-9) and (2-10) into Equation (2-8) and applying the resulting equation to an arbitrary region P , we obtain

$$\rho \dot{e} = \mathbf{t}^{(1)T} \cdot \dot{\mathbf{H}}^{(1)} + \mathbf{t}^{(2)T} \cdot \dot{\mathbf{H}}^{(2)} + \mathbf{p} \cdot \dot{\mathbf{d}} + \rho r + \text{div } \mathbf{q}, \quad (2-11)$$

where

$$\mathbf{d} = \mathbf{u}^{(1)} - \mathbf{u}^{(2)}. \quad (2-12)$$

From (2-10) and (2-11) we get the motion equations of the mixture:

$$\text{div } \mathbf{t}^{(1)T} - \mathbf{p} + \rho_1 \mathbf{f}^{(1)} = \rho_1 \ddot{\mathbf{u}}^{(1)}, \quad \text{div } \mathbf{t}^{(2)T} + \mathbf{p} + \rho_2 \mathbf{f}^{(2)} = \rho_2 \ddot{\mathbf{u}}^{(2)}. \quad (2-13)$$

As in [Green and Naghdi 1965], we now consider motions of the mixture which are such that the velocities differ from those of the given motion only by a superposed uniform rigid body angular velocity, the continua occupying the same position at time t . In this case $\dot{\mathbf{H}}^{(1)}$ and $\dot{\mathbf{H}}^{(2)}$ are replaced by $\dot{\mathbf{H}}^{(1)} + \mathbf{\Omega}$ and $\dot{\mathbf{H}}^{(2)} + \mathbf{\Omega}$, respectively, and $\dot{\mathbf{d}}$ is replaced by $\dot{\mathbf{d}} + \mathbf{\Omega} \mathbf{d}$, where $\mathbf{\Omega}$ is an arbitrary skew symmetric tensor. Equation (2-13) implies that

$$\mathbf{t}^{(1)} + \mathbf{t}^{(2)} = (\mathbf{t}^{(1)} + \mathbf{t}^{(2)})^T. \quad (2-14)$$

Now we assume that the constituents have a common temperature and adopt the following entropy production inequality [Green and Naghdi 1965; 1972]:

$$\frac{d}{dt} \int_P \rho \eta \, dv - \int_P \frac{1}{\theta} \rho r \, dv - \int_{\partial P} \frac{1}{\theta} \mathbf{q} \cdot \mathbf{da} \geq 0, \quad (2-15)$$

where η is the entropy per unit mass of the mixture, and $\theta (> 0)$ is the absolute temperature. If we get $\mathbf{q} = \mathbf{q} \cdot \mathbf{n}$ the inequality (2-15) reduces to

$$\rho \theta \dot{\eta} - \rho r - \text{div } \mathbf{q} + \frac{1}{\theta} \mathbf{q} \cdot \mathbf{\Theta} \geq 0, \quad (2-16)$$

where $\mathbf{\Theta} = \nabla \theta$. Introducing the Helmholtz free energy $\psi = e - \eta \theta$, the energy Equation (2-11) takes the form

$$\rho (\dot{\psi} + \dot{\theta} \eta + \theta \dot{\eta}) = \mathbf{t}^{(1)T} \cdot \dot{\mathbf{H}}^{(1)} + \mathbf{t}^{(2)T} \cdot \dot{\mathbf{H}}^{(2)} + \mathbf{p} \cdot \dot{\mathbf{d}} + \rho r + \text{div } \mathbf{q}. \quad (2-17)$$

Taking (2-17) into account, the inequality (2-16) becomes

$$\mathbf{t}^{(1)T} \cdot \dot{\mathbf{H}}^{(1)} + \mathbf{t}^{(2)T} \cdot \dot{\mathbf{H}}^{(2)} + \mathbf{p} \cdot \dot{\mathbf{d}} - \dot{\sigma} - \rho \eta \dot{\theta} + \frac{1}{\theta} \mathbf{q} \cdot \mathbf{\Theta} \geq 0, \quad (2-18)$$

where $\sigma = \rho \psi$.

3. Constitutive equations

In what follows we assume that the constituents s_α are viscoelastic materials of Kelvin–Voigt type. We consider materials characterized by the following set of independent constitutive variables

$$S = (\mathbf{H}^{(1)}, \mathbf{H}^{(2)}, \mathbf{d}, \dot{\mathbf{H}}^{(1)}, \dot{\mathbf{H}}^{(2)}, \dot{\mathbf{d}}, \theta, \Theta; X).$$

The constitutive equations take the form

$$\sigma = \sigma(S), \quad \mathbf{t}^{(\alpha)} = \mathbf{t}^{(\alpha)}(S), \quad \mathbf{p} = \mathbf{p}(S), \quad \eta = \eta(S), \quad \mathbf{q} = \mathbf{q}(S), \quad (3-1)$$

where the response functionals are assumed to be sufficiently smooth. We assume that there are not internal constraints. In order to satisfy the axiom of material-frame indifference, the functionals (3-1) must be expressible in the form

$$\sigma = \tilde{\sigma}(S^0), \quad \mathbf{t}^{(\alpha)} = \tilde{\mathbf{t}}^{(\alpha)}(S^0), \quad \mathbf{p} = \tilde{\mathbf{p}}(S^0), \quad \eta = \tilde{\eta}(S^0), \quad \mathbf{q} = \tilde{\mathbf{q}}(S^0), \quad (3-2)$$

where

$$S^0 = (\mathbf{E}, \mathbf{G}, \mathbf{d}, \dot{\mathbf{E}}, \dot{\mathbf{G}}, \dot{\mathbf{d}}, \theta, \Theta; X), \quad (3-3)$$

and

$$\mathbf{E} = \frac{1}{2}(\mathbf{H}^{(1)} + \mathbf{H}^{(1)T}), \quad \mathbf{G} = \mathbf{H}^{(1)T} + \mathbf{H}^{(2)}. \quad (3-4)$$

In view of (3-2), (3-3), and (3-4), the inequality (2-18) implies that σ is independent by $\dot{\mathbf{E}}$, $\dot{\mathbf{G}}$, $\dot{\mathbf{d}}$ and Θ , that is

$$\sigma = U(\mathbf{E}, \mathbf{G}, \mathbf{d}, \theta; X). \quad (3-5)$$

Moreover we have

$$\rho\eta = -\frac{\partial U}{\partial \theta}. \quad (3-6)$$

Using (3-5) and (3-6) the inequality (2-18) reduces to

$$\left(\mathbf{t}^{(1)T} - \frac{\partial U}{\partial \mathbf{E}} - \left(\frac{\partial U}{\partial \mathbf{G}} \right)^T \right) \cdot \dot{\mathbf{H}}^{(1)} + \left(\mathbf{t}^{(2)T} - \frac{\partial U}{\partial \mathbf{G}} \right) \cdot \dot{\mathbf{H}}^{(2)} + \left(\mathbf{p} - \frac{\partial U}{\partial \mathbf{d}} \right) \cdot \dot{\mathbf{d}} + \frac{1}{\theta} \mathbf{q} \cdot \Theta \geq 0. \quad (3-7)$$

We introduce the notations

$$\boldsymbol{\tau}^{(1)} = \mathbf{t}^{(1)} - \frac{\partial U}{\partial \mathbf{E}} - \frac{\partial U}{\partial \mathbf{G}}, \quad \boldsymbol{\tau}^{(2)} = \mathbf{t}^{(2)} - \left(\frac{\partial U}{\partial \mathbf{G}} \right)^T, \quad \boldsymbol{\pi} = \mathbf{p} - \frac{\partial U}{\partial \mathbf{d}}. \quad (3-8)$$

The functions $\boldsymbol{\tau}^{(\alpha)}$ and $\boldsymbol{\pi}$ are the dissipative parts of $\mathbf{t}^{(\alpha)}$ and \mathbf{p} . The inequality (3-7) may be written in the form

$$\boldsymbol{\tau}^{(1)T} \cdot \dot{\mathbf{H}}^{(1)} + \boldsymbol{\tau}^{(2)T} \cdot \dot{\mathbf{H}}^{(2)} + \boldsymbol{\pi} \cdot \dot{\mathbf{d}} + \frac{1}{\theta} \mathbf{q} \cdot \Theta \geq 0. \quad (3-9)$$

Let us introduce the functions $\boldsymbol{\Gamma}$ and $\boldsymbol{\Lambda}$ by

$$\boldsymbol{\tau}^{(1)} = \boldsymbol{\Gamma}(S^0) + \boldsymbol{\Lambda}(S^0), \quad \boldsymbol{\tau}^{(2)} = \boldsymbol{\Lambda}^T(S^0). \quad (3-10)$$

From (2-14) we deduce that

$$\boldsymbol{\tau}^{(1)} + \boldsymbol{\tau}^{(2)} = (\boldsymbol{\tau}^{(1)} + \boldsymbol{\tau}^{(2)})^T, \quad \boldsymbol{\Gamma} = \boldsymbol{\Gamma}^T. \quad (3-11)$$

In view of (3-10) and (3-11) the dissipation inequality (3-9) becomes

$$\mathbf{\Gamma} \cdot \dot{\mathbf{E}} + \mathbf{\Lambda} \cdot \dot{\mathbf{G}} + \boldsymbol{\pi} \cdot \dot{\mathbf{d}} + \frac{1}{\theta} \mathbf{q} \cdot \boldsymbol{\Theta} \geq 0. \quad (3-12)$$

The inequality (3-12) implies that

$$\mathbf{\Gamma}(S^*) = \mathbf{0}, \quad \mathbf{\Lambda}(S^*) = \mathbf{0}, \quad \boldsymbol{\pi}(S^*) = \mathbf{0}, \quad \mathbf{q}(S^*) = \mathbf{0}, \quad (3-13)$$

where

$$S^* = (\mathbf{E}, \mathbf{G}, \mathbf{d}, \mathbf{0}, \mathbf{0}, \mathbf{0}, \theta, \mathbf{0}; \mathbf{X}).$$

With the help of (3-6), (3-8), and (3-10), the energy balance reduces to

$$\rho \theta \dot{\eta} = \mathbf{\Gamma} \cdot \dot{\mathbf{E}} + \mathbf{\Lambda} \cdot \dot{\mathbf{G}} + \boldsymbol{\pi} \cdot \dot{\mathbf{d}} + \rho r + \operatorname{div} \mathbf{q}. \quad (3-14)$$

Let us denote

$$\theta = T + T_0, \quad T = \varepsilon T', \quad \varepsilon^n \cong 0 \quad \text{for } n \geq 2, \quad (3-15)$$

where T_0 is the constant absolute temperature of the body in the reference configuration and T' is independent of ε . In what follows we consider the case of centrosymmetric materials. We assume that U has the form

$$U = \frac{1}{2} \mathbf{E} \cdot \mathbf{A} \mathbf{E} + \mathbf{E} \cdot \mathbf{B} \mathbf{G} + \frac{1}{2} \mathbf{G} \cdot \mathbf{C} \mathbf{G} + \frac{1}{2} \mathbf{d} \cdot \mathbf{a} \mathbf{d} - (\boldsymbol{\beta}^{(1)} \cdot \mathbf{E} + \boldsymbol{\beta}^{(2)} \cdot \mathbf{G}) T - \frac{1}{2} a_0 T^2, \quad (3-16)$$

where \mathbf{A} , \mathbf{B} and \mathbf{C} are fourth order tensors, \mathbf{a} , $\boldsymbol{\beta}^{(1)}$ and $\boldsymbol{\beta}^{(2)}$ are second order tensors, and a_0 is a constant. The constitutive coefficients have the symmetries

$$A_{ijrs} = A_{jirs} = A_{rsij}, \quad B_{ijrs} = B_{jirs}, \quad C_{ijrs} = C_{rsij}, \quad a_{ij} = a_{ji}, \quad \beta_{ij}^{(1)} = \beta_{ji}^{(1)}. \quad (3-17)$$

Letting be \mathbf{M} a fourth order tensor, the transpose of \mathbf{M} is the unique tensor \mathbf{M}^T with the property

$$\mathbf{M} \mathbf{p} \cdot \mathbf{q} = \mathbf{p} \cdot \mathbf{M}^T \mathbf{q},$$

where \mathbf{p} and \mathbf{q} are second order tensors. Consequently by (3-17) we have $\mathbf{A} = \mathbf{A}^T$ and $\mathbf{C} = \mathbf{C}^T$. From (3-6), (3-8) and (3-16) we obtain

$$\begin{aligned} \mathbf{t}^{(1)} &= (\mathbf{A} + \mathbf{B}^T) \mathbf{E} + (\mathbf{B} + \mathbf{C}) \mathbf{G} - (\boldsymbol{\beta}^{(1)} + \boldsymbol{\beta}^{(2)}) T + \boldsymbol{\tau}^{(1)}, \\ \mathbf{t}^{(2)T} &= \mathbf{B}^T \mathbf{E} + \mathbf{C} \mathbf{G} - \boldsymbol{\beta}^{(2)} T + \boldsymbol{\tau}^{(2)T}, \\ \mathbf{p} &= \mathbf{a} \mathbf{d} + \boldsymbol{\pi}, \quad \rho \eta = \boldsymbol{\beta}^{(1)} \cdot \mathbf{E} + \boldsymbol{\beta}^{(2)} \cdot \mathbf{G} + a_0 T. \end{aligned} \quad (3-18)$$

The relations (3-13) leads to

$$\mathbf{\Gamma} = \mathbf{A}^* \dot{\mathbf{E}} + \mathbf{C}^* \dot{\mathbf{G}}, \quad \mathbf{\Lambda} = \mathbf{B}^* \dot{\mathbf{E}} + \mathbf{D}^* \dot{\mathbf{G}}, \quad \boldsymbol{\pi} = \mathbf{a}^* \dot{\mathbf{d}} + \mathbf{b}^* \nabla T, \quad \mathbf{q} = \mathbf{k} \nabla T + \mathbf{f} \dot{\mathbf{d}}, \quad (3-19)$$

where \mathbf{A}^* , \mathbf{B}^* , \mathbf{C}^* , and \mathbf{D}^* are fourth order tensors and \mathbf{a}^* , \mathbf{b}^* , \mathbf{k} , and \mathbf{f} are second order tensors. Using (3-19) the relations (3-10) can be put in the form

$$\boldsymbol{\tau}^{(1)} = (\mathbf{A}^* + \mathbf{B}^*) \dot{\mathbf{E}} + (\mathbf{C}^* + \mathbf{D}^*) \dot{\mathbf{G}}, \quad \boldsymbol{\tau}^{(2)T} = \mathbf{B}^* \dot{\mathbf{E}} + \mathbf{D}^* \dot{\mathbf{G}}. \quad (3-20)$$

Taking into account (3-15) the energy Equation (3-14) reduces to

$$\rho T_0 \dot{\eta} = \rho r + \operatorname{div} \mathbf{q}. \quad (3-21)$$

The basic equations of linear viscoelastic mixtures are: the equations of motion (2-13), the equation of energy (3-21), the constitutive equations (3-18) and (3-20), and the geometric equations (2-12) and (3-4). We remark that the relation (3-18)₃ generalizes Darcy's law. This relation has been obtained from constitutive assumptions and is frame-independent. In the case of isotropy, the constitutive equations (3-18) and (3-20) take the form

$$\begin{aligned} \mathbf{t}^{(1)} &= 2(\mu + \zeta) \mathbf{E} + (\lambda + \nu)(\operatorname{tr} \mathbf{E}) \mathbf{I} + (2\kappa + \zeta) \mathbf{G} + (2\gamma + \zeta) \mathbf{G}^T \\ &\quad + (\alpha + \nu)(\operatorname{tr} \mathbf{G}) \mathbf{I} - (\beta^{(1)} + \beta^{(2)}) T \mathbf{I} + 2(\mu^* + \zeta_1^*) \dot{\mathbf{E}} \\ &\quad + (\lambda^* + \nu_1^*)(\operatorname{tr} \dot{\mathbf{E}}) \mathbf{I} + (2\kappa^* + \zeta^*) \dot{\mathbf{G}} + (2\gamma^* + \zeta^*) \dot{\mathbf{G}}^T + (\alpha^* + \nu^*)(\operatorname{tr} \dot{\mathbf{G}}) \mathbf{I}, \\ \mathbf{t}^{(2)} &= 2\zeta \mathbf{E} + \nu(\operatorname{tr} \mathbf{E}) \mathbf{I} + 2\kappa \mathbf{G}^T + 2\gamma \mathbf{G} + \alpha(\operatorname{tr} \mathbf{G}) \mathbf{I} - \beta^{(2)} T \mathbf{I} \\ &\quad + 2\zeta_1^* \dot{\mathbf{E}} + \nu_1^*(\operatorname{tr} \dot{\mathbf{E}}) \mathbf{I} + 2\gamma^* \dot{\mathbf{G}} + 2\kappa^* \dot{\mathbf{G}}^T + \alpha^*(\operatorname{tr} \dot{\mathbf{G}}) \mathbf{I}, \\ \mathbf{p} &= a \mathbf{d} + a^* \dot{\mathbf{d}} + b^* \nabla T, \quad \rho \eta = \beta^{(1)} \operatorname{tr} \mathbf{E} + \beta^{(2)} \operatorname{tr} \mathbf{G} + a_0 T, \quad \mathbf{q} = k \nabla T + f \dot{\mathbf{d}}, \end{aligned} \quad (3-22)$$

where $\lambda, \mu, \gamma, \dots, f$ are constitutive coefficients, $\mathbf{I} = (\delta_{ji})_{3 \times 3}$ is the unit matrix, δ_{lj} is the Kronecker delta, $\mathbf{u}^{(1)} = (u_1^{(1)}, u_2^{(1)}, u_3^{(1)})$, $\mathbf{u}^{(2)} = (u_1^{(2)}, u_2^{(2)}, u_3^{(2)})$.

We introduce the notations

$$\begin{aligned} \alpha_1 &= \mu + 2\kappa + 2\zeta, & \alpha_2 &= \lambda + \mu + \alpha + 2\nu + 2\gamma + 2\zeta, \\ \alpha_3 &= 2\gamma + \zeta, & \alpha_4 &= \alpha + \nu + 2\kappa + \zeta, \\ \alpha_5 &= 2\kappa, & \alpha_6 &= \alpha + 2\gamma, \\ \alpha_1^* &= \mu^* + 2\kappa^* + \zeta^* + \zeta_1^*, & \alpha_2^* &= \lambda^* + \mu^* + \alpha^* + \nu^* + \nu_1^* + 2\gamma^* + \zeta^* + \zeta_1^*, \\ \alpha_3^* &= 2\gamma^* + \zeta^*, & \alpha_4^* &= \alpha^* + \nu^* + 2\kappa^* + \zeta^*, \\ \alpha_5^* &= 2\gamma^* + \zeta_1^*, & \alpha_6^* &= \alpha^* + \nu_1^* + 2\kappa^* + \zeta_1^*, \\ \alpha_7^* &= 2\kappa^*, & \alpha_8^* &= \alpha^* + 2\gamma^*, \\ \beta_1 &= \beta^{(1)} + \beta^{(2)} + b^*, & \beta_2 &= \beta^{(2)} - b^*, \\ \beta_3 &= T_0(\beta^{(1)} + \beta^{(2)}), & \beta_4 &= T_0 \beta^{(2)}. \end{aligned} \quad (3-23)$$

From (2-12), (2-13), (3-4), and (3-21)–(3-23) we have

$$\begin{aligned} &\alpha_1 \Delta \mathbf{u}^{(1)} + \alpha_2 \nabla \operatorname{div} \mathbf{u}^{(1)} + \alpha_3 \Delta \mathbf{u}^{(2)} + \alpha_4 \nabla \operatorname{div} \mathbf{u}^{(2)} - a(\mathbf{u}^{(1)} - \mathbf{u}^{(2)}) \\ &+ \alpha_1^* \Delta \dot{\mathbf{u}}^{(1)} + \alpha_2^* \nabla \operatorname{div} \dot{\mathbf{u}}^{(1)} + \alpha_3^* \Delta \dot{\mathbf{u}}^{(2)} + \alpha_4^* \nabla \operatorname{div} \dot{\mathbf{u}}^{(2)} - a^*(\dot{\mathbf{u}}^{(1)} - \dot{\mathbf{u}}^{(2)}) - \beta_1 \nabla T + \rho_1 \mathbf{f}^{(1)} = \rho_1 \ddot{\mathbf{u}}^{(1)}, \\ &\alpha_3 \Delta \mathbf{u}^{(1)} + \alpha_4 \nabla \operatorname{div} \mathbf{u}^{(1)} + \alpha_5 \Delta \mathbf{u}^{(2)} + \alpha_6 \nabla \operatorname{div} \mathbf{u}^{(2)} + a(\mathbf{u}^{(1)} - \mathbf{u}^{(2)}) \\ &+ \alpha_5^* \Delta \dot{\mathbf{u}}^{(1)} + \alpha_6^* \nabla \operatorname{div} \dot{\mathbf{u}}^{(1)} + \alpha_7^* \Delta \dot{\mathbf{u}}^{(2)} + \alpha_8^* \nabla \operatorname{div} \dot{\mathbf{u}}^{(2)} + a^*(\dot{\mathbf{u}}^{(1)} - \dot{\mathbf{u}}^{(2)}) - \beta_2 \nabla T + \rho_2 \mathbf{f}^{(2)} = \rho_2 \ddot{\mathbf{u}}^{(2)}, \\ &k \Delta T - a_0 T_0 \dot{T} - \operatorname{div}(\beta_3 \dot{\mathbf{u}}^{(1)} + \beta_4 \dot{\mathbf{u}}^{(2)}) + f \operatorname{div}(\dot{\mathbf{u}}^{(1)} - \dot{\mathbf{u}}^{(2)}) + \rho r = 0. \end{aligned} \quad (3-24)$$

The system (3-24) can be written as

$$\begin{aligned} \hat{a}_1 \Delta \mathbf{u}^{(1)} + \hat{a}_2 \nabla \operatorname{div} \mathbf{u}^{(1)} + \hat{a}_3 \Delta \mathbf{u}^{(2)} + \hat{a}_4 \nabla \operatorname{div} \mathbf{u}^{(2)} - \hat{\xi}(\mathbf{u}^{(1)} - \mathbf{u}^{(2)}) + \beta_1 \nabla T + \rho_1 \mathbf{f}^{(1)} &= \rho_1 \ddot{\mathbf{u}}^{(1)}, \\ \hat{a}_5 \Delta \mathbf{u}^{(1)} + \hat{a}_6 \nabla \operatorname{div} \mathbf{u}^{(1)} + \hat{a}_7 \Delta \mathbf{u}^{(2)} + \hat{a}_8 \nabla \operatorname{div} \mathbf{u}^{(2)} + \hat{\xi}(\mathbf{u}^{(1)} - \mathbf{u}^{(2)}) + \beta_2 \nabla T + \rho_2 \mathbf{f}^{(2)} &= \rho_2 \ddot{\mathbf{u}}^{(2)}, \\ k \Delta T - a_0 T_0 \dot{T} - (T_0 \beta_1 - T_0 b^* - f) \operatorname{div} \dot{\mathbf{u}}^{(1)} - (T_0 \beta_2 + T_0 b^* + f) \operatorname{div} \dot{\mathbf{u}}^{(2)} + \rho r &= 0, \end{aligned} \quad (3-25)$$

where

$$\hat{a}_j = \alpha_j + \alpha_j^* \frac{\partial}{\partial t}, \quad \hat{a}_l = \alpha_{l-2} + \alpha_l^* \frac{\partial}{\partial t}, \quad \hat{\xi} = a + a^* \frac{\partial}{\partial t}, \quad j = 1, 2, 3, 4, \quad l = 5, 6, 7, 8.$$

In the isothermal case from (3-25) we obtain the following system of equations of motion in the linear theory of viscoelastic mixtures:

$$\begin{aligned} \hat{a}_1 \Delta \mathbf{u}^{(1)} + \hat{a}_2 \nabla \operatorname{div} \mathbf{u}^{(1)} + \hat{a}_3 \Delta \mathbf{u}^{(2)} + \hat{a}_4 \nabla \operatorname{div} \mathbf{u}^{(2)} - \hat{\xi}(\mathbf{u}^{(1)} - \mathbf{u}^{(2)}) + \rho_1 \mathbf{f}^{(1)} &= \rho_1 \ddot{\mathbf{u}}^{(1)}, \\ \hat{a}_5 \Delta \mathbf{u}^{(1)} + \hat{a}_6 \nabla \operatorname{div} \mathbf{u}^{(1)} + \hat{a}_7 \Delta \mathbf{u}^{(2)} + \hat{a}_8 \nabla \operatorname{div} \mathbf{u}^{(2)} + \hat{\xi}(\mathbf{u}^{(1)} - \mathbf{u}^{(2)}) + \rho_2 \mathbf{f}^{(2)} &= \rho_2 \ddot{\mathbf{u}}^{(2)}. \end{aligned} \quad (3-26)$$

If the body forces $\mathbf{f}^{(1)}$ and $\mathbf{f}^{(2)}$ are assumed to be absent, and the partial displacement vectors $\mathbf{u}^{(1)}$ and $\mathbf{u}^{(2)}$ are postulated to have a harmonic time variation, that is,

$$\mathbf{u}^{(j)}(\mathbf{x}, t) = \operatorname{Re} [\mathbf{w}^{(j)}(\mathbf{x}) e^{-i\omega t}], \quad j = 1, 2,$$

then from system of equations of motion (3-26) we obtain the following system of equations of steady vibration in the linear theory of viscoelastic mixtures:

$$\begin{aligned} a_1 \Delta \mathbf{w}^{(1)} + a_2 \nabla \operatorname{div} \mathbf{w}^{(1)} + a_3 \Delta \mathbf{w}^{(2)} + a_4 \nabla \operatorname{div} \mathbf{w}^{(2)} + \xi_1 \mathbf{w}^{(1)} + \xi \mathbf{w}^{(2)} &= \mathbf{0}, \\ a_5 \Delta \mathbf{w}^{(1)} + a_6 \nabla \operatorname{div} \mathbf{w}^{(1)} + a_7 \Delta \mathbf{w}^{(2)} + a_8 \nabla \operatorname{div} \mathbf{w}^{(2)} + \xi \mathbf{w}^{(1)} + \xi_2 \mathbf{w}^{(2)} &= \mathbf{0}, \end{aligned} \quad (3-27)$$

where ω is the oscillation frequency ($\omega > 0$), and

$$\begin{aligned} a_j &= \alpha_j - i\omega \alpha_j^*, \quad a_l = \alpha_{l-2} - i\omega \alpha_l^*, \quad j = 1, 2, 3, 4, \quad l = 5, 6, 7, 8, \\ \xi &= a - i\omega a^*, \quad \xi_s = \rho_s \omega^2 - \xi, \quad s = 1, 2. \end{aligned}$$

In the second part of this paper (Sections 4 and 5) the fundamental solution of the system (3-27) is constructed in terms of elementary functions, and basic properties are established.

4. Fundamental solution of the system of equations of steady vibration

We introduce the matrix differential operator

$$\mathbf{R}(\mathbf{D}_x) = (R_{mn}(\mathbf{D}_x))_{6 \times 6},$$

where

$$\begin{aligned} R_{lj}(\mathbf{D}_x) &= (a_1 \Delta + \xi_1) \delta_{lj} + a_2 \frac{\partial^2}{\partial x_l \partial x_j}, & R_{l;j+3}(\mathbf{D}_x) &= (a_3 \Delta + \xi) \delta_{lj} + a_4 \frac{\partial^2}{\partial x_l \partial x_j}, \\ R_{l+3;j}(\mathbf{D}_x) &= (a_5 \Delta + \xi) \delta_{lj} + a_6 \frac{\partial^2}{\partial x_l \partial x_j}, & R_{l+3;j+3}(\mathbf{D}_x) &= (a_7 \Delta + \xi_2) \delta_{lj} + a_8 \frac{\partial^2}{\partial x_l \partial x_j}, \end{aligned}$$

$$\mathbf{x} = (x_1, x_2, x_3), \quad \mathbf{D}_x = \left(\frac{\partial}{\partial x_1}, \frac{\partial}{\partial x_2}, \frac{\partial}{\partial x_3} \right), \quad \xi_s = \rho_s \omega^2 - \zeta, \quad s = 1, 2, \quad l, j = 1, 2, 3.$$

The system (3-27) can be written as

$$\mathbf{R}(\mathbf{D}_x) \mathbf{W}(\mathbf{x}) = \mathbf{0},$$

where $\mathbf{W} = (\mathbf{w}^{(1)}, \mathbf{w}^{(2)})$ is a six-component vector function on E^3 .

We assume that the constitutive coefficients satisfy the condition

$$(a_1 a_7 - a_3 a_5)[(a_1 + a_2)(a_7 + a_8) - (a_3 + a_4)(a_5 + a_6)] \neq 0. \quad (4-1)$$

Definition. The fundamental solution of the system (3-27) (the fundamental matrix of operator $\mathbf{R}(\mathbf{D}_x)$) is the matrix $\Psi(\mathbf{x}) = (\Psi_{lj}(\mathbf{x}))_{6 \times 6}$ satisfying the condition [Hörmander 1983, Chapter 10; Lopatinsky 1951]

$$\mathbf{R}(\mathbf{D}_x) \Psi(\mathbf{x}) = \delta(\mathbf{x}) \mathbf{J}, \quad (4-2)$$

where δ is the Dirac delta, $\mathbf{J} = (\delta_{lj})_{6 \times 6}$ is the unit matrix, and $\mathbf{x} \in E^3$.

We consider the system of equations

$$\begin{aligned} a_1 \Delta \mathbf{w}^{(1)} + a_2 \nabla \operatorname{div} \mathbf{w}^{(1)} + a_5 \Delta \mathbf{w}^{(2)} + a_6 \nabla \operatorname{div} \mathbf{w}^{(2)} + \zeta_1 \mathbf{w}^{(1)} + \zeta \mathbf{w}^{(2)} &= \mathbf{F}', \\ a_3 \Delta \mathbf{w}^{(1)} + a_4 \nabla \operatorname{div} \mathbf{w}^{(1)} + a_7 \Delta \mathbf{w}^{(2)} + a_8 \nabla \operatorname{div} \mathbf{w}^{(2)} + \zeta \mathbf{w}^{(1)} + \zeta_2 \mathbf{w}^{(2)} &= \mathbf{F}'', \end{aligned} \quad (4-3)$$

where \mathbf{F}' and \mathbf{F}'' are three-component vector functions on E^3 .

As one may easily verify, the system (4-3) can be written in the form

$$\mathbf{R}^T(\mathbf{D}_x) \mathbf{W}(\mathbf{x}) = \mathbf{F}(\mathbf{x}), \quad (4-4)$$

where \mathbf{R}^T is the transpose of matrix \mathbf{R} , $\mathbf{F} = (\mathbf{F}', \mathbf{F}'')$, and $\mathbf{x} \in E^3$.

Applying the operator div to (4-3)₁ and (4-3)₂ we have

$$\begin{aligned} [(a_1 + a_2) \Delta + \zeta_1] \operatorname{div} \mathbf{w}^{(1)} + [(a_5 + a_6) \Delta + \zeta] \operatorname{div} \mathbf{w}^{(2)} &= \operatorname{div} \mathbf{F}', \\ [(a_3 + a_4) \Delta + \zeta] \operatorname{div} \mathbf{w}^{(1)} + [(a_7 + a_8) \Delta + \zeta_2] \operatorname{div} \mathbf{w}^{(2)} &= \operatorname{div} \mathbf{F}''. \end{aligned} \quad (4-5)$$

The system (4-5) may be written in matrix form:

$$\mathbf{Q}(\Delta) \mathbf{V} = \mathbf{f}, \quad (4-6)$$

where $\mathbf{V} = (\operatorname{div} \mathbf{w}^{(1)}, \operatorname{div} \mathbf{w}^{(2)})$, $\mathbf{f} = (f_1, f_2) = (\operatorname{div} \mathbf{F}', \operatorname{div} \mathbf{F}'')$, and

$$\mathbf{Q}(\Delta) = (Q_{lj}(\Delta))_{2 \times 2} = \begin{pmatrix} (a_1 + a_2) \Delta + \zeta_1 & (a_5 + a_6) \Delta + \zeta \\ (a_3 + a_4) \Delta + \zeta & (a_7 + a_8) \Delta + \zeta_2 \end{pmatrix}_{3 \times 3}.$$

System (4-6) implies

$$\Lambda_1(\Delta) \mathbf{V} = \Phi, \quad (4-7)$$

where

$$\begin{aligned} \Phi &= (\Phi_1, \Phi_2), \quad \Phi_j = \frac{1}{d_1} \sum_{l=1}^2 Q'_{lj} f_l, \quad \Lambda_1(\Delta) = \frac{1}{d_1} \det \mathbf{Q}(\Delta), \\ d_1 &= (a_1 + a_2)(a_7 + a_8) - (a_3 + a_4)(a_5 + a_6), \quad j = 1, 2, \end{aligned} \quad (4-8)$$

and Q'_{lj} is the cofactor of the element Q_{lj} of the matrix \mathbf{Q} ,

$$\begin{aligned} Q^*_{11} &= (a_7 + a_8)\Delta + \zeta_2, & Q^*_{12} &= -((a_3 + a_4)\Delta + \zeta), \\ Q^*_{21} &= -((a_5 + a_6)\Delta + \zeta), & Q^*_{22} &= (a_1 + a_2)\Delta + \zeta_1. \end{aligned}$$

It is easily seen that

$$\Lambda_1(\Delta) = (\Delta + k_1^2)(\Delta + k_2^2),$$

where k_1^2 and k_2^2 are the roots of the equation $\Lambda_1(-\chi) = 0$ (with respect to χ).

Applying the operator $\Lambda_1(\Delta)$ to (4-3)₁ and (4-3)₂, and taking (4-7) into account, we obtain

$$\begin{aligned} \Lambda_1(\Delta)((a_1\Delta + \zeta_1)\mathbf{w}^{(1)} + (a_5\Delta + \zeta)\mathbf{w}^{(2)}) &= \mathbf{F}_1, \\ \Lambda_1(\Delta)((a_3\Delta + \zeta)\mathbf{w}^{(1)} + (a_7\Delta + \zeta_2)\mathbf{w}^{(2)}) &= \mathbf{F}_2, \end{aligned} \quad (4-9)$$

where

$$\mathbf{F}_1 = \Lambda_1(\Delta)\mathbf{F}' - \nabla(a_2\Phi_1 + a_6\Phi_2), \quad \mathbf{F}_2 = \Lambda_1(\Delta)\mathbf{F}'' - \nabla(a_4\Phi_1 + a_8\Phi_2). \quad (4-10)$$

From system (4-9) we have

$$\Lambda_1(\Delta)\Lambda_2(\Delta)\mathbf{w}^{(1)} = \mathbf{H}_1, \quad \Lambda_1(\Delta)\Lambda_2(\Delta)\mathbf{w}^{(2)} = \mathbf{H}_2, \quad (4-11)$$

where

$$\Lambda_2(\Delta) = \frac{1}{d_2} \det \mathbf{Z}(\Delta), \quad d_2 = a_1a_7 - a_3a_5, \quad \mathbf{Z}(\Delta) = \begin{pmatrix} a_1\Delta + \zeta_1 & a_5\Delta + \zeta \\ a_3\Delta + \zeta & a_7\Delta + \zeta_2 \end{pmatrix}_{2 \times 2},$$

and

$$\mathbf{H}_j = \frac{1}{d_2} \sum_{l=1}^2 Z'_{lj}(\Delta)\mathbf{F}_l, \quad j = 1, 2. \quad (4-12)$$

Z'_{lj} is the cofactor of the element Z_{lj} of the matrix \mathbf{Z} .

$$\begin{aligned} Z'_{11} &= a_7\Delta + \zeta_2, & Z'_{12} &= -a_3\Delta - \zeta, \\ Z'_{21} &= -a_5\Delta - \zeta, & Z'_{22} &= a_1\Delta + \zeta_1. \end{aligned}$$

Obviously, $\Lambda_2(\Delta) = (\Delta + k_4^2)(\Delta + k_5^2)$, where k_4^2 and k_5^2 are the roots of the equation $\Lambda_2(-\chi) = 0$ (with respect to χ).

On the basis of (4-11) we get

$$\tilde{\Lambda}(\Delta)\mathbf{W}(\mathbf{x}) = \mathbf{H}(\mathbf{x}), \quad (4-13)$$

where $\mathbf{H} = (\mathbf{H}_1, \mathbf{H}_2)$ and $\tilde{\Lambda}(\Delta)$ is the diagonal matrix

$$\begin{aligned} \tilde{\Lambda}(\Delta) &= (\tilde{\Lambda}_{lj}(\Delta))_{6 \times 6}, \quad \tilde{\Lambda}_{11}(\Delta) = \tilde{\Lambda}_{22}(\Delta) = \dots = \tilde{\Lambda}_{66}(\Delta) = \Lambda_1(\Delta)\Lambda_2(\Delta), \\ \tilde{\Lambda}_{mn}(\Delta) &= 0, \quad m, n = 1, 2, \dots, 6, \quad m \neq n. \end{aligned}$$

In what follows we use the notations

$$\begin{aligned} m_{l1}(\Delta) &= \frac{1}{d_1}(a_2 Q'_{l1}(\Delta) + a_6 Q'_{l2}(\Delta)), & m_{l2}(\Delta) &= \frac{1}{d_1}(a_4 Q'_{l1}(\Delta) + a_8 Q'_{l2}(\Delta)), \\ n_{lj}(\Delta) &= -\frac{1}{d_2} \sum_{p=1}^2 m_{lp} Z'_{pj}, & l, j &= 1, 2. \end{aligned} \quad (4-14)$$

In view of (4-8), (4-10), and (4-14), from (4-12) we have

$$\mathbf{H}_j = \left(\frac{1}{d_2} Z'_{1j}(\Delta) \Lambda_1(\Delta) \mathbf{I} + n_{1j}(\Delta) \nabla \operatorname{div} \right) \mathbf{F}' + \left(\frac{1}{d_2} Z'_{2j}(\Delta) \Lambda_1(\Delta) \mathbf{I} + n_{2j}(\Delta) \nabla \operatorname{div} \right) \mathbf{F}'', \quad j = 1, 2, \quad (4-15)$$

where $\mathbf{I} = (\delta_{ij})_{3 \times 3}$ is the unit matrix.

Thus, from (4-15) we obtain

$$\mathbf{H}(\mathbf{x}) = \mathbf{L}^T(\mathbf{D}_\mathbf{x}) \mathbf{F}(\mathbf{x}), \quad (4-16)$$

where

$$\begin{aligned} \mathbf{L} &= (L_{lj})_{6 \times 6} = \begin{pmatrix} \mathbf{L}^{(1)} & \mathbf{L}^{(2)} \\ \mathbf{L}^{(3)} & \mathbf{L}^{(4)} \end{pmatrix}_{6 \times 6}, & \mathbf{L}^{(m)} &= (L_{lj}^{(m)})_{3 \times 3}, \\ \mathbf{L}^{(q)}(\mathbf{D}_\mathbf{x}) &= \frac{1}{d_2} Z'_{1q}(\Delta) \Lambda_1(\Delta) \mathbf{I} + n_{1q}(\Delta) \nabla \operatorname{div}, \\ \mathbf{L}^{(q+2)}(\mathbf{D}_\mathbf{x}) &= \frac{1}{d_2} Z'_{2q}(\Delta) \Lambda_1(\Delta) \mathbf{I} + n_{2q}(\Delta) \nabla \operatorname{div}, \\ q &= 1, 2, & m &= 1, 2, 3, 4. \end{aligned} \quad (4-17)$$

By virtue of (4-4) and (4-16), from (4-13) it follows that $\tilde{\mathbf{L}} \mathbf{W} = \mathbf{L}^T \mathbf{R}^T \mathbf{W}$. It is obvious that $\mathbf{L}^T \mathbf{R}^T = \tilde{\mathbf{L}}$ and, hence,

$$\mathbf{R}(\mathbf{D}_\mathbf{x}) \mathbf{L}(\mathbf{D}_\mathbf{x}) = \tilde{\mathbf{L}}(\Delta). \quad (4-18)$$

We assume that $k_l^2 \neq k_j^2 \neq 0$, that $l, j = 1, 2, 3, 4$, and that $l \neq j$.

Let

$$\begin{aligned} \mathbf{Y}(\mathbf{x}) &= (Y_{mn}(\mathbf{x}))_{6 \times 6}, & Y_{11}(\mathbf{x}) &= Y_{22}(\mathbf{x}) = \dots = Y_{66}(\mathbf{x}) = \sum_{j=1}^4 \eta_j h_j(\mathbf{x}), & Y_{mn}(\mathbf{x}) &= 0, \\ & & m, n &= 1, 2, \dots, 6, & m &\neq n, \end{aligned} \quad (4-19)$$

where

$$h_j(\mathbf{x}) = -\frac{1}{4\pi |\mathbf{x}|} e^{ik_j |\mathbf{x}|}, \quad \eta_j = \prod_{l \neq j, l=1}^4 (k_l^2 - k_j^2)^{-1}, \quad j = 1, 2, 3, 4. \quad (4-20)$$

Lemma 4.1. *The matrix \mathbf{Y} is the fundamental matrix of operator $\tilde{\mathbf{L}}(\Delta)$, that is*

$$\tilde{\mathbf{L}}(\Delta) \mathbf{Y}(\mathbf{x}) = \delta(\mathbf{x}) \mathbf{J}. \quad (4-21)$$

Proof. It is sufficient to show that

$$\Lambda_1(\Delta) \Lambda_2(\Delta) Y_{11}(\mathbf{x}) = \delta(\mathbf{x}).$$

Taking into account the equalities

$$\sum_{j=1}^4 \eta_j = 0, \quad \sum_{j=2}^4 \eta_j (k_1^2 - k_j^2) = 0, \quad \sum_{j=3}^4 \eta_j (k_1^2 - k_j^2)(k_2^2 - k_j^2) = 0,$$

$$\eta_4 (k_1^2 - k_4^2)(k_2^2 - k_4^2)(k_3^2 - k_4^2) = 1,$$

$$(\Delta + k_l^2)h_j(\mathbf{x}) = \delta(\mathbf{x}) + (k_l^2 - k_j^2)h_j(\mathbf{x}), \quad l, j = 1, 2, 3, 4, \quad \mathbf{x} \in E^3,$$

from (4-19) we have

$$\begin{aligned} \Lambda_1(\Delta)\Lambda_2(\Delta)Y_{11}(\mathbf{x}) &= (\Delta + k_2^2)\Lambda_2(\Delta) \sum_{j=1}^4 \eta_j (\delta(\mathbf{x}) + (k_1^2 - k_j^2)h_j(\mathbf{x})) \\ &= \Lambda_2(\Delta) \sum_{j=2}^4 \eta_j (k_1^2 - k_j^2) (\delta(\mathbf{x}) + (k_2^2 - k_j^2)h_j(\mathbf{x})) \\ &= (\Delta + k_4^2) \sum_{j=3}^4 \eta_j (k_1^2 - k_j^2)(k_2^2 - k_j^2) (\delta(\mathbf{x}) + (k_3^2 - k_j^2)h_j(\mathbf{x})) \\ &= (\Delta + k_4^2)h_4(\mathbf{x}) = \delta(\mathbf{x}). \end{aligned} \quad \square$$

We introduce the matrix

$$\Psi(\mathbf{x}) = L(D_x)Y(\mathbf{x}). \quad (4-22)$$

Using identity (4-18) from (4-21) and (4-22) we obtain

$$R(D_x)\Psi(\mathbf{x}) = R(D_x)L(D_x)Y(\mathbf{x}) = \tilde{\Lambda}(\Delta)Y(\mathbf{x}) = \delta(\mathbf{x})J.$$

Hence, $\Psi(\mathbf{x})$ is a solution to (4-2). We have thereby proved:

Theorem 4.2. *The matrix $\Psi(x)$ defined by (4-22) is the fundamental solution of system (3-27).*

Obviously, the matrix $\Psi(x)$ can be written in the form

$$\Psi = (\Psi_{mn})_{6 \times 6} = \begin{pmatrix} \Psi^{(1)} & \Psi^{(2)} \\ \Psi^{(3)} & \Psi^{(4)} \end{pmatrix}_{6 \times 6},$$

where

$$\Psi^{(j)}(\mathbf{x}) = L^{(j)}(D_x)Y_{11}(\mathbf{x}), \quad j = 1, 2, 3, 4. \quad (4-23)$$

5. Basic properties of the matrix $\Psi(x)$

Theorem 4.2 leads to the following results.

Corollary 5.1. *Each column of the matrix $\Psi(x)$ is the solution of system (3-27) at every point $x \in E^3$ except the origin.*

Corollary 5.2. *The fundamental solution of the system*

$$\begin{aligned} a_1 \Delta \mathbf{w}^{(1)} + a_2 \nabla \operatorname{div} \mathbf{w}^{(1)} + a_3 \Delta \mathbf{w}^{(2)} + a_4 \nabla \operatorname{div} \mathbf{w}^{(2)} &= \mathbf{0}, \\ a_5 \Delta \mathbf{w}^{(1)} + a_6 \nabla \operatorname{div} \mathbf{w}^{(1)} + a_7 \Delta \mathbf{w}^{(2)} + a_8 \nabla \operatorname{div} \mathbf{w}^{(2)} &= \mathbf{0}, \end{aligned} \quad (5-1)$$

is the matrix

$$\tilde{\Psi} = (\tilde{\Psi}_{mn})_{6 \times 6} = \begin{pmatrix} \tilde{\Psi}^{(1)} & \tilde{\Psi}^{(2)} \\ \tilde{\Psi}^{(3)} & \tilde{\Psi}^{(4)} \end{pmatrix}_{6 \times 6},$$

where

$$\begin{aligned} \tilde{\Psi}^{(p)} &= (\tilde{\Psi}_{lj}^{(p)})_{3 \times 3}, \\ \tilde{\Psi}_{lj}^{(1)} &= \left(\frac{a_7 + a_8}{d_1} \frac{\partial^2}{\partial x_l \partial x_j} - \frac{a_7}{d_2} \left(\frac{\partial^2}{\partial x_l \partial x_j} - \Delta \delta_{lj} \right) \right) h_0(\mathbf{x}), \\ \tilde{\Psi}_{lj}^{(2)} &= \left(-\frac{a_3 + a_4}{d_1} \frac{\partial^2}{\partial x_l \partial x_j} + \frac{a_3}{d_2} \left(\frac{\partial^2}{\partial x_l \partial x_j} - \Delta \delta_{lj} \right) \right) h_0(\mathbf{x}), \\ \tilde{\Psi}_{lj}^{(3)} &= \left(-\frac{a_5 + a_6}{d_1} \frac{\partial^2}{\partial x_l \partial x_j} + \frac{a_5}{d_2} \left(\frac{\partial^2}{\partial x_l \partial x_j} - \Delta \delta_{lj} \right) \right) h_0(\mathbf{x}), \\ \tilde{\Psi}_{lj}^{(4)} &= \left(\frac{a_1 + a_2}{d_1} \frac{\partial^2}{\partial x_l \partial x_j} - \frac{a_1}{d_2} \left(\frac{\partial^2}{\partial x_l \partial x_j} - \Delta \delta_{lj} \right) \right) h_0(\mathbf{x}), \\ h_0(\mathbf{x}) &= -\frac{|\mathbf{x}|}{8\pi}, \quad l, j = 1, 2, 3, \quad p = 1, 2, 3, 4. \end{aligned} \quad (5-2)$$

Obviously, the relations

$$\tilde{\Psi}_{mn}(\mathbf{x}) = O(|\mathbf{x}|^{-1}), \quad (5-3)$$

and

$$\frac{\partial^q}{\partial x_1^{q_1} \partial x_2^{q_2} \partial x_3^{q_3}} \tilde{\Psi}_{mn}(\mathbf{x}) = O(|\mathbf{x}|^{-1-q}),$$

hold in a neighborhood of the origin, where $m, n = 1, 2, \dots, 6$, $q = q_1 + q_2 + q_3$, $q \geq 1$.

In what follows we shall use the following lemma.

Lemma 5.3. *If condition (4-1) is satisfied, then*

$$\Delta n_{ij}(\Delta) = \frac{1}{d_1} Q'_{lj}(\Delta) \Lambda_2(\Delta) - \frac{1}{d_2} Z'_{lj}(\Delta) \Lambda_1(\Delta), \quad l, j = 1, 2. \quad (5-4)$$

Proof. In view of (4-14), we have

$$d_1 d_2 \Delta n_{ij}(\Delta) = -\Delta (Z'_{1j}(\Delta) (a_2 Q'_{11}(\Delta) + a_6 Q'_{12}(\Delta)) + Z'_{2j}(\Delta) (a_4 Q'_{11}(\Delta) + a_8 Q'_{12}(\Delta))). \quad (5-5)$$

Taking into account the equalities

$$\begin{aligned} a_2 \Delta Q'_{l1} + a_6 \Delta Q'_{l2} &= \delta_{1l} d_1 \Lambda_1(\Delta) - ((a_1 \Delta + \xi_1) Q'_{l1} + (a_5 \Delta + \xi) Q'_{l2}), \\ a_4 \Delta Q'_{l1} + a_8 \Delta Q'_{l2} &= \delta_{2l} d_1 \Lambda_1(\Delta) - ((a_3 \Delta + \xi_{bot}) Q'_{l1} + (a_7 \Delta + \xi_2) Q'_{l2}), \\ (a_1 \Delta + \xi_1) Z'_{1j} + (a_3 \Delta + \xi) Z'_{2j} &= d_2 \delta_{1j} \Lambda_2(\Delta), \\ (a_5 \Delta + \xi) Z'_{1j} + (a_7 \Delta + \xi_2) Z'_{2j} &= d_2 \delta_{2j} \Lambda_2(\Delta), \end{aligned}$$

from (5-5) we obtain

$$\begin{aligned} d_1 d_2 \Delta n_{lj}(\Delta) &= \\ -d_1 (\delta_{1l} Z'_{1j} + \delta_{2l} Z'_{2j}) \Lambda_1(\Delta) + ((a_1 \Delta + \xi_1) Z'_{1j} + (a_3 \Delta + \xi) Z'_{2j}) Q'_{l1} + ((a_5 \Delta + \xi) Z'_{1j} + (a_7 \Delta + \xi_2) Z'_{2j}) Q'_{l2} \\ &= -d_1 Z'_{lj} \Lambda_1(\Delta) + d_2 (\delta_{1j} Q'_{l1} + \delta_{2j} Q'_{l2}) \Lambda_2(\Delta) = d_2 Q'_{lj} \Lambda_2(\Delta) - d_1 Z'_{lj} \Lambda_1(\Delta). \quad \square \end{aligned}$$

In what follows we use the notations

$$\begin{aligned} d_{pj} &= \eta_{1j} Q'_{1p}(-k_j^2), \quad d_{p+2;j} = \eta_{1j} Q'_{2p}(-k_j^2), \quad d_{pl} = \eta_{1l} Z'_{1p}(-k_l^2), \quad d_{p+2;l} = \eta_{1l} Z'_{2p}(-k_l^2), \\ \eta_{1j} &= \frac{(-1)^j}{d_1 k_j^2 (k_2^2 - k_1^2)}, \quad \eta_{1l} = \frac{(-1)^l}{d_1 k_l^2 (k_4^2 - k_3^2)}, \quad p, j = 1, 2, \quad l = 3, 4. \end{aligned} \quad (5-6)$$

Theorem 5.4. *If $\mathbf{x} \in E^3 \setminus \{0\}$, then*

$$\begin{aligned} \Psi_{mq}^{(p)}(\mathbf{x}) &= \frac{\partial^2}{\partial x_m \partial x_q} \sum_{j=1}^2 d_{pj} h_j(\mathbf{x}) - \left(\frac{\partial^2}{\partial x_m \partial x_q} - \Delta \delta_{mq} \right) \sum_{l=3}^4 d_{pl} h_l(\mathbf{x}), \\ m, q &= 1, 2, 3, \quad p = 1, 2, 3, 4. \end{aligned} \quad (5-7)$$

Proof. On the basis of (4-17), (4-19), (5-4) and equality

$$h_j(\mathbf{x}) = -\frac{1}{k_j^2} \Delta h_j(\mathbf{x}), \quad \mathbf{x} \in E^3 \setminus \{0\}, \quad j = 1, 2, 3, 4,$$

from (4-23) we obtain

$$\begin{aligned} \Psi_{mq}^{(1)}(\mathbf{x}) &= \left(\frac{1}{d_2} Z'_{11}(\Delta) \Lambda_1(\Delta) \delta_{mq} + n_{11}(\Delta) \frac{\partial^2}{\partial x_m \partial x_q} \right) Y_{11}(\mathbf{x}) \\ &= -\sum_{j=1}^4 \frac{\eta_j}{k_j^2} \left(\frac{1}{d_2} Z'_{11}(\Delta) \Lambda_1(\Delta) + \Delta n_{11}(\Delta) \right) \frac{\partial^2}{\partial x_m \partial x_q} h_j(\mathbf{x}) \\ &\quad + \sum_{j=1}^4 \frac{\eta_j}{d_2 k_j^2} Z'_{11}(\Delta) \Lambda_1(\Delta) \left(\frac{\partial^2}{\partial x_m \partial x_q} - \Delta \delta_{mq} \right) h_j(\mathbf{x}) \\ &= -\frac{\partial^2}{\partial x_m \partial x_q} \sum_{j=1}^4 \frac{\eta_j}{d_1 k_j^2} Q'_{11}(-k_j^2) \Lambda_2(-k_j^2) h_j(\mathbf{x}) \\ &\quad + \left(\frac{\partial^2}{\partial x_m \partial x_q} - \Delta \delta_{mq} \right) \sum_{j=1}^4 \frac{\eta_j}{d_2 k_j^2} Z'_{11}(-k_j^2) \Lambda_1(-k_j^2) h_j(\mathbf{x}). \end{aligned} \quad (5-8)$$

Using the identities (5-6) and the relations

$$\eta_j \Lambda_1(-k_j^2) = \begin{cases} 0, & j = 1, 2, \\ \frac{(-1)^j}{k_3^2 - k_4^2}, & j = 3, 4, \end{cases} \quad \eta_j \Lambda_2(-k_j^2) = \begin{cases} \frac{(-1)^j}{k_1^2 - k_2^2}, & j = 1, 2, \\ 0, & j = 3, 4, \end{cases}$$

from (5-8) we have

$$\begin{aligned} \Psi_{mq}^{(1)}(\mathbf{x}) &= \frac{\partial^2}{\partial x_m \partial x_q} \sum_{j=1}^2 \eta_{1j} Q'_{11}(-k_j^2) h_j(\mathbf{x}) - \left(\frac{\partial^2}{\partial x_m \partial x_q} - \Delta \delta_{mq} \right) \sum_{l=3}^4 \eta_{1l} Z'_{11}(-k_l^2) h_l(\mathbf{x}) \\ &= \frac{\partial^2}{\partial x_m \partial x_q} \sum_{j=1}^2 d_{1j} h_j(\mathbf{x}) - \left(\frac{\partial^2}{\partial x_m \partial x_q} - \Delta \delta_{mq} \right) \sum_{l=3}^4 d_{1l} h_l(\mathbf{x}). \end{aligned}$$

The other formulae of (5-7) can be proven quite similarly. □

Theorem 5.4 leads to the following result.

Corollary 5.5. *If $\mathbf{x} \in E^3 \setminus \{0\}$, then each element Ψ_{mn} of the matrix $\Psi(\mathbf{x})$ has the form*

$$\Psi_{mn}(\mathbf{x}) = \sum_{j=1}^4 \Psi_{mnj}(\mathbf{x}),$$

where Ψ_{mnj} satisfies the condition

$$(\Delta + k_j^2) \Psi_{mnj}(\mathbf{x}) = 0, \quad m, n = 1, 2, \dots, 6, \quad j = 1, 2, 3, 4.$$

Theorem 5.6. *The relations*

$$\Psi_{mn}(\mathbf{x}) - \tilde{\Psi}_{mn}(\mathbf{x}) = \text{const} + O(|\mathbf{x}|), \quad \frac{\partial^q}{\partial x_1^{q_1} \partial x_2^{q_2} \partial x_3^{q_3}} (\Psi_{mn}(\mathbf{x}) - \tilde{\Psi}_{mn}(\mathbf{x})) = O(|\mathbf{x}|^{1-q}), \quad (5-9)$$

and

$$\Psi_{mn}(\mathbf{x}) = O(|\mathbf{x}|^{-1}), \quad (5-10)$$

hold in a neighborhood of the origin, where $m, n = 1, 2, \dots, 6$, $q = q_1 + q_2 + q_3$, $q \geq 1$.

Proof. In view of (5-2) and (5-7) we obtain

$$\begin{aligned} \Psi_{mq}^{(1)}(\mathbf{x}) - \tilde{\Psi}_{mq}^{(1)}(\mathbf{x}) &= \\ &= \frac{\partial^2}{\partial x_m \partial x_q} \left(\sum_{j=1}^2 d_{1j} h_j(\mathbf{x}) - \frac{a_7 + a_8}{d_1} h_0(\mathbf{x}) \right) - \left(\frac{\partial^2}{\partial x_m \partial x_q} - \Delta \delta_{mq} \right) \left(\sum_{l=3}^4 d_{1l} h_l(\mathbf{x}) - \frac{a_7}{d_2} h_0(\mathbf{x}) \right). \end{aligned} \quad (5-11)$$

In a neighborhood of the origin, from (4-20) we have

$$h_p(\mathbf{x}) = -\frac{1}{4\pi |\mathbf{x}|} \sum_{n=0}^{\infty} \frac{(ik_p |\mathbf{x}|)^n}{n!} = h'(\mathbf{x}) - \frac{ik_p}{4\pi} - k_p^2 h_0(\mathbf{x}) + \tilde{h}_p(\mathbf{x}), \quad (5-12)$$

where

$$h'(\mathbf{x}) = -\frac{1}{4\pi |\mathbf{x}|}, \quad \tilde{h}_p(\mathbf{x}) = -\frac{1}{4\pi |\mathbf{x}|} \sum_{n=3}^{\infty} \frac{(ik_p |\mathbf{x}|)^n}{n!}, \quad p = 1, 2, 3, 4.$$

Obviously,

$$\begin{aligned} \tilde{h}_p(\mathbf{x}) = O(|\mathbf{x}|^2), \quad \frac{\partial}{\partial x_l} \tilde{h}_p(\mathbf{x}) = O(|\mathbf{x}|), \quad \frac{\partial^2}{\partial x_l \partial x_j} \tilde{h}_p(\mathbf{x}) = \text{const} + O(|\mathbf{x}|), \\ l, j = 1, 2, 3, \quad p = 1, 2, 3, 4. \end{aligned} \quad (5-13)$$

On the basis of (5-12) we obtain

$$\begin{aligned} \sum_{j=1}^2 d_{1j} h_j(\mathbf{x}) - \frac{a_7 + a_8}{d_1} h_0(\mathbf{x}) \\ = \sum_{j=1}^2 d_{1j} h'_j(\mathbf{x}) - \left(\sum_{j=1}^2 d_{1j} k_j^2 + \frac{a_7 + a_8}{d_1} \right) h_0(\mathbf{x}) + \sum_{j=1}^2 d_{1j} \left(-\frac{ik_j}{4\pi} + \tilde{h}_j(\mathbf{x}) \right), \\ \sum_{l=3}^4 d_{1l} h_l(\mathbf{x}) - \frac{a_7}{d_2} h_0(\mathbf{x}) = \sum_{l=3}^4 d_{1l} h'_l(\mathbf{x}) - \left(\sum_{l=3}^4 d_{1l} k_l^2 + \frac{a_7}{d_2} \right) h_0(\mathbf{x}) + \sum_{l=3}^4 d_{1l} \left(-\frac{ik_l}{4\pi} + \tilde{h}_l(\mathbf{x}) \right). \end{aligned} \quad (5-14)$$

Taking into account the equalities (5-14) and

$$\Delta h'(\mathbf{x}) = 0 \quad \text{for } \mathbf{x} \neq 0, \quad \sum_{j=1}^2 d_{1j} = \sum_{l=3}^4 d_{1l}, \quad \sum_{j=1}^2 d_{1j} k_j^2 + \frac{a_7 + a_8}{d_1} = 0, \quad \sum_{l=3}^4 d_{1l} k_l^2 + \frac{a_7}{d_2} = 0,$$

from (5-11) we have

$$\begin{aligned} \Psi_{mq}^{(1)}(\mathbf{x}) - \tilde{\Psi}_{mq}^{(1)}(\mathbf{x}) &= \frac{\partial^2}{\partial x_m \partial x_q} \sum_{j=1}^2 d_{1j} (h'_j(\mathbf{x}) + \tilde{h}_j(\mathbf{x})) - \left(\frac{\partial^2}{\partial x_m \partial x_q} - \Delta \delta_{mq} \right) \sum_{l=3}^4 d_{1l} (h'_l(\mathbf{x}) + \tilde{h}_l(\mathbf{x})) \\ &= \frac{\partial^2}{\partial x_m \partial x_q} \sum_{j=1}^2 d_{1j} \tilde{h}_j(\mathbf{x}) - \left(\frac{\partial^2}{\partial x_m \partial x_q} - \Delta \delta_{mq} \right) \sum_{l=3}^4 d_{1l} \tilde{h}_l(\mathbf{x}). \end{aligned}$$

In view of (5-13), we obtain from this the relation (5-9)₁, for $m, n = 1, 2, 3$. The other formulae of (5-9) can be proven in a similar manner.

The relation (5-10) can be obtained easily from (5-9)₁ and (5-3). □

Thus, the fundamental solution $\tilde{\Psi}(\mathbf{x})$ of the system (5-1) is the singular part of the matrix $\Psi(\mathbf{x})$ in a neighborhood of the origin.

6. Concluding remark

The fundamental solution $\Psi(\mathbf{x})$ of the system (3-27) makes it possible to investigate three-dimensional boundary value problems of the linear theory of viscoelastic binary mixtures with the boundary integral method (potential method). The main results obtained in the classical theory of elasticity, thermoelasticity and micropolar theory of elasticity with the potential method are given in [Kupradze et al. 1979]. A wide class of boundary value problems of steady vibration of the linear theory of thermoelasticity of binary mixtures is investigated using the potential method by Burchuladze and Svanadze [2000].

References

- [Aboudi 2000] J. Aboudi, “Micromechanical modeling of finite viscoelastic multiphase composites”, *Z. Angew. Math. Phys.* **51**:1 (2000), 114–134.
- [Atkin and Craine 1976a] R. J. Atkin and R. E. Craine, “Continuum theories of mixtures: applications”, *J. Inst. Math. Appl.* **17**:2 (1976), 153–207.
- [Atkin and Craine 1976b] R. J. Atkin and R. E. Craine, “Continuum theories of mixtures: basic theory and historical development”, *Q. J. Mech. Appl. Math.* **29**:2 (1976), 209–245.
- [Bedford and Drumheller 1983] A. Bedford and D. S. Drumheller, “Theory of immiscible and structured mixtures”, *Int. J. Eng. Sci.* **21**:8 (1983), 863–960.
- [Bedford and Stern 1972] A. Bedford and M. Stern, “Toward a diffusing continuum theory of composite elastic materials”, *J. Appl. Mech. (ASME)* **38** (1972), 8–14.
- [Bowen 1976] R. M. Bowen, “Theory of mixtures”, pp. 3–120 in *Continuum physics*, vol. 3, edited by A. C. Eringen, Academic Press, New York, 1976.
- [Burchuladze and Svanadze 2000] T. Burchuladze and M. Svanadze, “Potential method in the linear theory of binary mixtures of thermoelastic solids”, *J. Therm. Stresses* **23**:6 (2000), 601–626.
- [Green and Naghdi 1965] A. E. Green and P. M. Naghdi, “A dynamical theory of interacting continua”, *Int. J. Eng. Sci.* **3**:2 (1965), 231–241.
- [Green and Naghdi 1969] A. E. Green and P. M. Naghdi, “On basic equations for mixtures”, *Q. J. Mech. Appl. Math.* **22**:4 (1969), 427–438.
- [Green and Naghdi 1972] A. E. Green and P. M. Naghdi, “On continuum thermodynamics”, *Arch. Ration. Mech. An.* **48**:5 (1972), 352–378.
- [Gurtin 1972] M. E. Gurtin, “The linear theory of elasticity”, in *Handbuch der Physik*, vol. VIa/2, edited by C. A. Truesdell, Springer, Berlin, 1972.
- [Hetnarski and Ignaczak 2004] R. B. Hetnarski and J. Ignaczak, *Mathematical theory of elasticity*, Taylor and Francis, New York, 2004.
- [Hills and Roberts 1987] R. N. Hills and P. H. Roberts, “Relaxation effects in a mixed phase region”, *J. Non Equilib. Thermodyn.* **12** (1987), 169–181.
- [Hills and Roberts 1988] R. N. Hills and P. H. Roberts, “On the formulation of diffusive mixture theories for two-phase regions”, *J. Eng. Math.* **22**:2 (1988), 93–100.
- [Hörmander 1983] L. Hörmander, *The analysis of linear partial differential operators, II: Differential operators with constant coefficients*, Springer, Berlin, 1983.
- [Iesan 2004] D. Iesan, “On the theory of viscoelastic mixtures”, *J. Therm. Stresses* **27**:12 (2004), 1125–1148.
- [Iesan and Nappa 2008] D. Iesan and L. Nappa, “On the theory of viscoelastic mixtures and stability”, *Math. Mech. Solids* **13**:1 (2008), 55–80.
- [Iesan and Quintanilla 2002] D. Iesan and R. Quintanilla, “On a theory of interacting continua with memory”, *J. Therm. Stresses* **25**:12 (2002), 1161–1178.
- [Kupradze 1965] V. D. Kupradze, *Potential methods in the theory of elasticity*, Israel Program for Scientific Translations, Jerusalem, 1965.
- [Kupradze et al. 1979] V. D. Kupradze, T. G. Gegelia, M. O. Bacheleishvili, and T. V. Burchuladze, *Three-dimensional problems of the mathematical theory of elasticity and thermoelasticity*, North-Holland, Amsterdam, 1979.
- [Lakes 2001] R. Lakes, “Viscoelastic properties of cortical bone”, Chapter 11, pp. 1–15 in *Bone mechanics handbook*, 2nd ed., edited by S. C. Cowin, Informa Healthcare, New York, 2001.
- [Lopatinsky 1951] Y. B. Lopatinsky, “Fundamental solution of elliptic system of differential equations”, *Ukrainian Math. J.* **3** (1951), 3–38.
- [Marinov 1978] P. Marinov, “Toward a thermo-viscoelastic theory of two-component materials”, *Int. J. Eng. Sci.* **16**:8 (1978), 533–544.

- [McCarthy and Tiersten 1983] M. F. McCarthy and H. F. Tiersten, “A theory of viscoelastic composites modeled as interpenetrating solid continua with memory”, *Arch. Ration. Mech. An.* **81**:1 (1983), 21–51.
- [Quintanilla 2005] R. Quintanilla, “Existence and exponential decay in the linear theory of viscoelastic mixtures”, *Eur. J. Mech. A Solids* **24**:2 (2005), 311–324.
- [Rajagopal and Tao 1995] K. R. Rajagopal and L. Tao, *Mechanics of mixtures*, World Scientific, Singapore, 1995.
- [Samohyl 1987] I. Samohyl, *Thermodynamics of irreversible processes in fluid mixtures*, Teubner, Leipzig, 1987.
- [Svanadze 1988] M. Svanadze, “The fundamental matrix of the linearized equations of the theory elastic mixtures”, *Proc. I. Vekua Inst. Appl. Math.* **23** (1988), 133–148.
- [Svanadze 1990] M. Svanadze, “Fundamental solutions of equations of stable oscillation and pseudo-oscillation of a two-component elastic mixtures”, *Proc. I. Vekua Inst. Appl. Math.* **39** (1990), 227–240.
- [Wilmanski 2003] K. Wilmanski, “Some questions on material objectivity arising in models of porous materials”, pp. 123–137 in *Rational continua, classical and new*, edited by P. Podio-Guidugli and M. Brocato, Springer, Milan, 2003.

Received 14 Oct 2008. Revised 8 Jan 2009. Accepted 12 Jan 2009.

SIMONA DE CICCO: decicco@unina.it

Dipartimento di Costruzioni e Metodi Matematici in Architettura, Università di Napoli “Federico II”, Via Monteoliveto 3, 80134 Napoli, Italy

MERAB SVANADZE: svanadze@gmail.com

Faculty of Physics and Mathematics, Ilia Chavchavadze State University, I. Chavchavadze Ave. 32, 0179 Tbilisi, Georgia

AN ENERGY-MOMENTUM CONSERVING ALGORITHM FOR NONLINEAR TRANSIENT ANALYSIS WITHIN THE FRAMEWORK OF HYBRID ELEMENTS

C. S. JOG AND PHANI MOTAMARRI

This work deals with the formulation and implementation of an energy-momentum conserving algorithm for conducting the nonlinear transient analysis of structures, within the framework of stress-based hybrid elements. Hybrid elements, which are based on a two-field variational formulation, are much less susceptible to locking than conventional displacement-based elements within the static framework. We show that this advantage carries over to the transient case, so that not only are the solutions obtained more accurate, but they are obtained in fewer iterations. We demonstrate the efficacy of the algorithm on a wide range of problems such as ones involving dynamic buckling, complicated three-dimensional motions, et cetera.

1. Introduction

In the absence of loading in a pure traction initial boundary-value problem, the linear and angular momenta, and, if the body is elastic, the energy as well, are conserved. [Simo and Tarnow \[1992; 1994\]](#) were the first to develop algorithmic approximations that would, similarly to continuum dynamics, conserve these properties. Since with the use of these schemes there is no blow-up of the solution in the absence of loading, these algorithms can be said to be inherently stable. For this reason, there has been an extensive literature on these classes of time stepping algorithms. [Laursen and Meng \[2001\]](#) and [Gonzalez \[2000\]](#) extended the method of Simo and Tarnow to nonlinear constitutive models, albeit by different methods. [Brank et al. \[1998\]](#) and [Sansour et al. \[2004\]](#) considered the application of these methods to the motion of shells. [Betsch and Steinmann \[2001\]](#) developed a time finite element method and introduced the assumed strain method in time which simplifies the design of energy-momentum conserving algorithms for nonlinear constitutive models. [Armero and Romero \[2001a; 2001b\]](#), [Bauchau and Joo \[1999; 2003\]](#), and [Kuhl et al. \[Kuhl and Crisfield 1999; Kuhl and Ramm 1996; 1999\]](#) introduced the use of unconditionally stable energy-momentum conserving time-integration schemes with high-frequency numerical dissipation. [Balah and Al-Ghamedy \[2005\]](#) extended the method of Simo and Tarnow to the nonlinear dynamics of laminated shells. Most of the works cited above including that of Simo and Tarnow use the displacement-based formulation.

It is well known that the standard displacement-based formulation locks in the case of static problems for shell-type structures, and the adverse effects of this over stiff stiffness matrix are also seen in transient problems. Ever since the pioneering work of [Pian et al. \[Pian and Sumihara 1984; Pian and Tong 1986\]](#), it has been known that hybrid stress-based formulations are much less susceptible to locking than the standard displacement-based formulation. Our goal in this work, which is a generalization of the work

Keywords: nonlinear transient analysis, hybrid elements, energy-momentum conservation.
We gratefully acknowledge the financial support of the ISRO-IISc Space Technology Cell.

in [Jog and Kelkar 2006] to transient problems, is to develop the formulation and implementation of an energy-momentum conserving time stepping strategy for three-dimensional hexahedral and axisymmetric hybrid stress elements.

As pointed out in [Jog and Kelkar 2006], since the treatment is fully three-dimensional, it can be used (with no modification of the formulation) in tackling problems as diverse as shells with variable thickness, laminated composites, ply drop-offs on the one hand, and problems with thick geometries on the other. Material nonlinearities are also handled easily since no reduction of the three-dimensional constitutive relations based on plane-stress assumptions or any other such assumption needs to be carried out.

In Section 2, we present a two-field variational formulation for the transient nonlinear elasticity problem that enforces the balance of the linear momentum and the traction boundary condition, and the strain-displacement relations in a weak sense. These variational statements are then linearized and discretized in Section 3 to develop an incremental total Lagrangian finite element formulation. Next we show that the stress interpolation function for higher-order hybrid elements, which are derived based on static considerations alone, have to be modified slightly in order to prevent instabilities that can arise during transient solutions of some problems. Several challenging numerical examples which include problems involving dynamic buckling, impact problems, complicated three-dimensional motions of shell-type structures, et cetera are presented in Section 4. We shall see in this section that not only do we obtain good coarse-mesh accuracy, but also obtain the solutions to many demanding problems with comparatively large time steps. Section 5 presents the conclusions.

We note the conventions followed throughout this work. Scalars are denoted by lightface letters, while vectors and higher-order tensors are denoted by boldface letters. $\mathbf{A} \cdot$ denotes contraction over one index, and a colon contraction over two indices. For example, $\mathbf{t} \cdot \mathbf{u} = t_i u_i$, $\mathbf{S} : \mathbf{E} = S_{ij} E_{ij}$, et cetera, with the summation convention over repeated indices implied. If $\mathbf{G}(\mathbf{T})$ is a tensor-valued function of a tensor \mathbf{T} , the directional derivative of \mathbf{G} evaluated at \mathbf{T} in the direction \mathbf{U} , defined by

$$D\mathbf{G}(\mathbf{T})[\mathbf{U}] := \left. \frac{d}{d\alpha} \mathbf{G}(\mathbf{T} + \alpha\mathbf{U}) \right|_{\alpha=0}, \quad (1)$$

will play a key role in the linearizations that are carried out during the finite element formulation.

2. Formulation

In this section, we first present the two-field variational formulation that is later used to derive the finite element equations. Since the deformed configuration is not known in advance, all equations are written with respect to the reference configuration Ω whose boundary Γ is composed of two open, disjoint regions: $\Gamma = \bar{\Gamma}_u \cup \bar{\Gamma}_t$. The spatial variables in the reference and deformed configurations are denoted by \mathbf{X} and \mathbf{x} , respectively. We assume a one-to-one mapping χ that takes \mathbf{X} to \mathbf{x} , that is, $\mathbf{x} = \chi(\mathbf{X}, t) = \mathbf{X} + \mathbf{u}(\mathbf{X}, t)$, where \mathbf{u} is the displacement field. The deformation gradient is given by $\mathbf{F} := \nabla \chi = \mathbf{I} + \nabla \mathbf{u}$, where the gradient is with respect to the material coordinates \mathbf{X} ; the traction \mathbf{t}^0 is given by $\mathbf{F} \mathbf{S} \mathbf{n}^0$; and we let

$$\bar{\mathbf{E}}(\mathbf{u}) := \frac{1}{2} [(\nabla \mathbf{u}) + (\nabla \mathbf{u})^T + (\nabla \mathbf{u})^T (\nabla \mathbf{u})]. \quad (2)$$

Within the context of the two-field variational formulation developed below, the strains are recovered from the stresses by means of the constitutive relation

$$\mathbf{E} = \hat{\mathbf{E}}(\mathbf{S}) \text{ on } \Omega. \quad (3)$$

This does not imply that the stress-strain relation $\mathbf{S} = \hat{\mathbf{S}}(\mathbf{E})$ has to be analytically inverted—only that, given the state of stress, we find the state of strain using the stress-strain relation as discussed in [Jog and Kelkar 2006].

The two-field variational principle on which our finite element formulation is based enforces the balance of linear momentum, traction boundary condition, and the strain-displacement relation in a weak sense. If

$$V_u := \{\mathbf{u}_\delta \in H^1(\Omega) : \mathbf{u}_\delta = \mathbf{0} \text{ on } \Gamma_u\}, \quad V_S := \{\mathbf{S}_\delta \in L^2(\Omega) : \mathbf{S}_\delta^T = \mathbf{S}_\delta \text{ on } \Omega\},$$

denote the space of variations of the displacements and the second Piola–Kirchhoff stress, the two-field variational formulation obtained after incorporating the transient terms in the formulation presented in [Jog and Kelkar 2006] is given by

$$\int_\Omega \rho_0 \mathbf{u}_\delta \cdot \frac{\partial \mathbf{v}}{\partial t} d\Omega + \int_\Omega \mathbf{S} : \bar{\mathbf{E}}_\delta d\Omega = \int_\Omega \rho_0 \mathbf{u}_\delta \cdot \mathbf{b}^0 d\Omega + \int_{\Gamma_t} \mathbf{u}_\delta \cdot \bar{\mathbf{t}}^0 d\Gamma, \quad \forall \mathbf{u}_\delta \in V_u, \quad (4)$$

$$\int_\Omega \mathbf{S}_\delta : [\bar{\mathbf{E}}(\mathbf{u}) - \hat{\mathbf{E}}(\mathbf{S})] d\Omega = 0, \quad \forall \mathbf{S}_\delta \in V_S, \quad (5)$$

where $\bar{\mathbf{E}}$ is given by (2), and its variation $\bar{\mathbf{E}}_\delta$ is given by

$$\bar{\mathbf{E}}_\delta(\mathbf{u}, \mathbf{u}_\delta) = \frac{1}{2} [\mathbf{F}^T \nabla \mathbf{u}_\delta + (\nabla \mathbf{u}_\delta)^T \mathbf{F}] = \frac{1}{2} [(\nabla \mathbf{u}_\delta) + (\nabla \mathbf{u}_\delta)^T + (\nabla \mathbf{u})^T (\nabla \mathbf{u}_\delta) + (\nabla \mathbf{u}_\delta)^T (\nabla \mathbf{u})]. \quad (6)$$

In this variational formulation, $\rho_0 = (\det \mathbf{F})\rho$ is the density in the reference configuration in terms of the density ρ in the deformed configuration, \mathbf{v} is the velocity, \mathbf{n}^0 is the outward normal to Γ , $\mathbf{t}^0 := \|(\text{cof } \mathbf{F})\mathbf{n}^0\| \mathbf{t}$ are the tractions defined on the reference configuration in terms of the actual tractions \mathbf{t} on the deformed configuration, and $\mathbf{b}^0(\mathbf{X}, t) := \mathbf{b}(\boldsymbol{\chi}(\mathbf{X}, t))$ is the body force field on the reference configuration.

In what follows, we shall develop a time stepping strategy where we focus attention on a typical time interval $[t_n, t_{n+1}]$, and let $t_\Delta := t_{n+1} - t_n$ denote the corresponding time step size. The variables at times t_n and t_{n+1} will be denoted by the subscripts n and $n+1$, respectively. We consider the material to be hyperelastic with strain-energy density function $\hat{W}(\mathbf{E})$, so that the stress is given by

$$\mathbf{S} = \frac{\partial \hat{W}}{\partial \mathbf{E}}.$$

Within the context of our two-field variational formulation, we propose the following time stepping scheme which, as we shall subsequently show, conserves linear and angular momentum and energy in the absence of loading:

$$\frac{\mathbf{x}_{n+1} - \mathbf{x}_n}{t_\Delta} = \frac{\mathbf{u}_{n+1} - \mathbf{u}_n}{t_\Delta} = \frac{\mathbf{v}_n + \mathbf{v}_{n+1}}{2}, \quad (7)$$

$$\begin{aligned} \int_\Omega \rho_0 \mathbf{u}_\delta \cdot \left(\frac{\mathbf{v}_{n+1} - \mathbf{v}_n}{t_\Delta} \right) d\Omega + \int_\Omega \left(\frac{\bar{\mathbf{E}}_\delta)_n + (\bar{\mathbf{E}}_\delta)_{n+1}}{2} \right) : \mathbf{S}_{\text{alg}} d\Omega \\ = \int_\Omega \rho_0 \mathbf{u}_\delta \cdot \mathbf{b}_{\text{alg}} d\Omega + \int_{\Gamma_t} \mathbf{u}_\delta \cdot \bar{\mathbf{t}}_{\text{alg}} d\Gamma, \quad \forall \mathbf{u}_\delta \in V_u, \end{aligned} \quad (8)$$

$$\int_{\Omega} \mathbf{S}_{\delta} : [\bar{\mathbf{E}}(\mathbf{u}_m) - \hat{\mathbf{E}}(\mathbf{S}_m)] d\Omega = 0, \quad m = n, n+1, \quad \forall \mathbf{S}_{\delta} \in V_S, \quad (9)$$

where $\mathbf{b}_{\text{alg}} = (\mathbf{b}_n^0 + \mathbf{b}_{n+1}^0)/2$, $\bar{\mathbf{t}}_{\text{alg}} = (\bar{\mathbf{t}}_n^0 + \bar{\mathbf{t}}_{n+1}^0)/2$, and, in terms of $\tilde{\mathbf{E}}(\zeta) := [(1-\zeta)\mathbf{E}_n + (1+\zeta)\mathbf{E}_{n+1}]/2$, the algorithmic stress \mathbf{S}_{alg} given by

$$\mathbf{S}_{\text{alg}} = \frac{1}{2} \int_{-1}^1 \frac{\partial W(\tilde{\mathbf{E}})}{\partial \tilde{\mathbf{E}}} d\zeta, \quad (10)$$

This formula is similar to that presented in [Betsch and Steinmann 2001], except that here \mathbf{E} denotes the strain recovered from the constitutive relation, and not from the strain-displacement relation.

We now prove that as in the continuum problem, for the pure traction initial boundary-value problem, in the absence of tractions and body forces ($\bar{\mathbf{t}}_{\text{alg}} = \mathbf{b}_{\text{alg}} = \mathbf{0}$), the linear and angular momenta, and total (kinetic plus strain) energy are conserved.

2.1. Discrete linear and angular momentum conservation. To prove that the discrete linear momentum is conserved, choose for all time $\mathbf{u}_{\delta} = \mathbf{c}$ in (8), where \mathbf{c} is a constant vector. This choice is permissible since the entire boundary is free of displacement constraints. With this choice $(\bar{\mathbf{E}}_{\delta})_n = (\bar{\mathbf{E}}_{\delta})_{n+1} = \mathbf{0}$, and we get

$$\mathbf{c} \cdot \int_{\Omega} \rho_0 (\mathbf{v}_{n+1} - \mathbf{v}_n) d\Omega = 0,$$

which by virtue of the arbitrariness of \mathbf{c} , proves the conservation of the discrete linear momentum.

To prove the conservation of the discrete angular momentum, $\mathbf{J}_{n+1} = \mathbf{J}_n$, choose

$$\mathbf{u}_{\delta} = \mathbf{c} \times (\mathbf{x}_n + \mathbf{x}_{n+1}) = \mathbf{W}(\mathbf{x}_n + \mathbf{x}_{n+1}),$$

where \mathbf{W} is the skew-symmetric tensor of which \mathbf{c} is the axial vector. Substituting $\nabla \mathbf{u}_{\delta} = \mathbf{W}(\mathbf{F}_n + \mathbf{F}_{n+1})$ into (6), we get

$$(\bar{\mathbf{E}}_{\delta})_n + (\bar{\mathbf{E}}_{\delta})_{n+1} = \frac{1}{2} [(\mathbf{F}_n + \mathbf{F}_{n+1})^T \mathbf{W}(\mathbf{F}_n + \mathbf{F}_{n+1}) + (\mathbf{F}_n + \mathbf{F}_{n+1})^T \mathbf{W}^T(\mathbf{F}_n + \mathbf{F}_{n+1})] = \mathbf{0}.$$

Using the property $(\mathbf{p} \times \mathbf{q}) \cdot \mathbf{r} = \mathbf{p} \cdot (\mathbf{q} \times \mathbf{r})$, the first term in (8) simplifies to

$$\begin{aligned} & \int_{\Omega} \rho_0 \mathbf{c} \cdot (\mathbf{x}_n + \mathbf{x}_{n+1}) \times \left(\frac{\mathbf{v}_{n+1} - \mathbf{v}_n}{t_{\Delta}} \right) d\Omega \\ &= \frac{1}{t_{\Delta}} \mathbf{c} \cdot \int_{\Omega} \rho_0 [2(\mathbf{x}_{n+1} \times \mathbf{v}_{n+1} - \mathbf{x}_n \times \mathbf{v}_n) - (\mathbf{x}_{n+1} - \mathbf{x}_n) \times (\mathbf{v}_n + \mathbf{v}_{n+1})] d\Omega = \frac{2}{t_{\Delta}} \mathbf{c} \cdot [\mathbf{J}_{n+1} - \mathbf{J}_n], \end{aligned}$$

the last equality following by (7). Thus, with the given choice of \mathbf{u}_{δ} and in the absence of loading, (8) reduces to

$$\mathbf{c} \cdot [\mathbf{J}_{n+1} - \mathbf{J}_n] = 0,$$

which by virtue of the arbitrariness of \mathbf{c} leads to $\mathbf{J}_{n+1} = \mathbf{J}_n$.

By multiplying the spatially discretized versions of (8) and (9) by the vectors

$$[c_1 \ c_2 \ c_3 \ c_1 \ c_2 \ c_3 \ \dots]_{1 \times N} \quad \text{and} \quad [-c_3 z_2^{(1)} + c_2 z_3^{(1)} \quad c_3 z_1^{(1)} - c_1 z_3^{(1)} \quad -c_2 z_1^{(1)} + c_1 z_2^{(1)} \quad \dots]_{1 \times N},$$

where N is the total number of displacement degrees of freedom, c_1 , c_2 , and c_3 are constants, and $\mathbf{z}^{(i)} = \mathbf{x}_n^{(i)} + \mathbf{x}_{n+1}^{(i)}$, where i denotes the node number, we can show that the linear and angular momenta are conserved even after spatial discretization has been carried out.

2.2. Discrete energy conservation. To prove conservation of energy for a hyperelastic material with \mathbf{S}_{alg} given by (10), we choose $\mathbf{u}_\delta = \mathbf{u}_{n+1} - \mathbf{u}_n = \mathbf{x}_{n+1} - \mathbf{x}_n$. Substituting $\nabla \mathbf{u}_\delta = \mathbf{F}_{n+1} - \mathbf{F}_n$ into (6), we get

$$(\bar{\mathbf{E}}_\delta)_n + (\bar{\mathbf{E}}_\delta)_{n+1} = [\mathbf{F}_{n+1}^T \mathbf{F}_{n+1} - \mathbf{F}_n^T \mathbf{F}_n] = 2[\bar{\mathbf{E}}_{n+1} - \bar{\mathbf{E}}_n]. \quad (11)$$

On choosing $\mathbf{S}_\delta = \mathbf{S}_{\text{alg}}$ in (9) (this choice is permissible since $\mathbf{S}_{\text{alg}} \in V_S$), we have

$$\int_\Omega [\bar{\mathbf{E}}(\mathbf{u}_n) - \hat{\mathbf{E}}(\mathbf{S}_n)] : \mathbf{S}_{\text{alg}} d\Omega = 0, \quad \int_\Omega [\bar{\mathbf{E}}(\mathbf{u}_{n+1}) - \hat{\mathbf{E}}(\mathbf{S}_{n+1})] : \mathbf{S}_{\text{alg}} d\Omega = 0,$$

which leads to

$$\int_\Omega [\bar{\mathbf{E}}(\mathbf{u}_{n+1}) - \bar{\mathbf{E}}(\mathbf{u}_n)] : \mathbf{S}_{\text{alg}} d\Omega = \int_\Omega [\hat{\mathbf{E}}(\mathbf{S}_{n+1}) - \hat{\mathbf{E}}(\mathbf{S}_n)] : \mathbf{S}_{\text{alg}} d\Omega. \quad (12)$$

Using (11) and (12), the second term in (8) simplifies to

$$\begin{aligned} \int_\Omega \left[\frac{(\bar{\mathbf{E}}_\delta)_n + (\bar{\mathbf{E}}_\delta)_{n+1}}{2} \right] : \mathbf{S}_{\text{alg}} d\Omega &= \int_\Omega [\hat{\mathbf{E}}(\mathbf{S}_{n+1}) - \hat{\mathbf{E}}(\mathbf{S}_n)] : \mathbf{S}_{\text{alg}} \\ &= \int_\Omega \frac{\partial \tilde{\mathbf{E}}}{\partial \tilde{\boldsymbol{\zeta}}} : \int_{-1}^1 \frac{\partial W(\tilde{\mathbf{E}})}{\partial \tilde{\mathbf{E}}} d\tilde{\boldsymbol{\zeta}} \quad (\text{by (10)}) \\ &= \int_\Omega \int_{-1}^1 \frac{\partial W(\tilde{\mathbf{E}}(\tilde{\boldsymbol{\zeta}}))}{\partial \tilde{\boldsymbol{\zeta}}} d\tilde{\boldsymbol{\zeta}} = [\hat{W}_{n+1} - \hat{W}_n]. \end{aligned}$$

On using (7), the first term in (8) simplifies to

$$\begin{aligned} \int_\Omega \rho_0(\mathbf{u}_{n+1} - \mathbf{u}_n) \left(\frac{\mathbf{v}_{n+1} - \mathbf{v}_n}{t_\Delta} \right) d\Omega &= \frac{1}{2} \int_\Omega \rho_0(\mathbf{v}_{n+1} + \mathbf{v}_n) \cdot (\mathbf{v}_{n+1} - \mathbf{v}_n) d\Omega \\ &= \frac{1}{2} \int_\Omega \rho_0(\mathbf{v}_{n+1} \cdot \mathbf{v}_{n+1} - \mathbf{v}_n \cdot \mathbf{v}_n) d\Omega = (\text{K.E.})_{n+1} - (\text{K.E.})_n. \end{aligned}$$

Combining all the above results, we get from (8) in the absence of loading

$$(\text{K.E.})_n + \hat{W}_n = (\text{K.E.})_{n+1} + \hat{W}_{n+1}, \quad (13)$$

which is the desired result.

Ideally speaking, energy dissipation should be introduced into the numerical algorithm by using an appropriate numerical approximation of the continuum viscoelastic (or viscoelastoplastic) constitutive relation while formulating \mathbf{S}_{alg} . Thus, the algorithmic stress can be taken to be the sum of a conserving part \mathbf{S}_{cons} — as given by (10) — and a dissipative part \mathbf{S}_{diss} which is a numerical approximation of the viscoelastic part, that is, $\mathbf{S}_{\text{alg}} = \mathbf{S}_{\text{cons}} + \mathbf{S}_{\text{diss}}$. For illustrative purposes, we use the Kelvin–Voigt viscoelastic model in this work, which is

$$\mathbf{S}_{\text{diss}} = \frac{\alpha}{t_\Delta} (\bar{\mathbf{E}}_{n+1} - \bar{\mathbf{E}}_n), \quad \alpha > 0.$$

Since $(\bar{\mathbf{E}}_{n+1} - \bar{\mathbf{E}}_n) : (\bar{\mathbf{E}}_{n+1} - \bar{\mathbf{E}}_n) \geq 0$, instead of (13), we now get $(\text{K.E.})_{n+1} + \hat{\mathbf{W}}_{n+1} \leq (\text{K.E.})_n + \hat{\mathbf{W}}_n$, which shows that the total energy is a nonincreasing function of time. The energy conserving algorithm is recovered simply by setting α to zero. Having an energy dissipation strategy may be important when one is interested simply in the static steady-state solution, say in buckling problems where finding the static solution directly may involve the use of complicated path-following algorithms. In such cases, the use of the exact viscoelastic constitutive model is not needed.

On using (10), we get for a Saint-Venant–Kirchhoff material,

$$\mathbf{S}_{\text{cons}} = \frac{1}{2} (\mathbf{S}_n + \mathbf{S}_{n+1}).$$

For general nonlinear constitutive models, firstly it may be difficult to evaluate \mathbf{S}_{alg} analytically (note that the same problem exists for the single-field formulation also), and secondly even if one is able to analytically find \mathbf{S}_{alg} , in the fully discrete setting, the choice $\mathbf{S}_\delta = \mathbf{S}_{\text{alg}}$ may not lie in the admissible stress space. If we use a trapezoidal approximation for evaluating the integral in (10) (which is a first-order approximation similar to the approximations being made for the velocity and acceleration) for \mathbf{S}_{cons} , meaning $\mathbf{S}_{\text{cons}} = (\mathbf{S}_n + \mathbf{S}_{n+1})/2$, then one can realize the selection $\mathbf{S}_\delta = \mathbf{S}_{\text{alg}}$. As we shall show in Section 4 (see Section 4.7), this turns out to be a good approximation for nonlinear material models. With this approximation, and with the use of (7), (8) and (9) can be written as

$$\begin{aligned} 2 \int_{\Omega} \rho_0 \mathbf{u}_\delta \cdot \left(\frac{\mathbf{u}_{n+1} - \mathbf{u}_n}{t_\Delta^2} - \frac{\mathbf{v}_n}{t_\Delta} \right) d\Omega + \int_{\Omega} \left(\frac{\bar{\mathbf{E}}_\delta)_n + (\bar{\mathbf{E}}_\delta)_{n+1}}{2} \right) : \left(\frac{\mathbf{S}_n + \mathbf{S}_{n+1}}{2} + \frac{\alpha(\bar{\mathbf{E}}_{n+1} - \bar{\mathbf{E}}_n)}{t_\Delta} \right) d\Omega \\ = \int_{\Omega} \rho_0 \mathbf{u}_\delta \cdot \mathbf{b}_{\text{alg}} d\Omega + \int_{\Gamma_t} \mathbf{u}_\delta \cdot \bar{\mathbf{t}}_{\text{alg}} d\Gamma, \quad \forall \mathbf{u}_\delta \in V_u, \quad (14) \end{aligned}$$

$$\int_{\Omega} \mathbf{S}_\delta : [\bar{\mathbf{E}}(\mathbf{u}_{n+1}) - \hat{\mathbf{E}}(\mathbf{S}_{n+1})] d\Omega = 0, \quad \forall \mathbf{S}_\delta \in V_S. \quad (15)$$

3. Linearization and finite element approximation

3.1. Linearization of the variational formulation. With a view towards developing an iterative finite element scheme, we now linearize the variational statements in (14) and (15). For simplicity, we consider the loads to be dead loads (meaning loads that are independent of the deformation \mathbf{u}); the case of live loads such as pressure loading can be treated by using the results in [Jog and Kelkar 2006]. Let the superscripts k and $k+1$ denote the values of the field variables at the k and $(k+1)$ -th iterative steps, and let $(\mathbf{u}_\Delta, \mathbf{S}_\Delta)$ denote the increments in the displacement and stress fields at time t_{n+1} . Then, keeping in view that \mathbf{u} and \mathbf{S} are *independent* field variables, and by an application of the chain and product rules, we have, for example,

$$\begin{aligned} (\mathbf{S} : \bar{\mathbf{E}}_\delta)_{n+1}^{k+1} &\approx (\mathbf{S} : \bar{\mathbf{E}}_\delta)_{n+1}^k + D_u(\mathbf{S} : \bar{\mathbf{E}}_\delta)(\mathbf{u}_{n+1}^k, \mathbf{S}_{n+1}^k)[\mathbf{u}_\Delta] + D_S(\mathbf{S} : \bar{\mathbf{E}}_\delta)(\mathbf{u}_{n+1}^k, \mathbf{S}_{n+1}^k)[\mathbf{S}_\Delta] \\ &= (\mathbf{S} : \bar{\mathbf{E}}_\delta)_{n+1}^k + [(\nabla \mathbf{u}_\delta) \mathbf{S}_{n+1}] : (\nabla \mathbf{u}_\Delta) + \mathbf{S}_\Delta : (\bar{\mathbf{E}}_\delta)_{n+1}, \end{aligned} \quad (16)$$

$$\mathbf{S}_\delta : [\bar{\mathbf{E}}(\mathbf{u}_{n+1}^{k+1}) - \hat{\mathbf{E}}(\mathbf{S}_{n+1}^{k+1})] \approx \mathbf{S}_\delta : [\bar{\mathbf{E}}(\mathbf{u}_{n+1}^k) - \hat{\mathbf{E}}(\mathbf{S}_{n+1}^k)] + \mathbf{S}_\delta : D\bar{\mathbf{E}}(\mathbf{u}_{n+1}^k)[\mathbf{u}_\Delta] - \mathbf{S}_\delta : \mathbb{C}^{-1}[\mathbf{S}_\Delta], \quad (17)$$

where $\mathbb{C}^{-1} = \partial \hat{\mathbf{E}} / \partial \mathbf{S}$ is the (fourth-order) material compliance tensor and

$$D\bar{\mathbf{E}}(\mathbf{u}_{n+1}^k)[\mathbf{u}_\Delta] = \frac{1}{2} [(\nabla \mathbf{u}_\Delta) + (\nabla \mathbf{u}_\Delta)^T + (\nabla \mathbf{u}_{n+1}^k)^T (\nabla \mathbf{u}_\Delta) + (\nabla \mathbf{u}_\Delta)^T (\nabla \mathbf{u}_{n+1}^k)]. \quad (18)$$

The other terms in (14) and (15) are linearized in a similar manner to get the incremental forms of the variational equations.

For a computer implementation, it is convenient to express second-order tensors as vectors and fourth-order tensors as matrices. Hence, we define the engineering strains, stresses, and displacement-increment gradients as

$$\mathbf{E}_c(\mathbf{S}) = \begin{bmatrix} E_{11} \\ E_{22} \\ E_{33} \\ 2E_{12} \\ 2E_{23} \\ 2E_{13} \end{bmatrix}, \quad \bar{\mathbf{E}}_c(\mathbf{u}) = \begin{bmatrix} \bar{E}_{11} \\ \bar{E}_{22} \\ \bar{E}_{33} \\ 2\bar{E}_{12} \\ 2\bar{E}_{23} \\ 2\bar{E}_{13} \end{bmatrix}, \quad \mathbf{S}_c = \begin{bmatrix} S_{11} \\ S_{22} \\ S_{33} \\ S_{12} \\ S_{23} \\ S_{13} \end{bmatrix}, \quad (\nabla \mathbf{u}_\Delta)_c = \begin{bmatrix} (\nabla \mathbf{u}_\Delta)_{11} \\ (\nabla \mathbf{u}_\Delta)_{12} \\ (\nabla \mathbf{u}_\Delta)_{13} \\ (\nabla \mathbf{u}_\Delta)_{21} \\ (\nabla \mathbf{u}_\Delta)_{22} \\ (\nabla \mathbf{u}_\Delta)_{23} \\ (\nabla \mathbf{u}_\Delta)_{31} \\ (\nabla \mathbf{u}_\Delta)_{32} \\ (\nabla \mathbf{u}_\Delta)_{33} \end{bmatrix}, \quad (19)$$

the engineering form of the tensor $D\bar{\mathbf{E}}(\mathbf{u}^k)[\mathbf{u}_\Delta]$ as (with summation over i implied)

$$\{D\bar{\mathbf{E}}(\mathbf{u}_{n+1}^k)[\mathbf{u}_\Delta]\}_c = \begin{bmatrix} (\nabla \mathbf{u}_\Delta)_{11} + (\nabla \mathbf{u}_{n+1}^k)_{i1}(\nabla \mathbf{u}_\Delta)_{i1} \\ (\nabla \mathbf{u}_\Delta)_{22} + (\nabla \mathbf{u}_{n+1}^k)_{i2}(\nabla \mathbf{u}_\Delta)_{i2} \\ (\nabla \mathbf{u}_\Delta)_{33} + (\nabla \mathbf{u}_{n+1}^k)_{i3}(\nabla \mathbf{u}_\Delta)_{i3} \\ (\nabla \mathbf{u}_\Delta)_{12} + (\nabla \mathbf{u}_\Delta)_{21} + (\nabla \mathbf{u}_{n+1}^k)_{i1}(\nabla \mathbf{u}_\Delta)_{i2} + (\nabla \mathbf{u}_{n+1}^k)_{i2}(\nabla \mathbf{u}_\Delta)_{i1} \\ (\nabla \mathbf{u}_\Delta)_{23} + (\nabla \mathbf{u}_\Delta)_{32} + (\nabla \mathbf{u}_{n+1}^k)_{i2}(\nabla \mathbf{u}_\Delta)_{i3} + (\nabla \mathbf{u}_{n+1}^k)_{i3}(\nabla \mathbf{u}_\Delta)_{i2} \\ (\nabla \mathbf{u}_\Delta)_{13} + (\nabla \mathbf{u}_\Delta)_{31} + (\nabla \mathbf{u}_{n+1}^k)_{i1}(\nabla \mathbf{u}_\Delta)_{i3} + (\nabla \mathbf{u}_{n+1}^k)_{i3}(\nabla \mathbf{u}_\Delta)_{i1} \end{bmatrix}, \quad (20)$$

the stress matrix as

$$\mathbf{S}_M = \begin{bmatrix} S_{11} & S_{12} & S_{13} & 0 & 0 & 0 & 0 & 0 & 0 \\ S_{12} & S_{22} & S_{23} & 0 & 0 & 0 & 0 & 0 & 0 \\ S_{31} & S_{32} & S_{33} & 0 & 0 & 0 & 0 & 0 & 0 \\ 0 & 0 & 0 & S_{11} & S_{12} & S_{13} & 0 & 0 & 0 \\ 0 & 0 & 0 & S_{12} & S_{22} & S_{23} & 0 & 0 & 0 \\ 0 & 0 & 0 & S_{31} & S_{32} & S_{33} & 0 & 0 & 0 \\ 0 & 0 & 0 & 0 & 0 & 0 & S_{11} & S_{12} & S_{13} \\ 0 & 0 & 0 & 0 & 0 & 0 & S_{12} & S_{22} & S_{23} \\ 0 & 0 & 0 & 0 & 0 & 0 & S_{31} & S_{32} & S_{33} \end{bmatrix}, \quad (21)$$

and the engineering form of the material constitutive tensor as

$$\mathbb{C}_c = \begin{bmatrix} C_{1111} & C_{1122} & C_{1133} & C_{1112} & C_{1123} & C_{1113} \\ C_{2211} & C_{2222} & C_{2233} & C_{2212} & C_{2223} & C_{2213} \\ C_{3311} & C_{3322} & C_{3333} & C_{3312} & C_{3323} & C_{3313} \\ C_{1211} & C_{1222} & C_{1233} & C_{1212} & C_{1223} & C_{1213} \\ C_{2311} & C_{2322} & C_{2333} & C_{2312} & C_{2323} & C_{2313} \\ C_{1311} & C_{1322} & C_{1333} & C_{1312} & C_{1323} & C_{1313} \end{bmatrix}. \quad (22)$$

Note that $[\bar{\mathbf{E}}_\delta(\mathbf{u}_{n+1}^k)]_c = \{D\bar{\mathbf{E}}(\mathbf{u}_{n+1}^k)[\mathbf{u}_\delta]\}_c$, where \mathbf{u}_δ is the variation of \mathbf{u} .

In terms of these engineering quantities, the incremental form of the variational statements (14) and (15) is

$$\begin{aligned} & \frac{2}{t_\Delta^2} \int_\Omega \rho_0 \mathbf{u}_\delta^T \mathbf{u}_\Delta d\Omega \\ & + \frac{1}{4} \int_\Omega \left((\nabla \mathbf{u}_\delta)_c^T \left[\mathbf{S}_n + \mathbf{S}_{n+1}^k + \frac{2\alpha}{t_\Delta} (\bar{\mathbf{E}}_{n+1}^k - \bar{\mathbf{E}}_n) \right]_M (\nabla \mathbf{u}_\Delta)_c \right. \\ & \quad \left. + [D\bar{\mathbf{E}}(\mathbf{u}_n + \mathbf{u}_{n+1}^k)[\mathbf{u}_\delta]]_c^T \left[(\mathbf{S}_\Delta)_c + \frac{2\alpha}{t_\Delta} [D\bar{\mathbf{E}}(\mathbf{u}_{n+1}^k)[\mathbf{u}_\Delta]]_c \right] \right) d\Omega \\ & = \int_\Omega \rho_0 \mathbf{u}_\delta^T \mathbf{b}_{\text{alg}} d\Omega + \int_{\Gamma_i} \mathbf{u}_\delta^T \bar{\mathbf{t}}_{\text{alg}} d\Gamma - 2 \int_\Omega \rho_0 \mathbf{u}_\delta^T \left(\frac{\mathbf{u}_{n+1}^k - \mathbf{u}_n}{t_\Delta^2} - \frac{\mathbf{v}_n}{t_\Delta} \right) \\ & \quad - \frac{1}{4} \int_\Omega [D\bar{\mathbf{E}}(\mathbf{u}_n + \mathbf{u}_{n+1}^k)[\mathbf{u}_\delta]]_c^T \left[(\mathbf{S}_n)_c + (\mathbf{S}_{n+1}^k)_c + \frac{2\alpha}{t_\Delta} [(\bar{\mathbf{E}}_{n+1}^k)_c - (\bar{\mathbf{E}}_n)_c] \right] d\Omega, \quad \forall \mathbf{u}_\delta \in V_u, \quad (23) \end{aligned}$$

$$\begin{aligned} & \int_\Omega (\mathbf{S}_\delta)_c^T [D\bar{\mathbf{E}}(\mathbf{u}_{n+1}^k)[\mathbf{u}_\Delta]]_c d\Omega - \int_\Omega (\mathbf{S}_\delta)_c^T \mathbb{C}_c^{-1} (\mathbf{S}_\Delta)_c d\Omega \\ & = \int_\Omega (\mathbf{S}_\delta)_c^T [\hat{\mathbf{E}}_c(\mathbf{S}_{n+1}^k) - \bar{\mathbf{E}}_c(\mathbf{u}_{n+1}^k)] d\Omega, \quad \forall \mathbf{S}_\delta \in V_S. \quad (24) \end{aligned}$$

3.2. Finite element discretization. To obtain the finite element matrices, we introduce the discretizations

$$\mathbf{u} = \mathbf{N}\hat{\mathbf{u}}, \quad \mathbf{u}_\delta = \mathbf{N}\hat{\mathbf{u}}_\delta, \quad \mathbf{u}_\Delta = \mathbf{N}\hat{\mathbf{u}}_\Delta, \quad \mathbf{S}_c = \mathbf{P}\boldsymbol{\beta}, \quad (\mathbf{S}_\delta)_c = \mathbf{P}\boldsymbol{\beta}_\delta, \quad (\mathbf{S}_\Delta)_c = \mathbf{P}\boldsymbol{\beta}_\Delta. \quad (25)$$

The shape functions \mathbf{N} are the standard isoparametric displacement shape functions. The choice of the stress interpolation functions \mathbf{P} is discussed in Section 3.3. Using these interpolations, we have

$$\begin{aligned} \{D\bar{\mathbf{E}}(\mathbf{u}_{n+1}^k)[\mathbf{u}_\Delta]\}_c &= (\mathbf{B}_L)_{n+1} \hat{\mathbf{u}}_\Delta, & (\nabla \mathbf{u}_\Delta)_c &= \mathbf{B}_{NL} \hat{\mathbf{u}}_\Delta, \\ \{D\bar{\mathbf{E}}(\mathbf{u}_{n+1}^k)[\mathbf{u}_\delta]\}_c &= (\mathbf{B}_L)_{n+1} \hat{\mathbf{u}}_\delta, & (\nabla \mathbf{u}_\delta)_c &= \mathbf{B}_{NL} \hat{\mathbf{u}}_\delta, \end{aligned}$$

where $(\mathbf{B}_L)_{n+1} = \mathbf{B}_{L1} + \mathbf{B}_{L2}$, with

$$\mathbf{B}_{L1} = \begin{bmatrix} N_{1,1} & 0 & 0 & N_{2,1} & 0 & 0 & \dots \\ 0 & N_{1,2} & 0 & 0 & N_{2,2} & 0 & \dots \\ 0 & 0 & N_{1,3} & 0 & 0 & N_{2,3} & \dots \\ N_{1,2} & N_{1,1} & 0 & N_{2,2} & N_{2,1} & 0 & \dots \\ 0 & N_{1,3} & N_{1,2} & 0 & N_{2,3} & N_{2,2} & \dots \\ N_{1,3} & 0 & N_{1,1} & N_{2,3} & 0 & N_{2,1} & \dots \end{bmatrix},$$

$$\mathbf{B}_{L2} = \begin{bmatrix} (\nabla \mathbf{u}_{n+1}^k)_{11} N_{1,1} & (\nabla \mathbf{u}_{n+1}^k)_{21} N_{1,1} & (\nabla \mathbf{u}_{n+1}^k)_{31} N_{1,1} & \dots \\ (\nabla \mathbf{u}_{n+1}^k)_{12} N_{1,2} & (\nabla \mathbf{u}_{n+1}^k)_{22} N_{1,2} & (\nabla \mathbf{u}_{n+1}^k)_{32} N_{1,2} & \dots \\ (\nabla \mathbf{u}_{n+1}^k)_{13} N_{1,3} & (\nabla \mathbf{u}_{n+1}^k)_{23} N_{1,3} & (\nabla \mathbf{u}_{n+1}^k)_{33} N_{1,3} & \dots \\ (\nabla \mathbf{u}_{n+1}^k)_{12} N_{1,1} + (\nabla \mathbf{u}_{n+1}^k)_{11} N_{1,2} & (\nabla \mathbf{u}_{n+1}^k)_{22} N_{1,1} + (\nabla \mathbf{u}_{n+1}^k)_{21} N_{1,2} & (\nabla \mathbf{u}_{n+1}^k)_{32} N_{1,1} + (\nabla \mathbf{u}_{n+1}^k)_{31} N_{1,2} & \dots \\ (\nabla \mathbf{u}_{n+1}^k)_{13} N_{1,2} + (\nabla \mathbf{u}_{n+1}^k)_{12} N_{1,3} & (\nabla \mathbf{u}_{n+1}^k)_{23} N_{1,2} + (\nabla \mathbf{u}_{n+1}^k)_{22} N_{1,3} & (\nabla \mathbf{u}_{n+1}^k)_{33} N_{1,2} + (\nabla \mathbf{u}_{n+1}^k)_{32} N_{1,3} & \dots \\ (\nabla \mathbf{u}_{n+1}^k)_{11} N_{1,3} + (\nabla \mathbf{u}_{n+1}^k)_{13} N_{1,1} & (\nabla \mathbf{u}_{n+1}^k)_{21} N_{1,3} + (\nabla \mathbf{u}_{n+1}^k)_{23} N_{1,1} & (\nabla \mathbf{u}_{n+1}^k)_{31} N_{1,3} + (\nabla \mathbf{u}_{n+1}^k)_{33} N_{1,1} & \dots \end{bmatrix},$$

$$\mathbf{B}_{NL} = \begin{bmatrix} N_{1,1} & 0 & 0 & N_{2,1} & 0 & 0 & \dots \\ N_{1,2} & 0 & 0 & N_{2,2} & 0 & 0 & \dots \\ N_{1,3} & 0 & 0 & N_{2,3} & 0 & 0 & \dots \\ 0 & N_{1,1} & 0 & 0 & N_{2,1} & 0 & \dots \\ 0 & N_{1,2} & 0 & 0 & N_{2,2} & 0 & \dots \\ 0 & N_{1,3} & 0 & 0 & N_{2,3} & 0 & \dots \\ 0 & 0 & N_{1,1} & 0 & 0 & N_{2,1} & \dots \\ 0 & 0 & N_{1,2} & 0 & 0 & N_{2,2} & \dots \\ 0 & 0 & N_{1,3} & 0 & 0 & N_{2,3} & \dots \end{bmatrix}.$$

Let $\mathbf{M} := \int_{\Omega} \rho_0 \mathbf{N}^T \mathbf{N} d\Omega$. Using the arbitrariness of $\hat{\mathbf{u}}_{\delta}$ and $\boldsymbol{\beta}_{\delta}$, the matrix form of the incremental equations (23) and (24) can be written as

$$\mathbf{Q}\hat{\mathbf{u}}_{\Delta} + \mathbf{G}_1^T \boldsymbol{\beta}_{\Delta} = \mathbf{f}_1, \quad \mathbf{G}_2 \hat{\mathbf{u}}_{\Delta} - \mathbf{H} \boldsymbol{\beta}_{\Delta} = \mathbf{f}_2, \quad (26)$$

where

$$\begin{aligned} \mathbf{Q} &= \frac{2\mathbf{M}}{t_{\Delta}^2} + \frac{1}{4} \int_{\Omega} \mathbf{B}_{NL}^T \left[\mathbf{S}_n + \mathbf{S}_{n+1}^k + \frac{2\alpha}{t_{\Delta}} (\bar{\mathbf{E}}_{n+1}^k - \bar{\mathbf{E}}_n) \right]_M \mathbf{B}_{NL} d\Omega + \frac{\alpha}{2t_{\Delta}} \int_{\Omega_e} [(\mathbf{B}_L)_n + (\mathbf{B}_L)_{n+1}^k]^T (\mathbf{B}_L)_{n+1}^k d\Omega, \\ \mathbf{G}_1 &= \frac{1}{4} \int_{\Omega} \mathbf{P}^T [(\mathbf{B}_L)_n + (\mathbf{B}_L)_{n+1}^k] d\Omega, \\ \mathbf{G}_2 &= \int_{\Omega} \mathbf{P}^T (\mathbf{B}_L)_{n+1}^k d\Omega, \\ \mathbf{H} &= \int_{\Omega} \mathbf{P}^T \mathbb{C}_c^{-1} \mathbf{P} d\Omega, \\ \mathbf{f}_1 &= \int_{\Omega} \rho_0 \mathbf{N}^T \mathbf{b}_{\text{alg}} d\Omega + \int_{\Gamma_i} \mathbf{N}^T \bar{\mathbf{t}}_{\text{alg}} d\Gamma - \frac{1}{4} \int_{\Omega} [(\mathbf{B}_L)_n + (\mathbf{B}_L)_{n+1}^k]^T \left[\mathbf{S}_n + \mathbf{S}_{n+1}^k + \frac{2\alpha}{t_{\Delta}} [\bar{\mathbf{E}}_{n+1}^k - \bar{\mathbf{E}}_n] \right]_c d\Omega \\ &\quad - \frac{2}{t_{\Delta}^2} \int_{\Omega} \rho_0 \mathbf{N}^T (\mathbf{u}_{n+1}^k - \mathbf{u}_n) d\Omega + \frac{2}{t_{\Delta}} \int_{\Omega} \rho_0 \mathbf{N}^T \mathbf{v}_n d\Omega, \\ \mathbf{f}_2 &= \int_{\Omega} \mathbf{P}^T [\hat{\mathbf{E}}_c(\mathbf{S}_{n+1}^k) - \bar{\mathbf{E}}_c(\mathbf{u}_{n+1}^k)] d\Omega. \end{aligned} \quad (27)$$

Eliminating $\boldsymbol{\beta}_{\Delta}$ in (26), we get

$$\mathbf{K} \hat{\mathbf{u}}_{\Delta} = \mathbf{f}_{\Delta}, \quad (28)$$

where

$$\mathbf{K} = \mathbf{Q} + \mathbf{G}_1^T \mathbf{H}^{-1} \mathbf{G}_2 \quad \text{and} \quad \mathbf{f}_{\Delta} = \mathbf{f}_1 + \mathbf{G}_1^T \mathbf{H}^{-1} \mathbf{f}_2. \quad (29)$$

Due to the presence of the mass matrix \mathbf{M} , the stiffness matrix \mathbf{K} does not become singular even in dynamic buckling problems, circumventing the need for special strategies such as arc-length methods that are needed to find the load-deflection curve within the static framework.

Since the stress interpolation is allowed to be discontinuous across element boundaries, \mathbf{H}^{-1} is composed of distinct block matrices $\mathbf{H}_{(e)}^{-1}$ associated with each element. Thus, the element stiffness matrix

is given by

$$\mathbf{K}_{(e)} = \mathbf{Q}_{(e)} + (\mathbf{G}_{(e)})_1^T \mathbf{H}_{(e)}^{-1} (\mathbf{G}_{(e)})_2,$$

where, the subscript e indicates that the integrations in Equations (27) are carried out over the element domain Ω_e instead of over Ω . Once \mathbf{u}_Δ is obtained from (28), the stresses are updated using $\mathbf{S}_c^{k+1} = \mathbf{S}_c^k + (\mathbf{S}_\Delta)_c$, where

$$(\mathbf{S}_\Delta)_c^{(e)} = \mathbf{P}_{(e)}(\boldsymbol{\beta}_\Delta)_{(e)} = \mathbf{P}_{(e)} \mathbf{H}_{(e)}^{-1} [\mathbf{G}_2 \mathbf{u}_\Delta - \mathbf{f}_2]_{(e)},$$

and, finally, the strains \mathbf{E}^{k+1} are obtained using the constitutive relation $\mathbf{S}^{k+1} = \hat{\mathbf{S}}(\mathbf{E}^{k+1})$. The velocity field \mathbf{v}_{n+1} is recovered using (7).

In a standard displacement-based isoparametric formulation, the stiffness matrix is given by

$$\mathbf{K}_{(e)}^{\text{disp}} = \mathbf{Q}_{(e)} + \frac{1}{4} \int_{\Omega_e} [(\mathbf{B}_L)_n + (\mathbf{B}_L)_{n+1}^k]^T \mathbb{C}_c (\mathbf{B}_L)_{n+1}^k d\Omega, \quad (30)$$

while \mathbf{f}_Δ is simply given by \mathbf{f}_1 . Thus, the difference between the displacement-based and hybrid stiffness matrices is in the second term, similar to the static case. As we shall see in Section 4, this difference is critical in ensuring that the hybrid elements perform much better compared to displacement-based elements.

3.3. Choice of the stress interpolation function. For the 8-node hexahedral element, we use the stress interpolation given in [Pian and Tong 1986; Sze and Fan 1996], while for the 4-node axisymmetric element, we use the stress interpolation in [Jog and Annabattula 2006], which uses the same in-plane stress interpolation as the Pian–Sumihara 4-node quadrilateral element [Pian and Sumihara 1984]. These elements satisfy the inf-sup conditions [Xue et al. 1985].

Lee and Rhiu [1986] have developed a procedure for finding the stress interpolation for a 9-node planar quadrilateral element which leads to

$$\begin{aligned} S^{\zeta\zeta} &= \beta_1 + \beta_2\zeta + \beta_3\eta + \beta_4\zeta\eta + \beta_{13}\zeta\eta^2, \\ S^{\eta\eta} &= \beta_5 + \beta_6\zeta + \beta_7\eta + \beta_8\zeta\eta + \beta_{14}\zeta^2\eta, \\ S^{\zeta\eta} &= \beta_9 + \beta_{10}\zeta + \beta_{11}\eta + \beta_{12}\zeta\eta. \end{aligned}$$

The terms η^2 and ζ^2 are excluded from the interpolations for $S^{\zeta\zeta}$ and $S^{\eta\eta}$, respectively, since their exclusion gives rise to a zero-energy mode that is noncommunicable, and hence harmless. Although the above interpolation works extremely well for statics problems, we have found that when used within the context of a 9-node axisymmetric element, the exclusion of these terms causes an instability in the solution of the bar-impact problem discussed in Section 4.5. When the interpolation is modified so as to include these terms, meaning when we use

$$\begin{aligned} S^{\zeta\zeta} &= \beta_1 + \beta_2\zeta + \beta_3\eta + \beta_4\zeta\eta + \beta_5\eta^2 + \beta_6\zeta\eta^2, & S^{\zeta\eta} &= \beta_{13} + \beta_{14}\zeta + \beta_{15}\eta + \beta_{16}\zeta\eta, \\ S^{\eta\eta} &= \beta_7 + \beta_8\zeta + \beta_9\eta + \beta_{10}\zeta\eta + \beta_{11}\zeta^2 + \beta_{12}\zeta^2\eta, & S^{\theta\theta} &= \beta_{17} + \beta_{18}\zeta + \beta_{19}\eta + \beta_{20}\zeta\eta, \end{aligned} \quad (31)$$

the instability no longer occurs. One could also use an interpolation of the form

$$\begin{aligned} S^{\zeta\zeta} &= \beta_1 + \beta_2\zeta + \beta_3\eta + \beta_4\zeta\eta + \beta_5\eta^2 + \beta_6\zeta\eta^2, & S^{\zeta\eta} &= \beta_{13} + \beta_{14}\zeta + \beta_{15}\eta, \\ S^{\eta\eta} &= \beta_7 + \beta_8\zeta + \beta_9\eta + \beta_{10}\zeta\eta + \beta_{11}\zeta^2 + \beta_{12}\zeta^2\eta, & S^{\theta\theta} &= \beta_{16} + (J_{12}\zeta + J_{22}\eta)\beta_{17}, \end{aligned}$$

where J_{12} and J_{22} denote entries of the Jacobian matrix as in [Jog and Annabattula 2006]; this has the same normal stress interpolation as (31), it uses the minimum number of β parameters, and results in a full-rank stiffness matrix (apart from rigid-body modes). However, the exclusion of lower-order terms from the $S^{\xi\eta}$ and $S^{\theta\theta}$ interpolations leads to bad results even on statics problems. Thus, although the 20β model does result in a slight stiffening compared to the 17β model of [Jog and Annabattula 2006], it is more robust within the framework of transient problems. Of course, since a static solution can be considered to be steady-state solution of a transient problem, one should use the 20β model within the static framework also.

In a similar manner, for the 27-node hexahedral element developed in [Jog 2005], one now uses a normal stress interpolation that is obtained by differentiating the displacement interpolation field. Leaving out some terms may result in a full-rank stiffness matrix and may yield extremely good results on statics problems, as shown in [Jog 2005], but results in the same instability as mentioned above in the bar-impact problem. Carrying out this modification, we now use the following interpolation:

$$\begin{aligned}
S^{\xi\xi} &= \beta_1 + \beta_2\xi + \beta_3\eta + \beta_4\zeta + \beta_5\xi\eta + \beta_6\eta\zeta + \beta_7\xi\zeta + \beta_8\xi\eta\zeta + \beta_9\xi\eta^2 + \beta_{10}\xi\zeta^2 \\
&\quad + \beta_{11}\xi\eta\zeta^2 + \beta_{12}\xi\eta^2\zeta + \beta_{13}\xi\eta^2\zeta^2 + \beta_{14}\eta^2 + \beta_{15}\zeta^2 + \beta_{16}\eta^2\zeta + \beta_{17}\eta\zeta^2 + \beta_{18}\eta^2\zeta^2, \\
S^{\eta\eta} &= \beta_{19} + \beta_{20}\xi + \beta_{21}\eta + \beta_{22}\zeta + \beta_{23}\xi\eta + \beta_{24}\eta\zeta + \beta_{25}\xi\zeta + \beta_{26}\xi\eta\zeta + \beta_{27}\xi^2\eta + \beta_{28}\eta\zeta^2 \\
&\quad + \beta_{29}\xi^2\eta\zeta + \beta_{30}\xi\eta\zeta^2 + \beta_{31}\xi^2\eta\zeta^2 + \beta_{32}\xi^2 + \beta_{33}\zeta^2 + \beta_{34}\xi^2\zeta + \beta_{35}\xi\zeta^2 + \beta_{36}\xi^2\zeta^2, \\
S^{\zeta\zeta} &= \beta_{37} + \beta_{38}\xi + \beta_{39}\eta + \beta_{40}\zeta + \beta_{41}\xi\eta + \beta_{42}\eta\zeta + \beta_{43}\xi\zeta + \beta_{44}\xi\eta\zeta + \beta_{45}\xi^2\zeta + \beta_{46}\eta^2\zeta \\
&\quad + \beta_{47}\xi^2\eta\zeta + \beta_{48}\xi\eta^2\zeta + \beta_{49}\xi^2\eta^2\zeta + \beta_{50}\xi^2 + \beta_{51}\eta^2 + \beta_{52}\xi^2\eta + \beta_{53}\xi\eta^2 + \beta_{54}\xi^2\eta^2, \\
S^{\xi\eta} &= \beta_{55} + \beta_{56}\xi + \beta_{57}\eta + \beta_{58}\zeta + \beta_{59}\xi\eta + \beta_{60}\eta\zeta + \beta_{61}\xi\zeta + \beta_{62}\xi\eta\zeta + \beta_{63}\xi\zeta^2 + \beta_{64}\eta\zeta^2, \\
S^{\eta\zeta} &= \beta_{65} + \beta_{66}\xi + \beta_{67}\eta + \beta_{68}\zeta + \beta_{69}\xi\eta + \beta_{70}\eta\zeta + \beta_{71}\xi\zeta + \beta_{72}\xi\eta\zeta + \beta_{73}\xi^2\eta + \beta_{74}\xi^2\zeta, \\
S^{\xi\zeta} &= \beta_{75} + \beta_{76}\xi + \beta_{77}\eta + \beta_{78}\zeta + \beta_{79}\xi\eta + \beta_{80}\eta\zeta + \beta_{81}\xi\zeta + \beta_{82}\xi\eta\zeta + \beta_{83}\xi\eta^2 + \beta_{84}\eta^2\zeta. \tag{32}
\end{aligned}$$

The zero-energy modes that were earlier suppressed by the terms $\xi\eta\zeta^2$, $\xi^2\eta\zeta$, and $\xi\eta^2\zeta$ in the $S^{\xi\eta}$, $S^{\eta\zeta}$, and $S^{\xi\zeta}$ interpolations are now suppressed due to the inclusion of the terms $\eta^2\zeta^2$, $\xi^2\zeta^2$, and $\xi^2\eta^2$ in the $S^{\xi\xi}$, $S^{\eta\eta}$, and $S^{\zeta\zeta}$ interpolations, and hence these terms are excluded from the shear interpolation.

Similarly to the axisymmetric case, one could develop a 75β element, which has the same normal stress interpolation as above and which results in a full-rank stiffness matrix, as follows:

$$\begin{aligned}
S^{\xi\xi} &= \beta_1 + \beta_2\xi + \beta_3\eta + \beta_4\zeta + \beta_5\xi\eta + \beta_6\eta\zeta + \beta_7\xi\zeta + \beta_8\xi\eta\zeta + \beta_9\xi\eta^2 + \beta_{10}\xi\zeta^2 \\
&\quad + \beta_{11}\xi\eta\zeta^2 + \beta_{12}\xi\eta^2\zeta + \beta_{13}\xi\eta^2\zeta^2 + \beta_{14}\eta^2 + \beta_{15}\zeta^2 + \beta_{16}\eta^2\zeta + \beta_{17}\eta\zeta^2 + \beta_{18}\eta^2\zeta^2, \\
S^{\eta\eta} &= \beta_{19} + \beta_{20}\xi + \beta_{21}\eta + \beta_{22}\zeta + \beta_{23}\xi\eta + \beta_{24}\eta\zeta + \beta_{25}\xi\zeta + \beta_{26}\xi\eta\zeta + \beta_{27}\xi^2\eta + \beta_{28}\eta\zeta^2 \\
&\quad + \beta_{29}\xi^2\eta\zeta + \beta_{30}\xi\eta\zeta^2 + \beta_{31}\xi^2\eta\zeta^2 + \beta_{32}\xi^2 + \beta_{33}\zeta^2 + \beta_{34}\xi^2\zeta + \beta_{35}\xi\zeta^2 + \beta_{36}\xi^2\zeta^2, \\
S^{\zeta\zeta} &= \beta_{37} + \beta_{38}\xi + \beta_{39}\eta + \beta_{40}\zeta + \beta_{41}\xi\eta + \beta_{42}\eta\zeta + \beta_{43}\xi\zeta + \beta_{44}\xi\eta\zeta + \beta_{45}\xi^2\zeta + \beta_{46}\eta^2\zeta \\
&\quad + \beta_{47}\xi^2\eta\zeta + \beta_{48}\xi\eta^2\zeta + \beta_{49}\xi^2\eta^2\zeta + \beta_{50}\xi^2 + \beta_{51}\eta^2 + \beta_{52}\xi^2\eta + \beta_{53}\xi\eta^2 + \beta_{54}\xi^2\eta^2, \\
S^{\xi\eta} &= \beta_{55} + \beta_{56}\xi + \beta_{57}\eta + \beta_{58}\zeta + \beta_{59}\xi\eta + \beta_{60}\eta\zeta + \beta_{73}\eta\zeta^2 + \beta_{74}\xi\zeta^2, \\
S^{\eta\zeta} &= \beta_{61} + \beta_{62}\xi + \beta_{63}\eta + \beta_{64}\zeta + \beta_{65}\xi\eta + \beta_{66}\xi\zeta + \beta_{74}\xi^2\zeta + \beta_{75}\xi^2\eta,
\end{aligned}$$

$$S^{\xi\zeta} = \beta_{67} + \beta_{68}\xi + \beta_{69}\eta + \beta_{70}\zeta + \beta_{71}\xi\eta + \beta_{72}\eta\zeta + \beta_{73}\eta^2\zeta + \beta_{75}\xi\eta^2.$$

However, again, the exclusion of lower-order terms from the shear interpolation results in bad performance even on statics problems, and hence the 84β interpolation given by (32) is recommended for both statics and transient problems in view of its increased robustness in transient problems.

Note that the (numerical) instability problem discussed above does not arise in the case of lower-order elements since there the normal stress interpolation is already consistent with the one obtained by differentiating the displacement field.

4. Numerical examples

In this section, we present a wide variety of example problems, ranging from almost rigid to highly flexible beam or shell-type structures, to show the high accuracy and convergence rate of the proposed formulation. We shall denote the energy-momentum conserving displacement-based 27-node and the hybrid 8 and 27-node elements by I27, H8, and H27, respectively. Comparisons are carried out with different strategies presented in the literature by using coarser or equivalent meshes in the space domain, and by using larger or equivalent time steps in the time domain.

As in [Jog and Kelkar 2006], in order to ensure a fair comparison of the results between the I27, H8, and H27 elements, meshes with the *same number of global degrees of freedom* are used. For instance, results obtained using $8N$ H8 elements are compared against the results obtained using N H27 (or I27) elements, with identical nodal coordinate data and boundary conditions used in both meshes. For shell-type problems, one H27/I27 element and two H8 elements are used along the thickness direction. Uniform meshes and time steps are used in all the examples. Full integration is used to evaluate all the integrals arising in the formulation of the elements, and the WSMP sparse matrix solver [Gupta 2000; 2002] is used to solve the system of equations. A Saint-Venant–Kirchhoff material model is used in all the examples unless otherwise stated.

4.1. Flexible bar pendulum under gravity effect. This example was considered in [Yakoub and Shabana 2001]. A bar of length $l = 1$ m and uniform square cross-section (whose dimension is stated in each of the subcases), pinned at one end, oscillates under the effect of gravity, as shown in Figure 1. The bar is released at time $t = 0$ with initial velocity zero from a position $\theta = 90^\circ$. The gravitational acceleration g , the density of the bar ρ_0 , and the Poisson’s ratio are taken to be 9.81 m/s^2 , 7200 kg/m^3 , and 0.3 , respectively. We consider three cases, wherein for the first case, we start with an almost rigid pendulum,

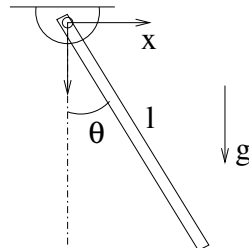


Figure 1. Geometry of the pendulum.

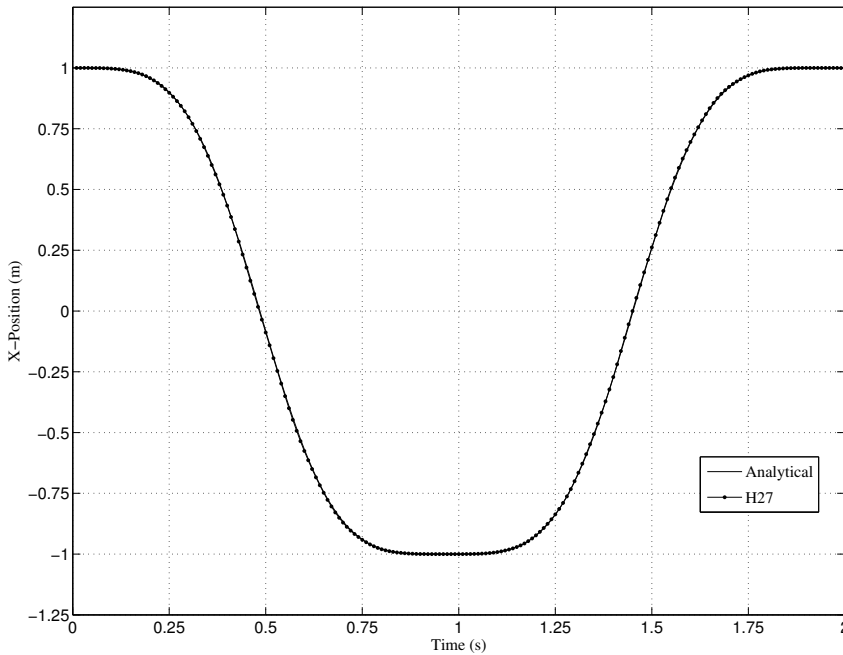


Figure 2. Comparison of the numerically obtained tip displacement of the pendulum with the analytical solution under [Case I](#).

and successively increase its flexibility in the next two cases. Consistent with the theory, the total energy (kinetic, strain, and potential) is obtained to be a constant in all the three cases.

Case I. The Young's modulus E and the cross-section dimension are taken to be 2×10^9 N/m² and 0.02 m, respectively. We use meshes of one H27 and I27 element, and an equivalent mesh for the H8 element. The simulation is carried out over the time interval $[0, 2]$ seconds with $t_{\Delta} = 0.05$ s. Since the flexural rigidity EI is quite high, the motion is almost rigid, and hence we compare our solution with the analytical solution for a rigid bar pendulum given by

$$\theta(t) = 2 \sin^{-1} \left[\frac{1}{\sqrt{2}} \operatorname{sn} \left(\sqrt{\frac{3g}{2l}} t, \frac{1}{\sqrt{2}} \right) \right],$$

where $\operatorname{sn}(\cdot, \cdot)$ denotes the elliptic sine function. As can be seen from [Figure 2](#), there is an almost perfect match between the numerically and analytically obtained solutions. [Yakoub and Shabana \[2001, Figure 6\]](#) also obtain an almost identical solution with 4 elements (the time step is not stated).

A comparison of the iterations taken by the H27 and I27 elements is shown in [Figure 3](#). It is evident that the number of iterations taken by the hybrid element is quite lower.

Case II. The Young's modulus E is decreased to a value 2×10^7 N/m², while the cross-section dimensions is kept the same. Four H27/I27 elements are used to discretize this flexible pendulum. A time step $t_{\Delta} = 0.01$ s is used. The x position of the tip of the pendulum obtained using H27/I27 elements is shown in [Figure 4](#). Eight I27 elements are required to get the same solution as obtained using four H27 elements. The coarse-mesh results of the H27 element match exactly with the ANSYS results presented

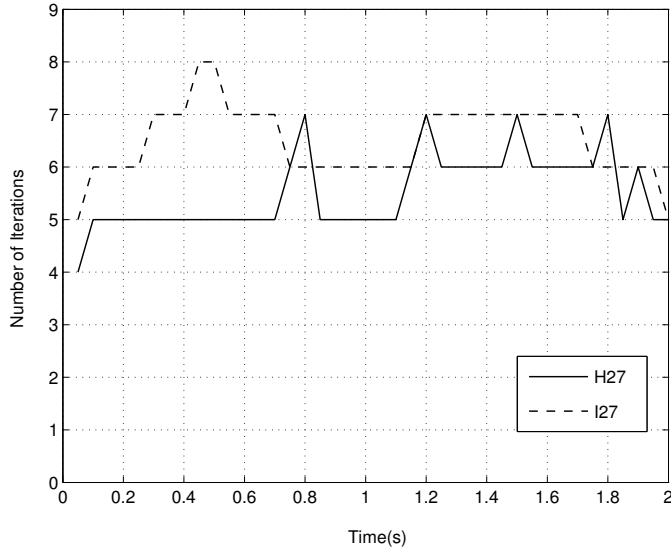


Figure 3. Comparison of the number of iterations taken by the H27 and I27 elements under [Case I](#).

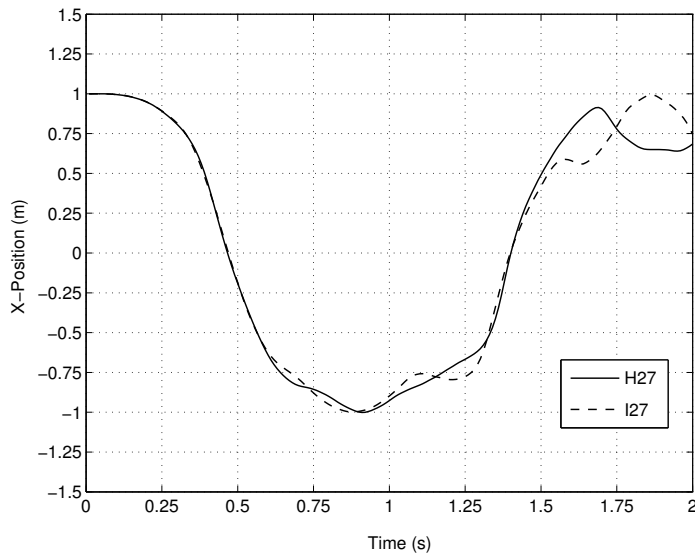


Figure 4. Tip displacement obtained using the H27 and I27 elements under [Case II](#).

in [Yakoub and Shabana 2001, Figure 7]. [Figure 5](#) shows the time history of the transverse deflection of the midpoint of the pendulum from the line joining the two ends of the pendulum, and again shows the substantial difference between the results obtained by the H27 (which match almost perfectly with the ANSYS results shown in [Yakoub and Shabana 2001, Figure 8]) and I27 elements.

Case III. The Young's modulus is maintained at the same value as in [Case II](#), but the cross-section dimension is reduced to 0.01 m. Eight H27/I27 elements are used to discretize the pendulum and the

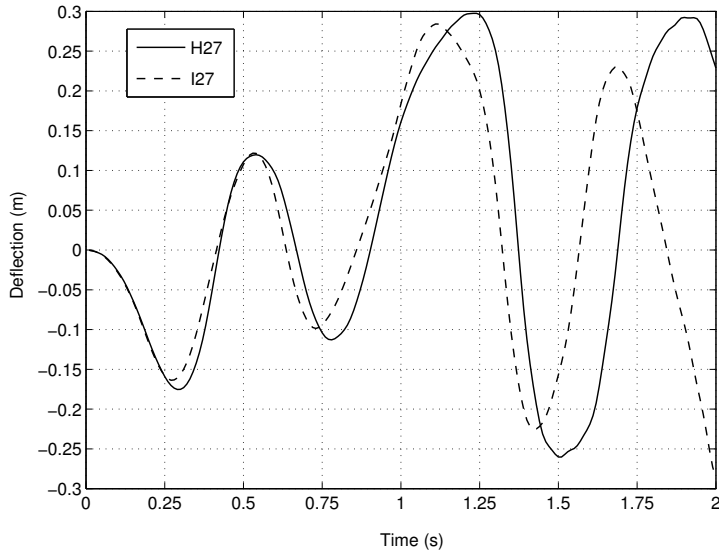


Figure 5. Deflection of the midpoint of the pendulum obtained using the H27 and I27 elements under **Case II**.

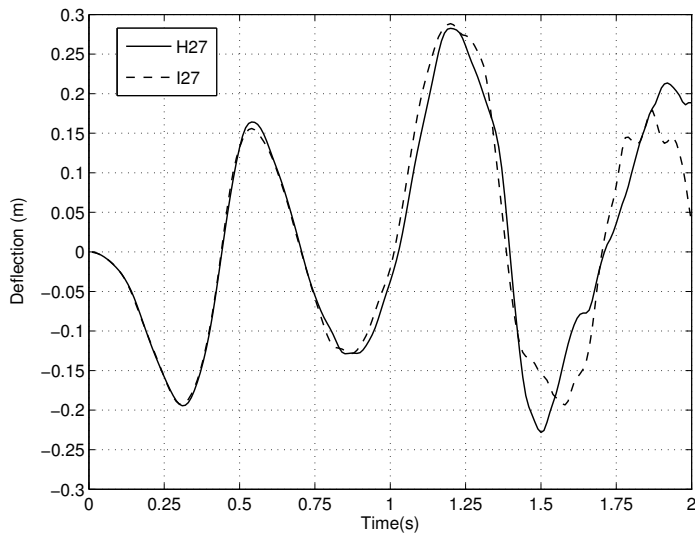


Figure 6. Deflection of the midpoint of the pendulum obtained using the H27 and I27 elements under **Case III**.

time step used is $t_{\Delta} = 0.01$ s. Once again there is a very good agreement between the H27 results shown in [Figure 6](#) and the ANSYS results presented in [[Yakoub and Shabana 2001](#), Figure 11].

4.2. Double pendulum under gravity effect. This example, which has been proposed in [[Cuadrado et al. 2001](#)], shows the performance of the algorithm in the case of rigid body motion with multiple links. The double pendulum chosen for study has two identical links of length 1.5 m, and uniform rectangular cross-section of width 0.018973 m and height 0.0632455 m. The acceleration due to gravity g , the Young's

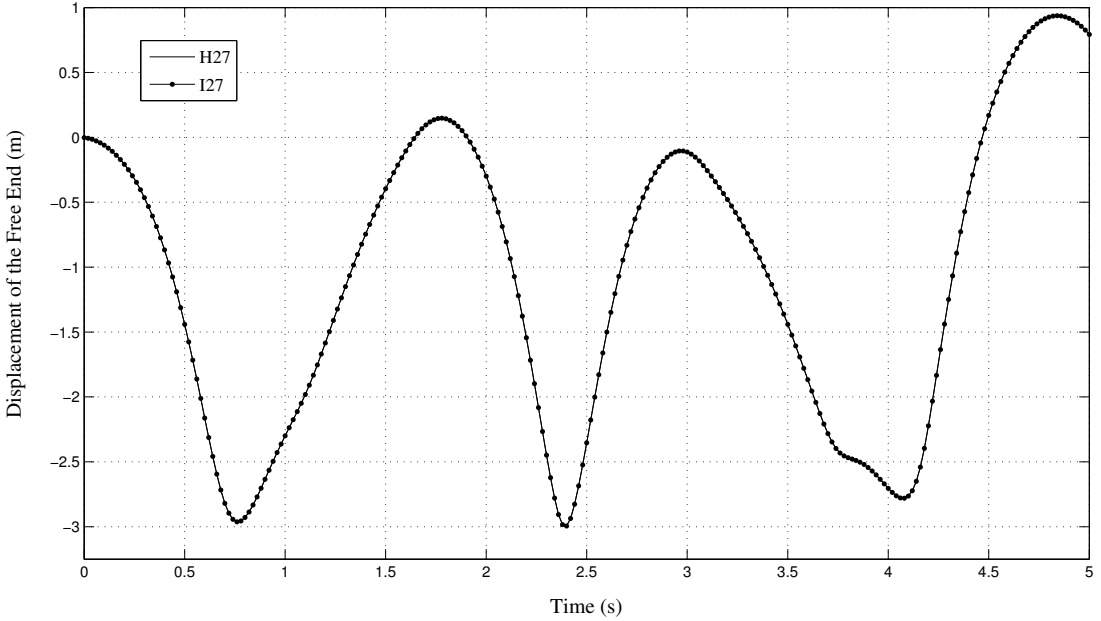


Figure 7. Time evolution of the vertical coordinate of the free end of the double pendulum.

modulus E , the Poisson's ratio, and the density are taken to be 9.81 m/s^2 , $7 \times 10^{10} \text{ N/m}^2$, 0.0 , and 2000 kg/m^3 , respectively. The double pendulum starts from rest in the horizontal position and falls under the action of gravity. The motion is studied in the interval $[0, 5]$ seconds with $t_{\Delta} = 0.02 \text{ s}$ (which is twenty times that used in [Cuadrado et al. 2001]). Two H27/I27 elements (one element per link) are used to carry out the simulation. The time evolution of the vertical coordinate of the free end of the double pendulum is shown in Figure 7, which is found to agree very well with the corresponding result presented in [Cuadrado et al. 2001, Figure 7]. The snapshots of the motion at one second intervals are shown in Figure 8. As in the single link pendulum of the previous example, the total energy (kinetic, strain, and potential) is conserved. Although the results obtained using the I27 element are almost identical to those obtained using the H27 element, the total number of iterations is much larger (4 to 5 iterations per time step for the H27 element versus 6 to 7 iterations per time step for the I27 element).

4.3. Dynamics of a tumbling cylinder. The dynamics of a short elastic cylinder, initially at rest, and subjected to an impulsive load have been studied by several researchers [Simo and Tarnow 1994; Brank et al. 1998; Balah and Al-Ghamedy 2005]. The geometry, finite element mesh for the H27 element, material parameters, and loading conditions are shown in Figure 9. The loads mentioned in Figure 9 are distributed across the height in a consistent manner. The simulation is carried out over the time interval $[0, 25]$ seconds with a time step $t_{\Delta} = 0.02 \text{ s}$. The cylinder is discretized using a mesh of 2×16 H27/I27 elements, and an equivalent mesh for H8 elements. The sequence of deformed shapes at 2 second intervals is depicted in Figure 10. Figures 11, 12, and 13 show the time history of the linear and angular momentum vector components, and the total (kinetic and strain) energy; the results of the H27 element are in very good agreement with the results presented in [Brank et al. 1998; Balah and Al-Ghamedy 2005]. In accordance with the design of the algorithm, these quantities are conserved after

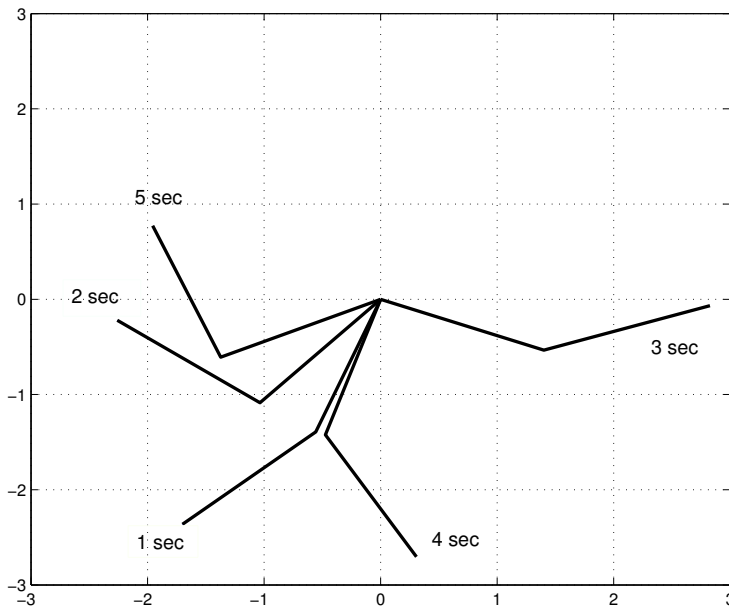


Figure 8. Snapshots of the motion of the double pendulum at one second intervals.

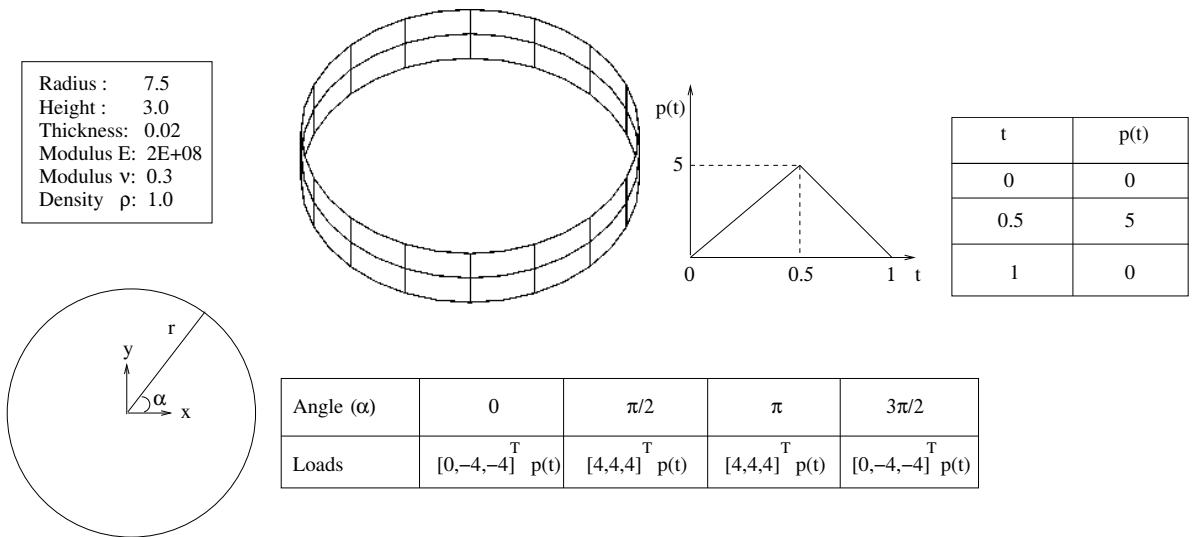


Figure 9. Short cylinder subjected to an impulsive load: geometry, material parameters, and loading conditions.

the removal of the external loads. Although the same linear momentum values are obtained using the H8 and I27/H27 elements, the angular momentum and energy values predicted by the H8 and I27 elements are different than those predicted by the H27 element, which indicates that they are susceptible to locking. One additional level of spatial refinement of the H8 element mesh yielded the same values of momentum and energy as the H27 element mesh. The algorithm also gave almost the same solution for $t_{\Delta} = 0.03$ s.



Figure 10. Sequence of deformed shapes of the tumbling cylinder at 2 second intervals.

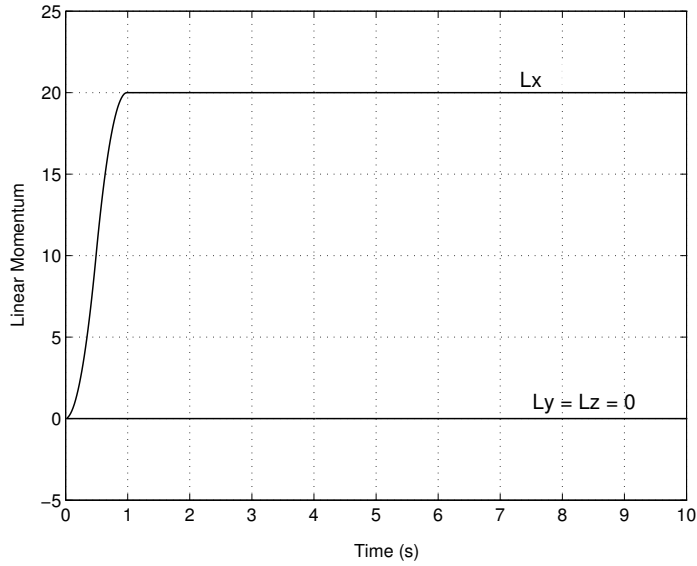


Figure 11. Tumbling cylinder: time history of linear momentum.

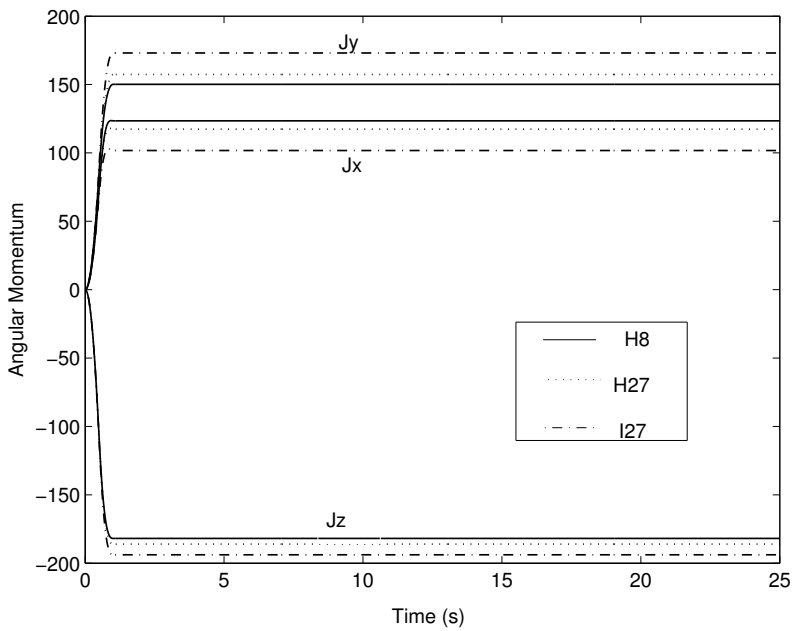


Figure 12. Tumbling cylinder: time history of angular momentum.

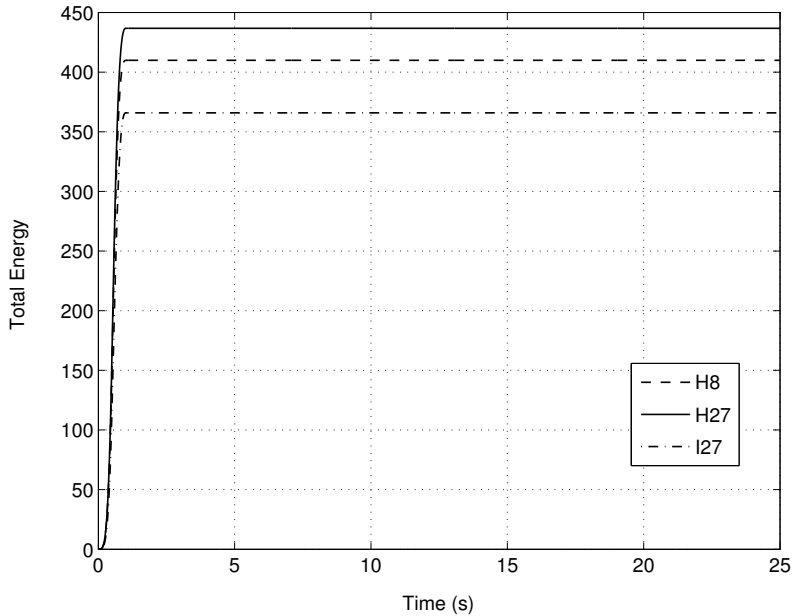


Figure 13. Tumbling cylinder: time history of total energy.

4.4. Snap-through of a cylindrical shell under concentrated vertex load. This dynamic-buckling problem has been studied by several researchers [Kuhl and Ramm 1996; 1999; Balah and Al-Ghamedy 2005]. The geometry, boundary conditions, material properties, and loading are shown in Figure 14. Two edges are simply supported as shown, and the load $R(t)$ is applied at the center of the panel. The panel first undergoes snap-through, and then shows high-frequency dominated behavior in the postbuckling phase. Due to symmetry, only one fourth of the domain is discretized using $4 \times 4 \times 1$ H27/I27 elements, and $8 \times 8 \times 2$ H8 elements, and we use a time step of $t_{\Delta} = 0.001$ s as in [Balah and Al-Ghamedy 2005]. The solutions obtained using the H27/I27 and H8 elements are shown in Figure 15; the H8 element results are in very good agreement with the third-order shear deformation theory-based element results presented in [Balah and Al-Ghamedy 2005, Figure 8]. Once again we see that the I27 and H8 elements are susceptible to locking. Refining the H8 element mesh to $16 \times 16 \times 2$ yields the same solution as the H27 element solution. We note that unlike Kuhl and Ramm [1999], we obtain the solution for $t_{\Delta} = 0.001$ s without adding any numerical dissipation or using reduced integration, and the number of iterations was also much less (around 6 iterations per time step). The snapshots of the snap-through process are shown in Figure 16.

4.5. Bar impact problem. This example has been considered in [Bauchau and Joo 1999]. A bar of length 4 m, square cross-section of dimension 1, Young's modulus $E = 1$ N/m², Poisson's ratio $\nu = 0$, and density $\rho_0 = 1$ kg/m³, travelling at a constant longitudinal velocity $v_0 = 10^{-3}$ m/s impacts a rigid wall at time $t = 0$. This impact results in a compressive stress wave which propagates with constant velocity from the left end of the bar to the right end. At time $t = 0$, all the nodes except those on the impacting face are given an initial velocity 10^{-3} m/s, and at subsequent times, the nodes on the impacting face

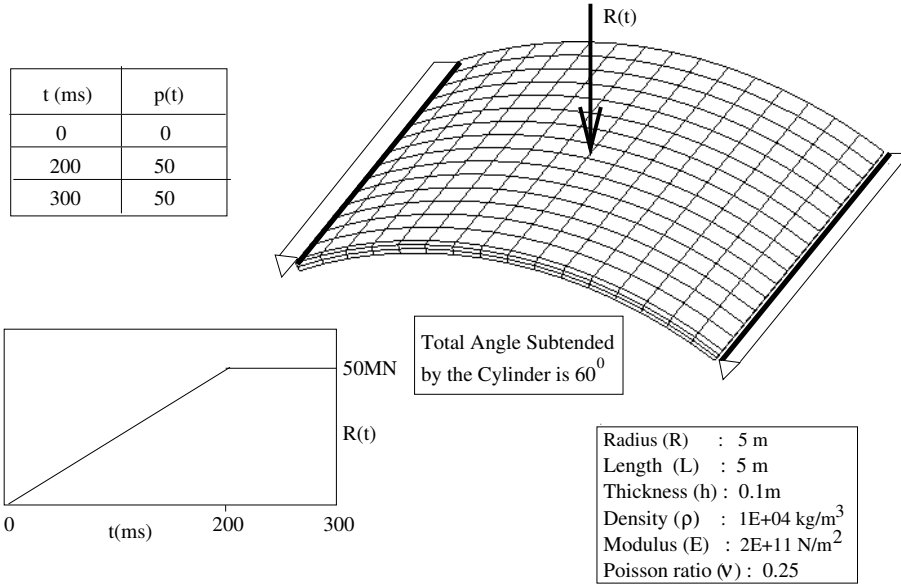


Figure 14. Dynamic buckling of a panel: geometry, material parameters and loading conditions.

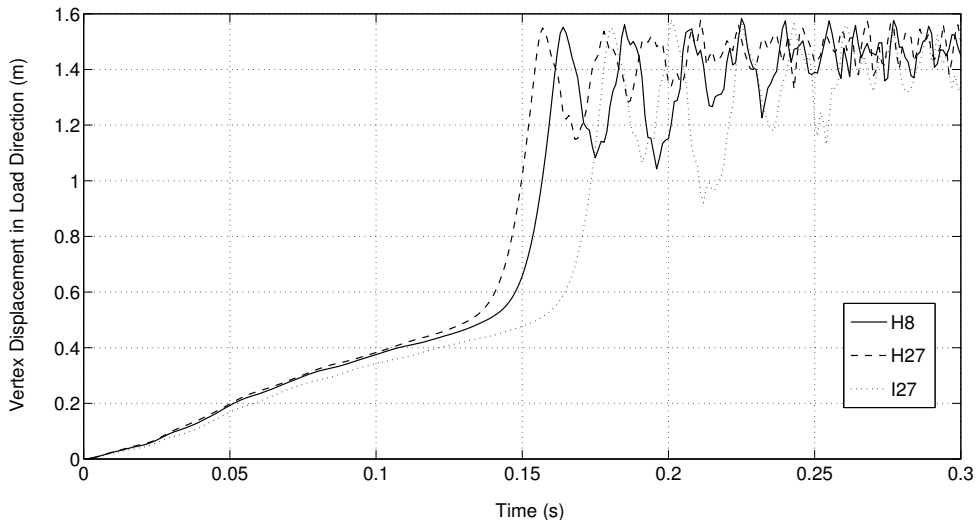


Figure 15. Snap-through of a panel: time history of the vertical displacement under the load for $t_\Delta = 0.001$.

are constrained. A time step of $t_\Delta = 0.01$ s is used. Meshes of 400 and 800 H27/I27 elements (along the length) and 1600 H8 elements are used to discretize the structure. Figure 17 shows the axial stress distribution for $x \in [2, 3]$ meters (for greater clarity) at $t = 2.56$ s, at which time the compressive stress wave is located at $x = 2.56$ m. Identical results as with the H27 element are obtained with the I27 element. In contrast with the results shown in [Bauchau and Joo 1999, Figure 14], where increasing the spatial refinement resulted in an increase in the error, with our formulation, the errors remain the same

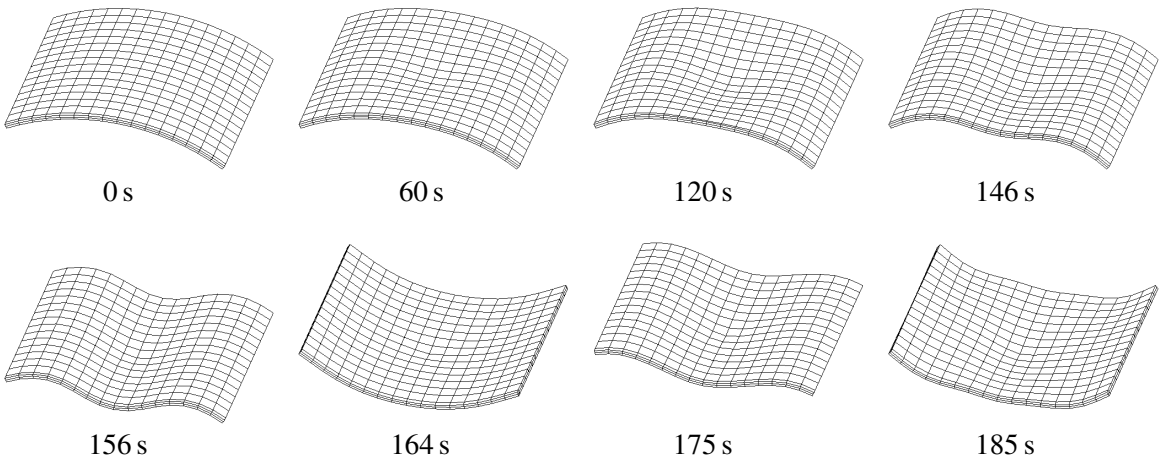


Figure 16. Panel problem: snapshots of the snap-through process.

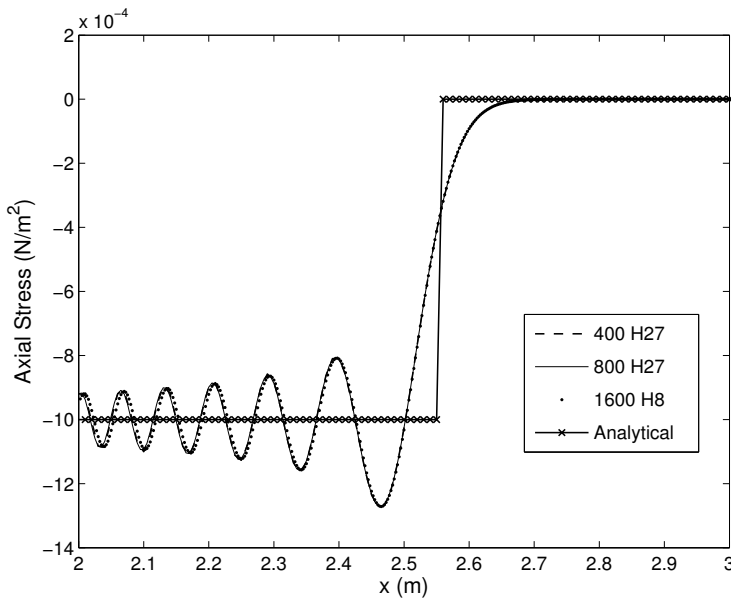


Figure 17. Bar impact problem: axial stress at time $t = 2.56$ s obtained with the energy-conserving scheme.

with spatial mesh refinement (keeping t_{Δ} fixed), thus bypassing the need for high-frequency dissipation (although, of course, introducing dissipation does smooth out the solution as discussed below). Reducing the t_{Δ} resulted in reduced amplitude and increased frequency in the oscillations. Figure 18 shows the temporal variation of the axial stress at $x = 1$ m obtained using the energy-conserving scheme.

The results obtained with the energy-dissipative scheme with α set to 0.001 are shown in Figure 19. The oscillations are damped out, and the solution is quite close to the exact solution. The decay in energy as a function of time is shown in Figure 20.

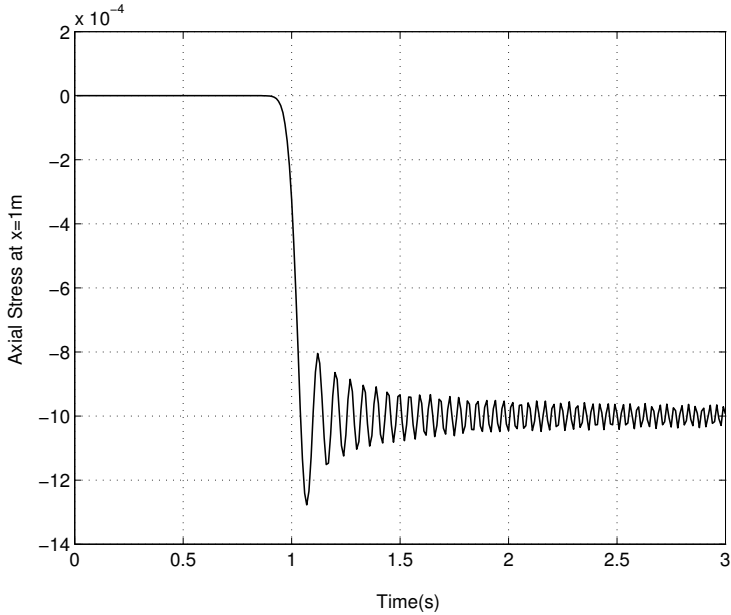


Figure 18. Bar impact problem: temporal variation of the axial stress at $x = 1$ m obtained with the 800 element H27 mesh and the energy-conserving scheme.

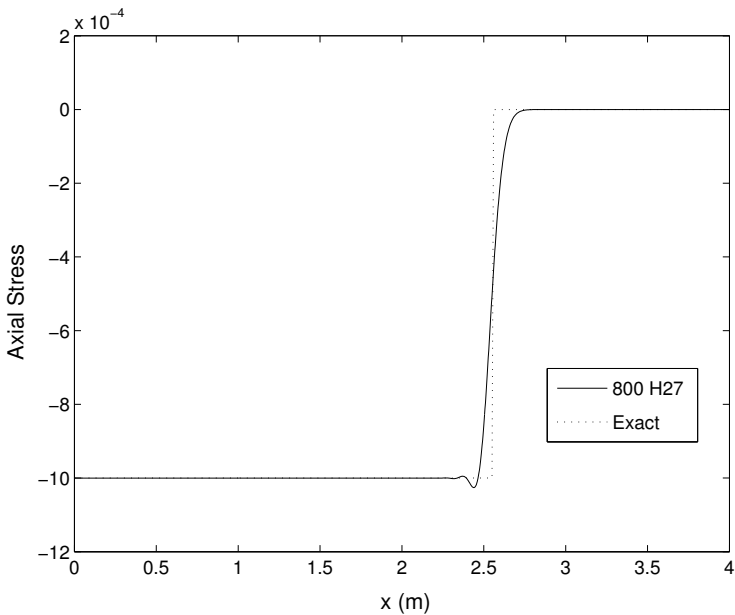


Figure 19. Bar impact problem: axial stress at time $t = 2.56$ s obtained with the energy-dissipative scheme.

The instabilities that arise in the solution with an inappropriate choice of the stress interpolation (see [Section 3.3](#)) occur around $t = 1.6$ s in the region near the impacting surface.

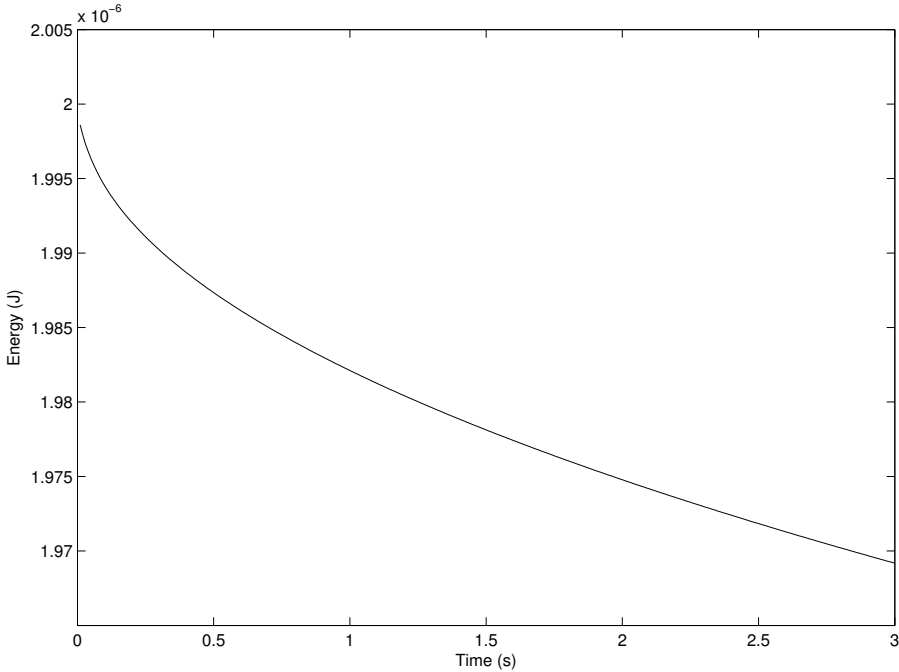


Figure 20. Bar impact problem: temporal variation of the energy obtained with the energy-dissipative scheme.

4.6. Motion of toss rule in space. This example shows the performance of the proposed algorithm when the motion is three-dimensional, and the forces are such that they cause bending, shear, and torsional deformations, and translational and rotational motion of the body [Kuhl and Ramm 1996; 1999]. The geometry, loads, and material properties are shown in Figure 21. The same time step as in [Kuhl and Ramm 1996; 1999], $t_{\Delta} = 50 \times 10^{-6}$, is used, and a mesh of 6×1 H27 elements is used. Simulations are also carried out using a refined mesh of 15×2 H27/I27 elements. The snapshots of the results until

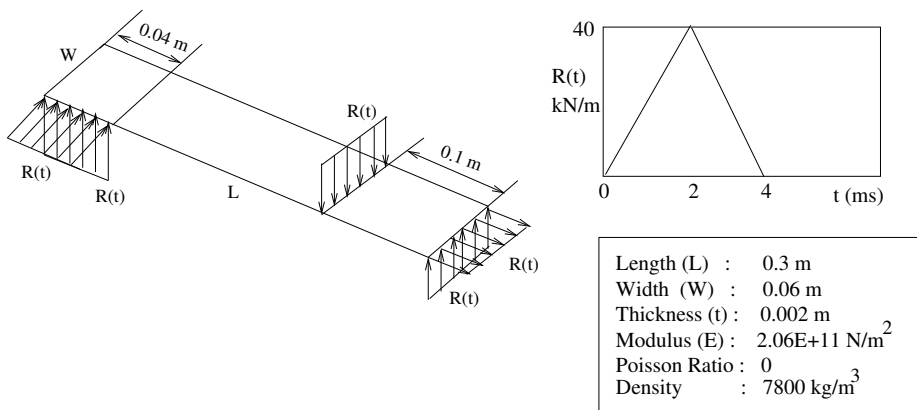


Figure 21. Toss rule problem: geometry, loads and material properties.

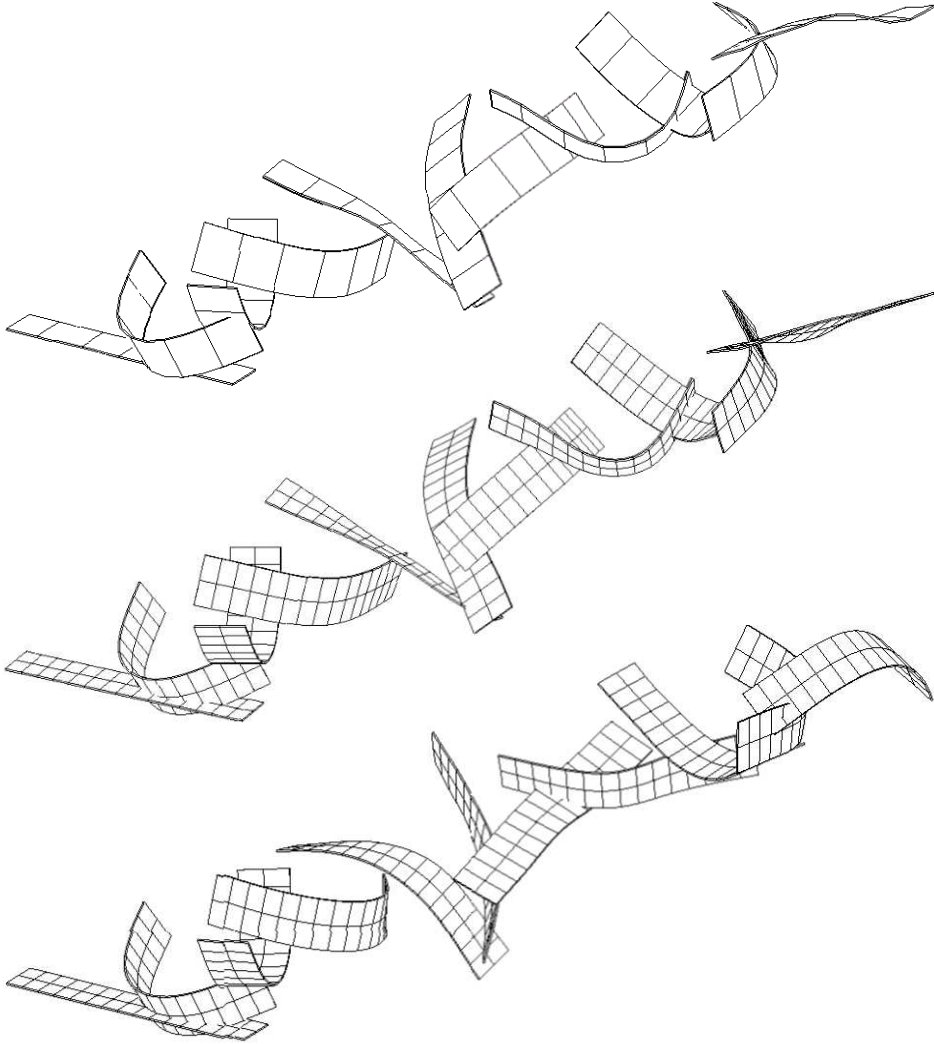


Figure 22. Motion of the toss rule obtained using a 6×1 H27 mesh (top), a 15×2 H27 mesh (middle) and a 15×2 I27 mesh (bottom).

$t = 0.04$ s at intervals of 0.004 s are shown in [Figure 22](#), and there is almost perfect agreement with the results presented in [\[Kuhl and Ramm 1999\]](#) until $t = 0.032$ s, and slight deviations thereafter. A possible explanation for the deviations might be that Kuhl and Ramm use numerical dissipation to compensate for the energy increase that they encounter due to the use of reduced integration (to prevent shear locking of their shell element). In contrast, no shear locking is observed even with the coarse H27 mesh, and the linear momentum, angular momentum, and energy are perfectly conserved after the removal of the loads, as seen in [Figure 23](#). Note that although the energy plot obtained using the I27 element is almost identical to that obtained using the H27 element, the motions are very different (compare the last two parts of [Figure 22](#)). This is because the total energy is obtained by integrating over the entire domain, so that different displacement and velocity fields can yield almost identical total energy values.

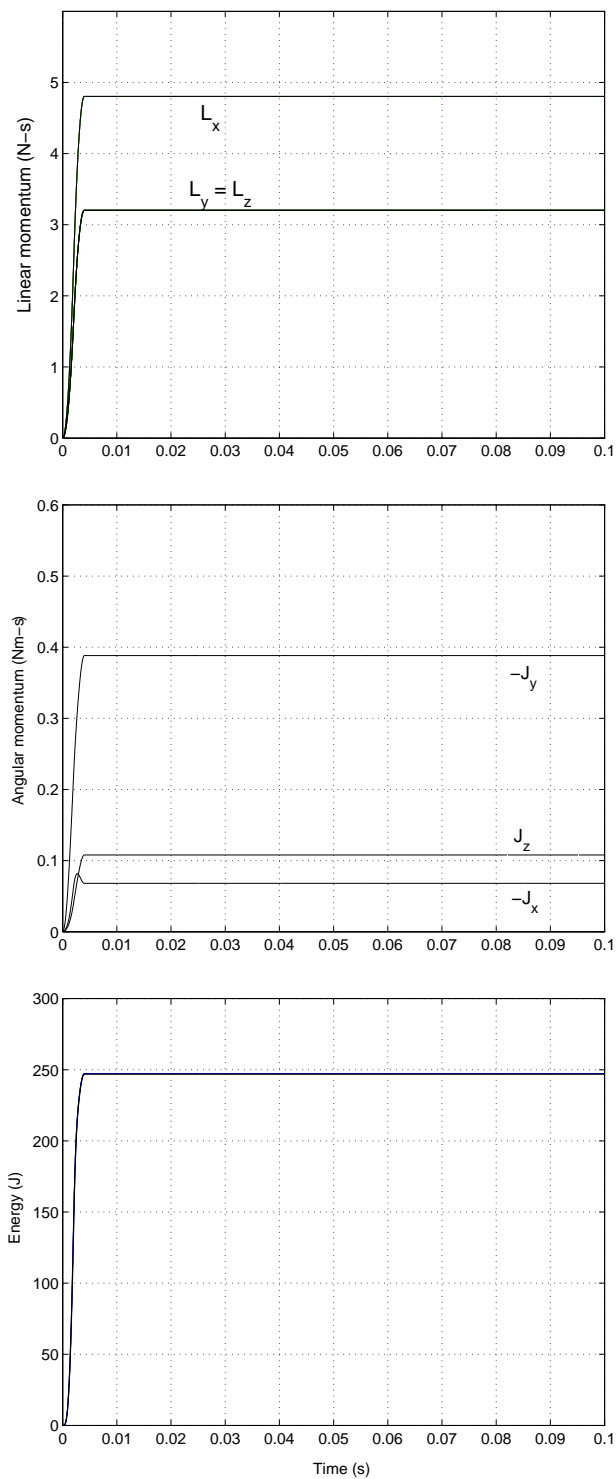


Figure 23. Toss rule problem: time history of the linear momentum (top), angular momentum (middle) and energy (bottom: H8, H27 and I27 elements).

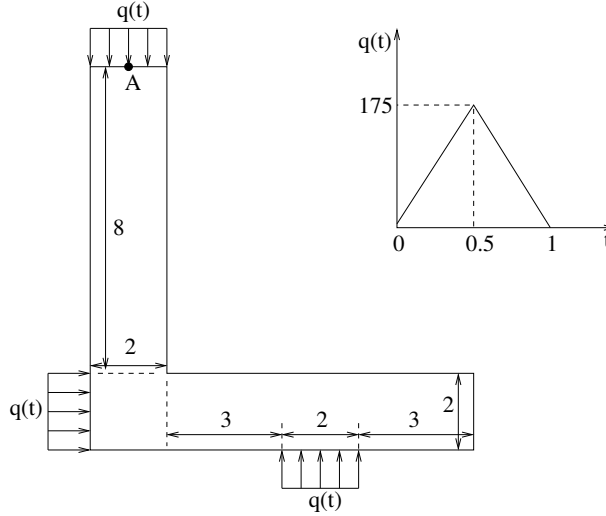


Figure 24. L-block problem: geometry and loading conditions.

4.7. L-block problem. This problem, paralleling one in [Betsch and Steinmann 2001], demonstrates the performance of the algorithm when the material model is nonlinear. An L-block under plane strain conditions is subjected to the loads shown in Figure 24. A compressible neoHookean material model with the strain-energy density function and the corresponding stress-strain relation given by

$$\hat{W} = \frac{\lambda}{8} (\ln \det \mathbf{C})^2 + \frac{\mu}{2} (\text{tr } \mathbf{C} - 3 - \ln \det \mathbf{C}), \quad \mathbf{S} = \frac{\lambda}{2} (\ln \det \mathbf{C}) \mathbf{C}^{-1} + \mu (\mathbf{I} - \mathbf{C}^{-1}).$$

is used with $\lambda = 2000$ and $\mu = 1000$. The density is $\rho_0 = 1$. A uniform mesh of 144 H27 elements is used to discretize the structure. Since the material is extremely flexible, a time step of $t_\Delta = 10^{-4}$ is used to capture the transients. The time histories of the x component of the linear momentum, the z component of the angular momentum, and the total (kinetic and strain) energy are shown in Figure 25. These values are seen to be constant after the removal of the loading. As seen in the bottom part of the figure, the energy value after the removal of the loads is 3340, while the corresponding value obtained using a coarser mesh of 36 uniform elements is 3328, showing that our mesh density is sufficient to capture the transient behavior. The (u_x, u_y) displacements of the midpoint of the top edge (point A in Figure 24) as a function of time are shown in Figure 26.

The example presented in [Betsch and Steinmann 2001] had the same geometry, but the parameters were $\lambda = 1000$, $\mu = 500$, and $\rho_0 = 0.5$. The solution given there is an unconverged solution, with a final energy value of roughly 3500, while we get a value of around 7700 with the 144-element mesh. However, a very fine time step is required to obtain this solution, and hence we have used the higher values of the material parameters given above.

5. Conclusions

A new energy-momentum conserving hybrid-stress formulation for conducting the transient analysis of nonlinear elastic structures has been presented. Since hybrid elements are less susceptible to locking compared to displacement-based elements, they can be used to conduct the transient analysis of

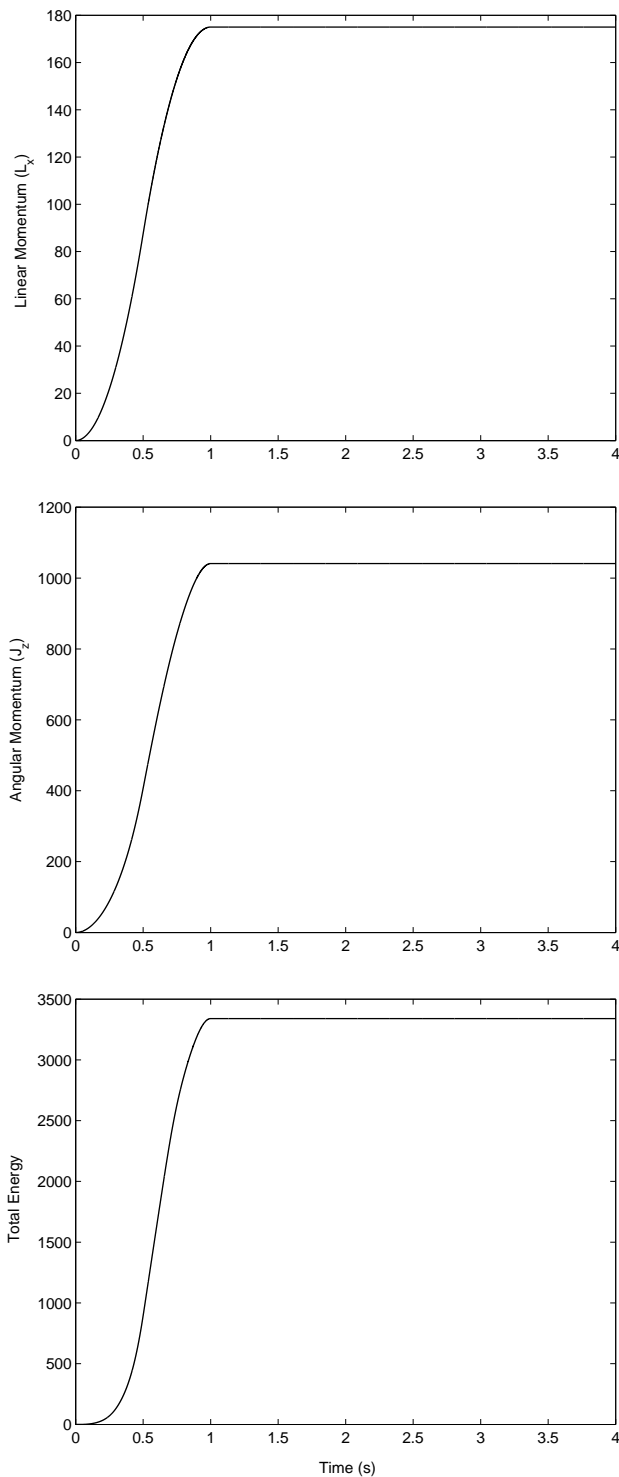


Figure 25. L-block problem: time history of the x component of the linear momentum (top), the z component of the angular momentum (middle), and total energy (bottom).

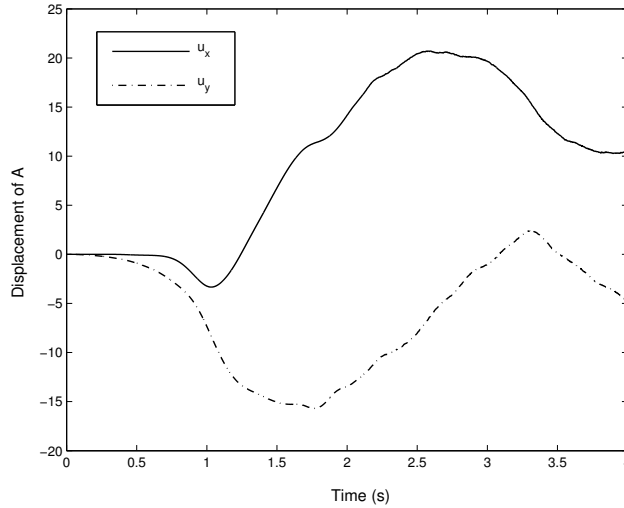


Figure 26. L-block problem: (u_x, u_y) displacements of point A.

beams/plates/shells, as well as “chunky” 3D structures, in an economical way. Good coarse-mesh accuracy is obtained even on demanding problems such as the panel buckling and toss rule problems, and since there appears to be no degradation in accuracy with mesh refinement (for a given time step), as opposed to some other strategies presented in the literature, an algorithmic modification that would dissipate higher frequencies introduced due to mesh refinement does not appear to be necessary. An exact tangent stiffness matrix has been formulated and used, resulting in a quadratic rate of convergence in the vicinity of the solution, and thereby resulting in a reduced number of iterations per time step compared with other strategies. Finally, since the stress parameters are condensed out at an element level, and the user works only with displacement degrees of freedom, the same input data structure used for standard displacement-based isoparametric hexahedral elements can also be used for these elements. Extensions of the current work to large-deformation plasticity and to contact problems would obviously be of interest.

References

- [Armero and Romero 2001a] F. Armero and I. Romero, “On the formulation of high-frequency dissipative time-stepping algorithms for nonlinear dynamics, I: Low-order methods for two model problems and nonlinear elastodynamics”, *Comput. Methods Appl. Mech. Eng.* **190**:20-21 (2001), 2603–2649.
- [Armero and Romero 2001b] F. Armero and I. Romero, “On the formulation of high-frequency dissipative time-stepping algorithms for nonlinear dynamics, II: Second-order methods”, *Comput. Methods Appl. Mech. Eng.* **190**:51-52 (2001), 6783–6824.
- [Balah and Al-Ghamedy 2005] M. Balah and H. N. Al-Ghamedy, “Energy-momentum conserving algorithm for nonlinear dynamics of laminated shells based on a third-order shear deformation theory”, *J. Eng. Mech. (ASCE)* **131**:1 (2005), 12–22.
- [Bauchau and Joo 1999] O. A. Bauchau and T. Joo, “Computational schemes for non-linear elasto-dynamics”, *Int. J. Numer. Methods Eng.* **45**:6 (1999), 693–719.
- [Bauchau et al. 2003] O. A. Bauchau, C. L. Bottasso, and L. Trainelli, “Robust integration schemes for flexible multibody systems”, *Comput. Methods Appl. Mech. Eng.* **192**:3-4 (2003), 395–420.

- [Betsch and Steinmann 2001] P. Betsch and P. Steinmann, “Conservation properties of a time FE method, II: Time-stepping schemes for non-linear elastodynamics”, *Int. J. Numer. Methods Eng.* **50**:8 (2001), 1931–1955.
- [Brank et al. 1998] B. Brank, L. Briseghella, N. Tonello, and F. B. Damjanić, “On non-linear dynamics of shells: implementation of energy-momentum conserving algorithm for a finite rotation shell model”, *Int. J. Numer. Methods Eng.* **42**:3 (1998), 409–442.
- [Cuadrado et al. 2001] J. Cuadrado, R. Gutiérrez, M. A. Naya, and M. P., “A comparison in terms of accuracy and efficiency between a MBS dynamic formulation with stress analysis and a non-linear FEA code”, *Int. J. Numer. Methods Eng.* **51**:9 (2001), 1033–1052.
- [Gonzalez 2000] O. Gonzalez, “Exact energy and momentum conserving algorithms for general models in nonlinear elasticity”, *Comput. Methods Appl. Mech. Eng.* **190**:13-14 (2000), 1763–1783.
- [Gupta 2000] A. Gupta, “WSMP: Watson Sparse Matrix Package, Part II – direct solution of general sparse systems”, Research Report RC 21888 (98472), IBM Corporation, Yorktown Heights, NY, 2000, Available at <http://www-users.cs.umn.edu/~agupta/doc/wsm2.pdf>.
- [Gupta 2002] A. Gupta, “Recent advances in direct methods for solving unsymmetric sparse systems of linear equations”, *ACM Trans. Math. Software* **28**:3 (2002), 321–324.
- [Jog 2005] C. S. Jog, “A 27-node hybrid brick and a 21-node hybrid wedge element for structural analysis”, *Finite Elem. Anal. Des.* **41**:11–12 (2005), 1209–1232.
- [Jog and Annabattula 2006] C. S. Jog and R. Annabattula, “The development of hybrid axisymmetric elements based on the Hellinger–Reissner variational principle”, *Int. J. Numer. Methods Eng.* **65**:13 (2006), 2279–2291.
- [Jog and Kelkar 2006] C. S. Jog and P. P. Kelkar, “Non-linear analysis of structures using high performance hybrid elements”, *Int. J. Numer. Methods Eng.* **68**:4 (2006), 473–501.
- [Kuhl and Crisfield 1999] D. Kuhl and M. A. Crisfield, “Energy-conserving and decaying algorithms in non-linear structural dynamics”, *Int. J. Numer. Methods Eng.* **45**:5 (1999), 569–599.
- [Kuhl and Ramm 1996] D. Kuhl and E. Ramm, “Constraint energy momentum algorithm and its application to non-linear dynamics of shells”, *Comput. Methods Appl. Mech. Eng.* **136**:3-4 (1996), 293–315.
- [Kuhl and Ramm 1999] D. Kuhl and E. Ramm, “Generalized energy-momentum method for non-linear adaptive shell dynamics”, *Comput. Methods Appl. Mech. Eng.* **178**:3-4 (1999), 343–366.
- [Laursen and Meng 2001] T. A. Laursen and X. N. Meng, “A new solution procedure for application of energy-conserving algorithms to general constitutive models in nonlinear elastodynamics”, *Comput. Methods Appl. Mech. Eng.* **190**:46-47 (2001), 6309–6322.
- [Lee and Rhiu 1986] S. W. Lee and J. J. Rhiu, “A new efficient approach to the formulation of mixed finite element models for structural analysis”, *Int. J. Numer. Methods Eng.* **23**:9 (1986), 1629–1641.
- [Pian and Sumihara 1984] T. H. H. Pian and K. Sumihara, “Rational approach for assumed stress finite elements”, *Int. J. Numer. Methods Eng.* **20**:9 (1984), 1685–1695.
- [Pian and Tong 1986] T. H. H. Pian and P. Tong, “Relations between incompatible displacement model and hybrid stress model”, *Int. J. Numer. Methods Eng.* **22**:1 (1986), 173–181.
- [Sansour et al. 2004] C. Sansour, P. Wriggers, and J. Sansour, “On the design of energy-momentum integration schemes for arbitrary continuum formulations: applications to classical and chaotic motion of shells”, *Int. J. Numer. Methods Eng.* **60**:15 (2004), 2419–2440.
- [Simo and Tarnow 1992] J. C. Simo and N. Tarnow, “The discrete energy-momentum method: conserving algorithms for nonlinear elastodynamics”, *Z. Angew. Math. Phys.* **43**:5 (1992), 757–792.
- [Simo and Tarnow 1994] J. C. Simo and N. Tarnow, “A new energy and momentum conserving algorithm for the non-linear dynamics of shells”, *Int. J. Numer. Methods Eng.* **37**:15 (1994), 2527–2549.
- [Sze and Fan 1996] K. Y. Sze and H. Fan, “An economical assumed stress brick element and its implementation”, *Finite Elem. Anal. Des.* **21**:3 (1996), 179–200.
- [Xue et al. 1985] W.-M. Xue, L. A. Karlovitz, and S. N. Atluri, “On the existence and stability conditions for mixed-hybrid finite element solutions based on Reissner’s variational principle”, *Int. J. Solids Struct.* **21**:1 (1985), 97–116.

[Yakoub and Shabana 2001] R. Yakoub and A. A. Shabana, “Three dimensional absolute nodal coordinate formulation for beam elements: implementation and applications”, *J. Mech. Des. (ASME)* **123**:4 (2001), 614–621.

Received 23 Nov 2008. Revised 7 Jan 2009. Accepted 5 Feb 2009.

C. S. JOG: jogc@mecheng.iisc.ernet.in

Department of Mechanical Engineering, Indian Institute of Science, Bangalore 560012, India

PHANI MOTAMARRI: phani.255@gmail.com

Department of Mechanical Engineering, Indian Institute of Science, Bangalore 560012, India

SUBMISSION GUIDELINES

ORIGINALITY

Authors may submit manuscripts in PDF format on-line. Submission of a manuscript acknowledges that the manuscript is *original and has neither previously, nor simultaneously, in whole or in part, been submitted elsewhere*. Information regarding the preparation of manuscripts is provided below. Correspondence by email is requested for convenience and speed. For further information, write to:

[Marie-Louise Steele](#)
Division of Mechanics and Computation
Durand Building, Room 262
Stanford University
Stanford CA 94305

LANGUAGE

Manuscripts must be in English. A brief abstract of about 150 words or less must be included. The abstract should be self-contained and not make any reference to the bibliography. Also required are keywords and subject classification for the article, and, for each author, postal address, affiliation (if appropriate), and email address if available. A home-page URL is optional.

FORMAT

Authors are encouraged to use L^AT_EX and the standard article class, but submissions in other varieties of T_EX, and, exceptionally in other formats, are acceptable. Electronic submissions are strongly encouraged in PDF format only; after the refereeing process we will ask you to submit all source material.

REFERENCES

Bibliographical references should be listed alphabetically at the end of the paper and include the title of the article. All references in the bibliography should be cited in the text. The use of B^BT_EX is preferred but not required. Tags will be converted to the house format (see a current issue for examples), however, in the manuscript, the citation should be by first author's last name and year of publication, e.g. "as shown by Kramer, et al. (1994)". Links will be provided to all literature with known web locations and authors are encouraged to provide their own links on top of the ones provided by the editorial process.

FIGURES

Figures prepared electronically should be submitted in Encapsulated PostScript (EPS) or in a form that can be converted to EPS, such as GnuPlot, Maple, or Mathematica. Many drawing tools such as Adobe Illustrator and Aldus FreeHand can produce EPS output. Figures containing bitmaps should be generated at the highest possible resolution. If there is doubt whether a particular figure is in an acceptable format, the authors should check with production by sending an email to:

production@mathscipub.org

Each figure should be captioned and numbered so that it can float. Small figures occupying no more than three lines of vertical space can be kept in the text ("the curve looks like this:"). It is acceptable to submit a manuscript with all figures at the end, if their placement is specified in the text by means of comments such as "Place Figure 1 here". The same considerations apply to tables.

WHITE SPACE

Forced line breaks or page breaks should not be inserted in the document. There is no point in your trying to optimize line and page breaks in the original manuscript. The manuscript will be reformatted to use the journal's preferred fonts and layout.

PROOFS

Page proofs will be made available to authors (or to the designated corresponding author) at a web site in PDF format. Failure to acknowledge the receipt of proofs or to return corrections within the requested deadline may cause publication to be postponed.

Journal of Mechanics of Materials and Structures

Volume 4, N^o 1 January 2009

Analysis of multiple axisymmetric annular cracks	EBRAHIM ASADI, SHAHRIAR FARIBORZ AND MOJTABA AYATOLLAHI	1
Classical and mixed advanced models for sandwich plates embedding functionally graded cores	SALVATORE BRISCHETTO	13
Vibration suppression analysis of FGM shells with higher order shear deformation theory	SURESH CHANDRA PRADHAN	35
Viscoelastic state of a semi-infinite medium with multiple circular elastic inhomogeneities	ANDREY V. PYATIGORETS AND SOFIA G. MOGILEVSKAYA	57
Comparative study of symmetric and asymmetric deformation of Al single crystal under microscale laser shock peening	SINIŠA VUKELIĆ, YOUNENG WANG, JEFFREY W. KYSAR AND Y. LAWRENCE YAO	89
Nonuniform interfacial slip in fibrous composites	XU WANG	107
Investigating the secondary buckling of thin films with a model based on elastic rods with hinges	GUILLAUME PARRY, CHRISTOPHE COUPEAU, JÉRÔME COLIN AND ALAIN CIMETIÈRE	121
Fundamental solution in the theory of viscoelastic mixtures	SIMONA DE CICCIO AND MERAB SVANADZE	139
An energy-momentum conserving algorithm for nonlinear transient analysis within the framework of hybrid elements	C. S. JOG AND M. PHANI SUDHEER	157